

Dissipation as a resource in circuit quantum electromechanics

THÈSE N° 8709 (2018)

PRÉSENTÉE LE 8 JUIN 2018

À LA FACULTÉ DES SCIENCES DE BASE

LABORATOIRE DE PHOTONIQUE ET MESURES QUANTIQUES (SB/STI)

PROGRAMME DOCTORAL EN PHOTONIQUE

ÉCOLE POLYTECHNIQUE FÉDÉRALE DE LAUSANNE

POUR L'OBTENTION DU GRADE DE DOCTEUR ÈS SCIENCES

PAR

László Dániel TÓTH

acceptée sur proposition du jury:

Prof. N. Grandjean, président du jury

Prof. T. Kippenberg, Dr O. Feofanov, directeurs de thèse

Prof. G. Steele, rapporteur

Prof. J. Fink, rapporteur

Prof. G. Villanueva, rapporteur



ÉCOLE POLYTECHNIQUE
FÉDÉRALE DE LAUSANNE

Suisse
2018

Without a constant misuse of language, there cannot be any discovery, any progress.
— Paul K. Feyerabend

To my family and friends, even if they have better things to do than reading this . . .

Acknowledgements

The work which is summarised in this thesis could not have been done without the help of many people. First, I would like to thank my supervisor, Tobias Kippenberg for giving his ideas and unlimited energy to the projects. And when I write unlimited, I mean literally endless. His guidance was essential in delivering the results and I have learned a great deal during this work. I also thank Alexey Feofanov for his ideas and his always prompt willingness to share his expertise and extensive knowledge on a wide variety of topics. We started this effort in the group from scratch and have sailed quite a long way - sometimes maybe losing sight of the shore and through choppy waters, but eventually arriving to agreeable lagoons. I also thank our theory collaborators in Cambridge, Andreas Nunnenkamp and Daniel Malz; their impressive theory knowledge is only surpassed by their patience and efficiency.

A special thanks goes to my coworker and friend, Nathan Bernier. Surely, his contributions were essential to the projects and this thesis would have taken a very different form without him but more importantly, he made these years in the lab and the office not only survivable but actually pretty fun. We probably surprised both external observers (i.e. office- and labmates) and ourselves by the fact that despite our extensive discussions on a wide variety of - sometimes rather obscure - topics, jokes on everything possible, beer and whisky tastings (strictly after working hours) and more, we did manage to get some things done.

There are many people in the group who made my time more memorable during the PhD. I thoroughly enjoyed the stimulating discussions with Vivishek, Dal, Nico, Clément, Nils and, in the early days, with Emmanuel and Wolfgang; the skiing and biking sessions with Victor; the concerts and skiing with Philippe, who also - almost voluntarily - became my cultural advisor. I thank John for, well, being very John in the good sense. I apologise to the “nano team”, Itay and Liu, for making so many internal jokes; I promise I am only half serious about them. I also thank all the master students who supported this work, in particular Akshay, Marie and Jeremy, as well as the new generation of PhD students - Nick and Amir - on the project. I wish them good luck; it will not be a walk in the park but that is for retirees anyway.

I met great people at EPFL who made me - and sometimes forced me to be - balanced and well-rounded. I was fortunate to have joined and spent a significant amount of time

Acknowledgements

in two associations: ShARE and The Consulting Society. Even though juggling the time was challenging, it kept me sane and it was a pleasure to work with Giel, Alex, Aleks, Fernando, Filip, Roman and many others. A sincere thanks to Galyna for all the personal support and friendship; to Svenja and Miguel for all the great snowboarding and other fun; to Anna for all the great activities; to Marie for the support and cultural input; and to Darja for enduring my imposed “therapy sessions”.

I also thank all my friends back at home and abroad; they have been continuously proving that I have excellent people to rely on at any time which is priceless to me.

A special thanks goes to Chika who could tolerate me even at these recent, occasionally difficult times. I appreciate her support and warmth and I am looking forward to our new adventures!

Finally, I cannot possibly express all the gratitude to my family. To my sister, who occupies the family philosopher position so I don’t have to; and to my parents, without whose continuous support this work would not have even been started, let alone finished. They have always let me be who I wanted to be, do what I wanted to do and I could always figure out my own ways. I am simply grateful.

Lausanne, 18 April 2018

L. D. T.

Abstract

A primary challenge in quantum science and technology is to isolate the fragile quantum states from their environment in order to prevent the irreversible leakage of energy and information which causes decoherence. In the late 1990s, however, a new paradigm emerged, in which the environment itself, as well as the coupling to this environment of the quantum state, are engineered in ways which, counterintuitively, facilitate the creation and stabilization of desired quantum properties. This paradigm, coined reservoir engineering, has been pursued experimentally in various implementations, in which the states of trapped ions, atomic clouds or artificial atoms based on superconducting circuits were driven into a desired target state using a dissipative reservoir. In all these cases, the cold electromagnetic environment served as the engineered reservoir, capitalizing on the fact that high frequency electromagnetic radiation is naturally cold, as well as on the tremendous progress in the ability to shape the modes of the electromagnetic field using masers and lasers.

In optomechanics, which is the study of the coupling between light and mechanical motion, a similar scenario has been prevalent. Light is used to read out and control the mechanical motion, and in the past few years, various optomechanical architectures both in the optical and microwave domain have enabled to push mechanical systems into the quantum regime. These results can be interpreted in the context of reservoir engineering: cooling and many other optomechanical phenomena exploit the cold, dissipative nature of light.

This thesis reports on the development of a multimode superconducting circuit with a mechanically compliant element - fitting into the field of circuit cavity electromechanics -, with which we pursue two themes. In the first set of experiments, reversing the roles of dissipation described above, we engineer the mechanical oscillator into a cold, dissipative environment *for* microwave light. The mechanical element is the fundamental mode of a free-standing top electrode of a capacitor, 100 nm thick and 32 μm in diameter made of aluminum with an effective mass of around 170 pg, vibrating at a resonance frequency of 5.5 MHz. The dissipative mechanical reservoir is prepared using an auxiliary microwave mode with engineered parameters. A key challenge - and ingredient - for the scheme is the vastly different energy decay rates of the two microwave modes, which we overcome by

Acknowledgements

a circuit design which supports a bright and a dark mode. Once the mechanical reservoir is prepared, we utilize it to control the properties - in particular, the susceptibility - of the electromagnetic field and to perform low-noise amplification close to the quantum limit. The noise analysis reveals that the reservoir is close to its quantum ground state with a mean thermal occupation number well below 1, demonstrating its utility as a resource in the quantum regime. We also show that the system can be driven to the parametric instability threshold, above which self-sustained oscillations of the microwave field (masing) is observed. Finally, we demonstrate injection locking of the maser using an external seed pump.

In a second set of experiments, a similar electromechanical circuit is used to implement a microwave isolator based on optomechanical interactions. The overarching theme is that dissipation of the mechanical oscillator, albeit intrinsic and not engineered via an auxiliary mode in this case, is a key ingredient for the device to function as a nonreciprocal frequency converter and isolator. In these experiments, an additional mechanical mode is used, such that a 4-mode optomechanical plaquette is realized. We demonstrate over 20 dB of isolation and the reconfigurability of the direction of isolation by tuning the relative phase of the control pumps.

Keywords: microwave optomechanics, multimode optomechanics, reservoir engineering, engineered dissipation, superconducting circuits, quantum-limited amplification, nonreciprocal devices, quantum noise

Zusammenfassung

Eine besondere Herausforderung für die Quantenwissenschaft besteht darin einzelne Quantenzustände von ihrer Umgebung zu isolieren und somit den irreversiblen Verlust von Energie und Information zu verhindern. Ein großer Durchbruch gelang in den 1990er Jahren, als man realisierte, dass die Manipulation von sowohl der Umgebung und als auch die Kopplung der Quantenzustände an die Umgebung die Erzeugung und Stabilisierung gewünschter Quanteneigenschaften vereinfacht. Die Technik des sogenannten «reservoir engineering»s wurde in verschiedenen Experimenten verwendet, um Zustände von gefangenen Ionen, atomaren Wolken oder künstlichen Atomen, bestehend aus supraleitenden Schaltkreisen, mittels eines dissipativen Reservoirs in einen gewünschten Zielzustand zu bringen. In all diesen Fällen diente die elektromagnetische Umgebung, welche von Natur aus bei hohen Frequenzen kalt ist, als Reservoir. Dies wurde durch den grossen Fortschritt in den Methoden, elektromagnetische Moden mit Hilfe von Masern und Lasern zu generieren, ermöglicht.

Im Feld der Optomechanik, welches die Interaktion zwischen Licht und mechanischen Bewegungen behandelt, wurde eine ähnliche Herangehensweise verwendet. Licht wird genutzt um mechanische Bewegungen zu messen und zu kontrollieren. Seit den letzten Jahren haben es optomechanische Systeme, sowohl im Optischen- als auch im Mikrowellenregime, geschafft, mechanische Systeme in das Quantenregime zu befördern. Diese Resultate können in den Kontext des «reservoir engineering»s gebracht werden: Kühlen und viele andere optomechanische Phänomene nutzen die kalte und dissipative Natur des Lichtes.

Diese Doktorarbeit beschreibt die Entwicklung eines mehrmodigen supraleitenden Schaltkreis mit einem mechanischen Element - passend in das Feld der «circuit cavity electro-mechanics» - mit dem zwei Zwecke verfolgt werden.

Durch das Vertauschen der Rollen zwischen Licht und der Mechanik in der Dissipation, bringen wir in einem ersten Satz von Experimenten den mechanischen Oszillator in eine kalte und dissipative Umgebung für das Mikrowellenlicht. Das mechanische Element ist die Fundamentalmode einer freistehenden Elektrode eines Kondensators aus Aluminum mit einer Dicke von 100 nm, einem Durchmesser von 32 μm , einer effektiven Masse von 170

Acknowledgements

pg und einer Vibrationsfrequenz von 5.5 MHz. The Vorbereitung des dissipativen mechanischen Reservoirs wurde durch eine weitere Mikrollenenmode realisiert. Die entscheidende Herausforderung - und Zutat – für das Schema sind die stark verschiedenen Abklingraten der zwei Mikrowellenmoden, welche wir durch einen Schaltkreis, der eine helle und dunkle mode besitzt, bewältigen. Sobald das mechanische Reservoir präpariert ist, benutzen wir es, um die Eigenschaften – insbesondere die Suszeptibilität – des elektromagnetischen Feldes zu manipulieren und rauscharme Verstärkung nahme am Quantenlimit zu betreiben. Eine sorgfältige Analyse des Rausches offenbart, dass das Reservoir Nahe an Quantengrundzustand mit einer mittleren thermischen Besetzungszahl von weniger als 1 ist, was die Nutzbarkeit des mechanischen Oszillators als Ressource im Quantenregime zeigt. Wir zeigen zusätzlich, dass das System über die parametrische Instabilitätsschwelle getrieben werden kann, wo selbsterhaltende Oszillationen des Mikrowellenfelds (Masing) beobachtet werden können. Zuletzt demonstrieren wir “Injection Locking” des Masers mittels eines schwachen externen Mikrowellentons (seed pump).

In einer zweiten Experimentierreihe wird ein elektromechanischer Schaltkreis benutzt, um einen Mikrowellenisolator basierend auf optomechanischen Interaktionen zu implementieren. Das allumfassende Thema ist, dass die Dissipation der mechanischen Oszillators, wenn auch in diesem Fall intrinsischer Natur und nicht erzeugt via einer zusätzlichen Mode, der Schlüsselfaktor für die Funktion des Geräts als nichtreziproker Frequenzwandler und Isolator ist. In den Experimenten wird eine viermodige optomechanische Plaqueette mittels einer zusätzlichen mechanischen Mode realisiert. Wir demonstrieren eine Isolation von über 20dB und die Einstellbarkeit der Richtung der Isolation durch das Verstellen der relativen Phase der Steuermikrowellentöne.

Stichwörter: Mikrowellenoptomechanik, mehrmodige Optomechanik, reservoir engineering, supraleitende Schaltkreise, quantenlimitierte Verstärkung, nichtreziproke Geräte, Quantenrauschen

Resumé

Un défi majeur en science et technologie quantiques est d'isoler les fragiles états quantiques de leur environnement, afin d'empêcher la perte irréversible d'énergie et d'information qui causerait la décohérence quantique. A la fin des années 90 cependant, un nouveau paradigme fut introduit, dans lequel l'environnement même ainsi que le couplage du système quantique à son environnement sont façonnés de manière à créer et stabiliser certaines propriétés quantiques désirées. Ce paradigme, nommé "reservoir engineering", a été réalisé expérimentalement de manières diverses, que ce soit pour façonner l'état quantique d'ions piégés, de nuages atomiques, ou d'atomes artificiels réalisés à partir de circuits supraconducteurs. Dans chacun des cas, l'environnement électromagnétique froid sert de réservoir, utilisant d'une part le fait que les ondes électromagnétiques, de haute fréquence, sont naturellement froides et d'autre part les progrès énormes dans la maîtrise des modes électromagnétiques par l'utilisation de lasers et masers.

En optomécanique, l'étude du couplage entre lumière et déplacement mécanique, un scénario similaire s'est déroulé. La lumière est utilisée pour mesurer et contrôler le mouvement mécanique. Dans les dernières années, de nouvelles architectures optomécaniques ont permis de pousser ce contrôle dans le régime quantique, dans le régime des fréquences optiques et micro-ondes. Ces résultats peuvent être interprétés dans le contexte du "reservoir engineering" : la basse température et l'aspect dissipatif des ondes électromagnétiques sont essentielles.

Cette thèse relate le développement d'un circuit supraconducteur multimode qui contient un élément mécanique (réalisant par là un système optomécanique) avec lequel nous réalisons des expériences avec deux thèmes distincts.

Dans le premier groupe d'expériences, nous inversons les rôles de dissipations décrits plus haut et transformons l'oscillateur mécanique en un environnement dissipatif froid pour le mode micro-onde. L'élément mécanique est le mode fondamental de l'électrode supérieure flottante d'un condensateur de 100 nm d'épaisseur et 32 μm de diamètre, fait d'aluminium avec une masse effective d'environ 170 pg, et vibrant à une fréquence de résonance de 5.5 MHz. Le réservoir dissipatif mécanique est préparé à l'aide d'un mode micro-onde auxiliaire aux propriétés déterminées. Un ingrédient nécessaire mais présentant un défi

Acknowledgements

majeur, est d’obtenir des taux de perte d’énergie à des échelles très différentes, pour les deux modes micro-ondes, ce que nous parvenons à réaliser par un design de circuit dans lequel des modes brillant et sombre sont formés. Une fois le réservoir mécanique préparé, nous l’utilisons pour contrôler les propriétés du mode électromagnétique, en particulier sa susceptibilité, de telle sorte à réaliser un amplificateur micro-onde proche de la limite quantique en terme de bruit. Une analyse du bruit révèle que le réservoir mécanique est proche de son état quantique fondamental, avec une occupation thermique bien en deçà d’un quanta, ce qui prouve qu’il constitue une ressource quantique utile. Nous montrons également que le système peut être placé dans le régime au-delà du seuil de l’instabilité paramétrique où il développe des oscillations amplifiées du champ micro-onde (maser). Pour finir, nous réalisons du “injection locking” du maser avec une source micro-onde externe.

Dans le second groupe d’expériences, un circuit électromécanique similaire est utilisé pour implementer un isolateur micro-onde basé sur les interactions optomécaniques. Ici également, la dissipation joue le rôle clé, bien qu’ici intrinsèque au mode et non-augmentée, et est nécessaire au fonctionnement nonréciproque du dispositif en tant que convertisseur de fréquence isolateur. Dans cette expérience, un mode mécanique additionnel est requis de telle sorte à réaliser une plaquette optomécanique constituée de 4 modes. Plus de 20 dB d’isolation sont réalisés dans un dispositif dont la direction d’isolation peut être reconfigurée en réglant les phases relatives des sources micro-ondes.

Mots clés : micro-onde optomécanique, reservoir engineering, dissipation, circuits supra-conducteurs, amplification limitée quantique, dispositif nonréciproque, bruit quantique

List of publications

- N. R. Bernier, **L. D. Tóth**, A. K. Feofanov and T. J. Kippenberg: Nonreciprocity in microwave optomechanical circuits. To appear in a special issue "Magnet-less Nonreciprocity in Electromagnetics" in IEEE Antennas and Wireless Propagation Letters.
- N. R. Bernier, **L. D. Tóth**, A. K. Feofanov and T. J. Kippenberg: Observation of level attraction in a circuit optomechanical system. Submitted.
Arxiv: <https://arxiv.org/abs/1709.02220>
- D. Malz, **L. D. Tóth**, N. R. Bernier, A. K. Feofanov, T. J. Kippenberg and A. Nunnenkamp: Quantum-limited directional amplifiers with optomechanics. *Physical Review Letters* **120**, 023601 (2018)
- **L. D. Tóth**, N. R. Bernier, A. Nunnenkamp, A. K. Feofanov and T. J. Kippenberg: A dissipative quantum reservoir for microwave light using a mechanical oscillator. *Nature Physics* **13**, 787-793 (2017)
Arxiv: <https://arxiv.org/abs/1602.05180>
- **L. D. Tóth**, N. R. Bernier, A. K. Feofanov and T. J. Kippenberg: A maser based on dynamical backaction on microwave light. *Physics Letters A*, In press, available online: <https://doi.org/10.1016/j.physleta.2017.05.045> (2017)
Arxiv: <https://arxiv.org/abs/1705.06422>
- N. R. Bernier, **L. D. Tóth**, A. Koottandavida, M. A. Ioannou, D. Malz, A. Nunnenkamp, A. K. Feofanov and T. J. Kippenberg: Nonreciprocal reconfigurable microwave optomechanical circuit. *Nature Communications* **8**, 604 (2017)
Arxiv: <https://arxiv.org/abs/1612.08223>
- C. Javerzac-Galy, K. Plekhanov, N. R. Bernier, **L. D. Tóth**, A. K. Feofanov and T. J. Kippenberg: On-chip microwave-to-optical quantum coherent converter based on a superconducting resonator coupled to an electro-optic microresonator. *Physical Review A* **94**, 053815 (2016) Arxiv: <https://arxiv.org/abs/1512.06442>

Contents

| | |
|---|------------|
| Acknowledgements | i |
| Abstract (English/Français/Deutsch) | iii |
| List of publications | ix |
| 1 Introduction | 1 |
| 2 Cavity optomechanics with superconducting circuits | 11 |
| 2.1 Optomechanics and electromechanics | 11 |
| 2.1.1 Dissipation and input-output theory | 14 |
| 2.1.2 Optomechanical cooling and amplification | 17 |
| 2.2 Elements of microwave engineering | 19 |
| 2.2.1 Transmission line theory | 19 |
| 2.2.2 RLC circuit coupled to the feedline | 22 |
| 2.3 The quantum limit of amplification | 26 |
| 3 Design and fabrication | 33 |
| 3.1 Background and process development | 33 |
| 3.1.1 Process overview | 35 |
| 3.1.2 Current recipe | 36 |
| 3.1.3 Additional methods: electron beam lithography and planarization . | 47 |
| 3.1.4 Experiments with titanium nitride | 49 |
| 3.2 Design: simulations and circuit layout | 51 |
| 3.2.1 Simulation methods: Sonnet and FastHenry | 51 |
| 3.2.2 Dual-mode circuit with a split-plate capacitor | 52 |
| 3.2.3 Hybrid-mode circuits | 53 |
| 4 Measurement setup and characterization | 57 |
| 4.1 Sample preparation and device packaging | 57 |
| 4.2 The dilution refrigerator | 58 |
| 4.2.1 Operation principle | 59 |

Contents

| | | |
|----------|---|------------|
| 4.2.2 | Microwave setup | 60 |
| 4.2.3 | Noise calibration of the HEMT amplifier | 68 |
| 4.3 | Device characterization | 72 |
| 4.3.1 | Extracting the parameters of the microwave resonance | 74 |
| 4.3.2 | Optomechanically induced transparency and reaching the strong coupling regime | 77 |
| 4.3.3 | Ring-down measurements | 79 |
| 4.3.4 | Thermalization, calibration of g_0 | 81 |
| 5 | A quantum reservoir for microwave light using a mechanical oscillator | 87 |
| 5.1 | Motivation | 87 |
| 5.2 | The role of dissipation in dynamical backaction | 88 |
| 5.3 | Optomechanical circuit with dark and bright modes | 91 |
| 5.3.1 | System-reservoir treatment of bright and dark modes | 94 |
| 5.4 | Realization of a dissipative mechanical reservoir | 95 |
| 5.5 | Experimental observation of dynamical backaction on microwave light | 97 |
| 5.5.1 | Maser action and amplification | 102 |
| 5.5.2 | Injection locking | 106 |
| 5.6 | Near-quantum-limited amplification | 107 |
| 5.7 | Notes on noise calibrations | 109 |
| 5.8 | Conclusions | 112 |
| 6 | Nonreciprocal microwave conversion using a mechanical oscillator | 115 |
| 6.1 | Introduction and motivation | 115 |
| 6.2 | A canonical nonreciprocal device: the gyrator | 117 |
| 6.3 | Theoretical model of nonreciprocity in the 4-mode plaquette | 119 |
| 6.3.1 | Conditions for isolation | 123 |
| 6.4 | Experimental results | 124 |
| 6.4.1 | Isolation | 126 |
| 6.4.2 | Noise properties | 127 |
| 7 | Summary and outlook | 131 |
| A | Fabrication process runcards | 135 |
| B | Wafer and chip layout | 139 |
| C | Derivation of the gain, added noise and output spectrum | 143 |
| D | Impact of noise on the microwave source | 147 |
| | Bibliography | 165 |

| | |
|------------------|-----|
| Curriculum Vitae | 167 |
|------------------|-----|

List of Figures

| | | |
|------|---|----|
| 1.1 | The multimode electromechanical device featured in the thesis. | 8 |
| 2.1 | Schematic representation of optomechanical systems in the optical and microwave domain | 12 |
| 2.2 | Circuit representation of lossless transmission lines | 20 |
| 2.3 | Visualisation of the microstrip line which serves as a feedline to couple microwave energy into the electromechanical circuit | 22 |
| 2.4 | An RLC circuit inductively coupled to a feedline | 23 |
| 2.5 | Plot of the S parameters for different port configurations and coupling ratios | 25 |
| 2.6 | Quadrature space representation of a signal | 27 |
| 2.7 | Schematic of a linear amplifier | 27 |
| 3.1 | Superconducting electromechanical device using a stressed nanostring . . . | 35 |
| 3.2 | The general overview of the process to fabricate a superconducting circuit with a mechanically compliant vacuum-gap capacitor | 37 |
| 3.3 | Main fabrication steps of the current, final process flow for fabricating superconducting electromechanical circuits | 38 |
| 3.4 | Details of patterning the sacrificial layer | 39 |
| 3.5 | Effect of the sidewall slope of the sacrificial layer | 42 |
| 3.6 | Visualization of the fabrication process from top view | 43 |
| 3.7 | Scanning electron micrograph of the vacuum-gap capacitor | 43 |
| 3.8 | Comparison of different release processes | 44 |
| 3.9 | Comparison of different thin film deposition methods of the top Al layer . | 45 |
| 3.10 | Example of a COMSOL simulation of displacement and stress of the vacuum-gap capacitor | 46 |
| 3.11 | Optical micrograph and topography of the electromechanical circuit | 47 |
| 3.12 | Interference microscopy measurements on various vacuum-gap capacitors . | 48 |
| 3.13 | Process flow for planarizing the sacrificial layer | 49 |
| 3.14 | Scanning electron micrograph and optical topography measurement of a split-plate vacuum-gap capacitor | 50 |
| 3.15 | Process flow for TiN on sapphire | 51 |

List of Figures

| | | |
|------|--|----|
| 3.16 | Circuit layout of the dual-mode circuit with a split-plate capacitor | 53 |
| 3.17 | Simulation of the first generation of the multi-mode circuit design | 54 |
| 3.18 | Simulation of the hybrid circuit with the bright and dark modes | 54 |
| 4.1 | Probing the vacuum-gap capacitor at room temperature using an interferometric optical setup | 58 |
| 4.2 | Photograph of the sample holder with the device | 59 |
| 4.3 | Schematic of the working principle and photograph of the dilution refrigerator | 61 |
| 4.4 | Properties of the He isotopes with respect to temperature | 62 |
| 4.5 | Overview of the experimental setup | 62 |
| 4.6 | Amplitude and phase noise of the employed sources measured at different output powers | 63 |
| 4.7 | Custom-made tunable copper filter cavity to reduce phase noise | 64 |
| 4.8 | Spectrum at the output of the fridge with and without tone cancellation . | 65 |
| 4.9 | Noise and filtering of a pump tone far away from the carrier frequency . . | 68 |
| 4.10 | cheme to describe the model of a noisy amplifier | 70 |
| 4.11 | Experimental scheme for calibrating the HEMT noise | 70 |
| 4.12 | Example of a calibration of the HEMT amplifier in terms of gain and noise temperature | 71 |
| 4.13 | Equivalent circuit representation of the 2-port system with impedance mismatches | 74 |
| 4.14 | Fitting the vector network analyser data to extract parameters of the microwave resonances | 76 |
| 4.15 | Equivalent circuit representation of the 1-port system with impedance mismatch | 77 |
| 4.16 | Experimental demonstration of optomechanically induced transparency . . | 79 |
| 4.17 | Power sweep of the pump placed at the red sideband versus the width of the OMIT feature for two different mechanical modes | 80 |
| 4.18 | Experimental observation of strong coupling using two-tone spectroscopy . | 80 |
| 4.19 | Experimental setup to perform ring-down measurements | 81 |
| 4.20 | Example of ring-down measurements | 82 |
| 4.21 | Thermalization of the mechanical oscillator | 83 |
| 4.22 | Schematic for calibrating the optomechanical vacuum coupling strength g_0 | 84 |
| 4.23 | The thermomechanical sideband for calibrating g_0 | 85 |
| 5.1 | The role of dissipation in dynamical backaction in the feedback picture . . | 91 |
| 5.2 | Schematic representation of a cold dissipative mechanical reservoir | 92 |
| 5.3 | Circuit realization of the electromechanical system with circuit topology, mode structure and frequency landscape | 93 |

| | | |
|------|--|-----|
| 5.4 | Optomechanically induced transparency on the bright mode demonstrating the preparation of the dissipative mechanical reservoir | 96 |
| 5.5 | Device, experimental setup, and characterization of the multi-mode electromechanical circuit | 98 |
| 5.6 | Linear response measurement of the hybrid-mode electromechanical device showing the bright and dark modes | 99 |
| 5.7 | Coherent response of the microwave cavity coupled to the mechanical reservoir | 99 |
| 5.8 | Modification of the microwave susceptibility on resonance | 100 |
| 5.9 | The mechanical spring effect | 101 |
| 5.10 | Amplified vacuum fluctuations and parametric instability of the microwave mode (masing) | 103 |
| 5.11 | Near-quantum-limited phase-preserving amplification with the dissipative mechanical reservoir | 105 |
| 5.12 | Injection locking of the maser based on dynamical backaction | 107 |
| 5.13 | Improvement of the signal-to-noise ratio over the HEMT amplifier in and out of band | 108 |
| 5.14 | Thermal occupancy of the microwave cavity with respect to pump power . | 112 |
| 6.1 | The gyrator and optomechanical frequency conversion | 118 |
| 6.2 | Gyrator-based isolator and its implementation in a multimode optomechanical scheme. | 120 |
| 6.3 | Optomechanical nonreciprocal transmission via interference of two asymmetric dissipative coupling pathways | 122 |
| 6.4 | Implementation of a superconducting microwave circuit optomechanical device for nonreciprocity. | 125 |
| 6.5 | Experimental demonstration of nonreciprocity | 126 |
| 6.6 | Asymmetric noise emission of the nonreciprocal circuit | 128 |
| 7.1 | Integrating a Josephson travelling wave parametric amplifier into the setup. | 132 |
| 7.2 | Frequency scheme for generating squeezed light with a dissipative mechanical reservoir. | 133 |
| 7.3 | Envisioned process flow to fabricated stressed NbSe ₂ vacuum gap capacitors. | 134 |
| B.1 | Layout of the wafer. | 140 |
| B.2 | Layout of a typical chip. | 141 |

List of Tables

| | | |
|-----|--|-----|
| 3.1 | Summary of the materials and release process developed by various groups to fabricate superconducting circuits with a vacuum-gap capacitor | 36 |
| 3.2 | Simulated parameters of the hybrid-mode circuit | 55 |
| 5.1 | Summary of the most important experimental parameters to demonstrate dynamical backaction on microwave light with a dissipative reservoir, device 1 | 97 |
| 5.2 | Summary of the most important experimental parameters to demonstrate masing and low-noise microwave amplification with a dissipative reservoir, device 2 | 102 |
| A.1 | Runcard for the standard direct laser lithography. | 137 |
| A.2 | Runcard for the standard direct laser lithography. | 137 |
| A.3 | Runcard for the standard cleaning (performed after each lithography step and at the very end before release). | 138 |

1 Introduction

In the past few decades quantum mechanics has become arguably the most tested theoretical framework in physics. Albeit over a century old, it continues to challenge our understanding of the natural world at the smallest - and nowadays even larger - scales and it describes a plethora of counterintuitive phenomena. Quantum mechanics, at the very fundamental level, states that our knowledge of the world cannot be complete and that uncertainty and randomness are intrinsically present. From a technological standpoint, this might project a gloomy outlook: clearly, the performance of our measurement apparatuses at some point can hit a hard boundary dictated by quantum mechanics, a point from which no improvement is possible even theoretically.

While it is true that in some cases quantum mechanics can pose a limit on the operation of measurement devices, recently a new paradigm had emerged which aims to harness the laws of quantum mechanics for *enhanced* functionalities and capabilities. These are dubbed quantum-enabled, quantum-enhanced or simply quantum technologies. The enhancement over classical physics comes from three unique features present in quantum theory. The first one is the superposition principle, which states that if two vectors in Hilbert space represent two possible states of the system, then their superposition is also a possible state; moreover, if the original two states are non-orthogonal, then there is a possibility of interference. This is at the heart of quantum computing, which relies on the fact that many quantum bits in a superposition state can be manipulated simultaneously as a superposition state. Second, quantum measurements unavoidably introduce randomness and disturbances; more precisely, nonorthogonal states cannot be distinguished with certainty. While this is traditionally viewed as a limitation, it can lead to enhanced cryptography protocols which are unbreakable even in principle as well as truly random number generation. Third, the superposition of two or more states in a composite system can contain correlations unexplainable classically, as well as to entanglement. Entanglement has been shown to constitute a resource which can, for

example, enhance the precision of atomic clocks and atom interferometers by mitigating the quantum projection noise [1] or cancel the effects of dispersion and aberration to improve imaging [2, 3].

The thesis work falls into the broad topic of quantum technologies, even though we do not use any of the three features explicitly. In fact, we are trying to avoid the second feature by an exquisite control of a rather macroscopic metallic membrane using microwave light down to the quantum level; once this control is achieved, we utilize this membrane *for* controlling microwave fields. In a second experiment, an isolator is implemented using purely optomechanical interactions which can be integrated on-chip and does not require magnetic fields, therefore it is compatible with superconducting architectures for quantum information processing. The work is at the intersection of multiple fields such as optomechanics, superconducting circuits and reservoir engineering. These fields are briefly introduced below and the structure of the thesis is laid out.

Light and mechanical motion

During the preparation of this thesis work, in 2015, the world had celebrated the International Year of Light as declared by the United Nations, for which the major impetus was the 150th anniversary of James Clerk Maxwell's revolutionary and celebrated paper "A Dynamical Theory of the Electromagnetic Field" [4]. In this paper, Maxwell unified electricity and magnetism and derived the electromagnetic wave equation. Astoundingly, the speed of the electromagnetic wave was shown to be in close agreement with the speed of light - previously measured by Ole Rømer with an accuracy of about 30% -, proving that visible light is simply a part of the electromagnetic spectrum. From the electromagnetic wave equation it also follows that, despite the fact that light has no mass, electromagnetic waves can exert pressure (termed radiation pressure).

The notion of radiation pressure had already been used by Kepler as early as 1619, who observed that the tail of comets always faces away from the Sun [5]. However, this pressure turns out to be extremely small as it is inversely proportional to the speed of light. More precisely, when a plane wave bounces off from a perfectly reflective object, the radiation pressure it exerts is given by

$$P_{\text{rad}} = \frac{2I}{c},$$

where I is the average intensity of the electromagnetic plane wave, given by $I = \frac{E_{\text{max}}B_{\text{max}}}{2\mu_0}$. As an example, in terms of force, light from a commercial laser pointer can exert around 1 aN on an object, while 800 m by 800 m solar sail would produce approximately 5 N at Earth's distance away from the Sun. Therefore, despite some earlier efforts which were

hindered by thermodynamic effects, it was until much later, in the very beginning of the 20th century when radiation pressure was first reliably measured in two experiments, one by Lebedew [6] and one by Nichols and Hull [7, 8]. Since then, radiation pressure and the associated radiative forces have found numerous applications such as manipulation of atoms, molecules and tiny particles, laser cooling and trapping, or forming exotic states of matter like optical crystals or Bose-Einstein condensates.

A parallel advancement in physics was the use of mechanical systems as precise measurement devices, in particular for force sensing. A notable example is the torsion pendulum, with which for example Cavendish performed the first accurate measurement of the gravitational force between test masses, Coulomb established the Coulomb law (describing the interaction between charge particles) and Eötvös tested the equivalence principle between inertial mass and gravitational mass with a claimed accuracy of 1 in 20 million. More recently, these mechanical systems have been on the way of miniaturization and already reached commercial maturity in the late 80s. Typically, the small mechanical devices are coupled to electrical circuits to form micro-electro-mechanical systems (MEMS) or nano-electro-mechanical systems (NEMS). MEMS and NEMS are frequently used as transducers and are nowadays widely exploited in accelerometers, controllers, microphones and in many other technological applications.

The advent of the laser gave a huge boost to precision sensing, especially through the technique called laser interferometry. The basic idea of an interferometer is to exploit the fact that the generated interference pattern when multiple waves are superimposed is extremely sensitive to the optical path lengths of the constituent waves. A particular application of large-scale interferometry, which has gathered significant attention lately, is gravitational wave detection. The gravitational wave detectors currently in operation (LIGO, located in Livingston, Louisiana and Hanford, Washington) use two long (≈ 4 km), perpendicular interferometric arms with suspended kilogram-scale mirrors at each end which trap light, i.e. form optical cavities. The circulating laser light in these arms is used to measure the distance of both arms extremely precisely; the distortion of space caused by gravitational waves can then be measured provided that the system is well isolated and all other sources which can cause a change of a path lengths are ruled out. The first gravitational waves have been detected during the preparation of this thesis work [9].

In the context of a future gravitational wave detector, Braginsky and coworkers analysed the effect of the radiation pressure force as early as 1967 [10]. They have described that while radiation pressure affects the motion of the suspended mirror, the mirror's movement also affects the light circulating in the interferometric arms (which can be modelled by a high-finesse Fabry-Perot cavity, i.e. a cavity with two parallel mirrors

trapping light); therefore, a coupling - called the optomechanical coupling - is realized between the two degrees of freedom (optomechanics is the field of study concerned with the phenomena related to the optomechanical coupling). Interestingly, the energy decay rate of the optical cavity (the inverse of the photon lifetime in the cavity) comes into play considering that it causes a retardation of the radiation pressure force. This gives rise to dynamical backaction, in which the mechanical oscillator's susceptibility is modified depending on the frequency of the injected light: it can cause damping (i.e. can act as an extra viscous force) or anti-damping, as well as change the resonance frequency of the mechanical mode [11, 12]. In turn, damping or anti-damping can cool or amplify the motion of the mirror [13]; moreover, when anti-damping overcomes the intrinsic losses of the mechanical object, it can cause a parametric oscillatory instability of the motion [14]. This latter has been shown to limit the amount of optical power an interferometer with suspended mirrors can handle and was recently demonstrated experimentally in Advanced LIGO [15]. Dynamical backaction cooling of mechanical motion has a strong analogy to laser cooling and trapping of atoms, ions and neutral particles [16, 17, 18, 19] by means of the radiation pressure force.

In the past decade, the revival in the interest and the experimental progress of optomechanics are a result of advancements in micro- and nanofabrication techniques. Micro- and nanoscale structures in which the light mode and the mechanical mode are colocalized or can be placed very closed to each other benefit from much stronger optomechanical coupling and larger zero-point motion due to the reduced mass. There has been a plethora of different geometries and platforms developed in the optical domain (c.f. [20, 21] for a review) and they have enabled the demonstration of cooling mechanical motion with light [22] (previously also shown with a macroscopic mirror [23]), parametric instability driven by radiation-pressure backaction [24], optomechanically induced transparency [25, 26] quantum-coherent coupling between the two degrees of freedom [27], ground state cooling [28] among many other results.

Where quantum comes into play

When considering the measurement sensitivity of interferometric setups or optomechanical devices, there is an important and interesting subtlety. Quantum mechanics dictates that nothing can be at complete rest, even at absolute zero temperature. Every object has a ground state, the lowest possible energy level and the energy at the ground state is finite. This statement is closely related to the Heisenberg uncertainty principle and has important consequences. The first is that any physical object (e.g. a particle, the mechanical element in a MEMS or NEMS device, or the macroscopic mirror in a gravitational wave detector) has a finite, unavoidable, completely random jitter in its movement, coined the zero-point fluctuation. This in itself can pose a limit whenever the mechanical object is used as a

transducer. The second consequence is that, since light is also an entity described by quantum mechanics, the arrival time of photons to a photodetector is fundamentally random causing another unavoidable source of noise, the shot noise. Third, because of radiation pressure described above, light imparts a momentum on the measured object and this momentum is random, called radiation pressure shot noise. This is a manifestation of the more general concept of quantum back-action: whenever an object is being measured, it is also being disturbed in a fundamentally random way. Carefully assessing these noise contributions reveals that while shot noise scales as inverse the square root of power of the laser (so it can be arbitrarily reduced in principle), radiation pressure shot noise scales as the square root of power. Therefore, whenever the position of an object is measured, the total noise on the measurement has an absolute minimum called the standard quantum limit. Moreover, this absolute minimum of the noise is precisely the zero-point motion of the object to be measured, which is a reformulation of Heisenberg's uncertainty principle for continuous measurements

Intriguingly, the standard quantum limit also applies to the case of amplification since any amplifier essentially performs a measurement on the signal to be amplified. This fact has dramatic consequences in experimental quantum information processing, where noise can seriously affect the fragile quantum information typically encoded in qubits.

Electromechanics with superconducting circuits

In the past two decades, another area has been established to extend the toolbox of cavity quantum electrodynamics: the field of superconducting quantum circuits. A superconducting circuit is made of a thin film superconductor patterned on a dielectric substrate to form an electrical circuit. Typically, the circuits can be addressed from the external world by inductive or capacitive coupling by itinerant microwave fields. Inductor-capacitor (LC) circuits can serve as resonators with resonance frequencies in the gigahertz range and using Josephson junctions - two superconducting electrodes separated by a thin insulator which essentially form nonlinear inductors -, artificial atoms can be designed and fabricated (replacing the optical cavity and natural atoms in quantum electrodynamics, respectively). Although these circuits are macroscopic in scale (with the total length of the wires in the order of cm), the unique properties of superconductors guarantee quantum coherence, as was shown for example by a groundbreaking experiment with devices where Cooper pairs were tunnelling between superconducting islands in a quantum coherent fashion [29]. The coupling between the artificial two-level system and the microwave field can also be large and the single photon strong coupling regime has been achieved over a decade ago [30].

With this in mind, the advantage (as well as the basis of the long term promise) of

superconducting quantum circuits becomes clear: with its resemblance to the printed circuit board which revolutionized traditional computing, and the various ways one can include tunable artificial atoms on-chip, it provides a potentially scalable and well-controlled platform to extend the studies of quantum electrodynamics and currently is a promising candidate for realizing a universal quantum computer. A particular challenge, however, is that these systems have to be operated at millikelvin temperatures. There are two reasons for this: first, the superconducting property has to be maintained (and although the transition temperature for the materials of choice such as Al, Nb, TiN etc. are typically above 1 K, lower temperatures are necessary to suppress quasi-particles which can deteriorate the resonators' quality factor); second, the thermal noise of microwaves has to be suppressed compared to one energy quantum associated with the microwave frequency ($kT \ll \hbar\omega$), necessitating $T < 50mK$ in the gigahertz range.

By including a mechanically compliant element, one can marry superconducting quantum circuits and optomechanics. Initially, the main motivation was sensing: Regal *et al.* demonstrated a mechanical force sensitivity of $3 \text{ aN}/\sqrt{\text{Hz}}$ with a displacement imprecision 30 times the standard quantum limit [31], and, in a similar setup, Teufel *et al.* demonstrated dynamical backaction of microwaves on the mechanical element [32] and a measurement of mechanical motion with an imprecision below that at the standard quantum limit (utilizing a close to quantum-limited detector at low temperatures) with a force sensitivity of $0.51 \text{ aN}/\sqrt{\text{Hz}}$ [33]. Back-action evading measurement of a single quadrature of the motion using a two-tone drive was also demonstrated, approaching the sensitivity of the zero-point fluctuation on that quadrature [34]. Based on the dynamical backaction mentioned above, Massel *et al.* showed above 25 dB of amplification of microwave signals [35] (with about 20 added noise quanta and a rather narrow bandwidth given by the mechanical oscillator) and Zhou *et al.* demonstrated low-distortion temporal control of microwave signals [36]. These latter two experiments pointed to an interesting change in the paradigm: to control the electromagnetic fields with the mechanical oscillator, as opposed to control the mechanical mode or read out its motion with the highest precision.

In all the experiments above in the circuit domain, the mechanically compliant element was a metallized nanostring (in the order of $100 \mu\text{m}$ long and 100 nm thick) capacitively coupled to the circuit which provided relatively low coupling (the multiphoton coupling strength was limited to a value at least an order of magnitude less than the energy decay rate of the microwave resonator). In terms of the device geometry, a significant improvement was to move away from the one dimensional nanostring geometry to a two dimensional planar geometry by developing a vacuum-gap capacitor with a circular, mechanically compliant top membrane [37, 38]. This had proven to enhance the coupling strength by several orders of magnitude and the multiphoton strong coupling regime was

demonstrated [39], which opened the field to implement various other optomechanical experiments (shortly afterwards, ground state cooling of the mechanical drum was achieved [40], as well as coherent state transfer and entanglement between the mechanical motion and the microwave field [41, 42] among others). Both from a physics and from an architecture point of view, another interesting direction is to include a qubit into the system and use it as a nonlinear readout or as a true quantum object whose state can be transferred to the mechanical motion or vica versa (mechanical quantum memory). This allows for accessing non-Gaussian mechanical states, relevant in quantum computation (non-Gaussian states cannot be efficiently simulated on a classical computer). In fact, the first ground state cooling work used a qubit to read out and control a high frequency (≈ 6 GHz) mechanical resonator down to the single phonon level [43]. Since then, various groups have achieved hybrid systems incorporating a microwave cavity, a superconducting qubit and a mechanical element [44, 45]. These efforts fit well into the other long-standing paradigm both in optomechanics and in hybrid quantum systems: to observe the “quantum mechanics of mechanics”, i.e. to test and exploit the quantum nature of macroscopic mechanical objects [46, 21, 47].

This work: utilising dissipation in circuit electromechanics

An important aspect of all opto- and electromechanical experiments described above is the hierarchy of dissipation rates of the coupled electromagnetic and mechanical modes. Since typically these two types of modes are well separated in frequency but feature similar quality factors, their energy decay rate differs by orders of magnitude. As an example, in the case of a typical superconducting electromechanical device [39], the frequency of the electromagnetic mode is in the GHz range, while the mechanical mode is in the MHz range. Both modes have a quality factor of around 10^5 and, therefore, their energy decay rate differs by three orders of magnitude. This hierarchy is in fact key in the derivation of dynamical back-action by Braginsky described above. It ensures that the electromagnetic field envelope can instantly adapt to the mechanical displacement which establishes a feedback loop which modifies the susceptibility of the mechanical resonator. In a broader context, phenomena such as optomechanical cooling can be viewed in the framework of reservoir engineering. Reservoir engineering, originally proposed by Poyatos, Cirac and Zoller [48], refers to a robust strategy in which a quantum state can be stabilized or synthesized by suitably manipulating the dissipative bath the state is coupled to. Dissipation then becomes an actual resource as it ensures that the state relaxes to the target state. In the example of optomechanical cooling, the electromagnetic mode provides the reservoir for the mechanical mode and its low thermal occupancy state - together with the coupling achieved by a detuned pump tone - enables cooling. A more explicit example of reservoir engineering in the circuit electromechanical domain is the

preparation of a quantum squeezed state - in which the uncertainty of one quadrature is below the zero-point level - of the mechanical mode [49]. Using a two-tone drive (pumping both the lower and upper motional sidebands with different amplitudes), the mechanical oscillator naturally relaxes to the new ground state, which is a squeezed state, and this method allows for the generation of above 3 dB of squeezing - a typical limit for parametric squeezing techniques.

The work described in this thesis moves away from this paradigm and reverses the role of the two - mechanical and electromagnetic - degrees of freedom. In particular, we use the - engineered or intrinsic - dissipation of the mechanical element to manipulate the electromagnetic mode. In the first set of experiments, the mechanical mode is engineered such that its energy dissipation rate exceeds that of the electromagnetic mode while still remaining close to the quantum ground state, constituting therefore a reservoir with which one can perform useful tasks close to the quantum-limit. The fact that the roles are reversed is apparent in how dynamical backaction manifests itself in this regime, which we experimentally show. In a second experiment, we build a nonreciprocal frequency converter based purely on optomechanical interactions. Again, dissipation is a key ingredient in achieving nonreciprocity and the experiment demonstrates that dissipation can constitute a resource in circuit electromechanics. Both set of experiments utilise a multimode superconducting electromechanical system shown in fig. 1.1.

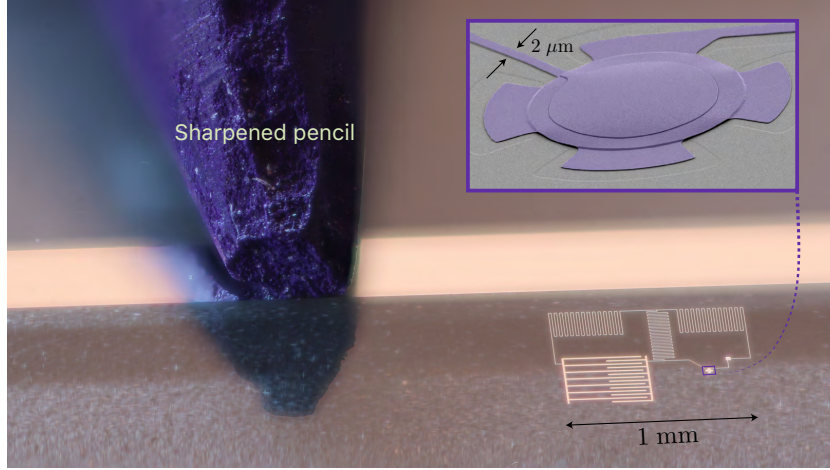


Figure 1.1 – **The multimode electromechanical device featured in the thesis.** The circuit supports two electromagnetic modes which are both coupled to the motion of a small, micrometer-scale membrane (shown as inset). Optical photograph courtesy of Nathan Bernier.

Structure of the thesis

The structure of the thesis is as follows. In chapter 2, the theoretical background is briefly exposed. The basics of optomechanics and electromechanics are discussed, as well as dissipation in quantum mechanics and some elements of microwave engineering. The quantum limit on added noise for any linear amplifier is also derived. In chapter 3, the details of the fabrication and the design - including simulation results - of the device are discussed. The fabrication process, based on existing literature, was developed *ab initio* during this thesis work. Chapter 4 describes in detail the measurement setup and the procedures to characterize the devices. The laboratory capabilities and procedures were also developed during this thesis work from the beginning with the project team. In chapter 5, one of the main results of the thesis is presented: the mechanical oscillator is engineered into a cold reservoir for microwave light. We demonstrate dynamical back-action on light caused by the mechanical motion and we implement a low-noise amplifier operating close to the quantum limit. The system can be driven to the parametric instability threshold, above which self-sustained oscillations of the microwave field (masing) is observed. This chapter is mainly based on [50, 51].

In chapter 6, nonreciprocal microwave conversion is demonstrated using purely optomechanical interactions. The architecture of the circuit is the same as in chapter 5, but an additional mechanical mode is utilized. Over 20 dB of isolation is demonstrated and its direction can be easily reconfigured by tuning the phase of the control pumps. The results of this chapter are mostly contained in [52] with a theoretical extension in [53]. In chapter 7, we summarize the results and briefly discuss possible directions for future work.

2 Cavity optomechanics with superconducting circuits

There have been many thorough reviews and introductions written on cavity opto- and electromechanics [54, 55, 46, 56, 21, 57, 58, 47, 20, 59]. Here we only give a short summary of the most important concepts and equations which are absolutely necessary for the results described in further chapters.

2.1 Optomechanics and electromechanics

An optomechanical system consists of a resonator for light coupled to a mechanical element. Two canonical examples are shown in fig. 2.1. The first example consists of a Fabry-Perot cavity, i.e. an optical cavity with two parallel mirrors, in which one of the mirrors is attached to a spring. The motion of the mirror modulates the resonance frequency of the cavity and, in turn, the light field in the cavity acts on the mirror through the radiation pressure force. The other mirror is semitransparent, which ensures that the system can be pumped from the outside with a laser and the laser light which leaks out can be collected for detection.

Another example is an LC circuit in which one of the capacitor's electrode is a mechanically compliant membrane. As the membrane vibrates, it modulates the capacitance, thus the resonance frequency of the LC circuit. The electric field within the capacitor also acts on the membrane and therefore a coupling between the electromagnetic field and the mechanical motion is established. In the remaining of the thesis, we only consider the LC circuit implementation of optomechanics (which is often called, and rightly so, electromechanics or, less rightly so, circuit optomechanics).

In the following, we consider the mode decomposition of both the electromagnetic field in the LC circuit, and the mechanical motion. A relevant example in our case for the mechanical mode is the fundamental mode of the circular membrane of the top electrode

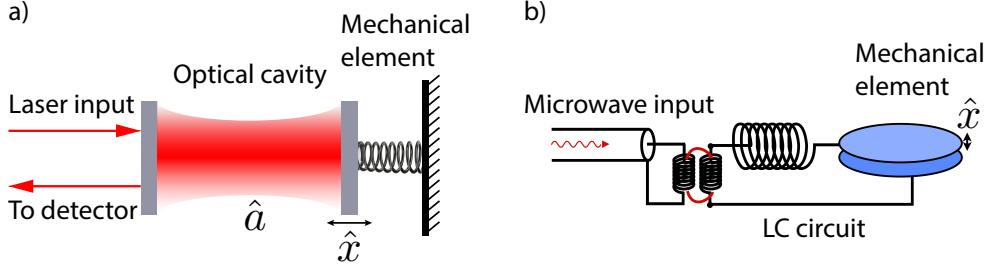


Figure 2.1 – **Schematic representation of optomechanical systems in the optical and microwave domain.** a) A canonical example of an optomechanical system in the optical domain is a Fabry-Perot cavity in which one of the end mirrors is suspended on a spring. b) In the microwave domain, the optomechanical coupling can be achieved by fabricating a mechanically compliant capacitor in a superconducting LC circuit. Panel b) taken from [60].

(an example of the mode shape is shown in fig. 4.17). Each mode is a harmonic oscillator which we can quantize (the procedure can be found in most books on quantum mechanics and a thorough treatment specific to cavity optomechanics can be found in [46]).

The energy (Hamiltonian) of the system is the sum of the energy in the electromagnetic mode and the energy of the mechanical mode. Using the bosonic annihilation (\hat{a}) and creation (\hat{a}^\dagger) operators for the cavity as well as for the mechanical mode \hat{b} and \hat{b}^\dagger , this energy can be written as

$$\hat{H} = \hbar\omega_c(\hat{x})\hat{a}^\dagger\hat{a} + \hbar\Omega_m\hat{b}\hat{b}^\dagger, \quad (2.1)$$

where $\omega_c(\hat{x})$ is the angular frequency of the electromagnetic mode (now dependent on the position \hat{x} of the mechanical mode) and Ω_m is the angular frequency of the mechanical mode. $\hat{a}^\dagger\hat{a}$ is the mean number of excitations (photons) in the electromagnetic mode, while $\hat{b}^\dagger\hat{b}$ is the mean number of excitations (phonons) in the mechanical mode. For simplicity, we have ignored the vacuum energy for now ($\frac{1}{2}\hbar\omega_c + \frac{1}{2}\hbar\Omega_m$).

Since the motion of the mechanical element is small compared to other dimensions of the system (e.g. the gap between the electrodes), we can expand the dependence of the cavity resonance frequency on the position up to first order

$$\omega_c(\hat{x}) \approx \omega_c + \underbrace{\hat{x} \frac{\partial \omega_c}{\partial x}}_{\equiv G}. \quad (2.2)$$

Here G is the cavity pulling factor, which describes how much the cavity's frequency is changing per unit motion. Plugging this back to eq. (2.1) one obtains the standard

optomechanical Hamiltonian

$$\hat{H} = \hbar\omega_c \hat{a}^\dagger \hat{a} + \hbar\Omega_m \hat{b} \hat{b}^\dagger - \underbrace{\hbar g_0 \hat{a}^\dagger \hat{a} (\hat{b} + \hat{b}^\dagger)}_{\hat{H}_{\text{int}}}, \quad (2.3)$$

where we defined

$$g_0 = \underbrace{\sqrt{\frac{\hbar}{2m\Omega_m}}}_{x_{\text{zpf}}} G. \quad (2.4)$$

x_{zpf} is the zero point motion of the mechanical mode (fluctuation of the position in the ground state). In the case of the vacuum-gap capacitors presented in this Thesis, $x_{\text{zpf}} \approx 6$ fm. Physically, the interaction Hamiltonian \hat{H}_{int} represents a potential which is proportional to the displacement of the mechanical oscillator, the number of photons in the cavity and the normalized coupling strength. The force, also called radiation pressure force associated to this potential is $\hat{F} = -d\hat{H}_{\text{int}}/dx = \hbar G \hat{a}^\dagger \hat{a}$. For example, in the case of an LC circuit modulated by the membrane, the coupling between the LC mode and the motion is given by the energy stored in the capacitor $E_{\text{capacitive}} = (1/2)C_{\text{total}}(x)V^2$ so that the radiation pressure is given by

$$F_{\text{rad}} = -\frac{1}{2} \frac{\partial C}{\partial x} V^2. \quad (2.5)$$

The energy is coupled into the system using an external microwave tone (or laser in the optical case) with frequency ω_d . It is beneficial to move to the rotating frame which rotates with this external drive, in order to remove the rapidly oscillating terms in the Hamiltonian. We make the substitution $\hat{a} \rightarrow \hat{a} e^{-i\omega_d t}$ and define the detuning from the cavity frequency $\Delta = \omega_d - \omega_c$ to obtain

$$\hat{H} = -\hbar\Delta \hat{a}^\dagger \hat{a} + \hbar\Omega_m \hat{b} \hat{b}^\dagger + \hat{H}_{\text{int}}. \quad (2.6)$$

Typically, the cavity is strongly pumped and the cavity field can be split into two parts: a coherent amplitude α and a fluctuating term $\delta\hat{a}$ so we can write $\hat{a} = \alpha + \delta\hat{a}$. Plugging this into interaction term in eq. (2.3) gives

$$\hat{H}_{\text{int}} = -\hbar g (\delta\hat{a} + \delta\hat{a}^\dagger) (\hat{b} + \hat{b}^\dagger), \quad (2.7)$$

where $g = \sqrt{n_c} g_0$ is the multiphoton coupling strength ($n_c = |\alpha|^2$ is the mean number of photons in the electromagnetic mode). In order to obtain the above expression, we have neglected the constant radiation pressure force and a term not proportional to α . The linear optomechanical Hamiltonian described by eq. (2.7) gives rise to various phenomena depending on the frequency of the external drive tone, such as optomechanical sideband cooling, squeezing or parametric instability. These phenomena, however, do depend on

the hierarchy of the dissipation rates of the modes as is outlined in section 2.1.2 and more explicitly explained in section 5.2, therefore we first introduce the concept of dissipation.

2.1.1 Dissipation and input-output theory

Both the electromagnetic and mechanical modes experience energy dissipation due to their coupling to the environment (for example, the electromagnetic energy stored in the LC resonator can be dissipated internally by two-level systems or can leak out to the feedline; the mechanical energy can be emitted to the substrate through the clamping points etc.). Phenomenologically, one can simply associate energy dissipation rates for the two modes: Γ_m for the mechanical mode and $\kappa = \kappa_0 + \kappa_{\text{ex}}$ for the electromagnetic mode, where κ_0 is the intrinsic dissipation and κ_{ex} is the external coupling rate (through which we can address the electromagnetic mode and can collect the energy which leaks out). The energy of the modes then exponentially decays with the characteristic rates of κ and Γ_m and, equivalently, the average photon (phonon) lifetime in the resonators is $\tau = \kappa^{-1}$ ($\tau_m = \Gamma_m^{-1}$). Alternatively, one can introduce the quality factor describing approximately the number of oscillations before the energy in the resonator decays: $Q \equiv \omega/\kappa$ ($\Rightarrow Q^{-1} = Q_0^{-1} + Q_{\text{ex}}^{-1}$) and equivalently for the mechanical mode.

The above discussion is fully classical and does not give insight into how dissipation may arise for the quantized modes. Here we briefly recall the theory developed by Gardiner and Collett [61, 62] (and previously by Haken [63]) and give an exposition on how dissipation can be treated quantum mechanically; our final goal is to arrive to the equations governing the evolution of the electromagnetic mode (quantum Langevin equations) as well as the input-output relation. These theoretical elements are also well-exposed in [64]. An alternative approach is to use the master equation formalism, which is rigorously developed for an optomechanical system for example in [65].

Consider the electromagnetic mode coupled to a dissipative environment (the derivation is general and one can substitute any mode of interest into the system Hamiltonian). We start by splitting the total Hamiltonian of the problem into two parts

$$\hat{H}_{\text{tot}} = \hat{H}_s + \hat{H}_{\text{diss}}, \quad (2.8)$$

where \hat{H}_s describes the system Hamiltonian (in our case, $\hat{H}_s = \hbar\omega_c \hat{a}^\dagger \hat{a}$) and \hat{H}_{diss} describes dissipation. We can further split \hat{H}_{diss} into two parts

$$\hat{H}_{\text{diss}} = \hat{H}_{\text{bath}} + \hat{H}_i, \quad (2.9)$$

where \hat{H}_{bath} describes the Hamiltonian of the environment the system is coupled to and \hat{H}_i describes the actual interaction to the bath. Now we make some assumptions on these

Hamiltonians. We assume that the bath consists of a continuum of harmonic oscillator modes

$$\hat{H}_{\text{bath}} = \int_{-\infty}^{+\infty} \hbar\omega \hat{B}(\omega) \hat{B}^\dagger(\omega) d\omega, \quad (2.10)$$

where \hat{B} and \hat{B}^\dagger are the annihilation and creation operators for the bath modes satisfying $[\hat{B}(\omega), \hat{B}^\dagger(\omega')] = \delta(\omega - \omega')$. Furthermore, the system is linearly coupled to the bath

$$\hat{H}_i = -i\hbar \int_{-\infty}^{+\infty} \gamma(\omega) [\hat{a}^\dagger \hat{B} - \hat{B}^\dagger \hat{a}] d\omega, \quad (2.11)$$

where $\gamma(\omega)$ is the linear coupling. We can now derive the Heisenberg equations of motion for the system and the bath operators to obtain

$$\frac{d\hat{a}(t)}{dt} = -i\omega_c \hat{a}(t) - \int \gamma(\omega) \hat{B} d\omega, \quad (2.12)$$

$$\frac{d\hat{B}(t)}{dt} = -i\omega \hat{B}(t) + \gamma(\omega) \hat{a}(t). \quad (2.13)$$

The procedure now is to eliminate the bath modes in order to solve for the dynamics of the system. One can formally integrate eq. (2.13) from some initial time t_0 to t which gives

$$\hat{B}(\omega) = \hat{B}_0(\omega) e^{-i\omega(t-t_0)} + \int_{t_0}^t \gamma(\omega) \hat{B}(t') e^{-i\omega(t-t')} dt', \quad (2.14)$$

where $\hat{B}_0(\omega)$ is the value of the bath operator at $t = t_0$. The last term in eq. (2.12) then becomes

$$\int \gamma(\omega) \hat{B} d\omega = \int \gamma(\omega) \hat{B}_0(\omega) e^{-i\omega(t-t_0)} d\omega + \int_{t_0}^t \int \frac{J(\omega)}{2\pi} \hat{a}(t') e^{-i\omega(t-t')} d\omega dt', \quad (2.15)$$

where we defined the kernel $J(\omega)$ as

$$J(\omega) = 2\pi \left| \frac{d\gamma}{d\omega} \right|^2 |\gamma(\omega)|^2. \quad (2.16)$$

Then, two more approximations are made in order to simplify the integral. The first, crucial approximation is that the kernel is constant within the bandwidth of the cavity (i.e. the coupling to the bath is frequency independent), such that we can write

$$J(\omega) = \kappa. \quad (2.17)$$

This approximation is called the first Markov approximation and it is equivalent to stating that the damping term depends only on the the system operators evaluated at time t and not at $t' < t$ (Markovian or memoryless bath). The second one is that the response of the

bath is assumed to be much faster than any timescale of the system and one can remove the fast frequency dependence of \hat{a} by transforming it to the slowly varying operator $\hat{a} \rightarrow \hat{a}e^{-i\omega_c t}$. With this, the integral simply becomes equal to $\frac{\kappa}{2}\hat{a}(t)$. It is useful to define

$$\hat{a}_{\text{in}}(t) = -\frac{1}{2\pi} \int \hat{B}_0(\omega) e^{-i\omega(t-t_0)} d\omega, \quad (2.18)$$

so we finally arrive to the equation

$$\frac{d\hat{a}(t)}{dt} = -i\omega_c \hat{a}(t) - \frac{\kappa}{2} \hat{a}(t) + \sqrt{\kappa} \hat{a}_{\text{in}}(t), \quad (2.19)$$

which is called the (forward) quantum Langevin equation. The operator $\hat{a}_{\text{in}}(t)$ can be interpreted as the noise operator induced by the bath (it depends on all the bath operators $\hat{B}_0(\omega)$, therefore generally it is rapidly oscillating) and is a manifestation of the fluctuation-dissipation theorem: in the presence of a damping (coupling to a dissipative environment), a fluctuating force appears. We should note that this term is necessary in eq. (2.19) to preserve the canonical commutation relation of \hat{a} and \hat{a}^\dagger . Such a force term is associated to every dissipative channel.

We can derive such a Langevin equation for any mode with a dissipative channel. In the case of optomechanics, the mechanical mode is thus also governed by

$$\frac{d\hat{b}(t)}{dt} = -i\Omega_m \hat{b}(t) - \frac{\Gamma_m}{2} \hat{a}(t) + \sqrt{\Gamma_m} \hat{b}_{\text{in}}(t), \quad (2.20)$$

One can consider the formal integration in eq. (2.14) backward in time (from time t_f to t)

$$\hat{B}(\omega) = \hat{B}_0(\omega) e^{-i\omega(t-t_f)} f \int_t^{t_f} \gamma(\omega) \hat{B}(t') e^{-i\omega(t-t')} dt'. \quad (2.21)$$

By repeating the same procedure outlined above, and by defining the output operator as

$$\hat{a}_{\text{out}}(t) = -\frac{1}{\sqrt{2\pi}} \int \hat{B}_0(\omega) e^{-i\omega(t-t_f)} d\omega, \quad (2.22)$$

to obtain the time-reversed quantum Langevin equation

$$\frac{d\hat{a}(t)}{dt} = -i\omega_c \hat{a}(t) + \frac{\kappa}{2} \hat{a}(t) + \sqrt{\kappa} \hat{a}_{\text{in}}(t). \quad (2.23)$$

From this the identity follows that

$$\hat{a}_{\text{out}}(t) = \hat{a}_{\text{in}}(t) - \sqrt{\kappa} \hat{a}(t), \quad (2.24)$$

which straightforwardly relates the output field to the input field through the internal

modes. Naturally, this equation also holds for \hat{b}_{in} and \hat{b}_{out} . The input and output fields satisfy the commutation relations

$$\left[\hat{a}_{\text{in}}(t), \hat{a}_{\text{in}}^\dagger(t') \right] = \delta(t - t'), \quad (2.25)$$

$$\left[\hat{a}_{\text{out}}(t), \hat{a}_{\text{out}}^\dagger(t') \right] = \delta(t - t'), \quad (2.26)$$

and all other commutators are zero. Typically, the state of the bath is assumed to be a thermal state in thermal equilibrium - although this assumption is not necessary and damping will occur even if the bath is a coherent state - and independent from the system at t_0 . In this case, the bath operators satisfy

$$\left\langle \hat{B}(\omega, t_0) \right\rangle = \left\langle \hat{B}(\omega, t_0) \hat{B}(\omega', t_0) \right\rangle = \left\langle \hat{B}^\dagger(\omega, t_0) \hat{B}^\dagger(\omega', t_0) \right\rangle = 0, \quad (2.27)$$

$$\left\langle \hat{B}^\dagger(\omega, t_0) \hat{B}(\omega', t_0) \right\rangle = n_{\text{th}}(\omega) \delta(\omega + \omega'), \quad (2.28)$$

where $\langle \dots \rangle$ represents the ensemble average and n_{th} is the thermal occupancy given by the Bose statistics

$$n_{\text{th}} = \frac{1}{\exp\left(\frac{\hbar\omega_c}{k_B T}\right) - 1}. \quad (2.29)$$

Furthermore, using the definition eq. (2.18) and the statistics of the bath operators above, one can easily show that the statistics of the noise input operators is given by

$$\langle \hat{a}_{\text{in}}(t) \rangle = \langle \hat{a}_{\text{in}}(t) \hat{a}_{\text{in}}(t') \rangle = \langle \hat{a}_{\text{in}}^\dagger(t) \hat{a}_{\text{in}}^\dagger(t') \rangle = 0, \quad (2.30)$$

$$\langle \hat{a}_{\text{in}}(t) \hat{a}_{\text{in}}^\dagger(t') \rangle = n_{\text{th}}(\omega_c) \delta(t - t'). \quad (2.31)$$

2.1.2 Optomechanical cooling and amplification

We turn back to the optomechanical interaction described, in the linearized form, by the Hamiltonian eq. (2.7). It gives rise to interesting phenomena - many of them analogous to phenomena in atomic physics - which have been exploited by numerous experiments. If one sets the pump frequency at $\omega_c - \Omega_m$ (corresponding to $\Delta = -\Omega_m$, which we call the lower motional sideband, or red sideband), the interaction Hamiltonian is simplified to

$$\hat{H}_{\text{int}} = -\hbar g \left(\delta \hat{a}^\dagger \hat{b} + \delta \hat{a} \hat{b}^\dagger \right), \quad (2.32)$$

where terms $\propto \delta \hat{a}^\dagger \hat{b}^\dagger$ and $\propto \delta \hat{a} \hat{b}$ are neglected because they are non-resonant (rotating wave approximation). This Hamiltonian corresponds to the coherent exchange of quanta between the electromagnetic and mechanical mode - thus sometimes also called the beam-splitter interaction - and leads to cooling the mechanical motion. In particular, in the resolved sideband regime ($\Omega_m \gg \kappa$), which is the relevant regime in our experiments, the final mechanical occupancy one can attain provided that there are no additional heating mechanisms present, is given by

$$n_{\text{min,th}} = \left(\frac{\kappa}{4\Omega_m} \right) < 1, \quad (2.33)$$

indicating that this type of cooling can bring the mechanical oscillator close to its quantum ground state [40, 28]. Physically, the cooling can be simply understood: although the Hamiltonian eq. (2.32) ensures the coherent exchange of energy between the modes, the energy taken out from the mechanical oscillator is rapidly dissipated in the cold optical bath. Therefore, it is important to note that the cooling mechanism relies on the dissipation hierarchy $\Gamma_m \ll \kappa$, which is naturally satisfied in many optomechanical experiments.

If the frequency of the external pump equals that of the electromagnetic cavity, we can write

$$\hat{H}_{\text{int}} = -\hbar g \left(\delta \hat{a}^\dagger \hat{b}^\dagger + \delta \hat{a} \right) \left(\hat{b} + \hat{b}^\dagger \right), \quad (2.34)$$

which can be used to read out the displacement of the mechanical motion with high precision.

Finally, when the frequency of the external pump is set to the upper motional (blue) sideband, the interaction Hamiltonian in the rotating wave approximation is

$$\hat{H}_{\text{int}} = -\hbar g \left(\delta \hat{a}^\dagger \hat{b}^\dagger + \delta \hat{a} \hat{b} \right), \quad (2.35)$$

also called the two-mode squeezing Hamiltonian. This interaction anti-damps the mechanical motion and can lead to parametric instability. At the same time, it can also be used to amplify microwave signals [35]. In chapter 5 we show how this interaction can be harnessed for ultra-low noise amplification of microwave signals, provided that the mechanical oscillator is cold.

2.2 Elements of microwave engineering

2.2.1 Transmission line theory

Transmission lines are electrical elements used to transmit electromagnetic power in the microwave domain. They are needed in order to probe the electromechanical resonators studied in this thesis and the theoretical aspects are also insightful to describe the circuits themselves. A good introduction to transmission lines, which this discussion follows as well, can be found in [66]. Typically, transmission lines consist of two separate conductors such that TEM waves can be supported. A piece of the transmission line is illustrated in fig. 2.2a. Important parameters characterizing the line are: R , the series resistance per unit length in Ω/m ; G , the shunt conductance per unit length in S/m ; L , the series inductance per unit length in H/m and C and the shunt capacitance per unit length in F/m .

Generally, the voltage and the current on the transmission line as a function of z can be found as the traveling wave solution to the standard propagation equation to give

$$V(z) = V_0^+ e^{-\gamma z} + V_0^- e^{\gamma z}, \quad (2.36)$$

$$I(z) = I_0^+ e^{-\gamma z} + I_0^- e^{\gamma z}, \quad (2.37)$$

where $\gamma = \sqrt{(R + i\omega L)(G + i\omega C)}$ the term $e^{-\gamma z}$ represents the traveling voltage (current) to the $+z$ direction. The characteristic impedance relates the voltage and the current on the line and can be calculated as

$$Z_0 \equiv \frac{V_0^+}{I_0^+} = \frac{V_0^-}{I_0^-} = \sqrt{\frac{R + i\omega L}{G + i\omega C}}. \quad (2.38)$$

The wavelength and the phase velocity of the traveling wave are

$$\lambda = \frac{2\pi}{\beta} \quad v_p = \frac{\omega}{\beta} = \lambda f, \quad (2.39)$$

where $\beta = \text{Im}(\gamma)$. In our experiments the circuits are made out of superconductors with minimal loss. Setting $R = G = 0$, the characteristic impedance of the lossless transmission line is

$$Z_0 = \sqrt{\frac{L}{C}}. \quad (2.40)$$

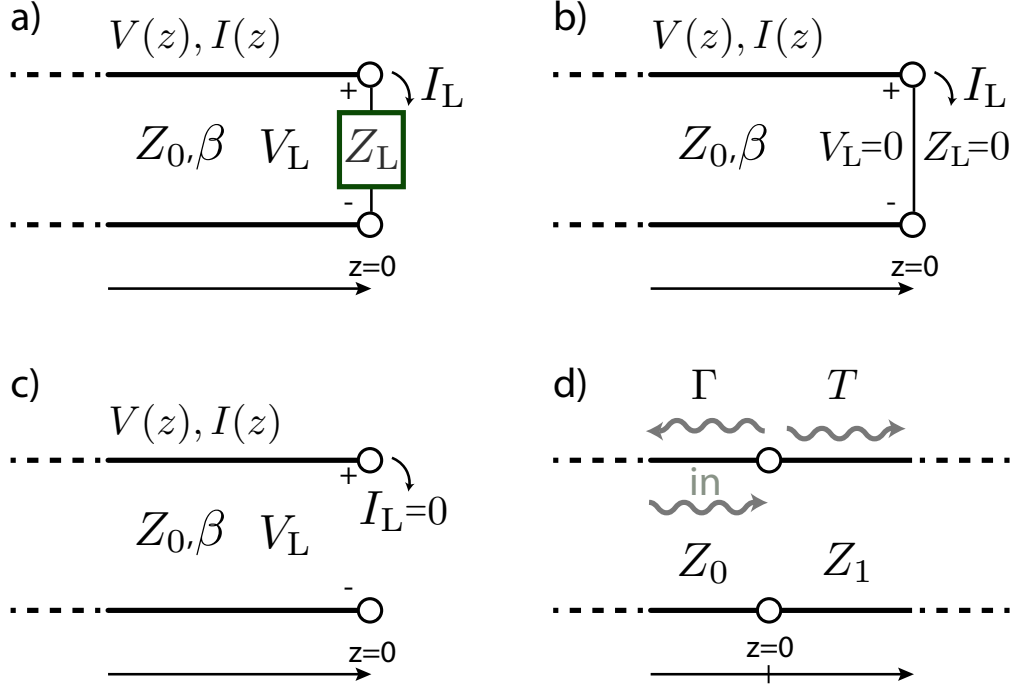


Figure 2.2 – **Circuit representation of lossless transmission lines.** a) A transmission line terminated with a load Z_L . b) A transmission line with a short circuit at the end. c) An open-circuited transmission line. d) A junction of two transmission lines with different characteristic impedances.

Lossless transmission line with a termination

Now assume that we inject an voltage wave at $z < 0$ in the form $V_0^+ e^{-i\beta z}$ to a transmission line which has a termination at $z = 0$ with a load Z_L . This gives the boundary condition that at $z = 0$ the equations must satisfy

$$Z_L = \frac{V(0)}{I(0)} = \frac{V_0^+ + V_0^-}{V_0^+ - V_0^-} Z_0. \quad (2.41)$$

An important quantity to calculate is the voltage reflection coefficient $\Gamma(l)$, which gives the amplitude of the voltage of the reflected wave normalized to the incident wave at any point on the line. From eq. (2.41) one obtains

$$\Gamma(l) \equiv \frac{V_0^- e^{-i\beta l}}{V_0^+ e^{i\beta l}} = \frac{Z_L - Z_0}{Z_L + Z_0} e^{-2i\beta l}. \quad (2.42)$$

From this equation it is trivial to see that in order to obtain no reflection, i.e. $\Gamma = 0$, one needs $Z_0 = Z_L$, so Z_L is a *matched load*. We can also conclude that the impedance 'seen'

by the feedline at a point $-l$ is not constant with l but is given by

$$Z_{\text{in}} = Z_0 \frac{Z_L + iZ_0 \tan(\beta l)}{Z_0 + iZ_L \tan(\beta l)}. \quad (2.43)$$

We consider a two special cases in terms of the length of the line. First, if one chooses the length of the feedline to be $\lambda/2$, one can easily see that the input impedance is equal to the load impedance everywhere on the line:

$$Z_{\text{in}} = Z_L \quad \forall \quad \beta l = \pi. \quad (2.44)$$

The load impedance is not transformed by the characteristic impedance of the line. In contrast, if one chooses $l = \lambda/4 + n\lambda/2$ where n is an integer, the input impedance is given by

$$Z_{\text{in}} = \frac{Z_0^2}{Z_L}, \quad (2.45)$$

indicating that the load impedance is transformed by the characteristic impedance of the line in an inverse manner. This type of line is often called a quarter-wave transformer.

We also consider two special cases in terms of the load. In one case (shown in fig. 2.2b), the line is short-circuited ($Z_L = 0$). As expected, this situation gives $V = 0$ at the load with maximum current and the input impedance is periodic and purely imaginary

$$Z_{\text{in}} = iZ_0 \tan(\beta l). \quad (2.46)$$

The reflection coefficient for such a scenario is $\Gamma = -1$.

Another special case is when the line is open-circuited (shown in fig. 2.2c), corresponding to $Z_L = \infty$. Now there is no current at the load and the input impedance is

$$Z_{\text{in}} = -iZ_0 \cotan(\beta l), \quad (2.47)$$

which is again purely imaginary and periodic. Importantly, the the reflection coefficient is unity $\Gamma = 1$, meaning that all the voltage wave is reflected.

Finally, consider the junction of two transmission lines with different characteristic impedances Z_0 and Z_1 , infinitely long on both sides (fig. 2.2d). When a voltage wave is coming in from the first line, it sees a characteristic impedance of Z_1 and is reflected at the junction with reflection and transmission coefficients

$$\Gamma = \frac{Z_1 - Z_0}{Z_1 + Z_0}, \quad T = 1 + \Gamma = \frac{2Z_1}{Z_1 + Z_0}. \quad (2.48)$$

Therefore, whenever two lines are connected (for example, a coaxial cable connected to an

SMA connector to a device), one has to make sure to match the characteristic impedances of the the connecting transmission lines, otherwise reflections occur creating standing waves and insertion loss is introduced (Insertion loss = $-20 \log |T|$ in dB).

Microstrip line

In order to couple microwave energy into the superconducting electromechanical circuits presented in this thesis, we fabricate a microstrip feedline on the chip. The geometry of the feedline is shown in fig. 2.3: it consists of a thin conductor of width W , the dielectric substrate with thickness d and a conducting ground plane. The microstrip line is one of the most popular planar transmission lines due to its simple geometry. Because the top conductor is situated at the dielectric-air interface, microstrip lines cannot support pure TEM waves but quasi-TEM waves (provided that the thickness of the conductor is much smaller than the thickness of the dielectric, which holds in our case). In order to avoid standing waves on the feedline, we design it to have a characteristic impedance of 50Ω according to [66]

$$\frac{W}{d} = \frac{8e^A}{e^{2A} - 2} \implies W \approx 510 \mu\text{m}, \quad (2.49)$$

with

$$A = \frac{Z_0}{60} \sqrt{\frac{\epsilon_r + 1}{2}} + \frac{\epsilon_r - 1}{\epsilon_r + 1} \left(0.23 + \frac{0.61}{\epsilon_r} \right),$$

where ϵ_r is the relative permittivity of the dielectric (in our case, sapphire has $\epsilon_r \approx 10$ parallel to the C-plane at low temperatures).

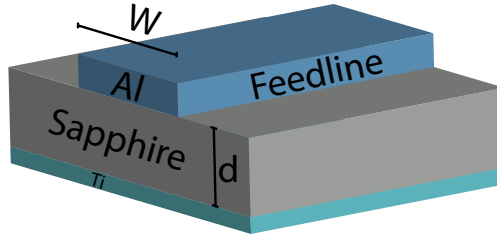


Figure 2.3 – **Visualisation of the microstrip line which serves as a feedline to couple microwave energy into the electromechanical circuit.** The feedline is designed to be 50Ω matched according to eq. (2.49).

2.2.2 RLC circuit coupled to the feedline

Now we consider a lumped element RLC circuit coupled to the feedline as shown in fig. 2.4. The resistor R is introduced to account for the intrinsic losses of the resonator. We furthermore consider inductive coupling meaning that the change in the current of

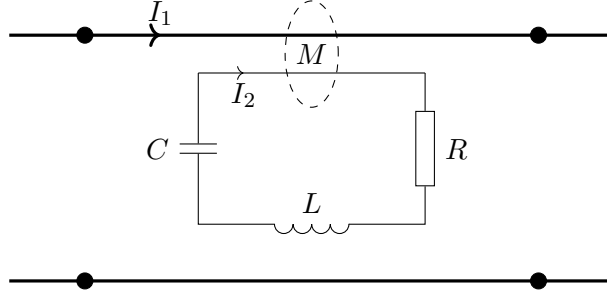


Figure 2.4 – An RLC circuit inductively coupled to a feedline.

the feedline induces a voltage across the inductor through electromagnetic induction. We derive the effective impedance and the external and internal Q factor in terms of the circuit parameters. The results are used in designing the circuit (further discussion in section 3.2.1), as well as fitting the resonance parameters as discussed in section 4.3.1.

Applying Kirchhoff's first law to the circuit gives

$$I_2 \left(i\omega L + \frac{1}{i\omega C} + R \right) + i\omega M I_1 = 0, \quad (2.50)$$

where M is the mutual inductance, I_1 is the current on the feedline and I_2 is the current flowing in the inductor of the circuit. The voltage induced on the feedline is

$$V_1 = i\omega M I_2 = \frac{\omega^2 M^2 I_1}{\left(i\omega L + \frac{1}{i\omega C} + R \right)}. \quad (2.51)$$

The effective impedance of the resonator seen by the feedline is then straightforwardly given by

$$Z_{\text{eff}} = \frac{V_1}{I_1} = \frac{\omega^2 M^2}{\left(i\omega L + \frac{1}{i\omega C} + R \right)}. \quad (2.52)$$

In order to derive the energy decay rate, consider a current $I(t) = I_0 \cos(\omega t)$ feeding the resonator. The total energy stored in the resonator is

$$E_{\text{stored}} = \frac{1}{2} L I_0^2. \quad (2.53)$$

To derive the energy decay rate, we first calculate the power which is dissipated to the feedline per cycle (in power units). For the case when the feedline is grounded at one end (1-port configuration), the dissipated power is given by

$$P = \left\langle \frac{V^2}{Z_0} \right\rangle = \frac{M^2}{Z_0} \left\langle \left(\frac{dI}{dt} \right)^2 \right\rangle = \frac{M^2 I_0^2 \omega^2}{2Z_0}. \quad (2.54)$$

Then the external coupling rate and quality factor can be calculated as

$$\kappa_{\text{ex}} = \frac{P}{E_{\text{stored}}} = \frac{M^2\omega^2}{LZ_0} \quad Q_{\text{ex}} = \frac{LZ_0}{M^2\omega}. \quad (2.55)$$

This result holds for a cavity which is coupled to a feedline with one grounded port. For a double port feedline, the impedance seen by the resonator is $2Z_0$, hence the external coupling rate is modified to

$$\kappa_{\text{ex}} = \frac{P}{E_{\text{stored}}} = \frac{M^2\omega^2}{2LZ_0} \quad Q_{\text{ex}} = \frac{2LZ_0}{M^2\omega}. \quad (2.56)$$

It is easy to show that the internal energy dissipation rate in the RLC resonator is

$$\kappa_0 = \frac{R}{L} \quad Q_0 = \frac{L}{\omega_0 R}, \quad (2.57)$$

independent of Z_0 (therefore this expression holds for both the one- and two-port cases).

ABCD matrix and S parameter

The ABCD matrix connects the voltages and currents in a two-port network. For the LC circuit inductively coupled to the feedline, it is given by

$$\begin{pmatrix} V_1 \\ I_1 \end{pmatrix} = \begin{pmatrix} a & b \\ c & d \end{pmatrix} \begin{pmatrix} V_2 \\ I_2 \end{pmatrix} \Rightarrow \begin{pmatrix} a & b \\ c & d \end{pmatrix} = \begin{pmatrix} 1 & Z_{\text{eff}} \\ 0 & 1 \end{pmatrix}, \quad (2.58)$$

where Z_{eff} is given by eq. (2.52). We also introduce the scattering matrix, which relates the voltage waves incident on the ports to those which are reflected from the port. This is a particularly useful quantity as it can be directly measured by a network analyser. Formally, for the N-port network, this gives the definition

$$S_{ij} = \left. \frac{V_i^-}{V_j^+} \right|_{V_k^+ = 0 \text{ for } k \neq j} \quad (2.59)$$

The S-matrix can be related to the ABCD matrix via

$$S = \begin{pmatrix} S_{11} & S_{12} \\ S_{21} & S_{22} \end{pmatrix} = \begin{pmatrix} \frac{a-d-cZ_0+\frac{b}{Z_0}}{a+d+cZ_0+\frac{b}{Z_0}} & \frac{2(ad-bc)}{a+d+cZ_0+\frac{b}{Z_0}} \\ \frac{2}{a+d+cZ_0+\frac{b}{Z_0}} & \frac{-a+d-cZ_0+\frac{b}{Z_0}}{a+d+cZ_0+\frac{b}{Z_0}} \end{pmatrix}. \quad (2.60)$$

It is convenient to express the scattering rewrite the effective impedance in terms of dimensionless parameters: For in the two port case, the elements of the scattering matrix

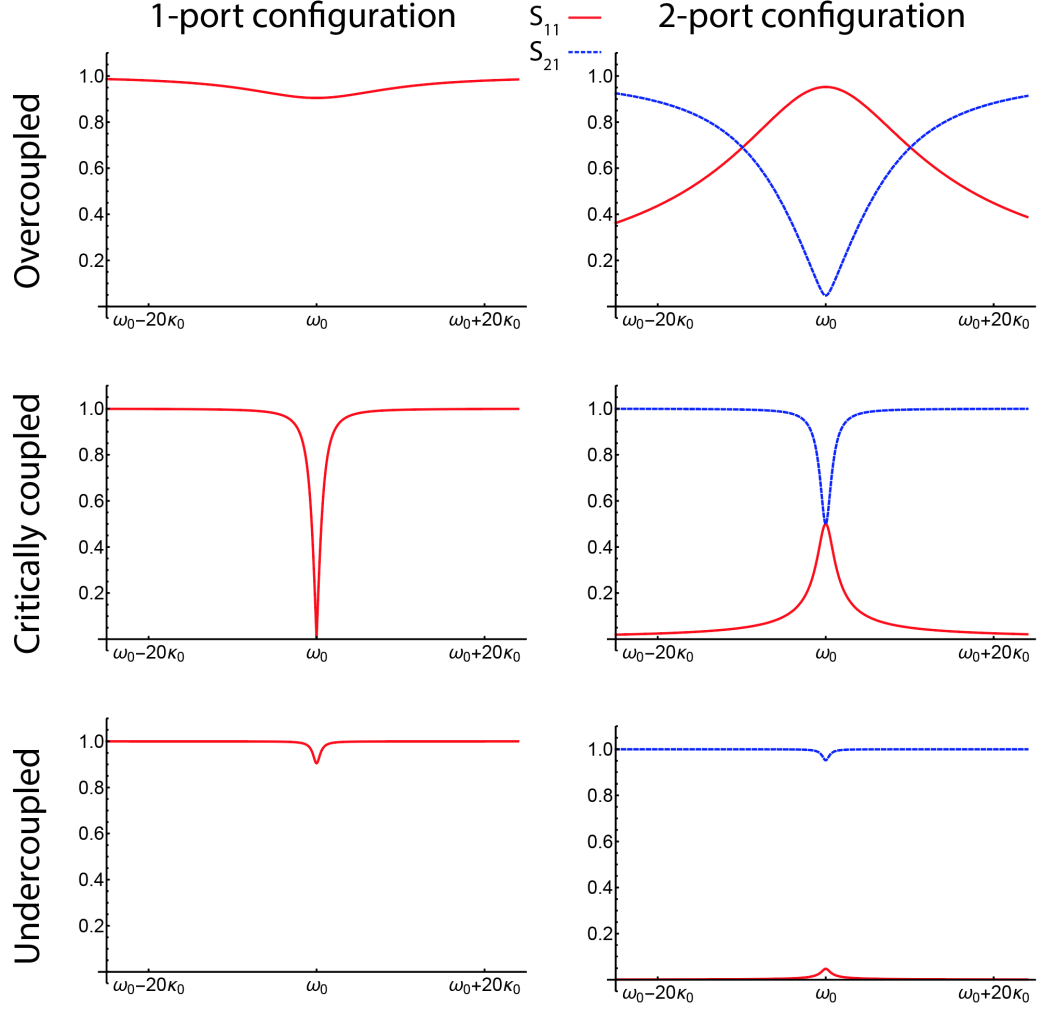


Figure 2.5 – **Plot of the S parameters for different port configurations and coupling ratios.** The 1-port configuration refers to case where one end of the feedline is grounded, therefore only S_{11} can be measured; in the 2-port configuration, both ends of the feedline are connected to the outside world and both transmission and reflection can be measured.

can be calculated as

$$S_{11}(\omega) = \frac{Q_{\text{ex}}^{-1} \tilde{\omega}^2}{Q_0^{-1} + i \frac{\tilde{\omega}^2 - 1}{\tilde{\omega}} + Q_{\text{ex}}^{-1} \tilde{\omega}^2}, \quad (2.61)$$

and

$$S_{12}(\omega) = \frac{Q_0^{-1} + i \frac{\tilde{\omega}^2 - 1}{\tilde{\omega}}}{Q_0^{-1} + j \frac{\tilde{\omega}^2 - 1}{\tilde{\omega}} + Q_{\text{ex}}^{-1} \tilde{\omega}^2}, \quad (2.62)$$

where $\tilde{\omega} = \frac{\omega}{\omega_c}$. fig. 2.5 plots the S parameters for different coupling regimes and port configurations; these are used later in the thesis.

2.3 The quantum limit of amplification

Every active component such as an amplifier or transmitter has its own internal noise. In this section we derive the ultimate limit on how small this noise can be based on the principles of quantum mechanics. Naturally, apart from this added quantum noise which is a theoretical minimum, the components typically have other sources of noise (e.g. generated by the fluctuations of the charge carriers or bound charges) which pose a practical limit. This is discussed in section 4.2.3.

In quantum mechanics, for any observable A one can associate a Hermitian operator \hat{A} . Let us define the standard deviation of \hat{A} as

$$\Delta\hat{A} = \sqrt{\langle\hat{A}^2\rangle - \langle\hat{A}\rangle^2}, \quad (2.63)$$

where $\langle\hat{A}\rangle$ is the expectation value. For two such operators \hat{A} and \hat{B} , the Heisenberg uncertainty relation - or in this form, often called the Robertson inequality - states that

$$\Delta\hat{A}\Delta\hat{B} \geq \frac{1}{2} |\langle[\hat{A}, \hat{B}]\rangle|, \quad (2.64)$$

where $[\hat{A}, \hat{B}] = \hat{A}\hat{B} - \hat{B}\hat{A}$ denotes the commutator. A well-known example is a simple harmonic oscillator with position \hat{x} and momentum \hat{p} . No matter the nature or physical implementation of the oscillator, \hat{x} and \hat{p} satisfy the commutation relation $[\hat{x}, \hat{p}] = i\hbar$, so we obtain the celebrated result

$$\Delta\hat{x}\Delta\hat{p} \geq \frac{\hbar}{2}. \quad (2.65)$$

In the following, we consider a narrow band linear amplifier such that both of its input and output signals are narrow band with bandwidth Δf . A general, time-dependent input signal $\hat{x}(t)$ can be expressed as

$$\hat{x}(t) = \hat{a}e^{-i\omega t} + \hat{a}^\dagger e^{i\omega t} = \hat{X}_1 \cos(\omega t) + \hat{X}_2 \sin(\omega t), \quad (2.66)$$

where \hat{a} and \hat{a}^\dagger are the annihilation and creation operators and \hat{X}_1 and \hat{X}_2 are the two slowly varying quadratures. We note that \hat{x} is a general signal - it does not directly represent the displacement of a harmonic oscillator - and we do not use any specific normalization, the unit of \hat{x} equals the unit of \hat{a} (in the case of \hat{x} representing the motion of a harmonic oscillator, the normalization factor would be the zero-point fluctuation). The quadrature representation of such a signal is visualized in fig. 2.6: because of the uncertainties in X_1 and X_2 , the signal is represented as an extended circle (sometimes referred to as the noise or uncertainty "blob"). Physically, if one takes $\langle\hat{X}_2\rangle = 0$, $\Delta\hat{X}_2$ represents the phase fluctuation ($\Delta\theta$ in the figure), while $\Delta\hat{X}_1$ represents the amplitude fluctuation. The bosonic operators \hat{a} and \hat{a}^\dagger have the commutation relation $[\hat{a}, \hat{a}^\dagger] = 1$,

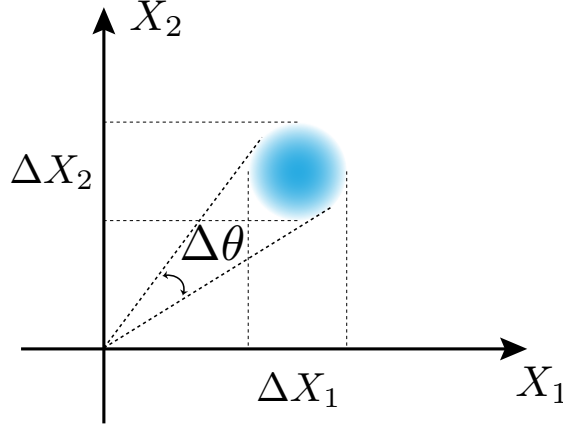


Figure 2.6 – **Quadrature space representation of a signal.** ΔX_1 and ΔX_2 correspond to the uncertainty in the X_1 and X_2 quadratures, respectively.

while the quadrature operators have $[\hat{X}_1, \hat{X}_2] = 2i$, therefore

$$\Delta \hat{X}_1 \Delta \hat{X}_2 \geq 1. \quad (2.67)$$

This implies that the area of the uncertainty blob is fundamentally limited. This has significant consequences of the added noise of any linear amplifier which we discuss below. Consider a linear amplifier depicted in fig. 2.7. With the input signal given in eq. (2.66),

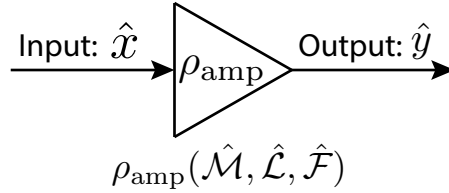


Figure 2.7 – **Schematic of a linear amplifier.** $\hat{\rho}_{\text{amp}}$ represents the internal state of the amplifier, initial disentangled from the signal. The amplifier amplifies the signal represented by linear operators $\hat{\mathcal{L}}$ and $\hat{\mathcal{M}}$ and also adds its internal noise.

the output signal can be written as

$$\hat{y}(t) = \hat{b}e^{-i\omega t} + \hat{b}^\dagger e^{i\omega t} = \hat{Y}_1 \cos(\omega t) + \hat{Y}_2 \sin(\omega t), \quad (2.68)$$

where \hat{b} is linearly related to the bosonic operators of the input signal. As a simple linear expression, one would be tempted to write then that

$$\hat{b} = \hat{\mathcal{M}}\hat{a} + \hat{\mathcal{L}}\hat{a}^\dagger, \quad (2.69)$$

where $\hat{\mathcal{M}}$ and $\hat{\mathcal{L}}$ are linear operators. However, this expression cannot be correct, as the fundamental bosonic commutation relation $[\hat{b}, \hat{b}^\dagger] = 1$ would not be satisfied. We therefore

need an extra term

$$\hat{b} = \hat{\mathcal{M}}\hat{a} + \hat{\mathcal{L}}\hat{a}^\dagger + \hat{\mathcal{F}}, \quad (2.70)$$

where $\hat{\mathcal{F}}$ is an operator representing the additional noise added by the amplifier and which satisfies

$$[\hat{\mathcal{F}}, \hat{\mathcal{F}}^\dagger] = 1 - |M|^2 + |L|^2. \quad (2.71)$$

Here, M and L represent the expectation values of $\hat{\mathcal{M}}$ and $\hat{\mathcal{L}}$ over the state of the amplifier (assume now an initial condition in which the amplifier state $\hat{\rho}_{\text{amp}}$ and the initial input state $\hat{\rho}_{\text{input}}$ are prepared in a product state, i.e. $\hat{\rho} = \hat{\rho}_{\text{input}} \otimes \hat{\rho}_{\text{amp}}$). We note that $\hat{\mathcal{M}}$, $\hat{\mathcal{L}}$ and $\hat{\mathcal{F}}$ are operators which depend only on the internal state of the amplifier, therefore they commute with the input mode operators \hat{a} and \hat{a}^\dagger . To proceed, we expand the internal amplifier operators around their operating state:

$$\hat{\mathcal{M}} = M + \delta\hat{\mathcal{M}}, \quad \hat{\mathcal{L}} = L + \delta\hat{\mathcal{L}} \quad \hat{\mathcal{F}} = F + \delta\hat{\mathcal{F}}, \quad (2.72)$$

and make a few assumptions. First, we neglect $\delta\hat{\mathcal{M}}$ and $\delta\hat{\mathcal{L}}$ (gain fluctuations) as these multiplicative noises are typically negligible in the operating state. Without loss of generality, we can also set $F = 0$ (constant offset of the output signal). eq. (2.70) becomes

$$\hat{b} = M\hat{a} + L\hat{a}^\dagger + \delta\hat{\mathcal{F}}. \quad (2.73)$$

It is useful to rearrange this in terms of quadratures

$$\hat{Y}_1 = (M + L)\hat{X}_1 + \hat{F}_1, \quad \hat{Y}_2 = (M - L)\hat{X}_2 + \hat{F}_2, \quad (2.74)$$

where the new noise operators are defined as

$$\hat{F}_1 = \frac{1}{2}(\hat{F} + \hat{F}^\dagger), \quad \hat{F}_2 = -\frac{i}{2}(\hat{F} - \hat{F}^\dagger). \quad (2.75)$$

The commutator eq. (2.71) straightforwardly implies - using the Robertson inequality in eq. (2.64) - that

$$\Delta\hat{F}_1 \cdot \Delta\hat{F}_2 \geq \frac{1}{4}|1 - |M|^2 + |L|^2|. \quad (2.76)$$

Now we just need to clarify the definitions to obtain something more physical. We recognize that the power gains for the different quadratures are

$$G_1 = (M + L)^2, \quad G_2 = (M - L)^2. \quad (2.77)$$

Then, the normalized fluctuations of the output quadratures can be written as

$$\frac{(\Delta\hat{Y}_i)^2}{G_i} = (\Delta\hat{X}_i)^2 + \frac{(\Delta\hat{F}_i)^2}{G_i} \equiv (\Delta\hat{X}_i)^2 + A_i, \quad (2.78)$$

where $i = 1, 2$ and A_i are the added noise quanta as an equivalent noise at the input. It is worthwhile to emphasize the unit of A_i . Since the input and output modes are traveling waves, they should be interpreted within a specific duration $\tau \simeq 1/\Delta f$, where Δf is the bandwidth of the amplifier (which is typically small compared to the operating frequency). The number of quanta in the input mode are related to the input power per bandwidth; therefore, all “units of quanta” should always be understood as units of an equivalent flux of quanta per unit bandwidth, i.e. quanta/(s·Hz).

Rewriting the relation eq. (2.76) gives

$$\sqrt{A_1 A_2} \geq \frac{1}{4} \left| 1 \pm \frac{1}{\sqrt{G_1 G_2}} \right|, \quad (2.79)$$

where the upper (lower) sign holds when $|M| \leq |L|$ ($|M| \geq |L|$). As a recap, we note that eq. (2.79) simply comes from the fact that introducing a noise operator in the output signal is necessary to preserve the canonical commutation relations and that the commutator of this noise operator with its adjoint is nonzero (except in the trivial case when the gain is 1). More physically, the noise operator \hat{F} is related to the fact that during the amplification process, other degrees of freedom are necessary (beyond the input and output modes). This is because every linear amplifier is a nonlinear system which has an energy source controlled by the input. Some of the energy (usually coming from a DC voltage or an extra pump) is redirected towards the output channel and some of it is redirected to other channels.

Phase-preserving linear amplifier

A phase-preserving (also called phase-insensitive) amplifier is one which amplifies both quadratures equally. In this case we have $G \equiv G_1 = G_2 = M^2$ and $A_1 = A_2 \equiv A/2$ (a similar case is the phase-conjugating amplifier, where $G \equiv G_1 = G_2 = L^2$). eq. (2.79) can be rewritten as

$$A \geq \frac{1}{2} \left| 1 \pm \frac{1}{G} \right| \longrightarrow \frac{1}{2} \quad \text{as } G \longrightarrow \infty. \quad (2.80)$$

Thus, a phase-preserving amplifier with a large gain must add at least half a quantum of noise to the input signal.

Phase-sensitive linear amplifier

In the case when the amplifier does not amplify the two quadratures equally, the added noise can be less than half a quantum for one of the quadratures. Consider for example

the case when $M^2 - L^2 = \sqrt{G_1 G_2} = G \gg 1$, so

$$A_1 A_2 \geq \frac{1}{4} \left| 1 - \frac{1}{G} \right| \rightarrow \frac{1}{4}.$$

If we choose $G_1 \gg 1$, the added noise A_1 can be below $1/4$, in the expense of added noise on the other quadrature ($A_2 > 1/4$). Another example is when one wishes to completely give up the information on one of the quadratures: $M = L = \sqrt{G}/2$, corresponding to $G_1 = G$ and zero gain for the other quadrature, $G_2 = 0$. One can amplify one quadrature perfectly; this scheme is analogue to the back-action evasion [67, 34, 68].

Noise temperature and noise figure

The added noise A_i is a convenient way to characterize the noise performance of a phase-insensitive amplifier as it is independent of the noise carried by the input signal. It is traditional, however, to characterize the noise in terms of noise temperature. We elaborate this in detail in section 4.2.3. Briefly, restricting ourselves to the phase-preserving case, the noise temperature is defined as the temperature which needs to be added to the input noise temperature in order to account for all the output noise (including the added noise by the amplifier) referred to the input. Specifically, let us first define the noise temperature of the input (which is assumed to be in a thermal state) by

$$(\Delta \hat{a})^2 = \frac{1}{2} \left[\exp \left(\frac{\hbar \omega}{k_B T} \right) - 1 \right]^{-1} = \frac{1}{2} \coth \left(\frac{\hbar \omega}{2 k_B T} \right). \quad (2.81)$$

Then, the definition of the noise temperature T_n becomes

$$\frac{1}{2} \coth \left(\frac{\hbar \omega}{2 k_B (T + T_n)} \right) \equiv \frac{(\Delta \hat{b})^2}{G} = A + \frac{1}{2} \coth \left(\frac{\hbar \omega}{2 k_B T} \right). \quad (2.82)$$

In the specific case of a quantum-limited input signal ($T = 0$), the minimum added noise in the phase-insensitive case given by eq. (2.80) can be reformulated in terms of the noise temperature as

$$T_n = \frac{\hbar \omega}{k_B} \ln(1 + A^{-1}) \geq \frac{\hbar \omega}{k_B} \left[\ln \left(\frac{3 - G^{-1}}{1 - G^{-1}} \right) \right]^{-1} \rightarrow \frac{\hbar \omega}{k_B \ln(3)} \quad \text{as } G \rightarrow \infty. \quad (2.83)$$

Another traditional quantity which describes the noise performance of an amplifier is the noise factor F (sometimes also called the noise figure; however, typically the noise figure is the noise factor expressed in dB), which is the ratio of the input signal-to-noise ratio to the output signal-to-noise ratio (both in power):

$$F = \frac{\text{SNR}_{\text{in}}}{\text{SNR}_{\text{out}}} = 1 + \frac{A}{(\Delta \hat{a})^2}. \quad (2.84)$$

2.3. The quantum limit of amplification

Again, for a quantum-limited input signal the noise factor is bounded by

$$F \geq 2 - G^{-1} \longrightarrow 2 \quad \text{as} \quad G \longrightarrow \infty. \quad (2.85)$$

It is apparent that these two quantities are not convenient measures to characterize the noise performance of an amplifier in general, as they depend on the amount of noise on the input signal; moreover, they are not well-defined in the case of $\hbar\omega \geq k_{\text{B}}T$.

3 Design and fabrication

In this chapter we describe the design ideas and fabrication process for producing the current generation of superconducting electromechanical devices. The chapter is focusing on the hybrid, dual-mode circuits but introduces previous and future designs as well. The purpose of this chapter is not only to demonstrate what worked but also to explain the idea behind the development; hopefully this can give a deeper understanding of the process and design details and can save other PhD students untold hours in the cleanroom.

3.1 Background and process development

The first generation of superconducting electromechanical devices was developed in the group by X. Zhou. It consisted of a quarter-wavelength coplanar waveguide resonator in which the mechanical element was a high-stress, Si_3N_4 nanomechanical beam metallized with niobium, as shown in fig. 3.1. This geometry is similar to the ones studied before to measure thermomechanical motion with a force sensitivity of $3 \text{ aN}/\sqrt{\text{Hz}}$ [31] as well as to measure with imprecision beyond that at the standard quantum limit [33]. The Schwab group had also developed this platform to demonstrate sideband cooling and back-action evasion measurements close to the quantum (i.e. single phonon) regime [69, 34]. The metallized beam structure developed in the group was used to demonstrate all-microwave controlled slowing and advancing of microwave signals with low loss, fast switching time and distortion-free delay at the millisecond scale [36].

The greatest drawback of this platform is essentially the low participation factor ϵ of the nanobeam, that is, how much of the total capacitance C is actually modulated by the mechanical motion. A typical value of ϵ in these structures is in the order of 10^{-4} . This has two consequences. First, it renders the vacuum coupling rate g_0 small, since

$$g_0 = x_{\text{zpf}} \frac{\partial \omega_c}{\partial x} = x_{\text{zpf}} \omega_c \frac{1}{2C} \frac{\partial C_m}{\partial x} \propto x_{\text{zpf}} \frac{\omega_c}{d} \frac{\epsilon}{2}. \quad (3.1)$$

Chapter 3. Design and fabrication

Typical values, consistent with measured data, give $g_0/2\pi \approx 1$ Hz. This limits the achievable cooperativity $C = \frac{4g_0^2}{\Gamma_m \kappa} n_p$ which in turn limits the performance of the device (e.g. minimum phonon occupancy for sideband cooling). We note that recently there has been a great effort to reduce the parasitic capacitance (and therefore to increase the participation factor) in this geometry, which resulted in over an order of magnitude of increase in g_0 [70].

Second, in these devices the 2nd order coupling $g_0^{(2)} \propto \frac{\partial^2 C}{\partial x^2}$ causing power dependent frequency shift is nonnegligible. In particular, $g_0^{(2)}$ will generate a power dependent spring shift $\Delta\Omega_m \propto \Omega_m k_{EM}/k$ where k is the bare mechanical spring constant and k_{EM} is the spring constant induced by the electromagnetic power circulating in the cavity. This quantity is given by

$$k_{EM} \propto \hbar\omega_c P g_0^{(2)}.$$

Then, when this frequency shift $\Delta\Omega_m$ becomes comparable to the bare mechanical linewidth Γ_m , the mechanical motion becomes self-oscillatory and, therefore, unstable. Since

$$\frac{\Delta\Omega_m}{\Gamma_m} \propto \frac{1}{\epsilon} \frac{Q_m}{Q_{ext}} \frac{\Gamma_{opt}}{\Omega_m},$$

one can estimate the maximum achievable optical damping rate this device can sustain and find $\Gamma_{opt} \approx 10$ kHz.

In order to mitigate these limitations, it was necessary to move away from the 1D geometry. The first device using a different, 2D planar geometry was developed at NIST (Ray Simmonds' group [37]). Having pioneered the vacuum gap capacitor technology, they have created a superconducting electromechanical circuit in which the capacitor has a suspended membrane as a top electrode. In this design, the modulated capacitance is much higher and the participation ratio can easily be pushed above 75% (3 orders of magnitude improvement compared to the nanostrings). For example, for a lumped element LC circuit with resonance frequency of 5 GHz and a circular vacuum gap capacitor with radius of $22.5 \mu\text{m}$ and a plate separation of 100 nm, the modulated capacitance is around 30 fF, which accounts for over 80 % of the total capacitance. The optomechanical coupling can be calculated as

$$G = \frac{\omega_c^2 Z_c}{2} \epsilon_0 \frac{A}{d^2},$$

where Z_c is the characteristic impedance of the circuit, A is the area of the capacitor and d is the plate separation. With reasonable parameters, this gives $G/2\pi \sim 50$ MHz/nm and $g_0/2\pi \sim 100$ Hz.

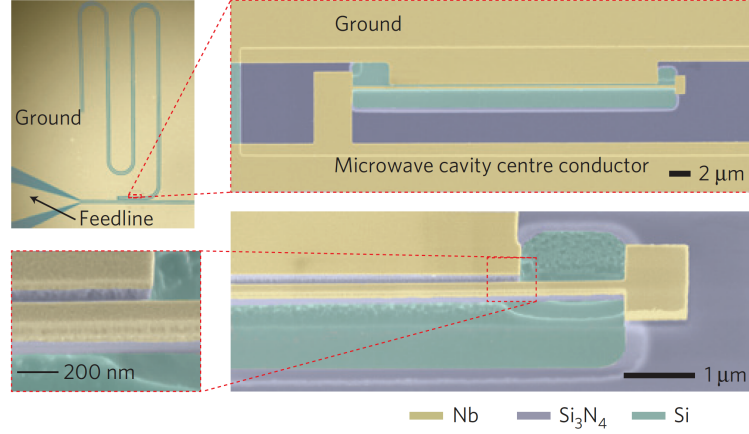


Figure 3.1 – **Superconducting electromechanical device using a stressed nanos-tring.** The device had previously been developed in the group. The mechanical element is a $30\ \mu\text{m}$ long, Si_3N_4 nanos-tring metallized by Nb. Figure taken from [36].

3.1.1 Process overview

The basic idea and first demonstration of a mechanically compliant membrane-like capacitor embedded in a superconducting circuit was done at the National Institute of Standards and Technology, Boulder CO USA as described in [39], with the main fabrication process outlined in [38, 37]. The original motivation to develop such a technology was to reduce the effect of dielectric losses in superconducting circuits coming from two-level effects. These two-level systems are believed to be coming from structural imperfections of the dielectrics and cause unwanted energy dissipation of superconducting circuits through dipole coupling to the electromagnetic field. For this reason, LC resonators using capacitors with dielectric filling lead to short energy relaxation times and can disrupt the operation of quantum circuits (reduced measurement fidelity, increased noise in the read out, unwanted qubit interactions etc.) [71]. There have been some strategies developed to eliminate the spurious TLS defects. One is simply to search for materials which have less TLSs. An example is enriching the silicon content of silicon nitride which has proven to improve the loss tangent by a factor of 50 [72]. Alternatively, one can use planarized components which do not use amorphous materials as dielectric filling but simply rely on vacuum and the crystalline substrate (typically Si or sapphire). Although good performance has been achieved with this strategy in terms of the quality factor, these designs have a large footprint (in the mm range) and related problems such as additional resonance frequencies or higher parasitic capacitance and inductance. Vacuum-gap capacitors were developed to address these challenges and to fabricate low-loss, small footprint superconducting circuits. It was later realized that the vacuum-gap capacitors have mechanical modes in the relevant frequencies and have relatively strong coupling to the electromagnetic mode for studying optomechanical phenomena.

Since the original conception of the fabrication process described above, at least three research groups have developed analogous devices. Table 3.1 summarizes the fabrication details of the various approaches. The general idea, however, remained the same (depicted in fig. 3.2): first, a part of the resonant LC circuit (bottom plate of the capacitor and connecting lines) is patterned out of a superconducting thin film. Then, a sacrificial layer is deposited and patterned, after which the rest of the circuit is deposited and patterned. Finally, the wafer is diced into chips and the sacrificial layer is etched away with a release process such that the capacitor's top membrane is released and becomes mechanically compliant. In some designs (e.g. in the case of a spiral inductor), vacuum bridges above inductor lines are also necessary.

| | Substrate | Metal 1 | Sacr. layer | Metal 2 | Release |
|----------------------|-----------|---------------------------|------------------|---------|-----------------------|
| NIST [39] | Sapphire | Al | SiN _x | Al | SF ₆ |
| Caltech 1st gen [73] | Si | NbTiN | SiO ₂ | NbTiN | buffered HF |
| Caltech 2nd gen [74] | Si | Al (on SiN _x) | Ge | Al | XeF ₂ |
| Caltech 3rd gen [67] | Si | Al | polymer | Al | Remover PG |
| Aalto 1st gen [44] | Sapphire | Al | PMMA | Al | O ₂ plasma |
| Aalto 2nd gen [75] | Quartz | Al | unknown | Al | unknown |
| This work | Sapphire | Al | Si | Al | XeF ₂ |

Table 3.1 – **Summary of the materials and release process developed by various groups to fabricate superconducting circuits with a vacuum-gap capacitor.** Various groups have developed a process to fabricate the circuit for the use in cavity circuit optomechanics. The typical choice of substrate and superconducting metal are sapphire and Al, respectively.

3.1.2 Current recipe

The key ideas of the process flow are similar to the ones developed by Cicak et al [38, 37], with differences in the material deposition techniques, sacrificial layer material and etch chemistries (including the release). The final process flow is visualized in fig. 3.3 and essentially it contains three deposition, four lithography and five etch steps in order to pattern the deposited material. Tables in Appendix A contain the detailed process run cards.

We start with a C-plane, single-side polished, 4 inch, 525 μm thick sapphire wafer. The wafers are treated with an initial surface cleaning step (full RCA) and anneal (1 hour at 1000 °C in N₂ atmosphere). Although this type of treatment was shown in literature to achieve a close to atomically flat surface and to increase the quality factor of microwave circuits fabricated on sapphire[cite], this initial step was later on reduced to a single piranha step (10 mins) and no significant degradation of the microwave quality factor

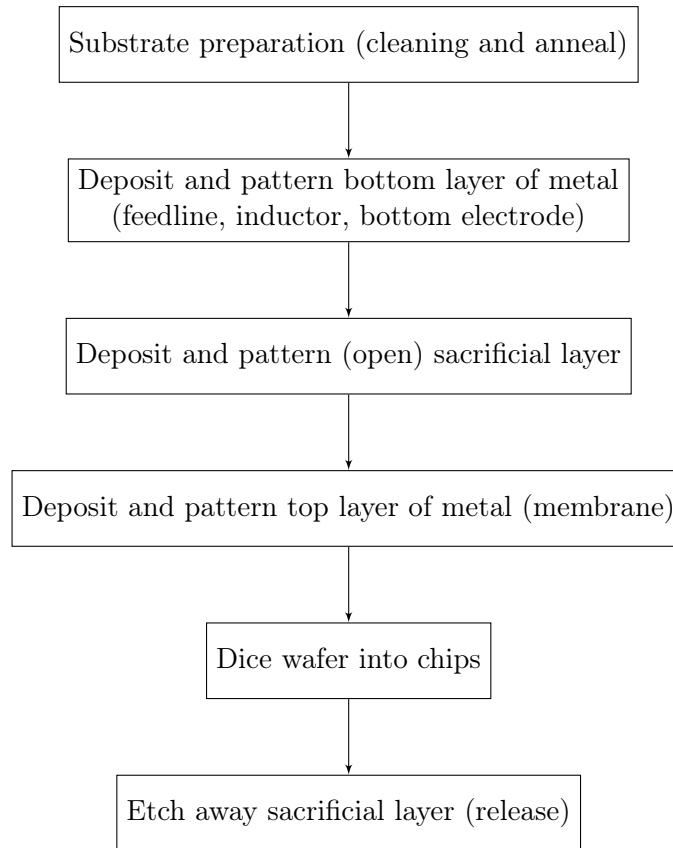


Figure 3.2 – **The general overview of the process to fabricate a superconducting circuit with a mechanically compliant vacuum-gap capacitor.** All processes summarized in table 3.1 follow the same idea. First, a part of the circuit is patterned from a thin-film metal on a substrate, after which a sacrificial layer and a top metal layer are deposited and patterned. The process ends with removing the sacrificial layer, thereby releasing the capacitor.

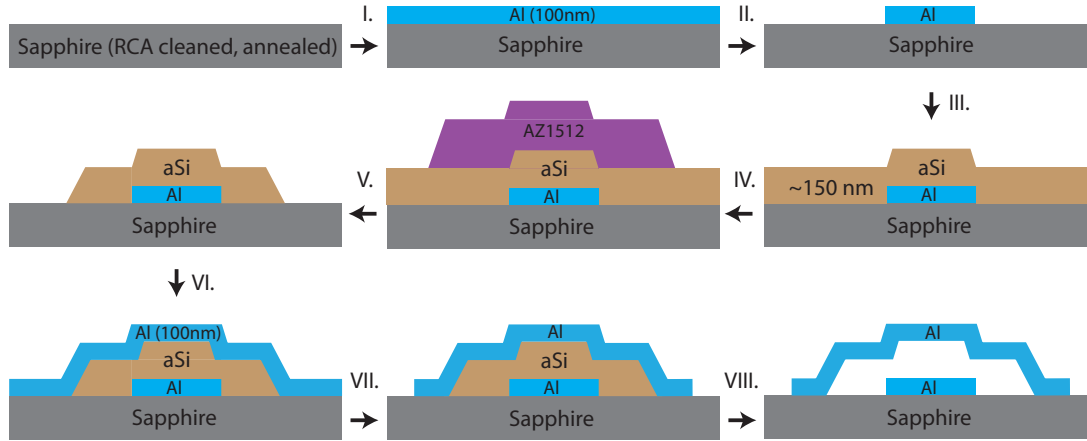


Figure 3.3 – Main fabrication steps of the current, final process flow for fabricating superconducting electromechanical circuits. The process starts with an RCA cleaned sapphire wafer and through 3 deposition, 4 optical lithography and 4 etch steps, the final devices on a chip are fabricated.

was observed.

After the surface of the wafer is cleaned, 100 nm of Al is deposited using e-gun evaporation (Leybold Optics LAB 600H). Then, 50 nm of Ti is deposited with the same technique on the backside of the wafer. This step ensures that the backside is conductive, which is important for the etch steps later on (some of the etchers use electrostatic clamping), and provides a uniform ground plane for the final circuit.

Photoresist (AZ1512, which is used for the other lithography steps as well, cf. Appendix A) is spin-coated on top of the Al layer and is patterned using direct laser lithography (Heidelberg MLA150). This technique turned out to be quite beneficial for this process because it made the prototyping of the multilayer lithography steps more flexible and eliminated the need for writing four new masks each time a modification was made on the design. It also made the alignment process easier and more accurate. This is the stage at which most of the wafer layout is defined (chip boundaries, feedline, circuit, except the top capacitor plate). The pattern of the photoresist is then transferred using a Cl_2/BCl_3 -based ICP dry etch (STS Multiplex). Initially, this step was done by a wet etch (Microchemicals ANP), which allows to save time, especially in case of batch processing. However, the etch rates - and therefore the exact dimensions of the pattern transferred - proved to be inconsistent.

After patterning and etching the first Al layer, the wafer is cleaned with a standard resist cleaning process (c.f. run card in the Appendix; it is worth emphasising that a long wet removal step is beneficial to get rid of all possible Cl residues coming from the etch process). Then, 200 nm of amorphous silicon is sputter deposited on the wafer (Pfeiffer

SPIDER600 or Alliance-Concept DP650, both DC magnetron sputtering machines). This layer serves as the sacrificial layer for the vacuum-gap capacitor and is patterned in two steps as shown in fig. 3.4. First, the pattern around the bottom electrode of the capacitor is exposed and developed, after which the resist is reflowed (wafer is put on a hotplate for 1 min 45 secs at 160 °C). This pattern is then transferred to the sacrificial layer by a Cl_2 -based Si etch. The selectivity of the process (probably around 1.5:1 for Si:photoresist), together with the reflow, ensure that the sidewall of the openings is slanted. This is important, as the top metal layer which is deposited at a later step needs a smooth transition from substrate to the surface of the sacrificial layer. If the layer is too sharp, the top metal film can break around the rim of the top plate of the drum, as shown in fig. 3.5. In the second patterning step of the sacrificial layer, this opening is extended using a fluorine-based chemistry (SPTS APS dielectric etcher). At this step, the connecting Al pad is exposed (this is where the top metal layer will connect to the rest of the circuit), which is the reason why the patterning of the layer cannot be done in a single Cl etch (it would attack the Al pad), a fluorine-based chemistry is necessary.

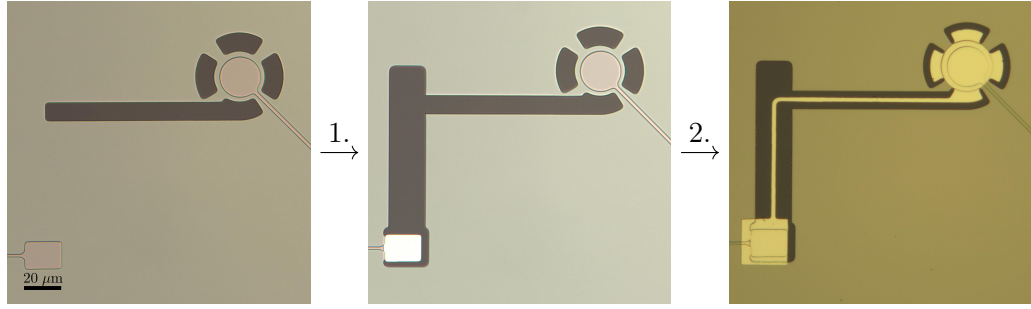


Figure 3.4 – **Details of patterning the sacrificial layer.** Patterning of the sacrificial (Si) layer around the vacuum-gap capacitor is done in two steps. First, after lithography and reflow of the resist, the Si layer is opened using a Cl dry etch chemistry around the bottom electrode. This ensures that the sidewall of the opening is slanted, which in turn ensures better step coverage and a smooth rim of the top capacitor plate. Second, the Si layer is opened with an SF_6 etch on top and around the connecting pad. Scale on the images are identical.

After the sacrificial layer is opened and the wafer is cleaned, the top Al layer is deposited. This layer will form the top, mechanically compliant electrode of the vacuum-gap capacitor. At this step, the deposition technique and conditions are crucial as they determine the stress in the film. A more thorough discussion of this is presented below but briefly, evaporation was showing more consistent (but not fully reproducible) results and the estimate of the stress of the film was slight tensile (in the order of 100 MPa).

This top metal layer is then patterned using direct laser lithography and a Cl_2/BCl_3 -based ICP dry etch (same recipe as the bottom layer). It is important that this etch is dry;

previous attempts with a wet chemistry failed because it damaged the sidewalls of the drum and broke the film (see fig. 3.5a). The wafer is cleaned and a thick layer of resist is spin-coated as a protection layer before it is diced into chips. The chips are cleaned (heated NMP bath preceded by a mild oxygen plasma) and the last, crucial step is to remove the amorphous Si layer and, consequently, to release the vacuum-gap capacitor. This is done by a pulsed, vapour XeF_2 etch which is an isotropic and controlled chemical etching method of Si on small samples with extreme selectivity to a range of materials (e.g. SiO_2 , Al).

An optical and SEM micrographs of the device, together with a 3D profile using an optical profilometer, are shown in fig. 3.11 and fig. 3.7, respectively.

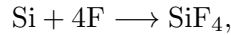
The release process

A critical step in the process to fabricate the vacuum-gap capacitors with a mechanically compliant top electrode is the release, i.e. the step during which the sacrificial layer (in our case sputtered amorphous silicon) is etched away. The challenge here is the very high aspect ratio of the structure: the capacitor is $\approx 30 \mu\text{m}$ in diameter and the thickness of the sacrificial layer (initial gap between the top and bottom electrodes) is 150-200 nm, giving an aspect ratio of > 150 . This requires an etch process which is able to penetrate the vacuum gap efficiently and which is extremely selective towards aluminium. Generally, for this task a dry vapour etch process is desirable to avoid no surface tension or bubble related problems, which can permanently damage the devices.

Initially, we have tried to use pure sulfur hexafluoride (SF_6) chemistry, which is a dry etch known to have high selectivity towards Al, as well as to be isotropic. This chemistry is available in a deep reactive ion etching (DRIE) system, mostly used and optimized for silicon and silicon-on-insulator etching. The SF_6 is ionized in the inductively coupled ion plasma, which creates a mixture of SF_x and F ions and radicals ($1 \leq x \leq 5$). A typical dissociation reaction is



Then, the F ions reach the Si to be etched to generate the final etch product of SiF_4 through the reaction

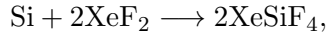


where Si is in the solid phase. In principle, this gas has a selectivity to photoresist versus Si above a 100, and a selectivity to Al versus Si above 500, making it an attractive etch choice for releasing MEMS structures. The etch rates in our system (Adixen AMS200; recipe: Si release, 400 sccm of pure SF_6) are $\approx 2 \mu\text{m}$ in the lateral and $\approx 4 \mu\text{m}$ in the vertical direction, calibrated on Si micropillars. This would mean that a vacuum-gap

3.1. Background and process development

capacitor of 30 μm in diameter could be released in < 10 minutes. However, these rates are design dependent and we found that even after 16 mins, the vacuum-gap capacitors could not be released and the etch rate diminished above some etching time (see example in fig. 3.8). Another complication is that even though the chemistry itself is very selective to Al, there is some amount of physical etching occurring caused by ion bombardment which damages the circuit (note that at this stage the chips are not covered by any resist and no additional protection is possible, as after release the device is very sensitive). An additional, smaller annoyance is that the chip has to be glued on a wafer and removing the glue after the release is tedious and risks damaging the mechanically compliant membrane.

Therefore, we changed the release process to an alternative one which uses gaseous xenon difluoride. It provides a highly selective isotropic etch for Si, Mo and Ge and is an ideal solution for etching sacrificial layers to release moving components within MEMS devices. The reaction of the gas with Si is described by



where only Si is in the solid phase. This type of etching provides some unique advantages and capabilities compared to wet and SF_6 plasma etch options. First, the selectivity towards Al is essentially infinite, therefore very long undercuts are possible. Second, the etcher does not use plasma; it simply insert the gas into the etching chamber and pumps it out after some time, minimizing the possibility of device damage and keeping all parts of the circuit intact. Third, the etch rate is fast, above 4 μm per minute depending on the pressure and amount of exposed Si on the chip.

We have succeeded to remove all the sacrificial layer and release the vacuum-gap capacitors in less than 8 mins of actual etching time (16 pulses of 30 seconds; exact parameters are in Appendix A). Even after 30 seconds of etching, it showed significant progress in removing the layer between the Al electrodes, as shown in fig. 3.8. There are two facts to keep in mind, however. One is that the XeF_2 gas interacts with water and forms HF vapour, which is toxic, as well as it damages the surface of Al. Therefore, one has to make sure that the chips are dehydrated before release (2 mins of O_2 plasma is suggested). Second, the reaction of Si etching with the XeF_2 gas is exothermic, leading to local heating of the Al membrane being released. It has been speculated, though not rigorously confirmed, that this heating can cause local annealing of the film, therefore creating a non-uniform stress.

There are multiple ways to check whether the release step was successful or not. To calibrate the etch rate, we have prepared multiple chips with vacuum-gap capacitors and did the release process one by one with increasing number of etch pulses. Then, the top Al layer can be etched away to reveal the remaining sacrificial layer as shown in

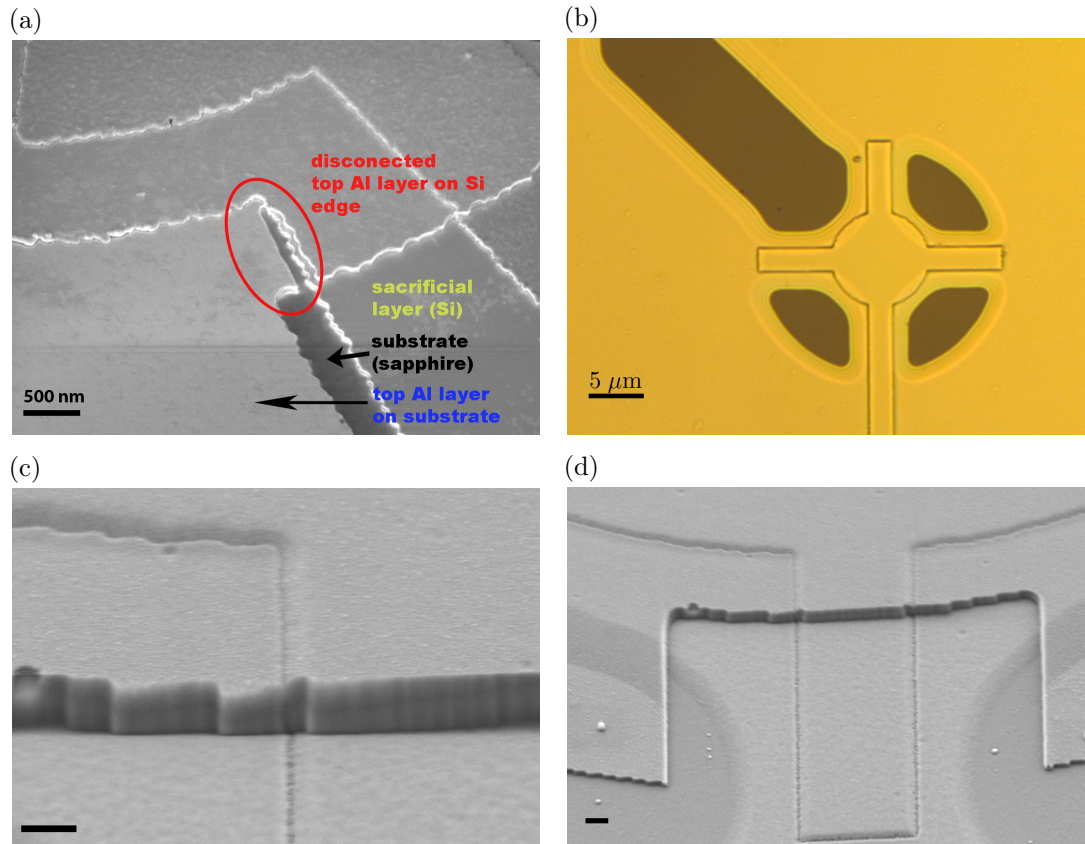


Figure 3.5 – **Effect of the sidewall slope of the sacrificial layer** a) Broken support legs of top membrane on the edge of the sacrificial layer openings, due to, on one hand, sharp sacrificial layer edge and, on the other, wet etch of top Al layer. b)-d) Slanted sacrificial layer sidewall and smooth top Al layer after reflow and dry etch using a Cl chemistry. The scale bars in c-d) indicate 500 nm.

fig. 3.8. Another invasive way is to use strong duct tape to tape off the released part of the membrane. Ultimately, the most effective way to test the release is to use an optical profilometer to perform a topography measurement over the surface of the membrane (example shown in fig. 3.11). Once this topography measurement yielded positive results, in some cases we tested the capacitors by means of optical fiber interferometry to measure the mechanical frequency at room temperature. This method is briefly described in section 4.1; however, it is worth noting that the method did not give consistent results (in many cases the capacitors did not have a mechanical mode in the 1 - 10 MHz at room temperature but were not collapsed).

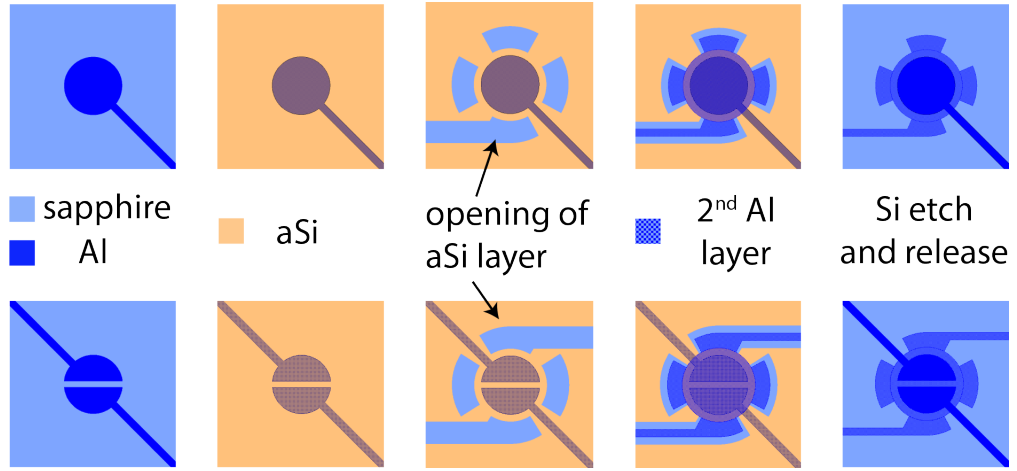


Figure 3.6 – **Visualization of the fabrication process from top view.** The top view is shown for two different vacuum-gap capacitor designs: capacitors with a single (top panel) and with a segmented bottom electrode (bottom panel), respectively.

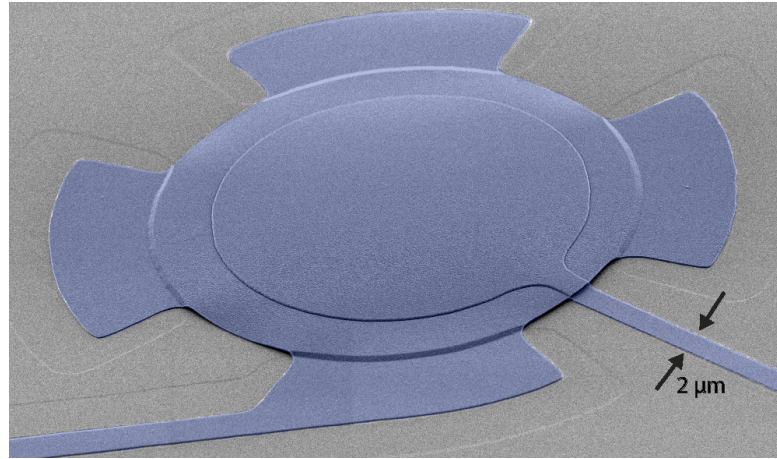


Figure 3.7 – **Scanning electron micrograph of the vacuum-gap capacitor.** The false-coloured electron micrograph shows the mechanically compliant part of the microwave optomechanical circuit. The vacuum-gap capacitor is $\approx 30 \mu\text{m}$ in diameter with a gap separation of $\approx 40 \text{ nm}$ at cryogenic temperatures.

Stress of the top film, collapse issues

The most crucial aspect of the fabrication process in terms of the survival (i.e. non-collapse) of the vacuum-gap capacitors is the stress in the top metal film. However, the stress of a 100 nm thick Al film was found to have large variations even when the deposition parameters were nominally the same. This issue is not completely understood - and this lack of understanding is consistent with literature - but some aspects are described below.

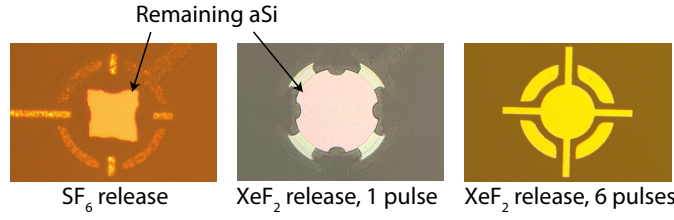


Figure 3.8 – **Comparison of different release processes.** Drum capacitors after a release etch with the top Al plate (taped off or etched). The etch process with pure SF_6 was unable to remove the sacrificial layer even after 14 mins, after which the Al appeared damaged due to physical etching (ion bombardment). In contrast, the XeF_2 process was able to release the capacitor.

Originally, sputtering was used to deposit the top layer - in order to ensure better step coverage - and the suspended drums could be fabricated with a non-negligible yield. This yield dropped significantly in course of Spring 2015 and the deposition was changed to evaporation which, again, produced good yield and working structures even at millikelvin temperatures. The yield, however, has been fluctuating since then and the Author of this thesis speculates that the stress is responsible for this.

The stress of a 100 nm thick Al film deposited on Si was measured to be very slightly tensile (50-100 MPa) regardless of deposition method (sputtered with SPIDER600, DP650 or evaporated with LAB600). This is consistent with literature [78, 76]; however, the stress can be highly dependent on the argon pressure during the deposition [79, 80]. Repeating the same stress measurement on the sapphire + 200nm of aSi stack, however, is difficult. This is because the stress is calculated from the curvature change caused by the addition of the film (tool: Toho FLX 2320-S). The key point is that the tool measures the curvature of the wafer caused by the film deposition using a scanned laser. The stress of the film can then be calculated using elasticity equations. Since stress is force normalized by area, it is a field variable, and therefore it cannot be measured directly; only the effect of stress is measurable. However, sapphire is semi-transparent, therefore there is not enough laser light to be collected. One method is to use the backside of the wafer, which is anyway coated with a reflective Ti layer. This measurement gave anything from slight compressive to slight tensile, although with large error bars (generally, the error of the tool is in the order of 30-40 MPa anyway), therefore not providing any conclusive results. Therefore, we can only speculate that depositing Al on sapphire + aSi stack gives the same results as measured on an Si wafer.

An observation which contradicts this conclusion (i.e. slight tensile stress) is the topographic measurement of the released membranes. In many cases when the membranes were not collapsed, these measurements revealed that the drums buckle up (see in fig. 3.11 and fig. 3.12): the original height of the membrane can be 100s of nanometers more than

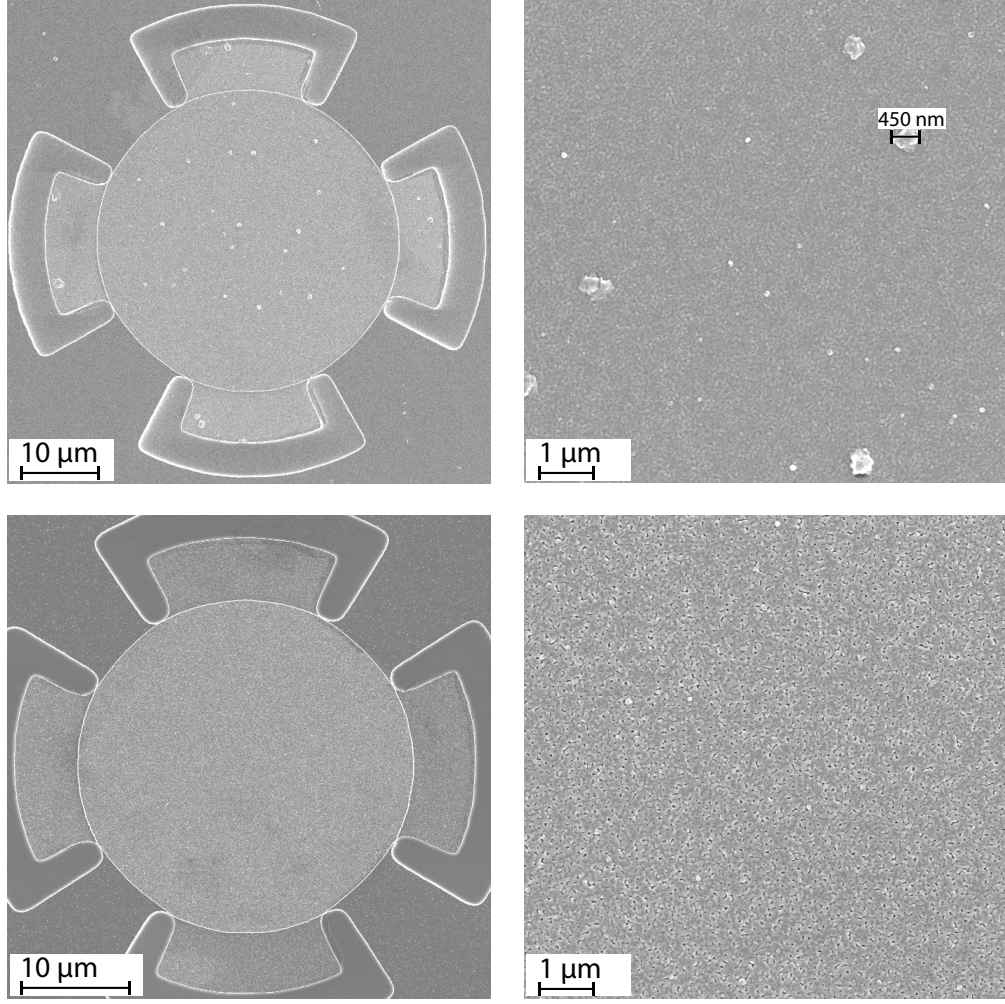


Figure 3.9 – **Comparison of different thin film deposition methods of the top Al layer.** Top row shows a fabricated drum-type capacitor (before the final release step) with DC Magnetron sputtered - machine: Alliance-Concept DP 650 - top metal layer (100 nm of Al). Bottom row shows the same but the top metal layer was deposited using the Leybold Optics LAB 600H electron beam evaporator. The sputtered Al thin film shows larger grain size and hillocks, potentially indicating more compressive stress [76, 77].

the thickness of the sacrificial layer. Based on COMSOL simulations of the structure (see fig. 3.10), this indicates compressive stress in the range of 350-400 MPa. In fact, all drums which showed desirable optomechanical properties were buckled up and this was sustained after the thermal cycle in the dilution refrigerator (sometimes the height even increased; and sometimes the drum collapsed). One explanation for why compressive stress helps the survival of the membrane is that during cooldown the film's stress becomes slight tensile due to the mismatch in the thermal expansion coefficient between the substrate and the metal film ($C_{T,sapp.} \approx$ and $C_{T,Al} \approx$). Therefore, starting with 350 MPa of compressive stress at room temperature actually results in slight tensile stress at 10 mK.

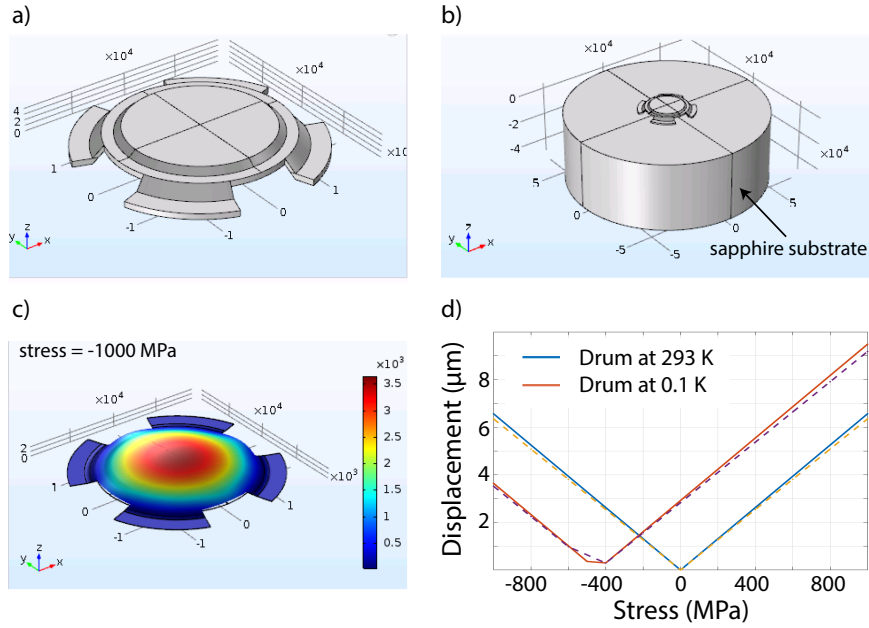


Figure 3.10 – **Example of a COMSOL simulation of displacement and stress of the vacuum-gap capacitor.** **a)** Geometry of the vacuum-gap capacitor set up in COMSOL, mimicking the same sidewall angle as produced in a real sample. **b)** The simulation takes into account the real material parameters of the substrate. **c)** Displacement profile of the suspended top plate for a certain stress (1 GPa compressive). As also experimentally verified (cf. fig. 3.12), the membrane buckles up (the scale of the color bar is in nm). **d)** Displacement at the center point versus the stress in the film at room temperature and at low temperature (i.e. after the stress membrane is released and cooled down). As expected, the mismatch in the thermal expansion coefficient of the substrate and the metal film induces tensile stress. The dashed lines show a simulation with different sizes (in terms of angle) of the four leg supports; no significant change is the result is observed.

There are a few other considerations to take into account, most of which are not fully understood. One is that the release process with XeF_2 is exothermic. This may result in a local annealing of the membrane, especially severe in the middle, which in turn may result in non-local stress. This has also been reported by at least one other group (private communication). Moreover, when the released capacitors are annealed at a temperature 150-200 °C, the height of the buckling increases even after the devices are back at room temperature (hysteresis) and this was observed to improve mechanical properties at low temperatures (the mechanical mode was more stable). Finally, the stress can relax over time: in some (but not all) cases, it was observed that after a few months the buckling of the membrane significantly decreased.

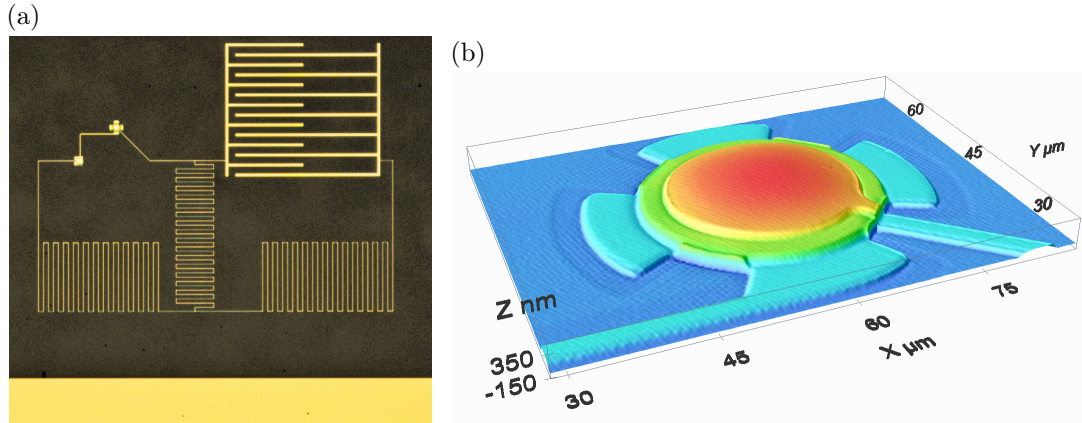


Figure 3.11 – **Optical micrograph and topography of the electromechanical circuit.** a) The optical micrograph of the hybrid-mode electromechanical device with a meander-type inductors, a vacuum-gap capacitor, an interdigitated capacitor and part of the feedline. b) Optical measurement of the vacuum-gap capacitor after release using a confocal topography profiler. The measurement is used to determine whether the drum is collapsed.

3.1.3 Additional methods: electron beam lithography and planarization

Fabrication of electromechanical devices using electron beam lithography

During the first phase of the development, there has been significant effort devoted to implement the fabrication of superconducting circuits with a mechanically compliant capacitor using electron beam lithography. This was mostly motivated by the ease of rapid prototyping of multilayer processes with ebeam (at that time direct laser writing was not available, standard lithography with a mask wasn't developed for sapphire substrates in the clean room and prototyping a 4-layer process - with accurate alignment requirements - with masks is cumbersome). Although this process was developed, it had its own challenges. Most important of those challenges and their solutions are listed below.

1. Choice of resist. Writing with ebeam is slow and expensive, therefore a negative resist (for the two steps for Al patterning) with low-dose requirements is necessary. There was only one resist at CMi which fulfilled these requirements: AZ nLOF 2020 from MicroChemicals. However, working with nLOF is difficult (painful, in fact) for two reasons: first, the results are extremely sensitive to the postbake temperature and duration (which is especially difficult to calibrate with sapphire, which has a very different thermal conductivity than Si) and second, it crosslinks during the ebeam writing and is very difficult to remove.

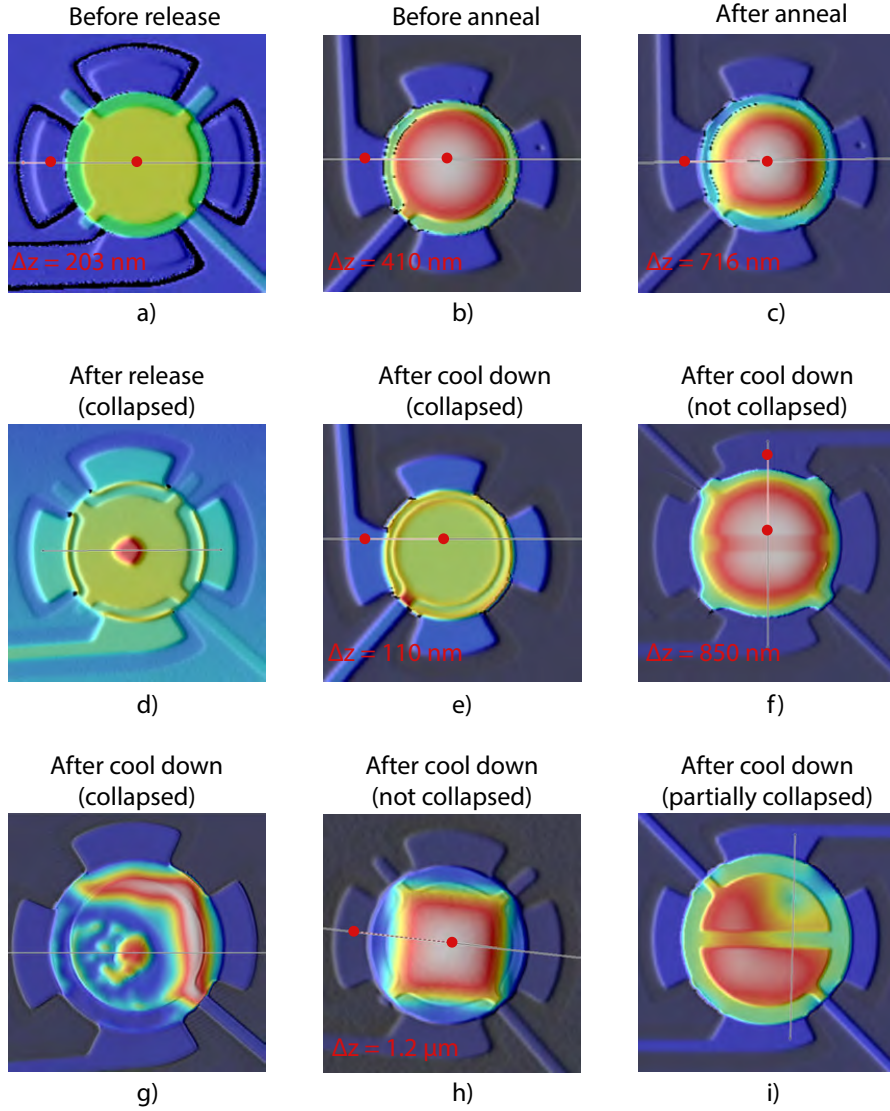


Figure 3.12 – **Interference microscopy measurements on various vacuum-gap capacitors.** The 3D optical profile at room temperature shows whether the devices are collapsed, as well as it indicates the amount of local stress in the suspended Al thin film.

2. Density of the pattern cannot be too high and lowest resolution beam settings have to be used in order to keep writing times and cost reasonable. With minimalistic chip and circuit design and using the highest spotsize electron beam, writing time could be kept below 40 mins per wafer.
3. Alignment marks: additional preprocessing steps are necessary to define alignment marks with a material which is recognized by the ebeam machine. Prepatterning the sapphire substrate is not suitable as it is non-conducting, neither it is possible to use the first layer of Al for the marks as it is a very light material, invisible to

the electron beam. This was solved by evaporating Ti + Pt (10 nm + 100 nm) on the substrate as a first step and direct etching using ion beams (IBE), or a double layer (PMMA+MMA) lift-off process.

Planarization of the sacrificial layer

We have fabricated designs in which the bottom electrode of the mechanically compliant drum-type capacitor was segmented (see e.g. section 3.2.2). The segmentation results in a non-planar sacrificial layer and, in turn, a non-planar top metal layer. This has a - potentially negative, although not fully confirmed - effect on the mechanical resonance frequency as well as on the stability of the top plate (especially considering that the topography of the top metal layer is comparable to its thickness). In order to mitigate this problem, a planarization method of the sacrificial layer was developed. Although there were initial trials to achieve this using chemical-mechanical polishing, the sputtered aSi layer did not have enough adhesion to the substrate and peeled off. A more successful approach involves spin coating a thick layer of resist and etching it away with a process which has a selectivity $\approx 1:1$ for resist:aSi. Specifically, we use a thick layer ($\approx 1\mu\text{m}$) of flowable oxide and ion beam etching, after which the topography of the sacrificial layer reduced from 100 nm to ≈ 15 nm with much smoother edges.

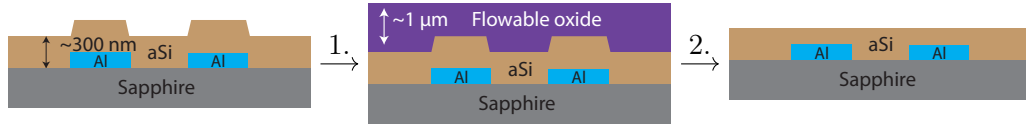


Figure 3.13 – **Process flow for planarizing the sacrificial layer.** Planarization of the sacrificial layer was developed for the segmented electrode designs in order to ensure smoothness of the top metal film. Originally, the sacrificial layer had a topography of ~ 100 nm (as the sacrificial layer follows the topography of the bottom electrode). After one iteration of the planarization process, this topography can be reduced to ~ 30 nm with smoother edges.

3.1.4 Experiments with titanium nitride

In the past few years, there has been a growing interest in using titanium nitride for superconducting microwave resonator fabrication, due to multiple factors. First, there is a possibility to tune its superconducting transition temperature by changing the deposition conditions (N content). Second, it has large surface inductance and third, it features high internal quality factors (potentially the better than Al, Nb or Re [81, 82]). In

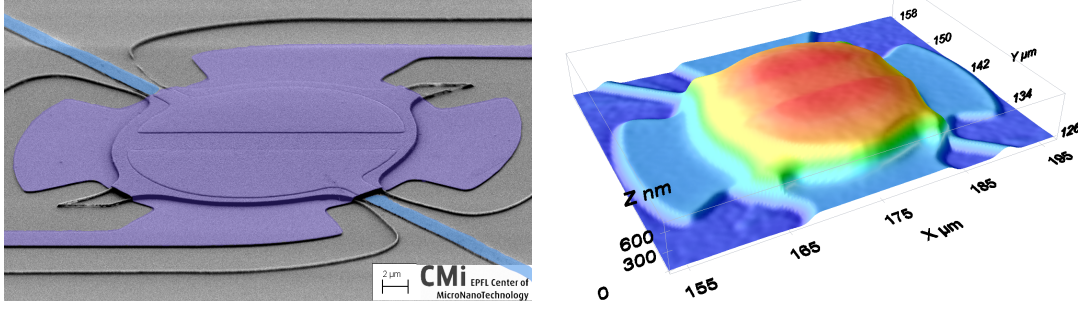


Figure 3.14 – **Scanning electron micrograph and optical topography measurement of a split-plate vacuum-gap capacitor.** The capacitors were fabricated with additional process steps to planarize the sacrificial layer, cf. fig. 3.13.

particular, Q_i at high powers was shown to be $\approx 2 \cdot 10^7$ and at low powers (single photon) of around 10^6 [83]. Motivated by these advances, we explored the possibility to fabricate superconducting microwave resonators with TiN for quantum optomechanics.

TiN has its own challenges, especially when it comes to producing a high-quality film with desired properties. For example, it was shown that the microwave quality factors strongly depend on the crystalline properties; crystalline orientation of the film [84], in turn, has a nontrivial dependence on the sputtering environment. Oxygen and other contaminants get easily absorbed during deposition, which can alter the quality significantly [82]. Microwave losses of the final structures strongly depend on the etch chemistry and parameters used to pattern the TiN film [85].

We successfully deposited TiN on Si with a predominant (2,0,0) orientation, as measured by X-ray diffraction (this orientation has been shown to be preferred for better microwave quality factors [84]). The deposition is done in the SPIDER600 sputtering machine using a customized recipe at high temperatures (deposition chamber: PM1, temperature: 350 °C, flow of nitrogen: 3 sccm, flow of argon: 8 sccm). However, the measured quality factors are still far from state-of-the-art results in the literature (best loaded Q-factors measured were in the range of 150000). Further assessment of the film, as well as optimized etching conditions are potential future directions. Additionally, we experimented with a full TiN device including the top metal layer but no signatures of mechanical motion could be measured. A simplified process flow is shown in fig. 3.15.

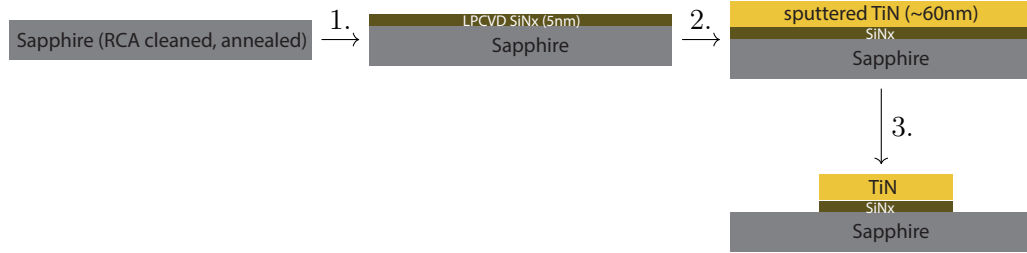


Figure 3.15 – **Process flow for TiN on sapphire.** The process flow shows the first few steps for fabricating the bottom metal layer using TiN. A thin low-stress SiN_x layer is used to facilitate the growth of the preferred (2,0,0) orientation.

3.2 Design: simulations and circuit layout

3.2.1 Simulation methods: Sonnet and FastHenry

In order to aid the design of multimode electromechanical circuits used in the experiments, we performed simulations with various software of the electromagnetic properties of the circuits, as well as the mechanical properties of the vacuum-gap capacitor.

Sonnet

Sonnet provides electronic design automation solutions for high-frequency RF and microwave electromagnetic analysis. Sonnet's main solver analyses 3D structures embedded in planar multilayered dielectrics. It uses a surface meshing technique (i.e. it meshes only the surface of the metallized circuit), therefore it is mainly used for planar circuits (sometimes also called 2.5D technique, as the metallization is modelled as a zero-thickness metal between the dielectric layers) but with significant speed-up compared to volume meshing techniques. It evaluates the electric field in the entire space due to the current in a single element (subsection) of the meshed circuit and repeats this for all elements one by one. The currents themselves are calculated using the method of moments such that the boundary conditions are satisfied (no voltage is allowed across a perfect conductor, therefore the total tangential electric field is zero on the surface of any conductor). Once the currents are obtained, the S- (or Y- or Z-) parameters can be calculated straightforwardly.

FastHenry

FastHenry uses the magneto-quasistatic approximation to compute the frequency-dependent self and mutual inductances and resistances of a generic 3D conductive structure. Essen-

tially it calculates inductances and resistances by approximating a conductor as a series of discretized rectangular filaments, each having a lumped resistance and inductance (i.e. under the assumption that the current is uniform in each filament). Using mesh analysis, it derives a set of complex linear equations for the filaments and uses advanced numerical tools such as GEMRES, along with a multipole approach to approximate the integrals of the self and mutual inductance that are performed for each filament. Specifically, the integral for the self-inductance is given by

$$L = \frac{\mu_0}{4\pi} \int \frac{f_1 f'_1}{r} dV dV', \quad (3.2)$$

where f represents the ratio of the current density J_1 to the current I_1 (f is taken for a current field point, while f' is for a current source point); r is the distance between the volume elements dV and dV' .

3.2.2 Dual-mode circuit with a split-plate capacitor

In chapter 5 we describe in detail one of the goals of this thesis, namely to experimentally realize the reverse dissipation regime in circuit optomechanics. The scheme consists of two microwave modes coupled to the same mechanical oscillator; provided that one of these microwave modes (the "auxiliary" mode) has a much larger energy decay rate than the other, one can sideband cool and damp the mechanical oscillator with this mode and achieve the reversed dissipation regime with respect to the other ("main") mode. Therefore, this requirement reduces to having the external coupling rate of the auxiliary mode much larger than that of the main mode, i.e.

$$\kappa_{\text{ex}}^{(\text{aux})} \gg \kappa_{\text{ex}}^{(\text{main})}. \quad (3.3)$$

A first attempt to design such a multimode circuit used two independent LC oscillators, in which the capacitors were modulated by a shared vibrating top electrode. One of the circuits was designed to be further from the feedline, therefore reducing the mutual inductance between the circuit and the feedline. This reduces the external coupling rate, as this is given by (cf. section 2.2.2)

$$\kappa_{\text{ex}} = \frac{M^2 \omega^2}{L Z_0} = \left(\frac{M}{L} \right)^2 \frac{1}{Z_0 C}. \quad (3.4)$$

However, measurements showed that the external coupling rates were similar (typically measured $\kappa_{\text{ex}}^{(\text{aux})} \approx \kappa_{\text{ex}}^{(\text{main})} \approx 1$ MHz). Simulations revealed that this is - most likely - due to additional capacitive coupling to the feedline of the main mode. As shown in fig. 3.17, the modes of the circuit are not fully in the lumped element regime due to the

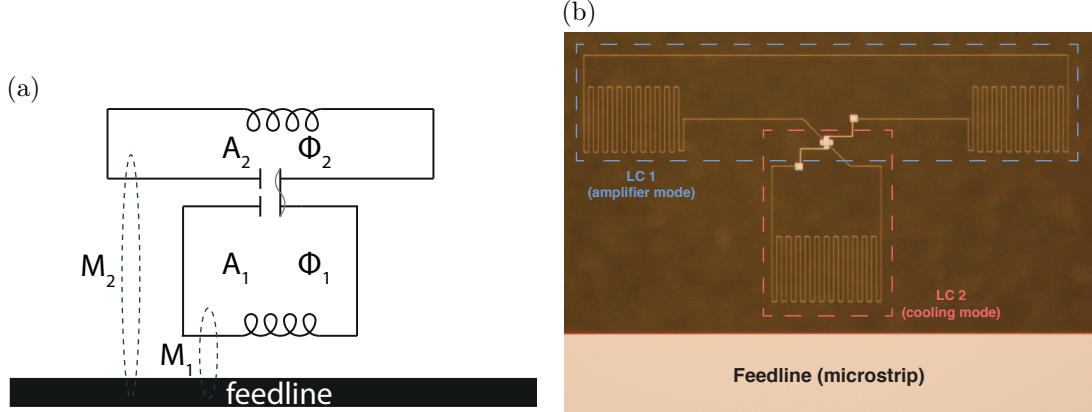


Figure 3.16 – **Circuit layout of the dual-mode circuit with a split-plate capacitor.** **a)** The first generation of the multi-mode electromechanical circuit designed to satisfy the external coupling rate hierarchy given by eq. (3.3). Based on eq. (3.4), the external coupling rate of the top circuit is - ideally - suppressed compared to the lower circuit. **b)** Optical microscope image of the fabricated circuit.

long inductors. When the circuit is excited at the resonance frequency of the upper mode, there is an appreciable charge density on the inductor lines on the lower part of the circuit (which ideally should be far from resonant at this frequency). This significantly increases the external coupling: without the lower part of the circuit, it is over 20 times less. The capacitive coupling also modifies the resonance frequencies.

3.2.3 Hybrid-mode circuits

In order to address the challenges of the circuit described in the previous section and to achieve the required hierarchy in external coupling rates given by eq. (3.3), we have designed, simulated and fabricated a circuit with a different topology which we call a hybrid circuit. The idea is to have two LC circuits with similar resonance frequencies (ω_1, ω_2) coupled together inductively (let us call the strength of this coupling J). The capacitor in one of the circuits is mechanically compliant, the other is a planar interdigitated capacitor. If the strength of this coupling is strong compared to the difference in the bare resonance frequencies ($J \gg |\omega_2 - \omega_1|$), the modes of the LC oscillators hybridise and normal-mode splitting occurs. Importantly, the new normal modes will have symmetric and antisymmetric current distributions in the LC loops (in the former, the current is flowing in the same direction in the two loops, while in the latter it flows in opposite directions). A useful consequence of this in terms of the design requirement described by eq. (3.3) is that, provided that the circuit is appropriately placed with respect to the feedline as shown in fig. 3.18, the symmetric mode will have a large external coupling

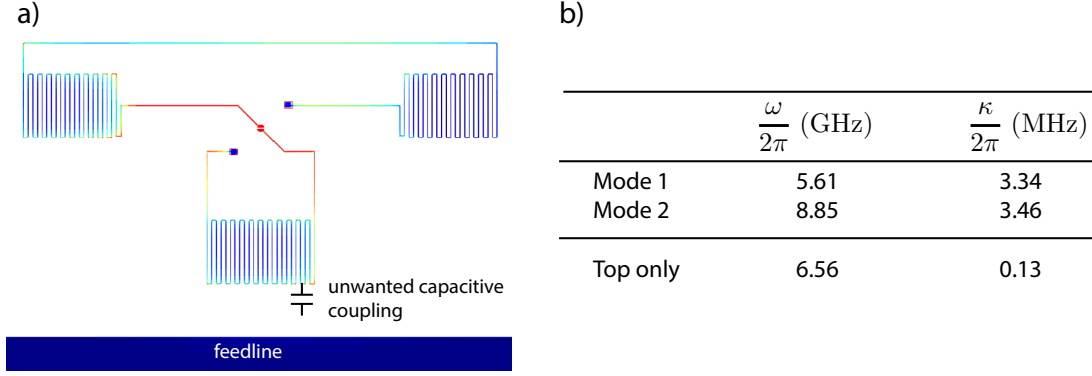


Figure 3.17 – **Simulation of the first generation of the multi-mode circuit design.**

a) Charge density of the upper mode, revealing that the mode is not in the lumped-element regime, as well as that the distributed charge on the lower part of the circuit causes capacitive coupling which increases the external coupling to the feedline. **b)** Simulation results of the two-mode circuit. Top mode only refers to the scenario when the bottom part of the circuit is completely removed; in this case, the external coupling rate is indeed suppressed, as expected.

rate to the feedline while the antisymmetric mode will have a negligible coupling.

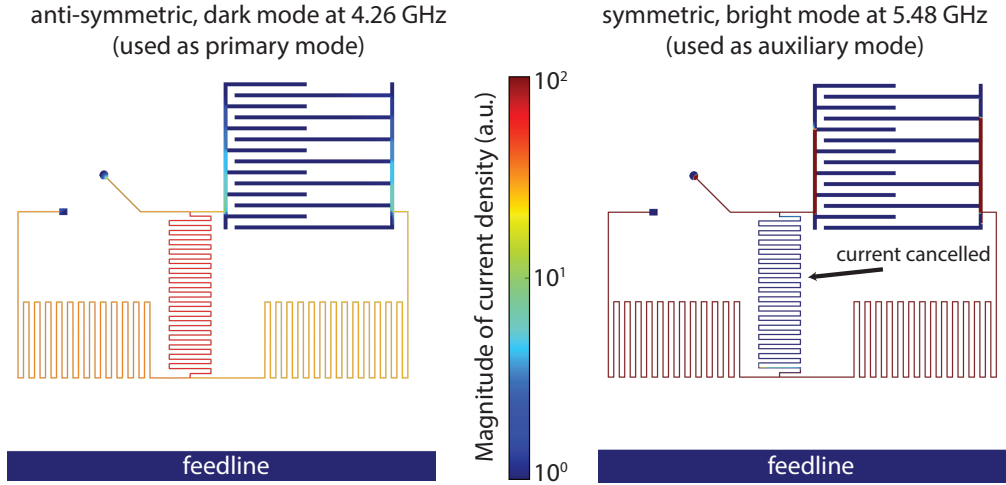


Figure 3.18 – **Simulation of the hybrid circuit with the bright and dark modes.**

The symmetric, bright mode has no current on the coupling inductor (the meandering line in the middle). The anti-symmetric mode has current flowing in the opposite direction on the lower inductors, therefore its external coupling to the feedline is suppressed.

Design of the vacuum-gap capacitor

Here we briefly comment on the choice of the vacuum-gap capacitor geometry. There are three main considerations for the size of the capacitor. First, there are constraints on the

3.2. Design: simulations and circuit layout

| Parameter | Simulated value |
|---|--------------------------------------|
| $\omega_c/2\pi$ | 4.348 GHz (< 2% deviation from exp.) |
| $\omega_{\text{aux}}/2\pi$ | 5.482 GHz (< 2% deviation from exp.) |
| Inductance of individual LC circuit | ≈ 11 nH |
| Capacitance of the interdigitated capacitor | ≈ 104 fF |
| Plate separation of vacuum-gap capacitor | ≈ 38 nm (inferred from exp.) |

Table 3.2 – **Simulated parameters of the hybrid-mode circuit.** The results show excellent agreement with the experimental results with one free parameter (the plate separation). The inductance is calculated using FastHenry.

fabrication. Although we did not test the ultimate limitations of how big capacitors can be released, it was observed that capacitors with a diameter of $40\ \mu\text{m}$ collapse with a higher probability than capacitors with a diameters of $32\ \mu\text{m}$ or less. The time of the release etch also increases significantly. Second, the resonance frequency of the circuit constrains the capacitance both from below and above. If the capacitor is too small, the inductor has to be designed too long and the lumped-element regime is violated. If the capacitor is too large, the inductor has to be smaller and the external coupling rate, as well as the coupling of the two degenerate LC circuits cannot meet the requirements. Third, g_0 depends on the size of the capacitor. We note that the separation of the gap is not under control: we observed that regardless of the thickness of the sacrificial layer, at low temperatures the effective gap settles at around $40\ \text{nm}$ for devices which work well.

The scaling of g_0 and the cooperativity \mathcal{C} with drum diameter and gap separation is in fact non-trivial. In the following discussion, C is the capacitance, D is the diameter of the drum and d is the cap between the electrodes (top and bottom plate). The zero point motion of the membrane is $x_{\text{zpf}} = \sqrt{\frac{\hbar}{2m\Omega_m}}$, so as $m \propto D^2$ and $\Omega_m \propto D^{-1}$,

$$x_{\text{zpf}} \propto D^{-1/2}.$$

Now, we also know that

$$g_0 = x_{\text{zpf}} \frac{\partial \omega}{\partial x} = x_{\text{zpf}} \frac{\omega_0}{2C} \frac{dC}{dx} \approx \frac{\omega_0 x_{\text{zpf}}}{2d}.$$

Since $\omega_0 \propto C^{-1/2} \propto (d/A)^{1/2} \propto d^{1/2} D^{-1}$ (using the fact that $C \propto A/d$ where d is the plate separation), we finally get that

$$g_0 \propto \frac{1}{\sqrt{dD^3}}.$$

The scaling of the cooperativity \mathcal{C} is then (again, in the following expression C is the

capacitance)

$$\mathcal{C} \propto \frac{g_0^2}{\kappa_{int}} \propto \frac{d^{-1}D^{-3}}{C^{-1}} \propto \frac{d^{-1}D^{-3}}{D^{-2}d} \propto \frac{1}{d^2D}$$

Therefore, as expected, smaller gapsize is preferred, as well as (for a given bottom plate size) a smaller top plate.

4 Measurement setup and characterization

This chapter describes in detail the measurement setup and most of the measurement procedures employed in order to obtain the results in the following chapters. Some of the data analysis methods, such as extracting the parameters of the microwave resonance from the network analyser data or the mechanical dissipation rate from ring-down measurements is also discussed. The detailed measurement setup shown was used to obtain the results in chapter 5 but most of the techniques were also employed in chapter 6. We comment on the slight differences in the corresponding sections.

4.1 Sample preparation and device packaging

The result of the fabrication described in chapter 3 is a $9.6 \text{ mm} \times 6.5 \text{ mm}$ sapphire chip (the device under test [DUT]) with a 50 Ohm matched central microstrip feedline. At room temperature, the circuits are not tested electrically as the resistance of thin-film Al is high (and the gap separation is much higher than at millikelvin temperatures, rendering the LC resonance frequency high) but the vacuum-gap capacitor can be tested by interferometric means. First, as described in section 3.1.1, optical topography measurements can be performed to filter out devices with collapsed capacitors. Second, the driven motion of the top plate can be detected in an interferometric setup shown in fig. 4.1.

In order to probe the circuits on the chip at low temperatures, the DUT has to be connected to coaxial microwave cables. First, we glue the DUT into a sample holder using electrically conducting silver paint. The sample holder is made of oxygen-free high thermal conductivity copper, which enables efficient thermal contact even at very low temperatures. It is also light-tight in order to suppress unwanted radiation reaching the sample. There are two small printed circuit boards glued with epoxy to the sample holder as well, each featuring a 50 Ohm matched microstrip line made of copper. The chip is wire-bonded to these circuit boards on each side using aluminium wires. An SMA

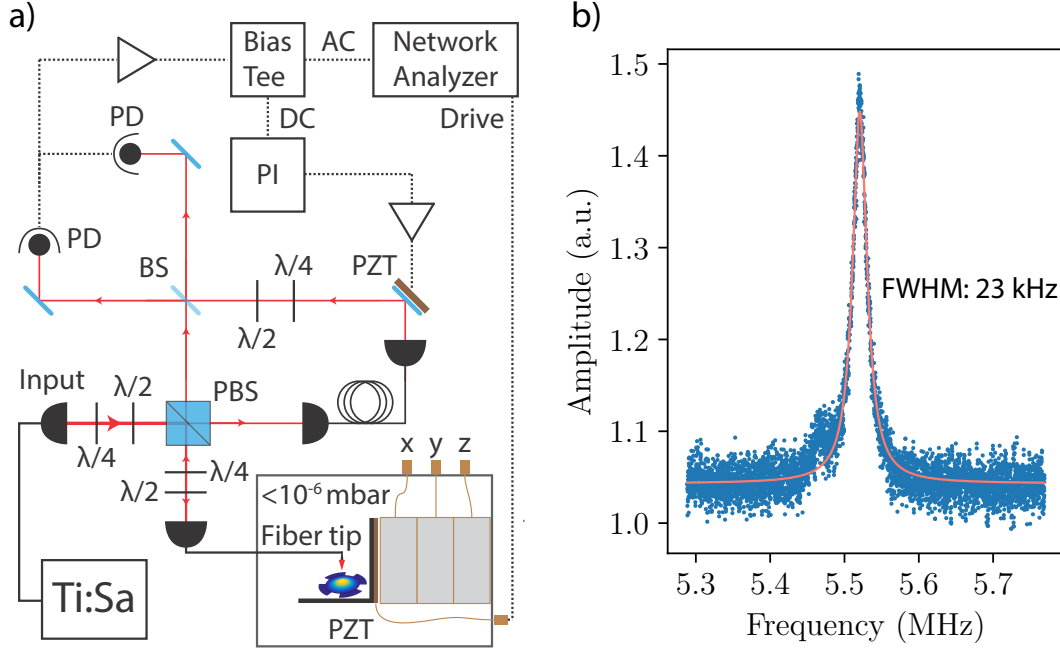


Figure 4.1 – **Probing the vacuum-gap capacitor at room temperature using an interferometric optical setup.** **a)** Schematic of the optical measurement setup. $\lambda/2$: Half-wave plate. $\lambda/4$: Quarter-wave plate. PBS: Polarizing beam-splitter. BS: 50/50 beamsplitter. PZT: Piezoelectric transducer. PI: Proportional-integral loop filter. PD: Photodiode. Figure modified from [86]. **b)** Driven spectra of the mechanical motion revealing the mechanical mode at $\Omega_m/2\pi \approx 5.52$ MHz with a Q-factor of ~ 230 at room temperature.

connector is screwed at each side of the sample holder, and the end of these connectors - the pins - are soldered to the copper microstrip line. As described later in chapter 5, most of the experiments later on were operated in reflection mode, in which one of the connectors was grounded (in some cases, one end of the feedline was directly wire-bonded to the sample box, in order to shorten the reflection path and to suppress capacitive coupling of the circuit close to the grounded end).

4.2 The dilution refrigerator

At the heart of the measurement setup is a BlueFors LD250 cryogen-free dilution refrigerator (DR) system. These DR systems use the heat of mixing of two isotopes of helium (helium-3 and helium-4) in order to provide continuous cooling power. These refrigerators are the only cryogenic devices which can provide such cooling below ~ 300 mK. Although there is no fundamental lower limit of the temperature DR systems can achieve, for practical reasons - related to the viscosity and thermal conductivity of the

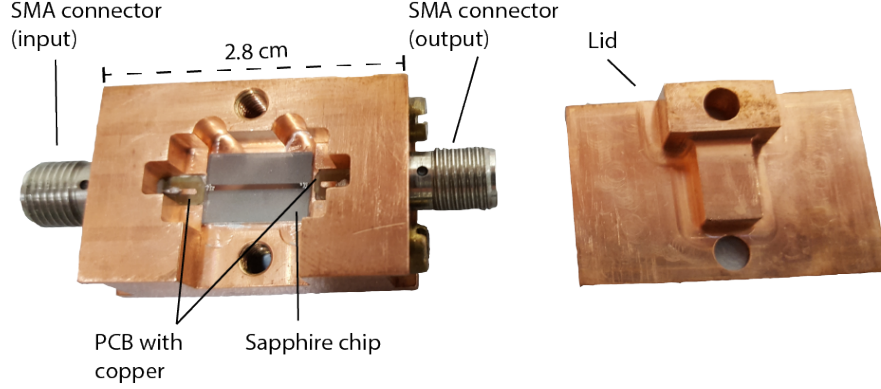


Figure 4.2 – **Photograph of the sample holder with the device.** The sample holder is made of oxygen-free high conductivity copper to ensure good thermal contact at millikelvin temperatures and it is light-tight to protect the superconducting circuit from unwanted radiation.

circulating fluid - they operate above 2 mK. Specifically, our system can achieve a base temperature of ~ 7 mK and it has a cooling power of $15\mu\text{W}$ at 20 mK (or $450\mu\text{W}$ at 100 mK). Practically, with all the wires in place and at reasonable microwave pumping, the fridge was operated at 10 – 15 mK for most of the experiments described in further chapters.

These systems have been and are being used for pushing the limits of low-temperature science and advancing physics on multiple fronts, studying e.g. topological insulators, quantum information processing with superconducting circuits, quantum dots or 2D materials. Two Nobel Prizes were awarded to breakthroughs which were using this technique (superfluidity in He-3 by Lee, Osheroff and Richardson and fractional quantum Hall effect by Tsui, Stořmer and Laughlin) and nowadays the technology reached the maturity to be commercialised.

4.2.1 Operation principle

The cooling in a DR systems happens because of special properties of the two helium isotope mixture. The fundamental differences between He-3 and He-4 are:

1. He-3 is lighter than He-4, therefore it has a lower latent heat of evaporation (binding energy between the atoms in the liquid is weaker)
2. He-3 is a fermion (3 nucleons), while He-4 is a boson (4 nucleons)

These differences give rise to the rather unusual phase diagram of a He-4 + He-3 mixture, see fig. 4.4a. Depending on the He-3 concentration, at a certain temperature the mixture

undergoes a phase transition into a state in which He-4 is superfluid and He-3 is a Fermi-liquid (this demarkation on the phase diagram is called the λ -line). The transition, which happens at lower temperatures for larger He-3 concentration, results in vastly different properties of the two isotopes. Below a certain temperature, another transition happens: two distinct phases are formed, one which is rich in He-3 (concentrated phase) and one which is poor in He-3 (dilute phase). The former tends to pure He-3 as we approach the absolute zero temperature, while in the latter a certain amount of He-3 (6.4 %) remains; this finite solubility of He-3 in He-4 is key to the operation of the dilution refrigerator, as well as the fact that the concentrated phase is lighter, therefore it floats on top of the dilute phase. Crucially, the enthalpy of He-3 in the concentrated phase is smaller than that of the dilute phase, therefore cooling can occur if one forces through the He-3 atoms from the concentrated phase to the dilute phase.

All dilution refrigerators use a cold, stable environment at 4 K. In a wet DR system, this is achieved with a liquid He bath; in a dry dilution refrigerator such as ours, this is achieved by a two-stage pulse tube cooler (they can typically provide 1.5 W at 4 K with a power consumption of 8 kW). After the DR is precooled to 4 K, the mixture has to be condensed into the system through the condensing line. This is done by a compressor, which raises the pressure of the mixture to ~ 2 bar. Additionally, heat exchangers on the line pre-cool the mixture such that it partly condenses and can fill the mixing chamber, the heat exchangers and part of the still.

The standard DR cycle can now be started by pumping the still (i.e. the distiller, which distills the He-3 from He-4), which results in evaporative cooling. This cools the still below 0.8 K, therefore phase separation can occur according to the phase diagram in fig. 4.4a and the dilute phase will be collected at the bottom of the mixing chamber, as shown in fig. 4.3. After the He-3 is forced through the phase boundary and cooling occurs in the mixing chamber, the osmotic pressure difference between the still and the mixing chamber pulls the He-3 towards the still. Here, the He-3 can be distilled due to the difference in vapour pressure of He-3 and He-4 (see fig. 4.4b).

4.2.2 Microwave setup

The circuit diagram for our microwave measurements is shown in fig. 4.5. Up to five sources (not all shown on the schematic diagram), as well as the vector network analyser, are combined at room temperature,

filtered, and sent into the dilution refrigerator. The sources are attenuated at various temperature stages to decrease the room-temperature thermal noise, and then sent into the input port of the device. At the output, the transmitted pump power and noise

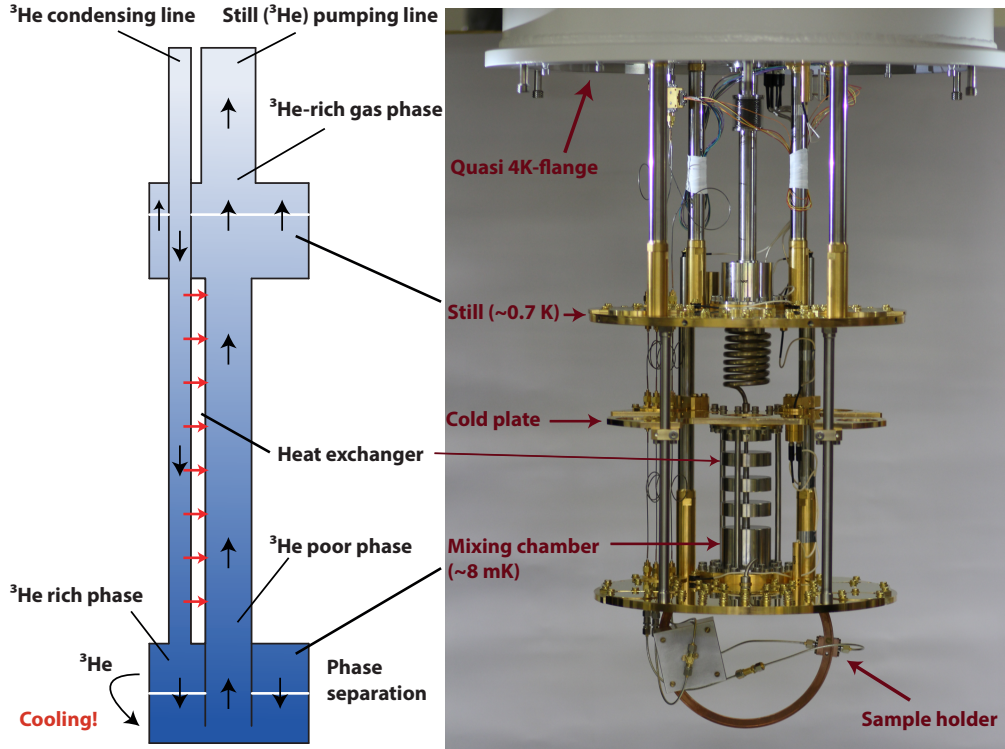
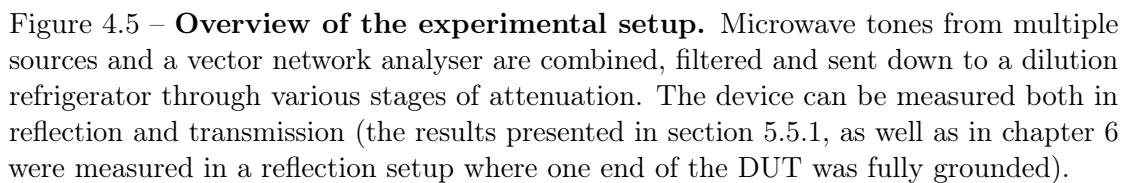
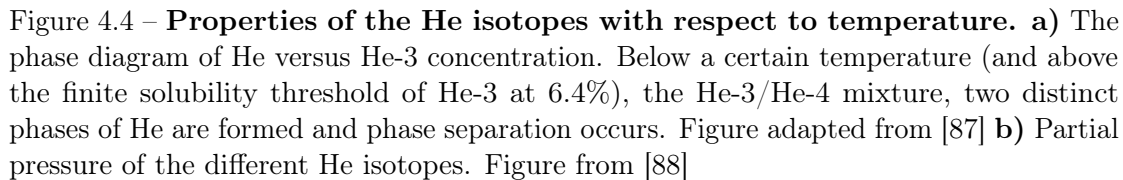


Figure 4.3 – **Schematic of the working principle and photograph of the dilution refrigerator.** The refrigerator pumps He in a closed circuit through different temperature stages and uses the special properties of He-3 and He-4 to achieve cooling down to ~ 10 mK. The sample is thermalized to the mixing chamber, the coldest part of the system.

spectrum from the device are amplified at two stages (at 4 K with a HEMT amplifier and at room temperature) and then measured. Each part of this process is discussed further in the following sections.

The input line

The microwave sources required for the experiment are off-the-shelf microwave generators. For the experiment described in chapter 5, we use a R&S SMF and a Keysight N5183B-UNY as main signal generators, as well as a R&S SMA100 for calibrations. These devices have a phase noise level between -140 and -150 dBc/Hz, depending on the generator, the detuning from the carrier, the carrier frequency and the power. The amplitude and phase noise level were carefully measured for all sources using a R&S FSUP signal source analyser (an example is shown in fig. 4.6b for three of the sources for various powers). The room temperature thermal noise limit is -174 dBm/Hz; therefore, at higher powers (above ~ 25 dBm at the output of the sources), additional filtering is required to ensure that the signal we send to the sample is thermal noise limited.



Phase noise and filtering

Excess phase noise provides an additional hot bath for the microwave cavity and limits the final phonon occupancy for sideband cooling, as well as noise properties of the optomechanical amplifier using the mechanical reservoir described in chapter 5. Specifically, the added noise (phonons) coming from phase noise, calculated for a given cooling power (i.e. fixed Γ_{eff}), is given by (see Appendix D for derivation)

$$n_{\text{added}} = \frac{(\kappa/2)^2 + \Omega_m^2}{4g_0^2} \Gamma_{\text{eff}} \mathcal{S}_{\varphi\varphi}, \quad (4.1)$$

where $\mathcal{S}_{\varphi\varphi}$ is the phase noise of the source expressed in power below the carrier per unit bandwidth (unit of dBc/Hz). From this expression one can calculate the maximum tolerable phase noise such that the mechanical occupancy is affected by less than 1 quantum (so ground state cooling is possible). For example, assuming a phase noise of -147 dBc/Hz with a mechanical frequency of 6 MHz, plugging the parameters from table 5.1 we obtain $n_{\text{added}} \approx 9$. This necessitates the reduction of phase noise.

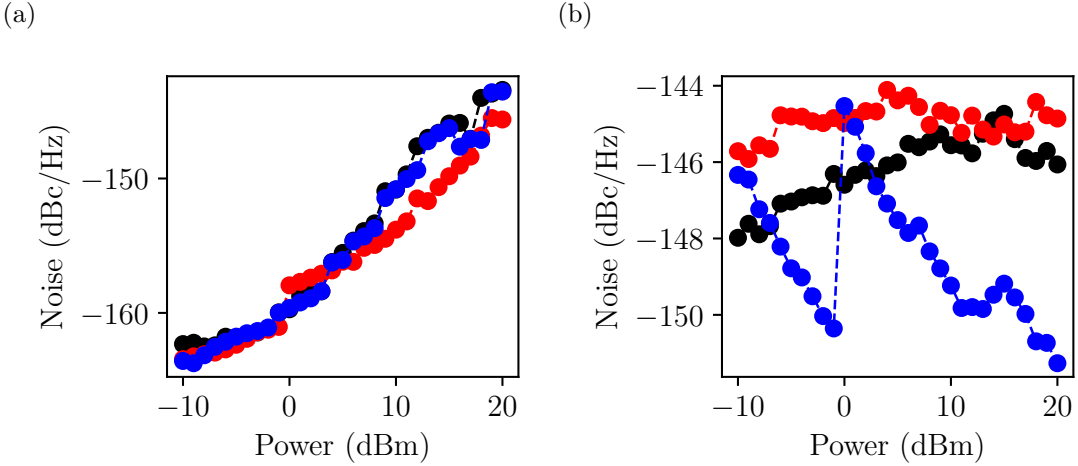


Figure 4.6 – **Amplitude (left panel) and phase (right panel) noise of the employed sources measured at different output powers.** The employed sources are: R&S SMB100A (red and black; two different units), R&S SMF100A (blue), amplitude and phase noise measured at 4.8 MHz away from the carrier with a R&S FSUP Signal Source Analyzer.

In order to suppress the phase noise of the pumps, we use custom built filter cavities made of copper as shown in fig. 4.7. These are 1-port devices in which the reflected signal is picked off with a circulator to form a band-reject filter. The bandwidth of the cavities is ~ 1 MHz, tunable by modifying the pin of the SMA connector (which forms the port

and provides the external coupling). The rejection also depends on the bandwidth (in this notch configuration, one needs to be close to critically coupled to achieve the best rejection around the resonance frequency; see also fig. 2.5). The cavities are formed by two half copper tubes with threads. By adjusting the length of the cavity, the frequency can be tuned within a large range (~ 0.5 GHz).

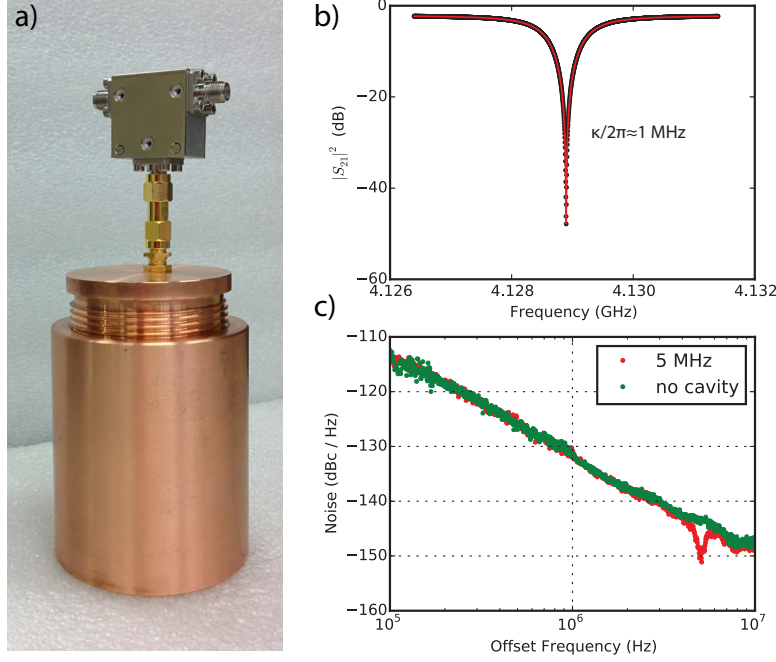


Figure 4.7 – **Custom-made tunable copper filter cavity to reduce phase noise.** **a)** Photograph of the cavity with a circulator attached (notch configuration). The cavity is made out of two half tubes with threads ensuring frequency tunability in the relevant frequency range (4 - 5.5 GHz). **b)** Frequency response of the filter cavity. The bandwidth is ~ 1 MHz, with a maximum rejection of around 30 dB. **c)** Phase noise measurement of one of the sources with and without the filter cavity in place. When the cavity is used, the phase noise is suppressed within the bandwidth at a detuning of 5 MHz. The phase noise was measured with the R&S spectrum analyzer which has a noise floor at around -152 dBm (therefore, the exact magnitude of the suppression appears to be smaller than it is expected from the depth of the filter cavity).

Apart from the filter cavities, wideband low-pass filters (K&L tubular low pass 0-12 GHz) are employed on all input and output lines to filter out any unwanted high-frequency radiation. Moreover, the pumps are also connected to narrower band low-pass and high-pass filters as it was observed that the sources emit an observable amount of noise *far away* from the carrier frequency (fig. 4.9). This is relevant in the experiment where we utilize multiple modes; the pumps around the lower frequency microwave resonance (e.g. at 4.1 GHz) can emit noise at the higher frequency mode (at 5.3 GHz) and vice versa.

Tone cancellation

Generally, in optomechanical experiments one needs large pumps such that the multiphoton cooperativity (proportional to the intracavity photon number) is sufficiently enhanced. This is especially true for the experiment described in chapter 5, where achieving the reverse dissipation regime requires multiphoton cooperativities in the order of 10^4 . The actual signal or noise power we are interested in measuring (e.g. thermomechanical sidebands) is much smaller - typically more than 80 dB - than the pump carrier. These strong pumps can saturate the amplification chain, particularly the HEMT amplifier, and hinder the detection of the signal of interest. Moreover, small backreflections from isolators can become significant at these power levels, which can interfere with the signal.

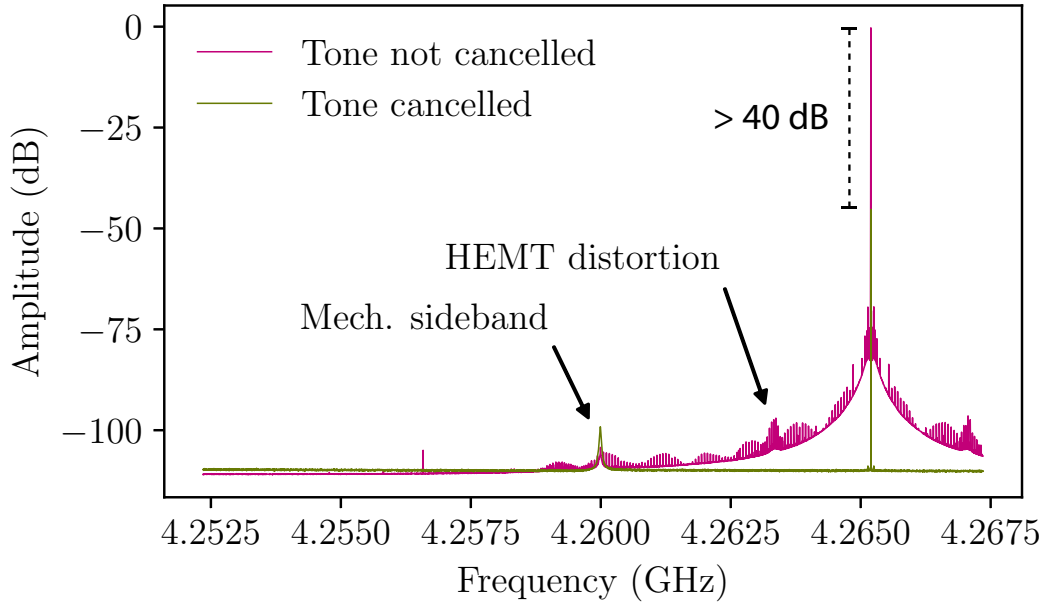


Figure 4.8 – **Spectrum at the output of the fridge with and without tone cancellation.** Without tone cancellation, the HEMT produces distortion sidebands, as well as a non-flat noise background. The large pump power also suppresses the HEMT gain, thus the noise floor appears below that of the tone-cancelled background. After tone cancellation (of over 40 dB in this case), the distortion sidebands disappear.

To compensate for this, we implemented a tone cancellation scheme. We split the pump tone which needs to be cancelled with a 50:50 power splitter and inject it into the fridge through a secondary line (shown in fig. 4.5). The secondary line contains a variable attenuator and phase shifter and the same amount of explicit attenuators as the primary line. The secondary line recombines at the mixing chamber with the primary line using a directional coupler. By appropriately adjusting the phase and the amplitude of the pump

going through the secondary line, the strong pump can be cancelled by interference.

Thermal noise suppression

Once the phase noise of the tones is sufficiently filtered, the noise becomes dominated by the room-temperature thermal noise. Thermal noise in electrical circuits, also called the Johnson or Nyquist noise, is caused by the random thermal fluctuation of bound charges. More specifically, in a resistor with resistance R thermalized to temperature T , the kinetic energy of the electrons - which is proportional to T - will produce a nonzero rms voltage fluctuation given by

$$V_n = \sqrt{\frac{4hfBR}{\exp(hf/k_B T) - 1}}, \quad (4.2)$$

where $h \approx 6.63 \cdot 10^{-34}$ Js is the Planck constant, $k_B \approx 1.38 \cdot 10^{-23}$ J/K is the Boltzmann constant and B is the bandwidth of the system. If one considers $kT \gg hf$ (Rayleigh-Jeans approximation), this expression simplifies to the well-known formula

$$V_n = \sqrt{4k_B T B R}. \quad (4.3)$$

For example, a $100 \, \Omega$ resistor has a rms voltage fluctuation of $\sim 1.29 \, \text{nV}/\sqrt{\text{Hz}}$ at room temperature ($T = 300 \, \text{K}$). eq. (4.3) implies an rms for the current of

$$I_n = \sqrt{\frac{4k_B T B}{R}} \quad (4.4)$$

and the resulting noise power emitted by the resistor is simply

$$P_n = k_B T B. \quad (4.5)$$

In a $1 \, \text{Hz}$ bandwidth, the thermal noise power of a room temperature resistor is $3.98 \cdot 10^{-18}$ mW, or -174 dBm. It is important to note that the noise power is independent of frequency - i.e. it is a white noise source - and is directly proportional to the bandwidth.

We combine the pumps and the probe from the network analyser. This line then reaches the sample through various stages of attenuation to suppress Johnson-noise (total attenuation in the dilution refrigerator, including cables and connections, of about 50 dB). Any attenuator at a certain temperature attenuates the noise at its input and replaces it with its own thermal noise according to the fluctuation-dissipation theorem.

Specifically, if noise with power $P_{n,\text{in}}$ reaches an attenuator which is thermalized to T_0 (therefore which produces its own noise power $P_{n,0}$) and which has attenuation $\alpha < 1$,

the resulting noise power at the output of the attenuator is given by

$$P_{n,\text{out}} = \alpha P_{n,\text{in}} + (1 - \alpha) P_{n,0}. \quad (4.6)$$

After the attenuation chain presented in fig. 4.5 (20 dB attenuator at 3 K, 6 dB at 800 mK and 20 dB at base temperature), we attain an equivalent noise temperature of the input of ~ 68 mK. We note that while converting back to the equivalent noise temperature from eq. (4.6), one needs to use the quantum formula eq. (4.2), as at these low temperatures the Rayleigh-Jeans approximation is not valid anymore.

We also note that apart from suppressing the phase noise and the thermal noise, one needs to make sure that there is no high frequency radiation reaching the superconducting device. In the case of aluminium, for which the superconducting energy gap $\Delta/e \approx 200 \mu\text{V}$, extra dissipation from breaking the Cooper pairs can occur if its irradiated above $2\Delta/h \approx 100$ GHz. The mixing chamber of our dilution refrigerator is light tight and the inner shield was painted with a high loss microwave absorber (ECCOSORB[®] CR-124). We also have low pass filters on all lines (however, these might have a transparency window above a few 10s of GHz, therefore a potential improvement is to use homemade filters made of the same absorber which certainly suppress all radiation above a designed cutoff frequency).

The output line

One port of the sample holder is grounded; however, for device 1 in chapter 5, it is still connected to an output line (“T” line on the schematics) and can be measured for the characterization of the cavities resonances (at a level 20 dB below the reflected signal). The transmission signal first goes through two stages of isolation at base temperature (using Raditek RADC-4-8-Cryo 4-8 GHz circulators), then a HEMT amplifier (LNF-LNC4-16A 4-16 GHz cryogenic low noise amplifier from Low Noise Factory) at 3 K. Finally, at room temperature, it is isolated and amplified again (isolator: Narda 2-stage isolator; amplifier: Minicircuit ZVA183+ 24-26 dB). Most of the signal from the device is reflected and directed to the reflection line (“R” line on the schematics) with a directional coupler (Pasternak PE2204-20 4-8 GHz). This line goes through two stages of isolation at base temperature (using Quinstar QCI-075900XM00 3-12 GHz isolators), then a HEMT amplifier (LNF-LNC1-12A 1-12 GHz cryogenic low noise amplifier from Low Noise Factory) at 3 K. Finally, at room temperature, it is isolated and amplified again (isolator: Innowave 2-stage isolator; amplifier: 2 in-series Minicircuit ZX60-14012L-S+ 12 dB). All the lines between the 3 K stage and the mixing chamber are wired using 0.86 mm CuNi cables with silver plated center conductor (for input lines) and NbTi superconducting cables (for output lines), while formable Cu cables are used at the mixing chamber stage. Both the reflection and transmission lines can be measured with a vector network analyser

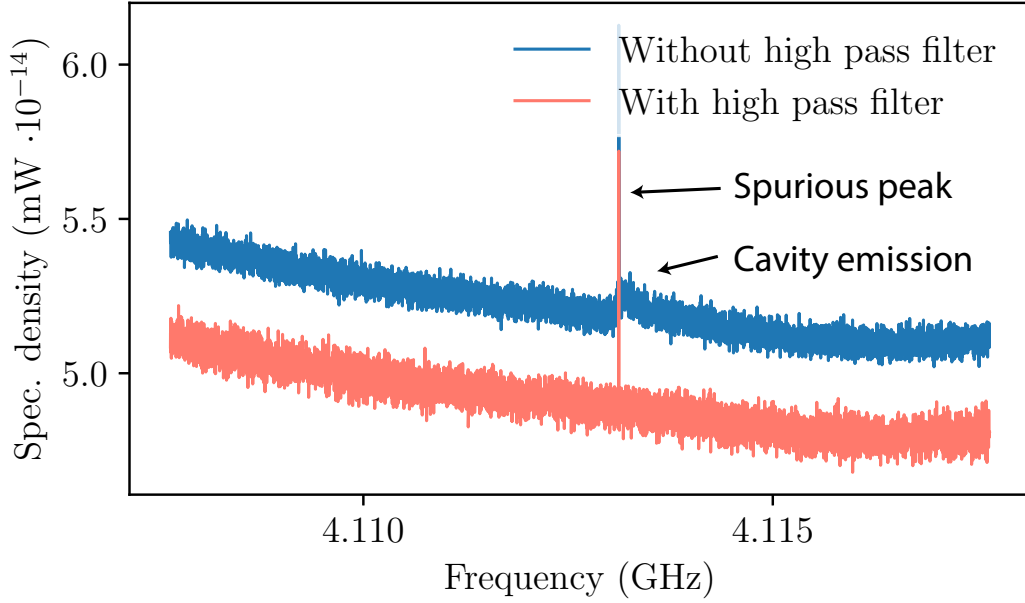


Figure 4.9 – **Noise and filtering of a pump tone far away from the carrier frequency.** Pumping at the high frequency LC mode at 5.3 GHz and measuring noise emission at the lower frequency LC mode with and without a high-pass filter in place with a cutoff frequency of 5 GHz. With the high-pass filter, the measured noise is significantly lower and no thermal emission (which occurs due to heating the cavity with the broadband source emitted by the source) is observed. Source used: Keysight N5183B-UNY (also reproduced with R&S SMF100A).

(R&S ZNB20) or the electromagnetic spectrum analyser (R&S FSW26).

4.2.3 Noise calibration of the HEMT amplifier

Internal noise sources and equivalent noise temperature

In addition to the external noises which can couple to a propagating electric signal, all components (amplifiers, receivers, transmitters) have their own internal noise. The level of internal noise limits - from below - the power of the signal which can be detected. Usually, noise is generated by the random fluctuation of charges (or charge carriers) in the devices, caused by various mechanisms. The best known example is thermal noise, also called Johnson or Nyquist noise, originating from the thermal vibration of bound charges. It can be suppressed by lowering the temperature of the device (see discussion above). Another type of noise is shot noise, caused by the random fluctuations of charge carriers in a solid-state device. Yet another example is flicker noise, which occurs in

solid-state devices, as well as vacuum tubes; it is also called 1/f noise, as the noise power varies inversely with frequency (thus, it becomes important at lower frequencies, typically in audio range). Finally, the quantized nature of the charges and photons gives rise to quantum noise, as discussed in section 2.3. Generally, these noise contributions are independent of each other and simply add up in variance.

In order to describe the above in a simple model, consider an amplifier with gain G and bandwidth B , to which some white noise is injected with an average noise spectral density of N_{in} . One can measure the noise N_{out} at the output of the amplifier, which consists of the amplified input noise plus the noise added by the amplifier internally which we denote by N_{n} . N_{out} is typically not wideband, but instead is higher and close to uniform in the bandwidth of the amplifier as shown in fig. 4.10. The noise power at the output is can be calculated by

$$P_{\text{n}}^{\text{out}} = \int_0^\infty N(f)df \approx \int_{f_1}^{f_2} N_{\text{out}}df = BN_{\text{out}}. \quad (4.7)$$

Since the input noise and the added noise are independent, they can simply be added in variance, so

$$N_{\text{out}} = GN_{\text{in}} + N_{\text{n}} \quad (4.8)$$

The input and output noise temperature is simply defined by $T_{\text{in}} = N_{\text{in}}/k_{\text{B}}$ and $T_{\text{out}} = N_{\text{out}}/k_{\text{B}}$ (see also discussion in section 2.3). Similarly, the internal amplifier noise can be modelled as a thermal noise source which is added to the - now ideal, noiseless - amplifier's input and which is at a temperature T_{n} :

$$T_{\text{n}} = \frac{N_{\text{n}}}{Gk_{\text{B}}}. \quad (4.9)$$

T_{n} is the equivalent (input) noise temperature of the amplifier and is a common metric to characterize how noisy an amplifier is.

Another commonly used concept to characterize the noise property of an amplifier is the noise factor. It is essentially a measure of the degradation of the signal-to-noise ratio between the input and the output of the amplifier. The noise factor is defined as the ratio of the output noise power of a device to the portion thereof attributable to thermal noise in the input at a specified standard noise temperature T_0 (typically 290 K). More precisely, it is given by

$$F = \frac{\text{SNR}_{\text{in}}}{\text{SNR}_{\text{out}}}, \quad (4.10)$$

where $\text{SNR}_{\text{in}} = S_{\text{i}}/N_{\text{i}} = S_{\text{i}}/(k_{\text{B}}T_0B)$.

In order to perform the experiments in chapter 5, we measured the noise properties of

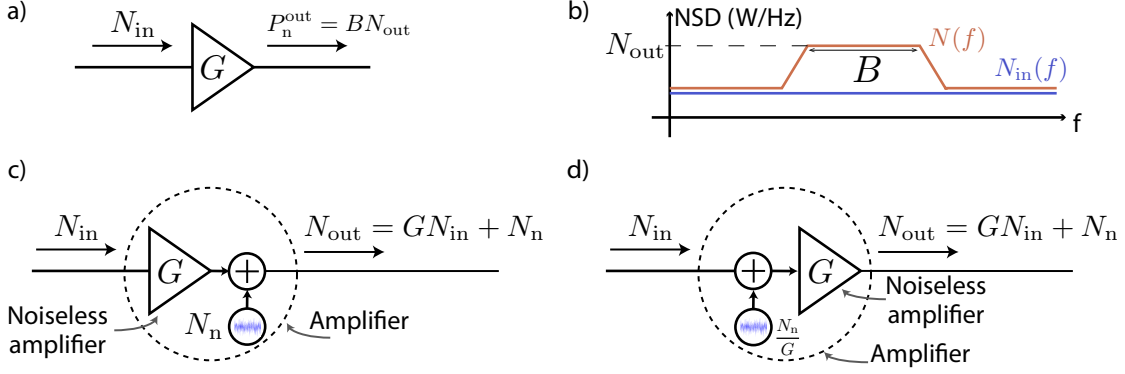


Figure 4.10 – **Scheme to describe the model of a noisy amplifier.** a) An amplifier with noise N_{in} has an integrate noise power at the output of P_n^{out} . b) The noise spectral density of an amplifier versus frequency. The output noise is the input noise, which is amplified within the bandwidth. c) Model of a noisy amplifier consisting of a noiseless amplifier and a noise source the output. d) Model of a noisy amplifier consisting of a noiseless amplifier and a noise source the input. In this case the noise added by this source N_n/G is said to be referred back to the input.

all HEMT amplifiers in separate cooldowns. This can be done by connecting the HEMT amplifier to a 50 Ohm termination, placed at the mixing chamber as shown in fig. 4.11. The matched 50 Ohm load serves as a Johnson noise source and gives an rms voltage fluctuation given by eq. (4.2). The temperature of the mixing chamber is varied (during a controlled warmup) from 10 mK to 10 K and the output noise power spectrum is measured for each temperature point for the entire bandwidth of the amplifier. An

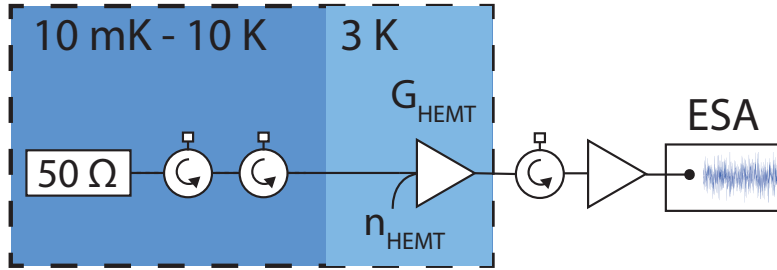


Figure 4.11 – **Experimental scheme for calibrating the HEMT noise.** The HEMT amplifier is connected to a 50 Ohm termination, placed at the mixing chamber. The temperature of the mixing chamber is swept from 10 mK to about 10 K in a controlled warmup.

example of the result of such a sweep is presented in fig. 4.12. The output noise is given by

$$N_{out} = G \cdot G_{HEMT} (N_{HEMT} + N_{load}) = A \cdot G \cdot G_{HEMT} (T_n^{(HEMT)} + T_n^{(load)}), \quad (4.11)$$

where A a proportionality constant, G the total gain along the output line, and where

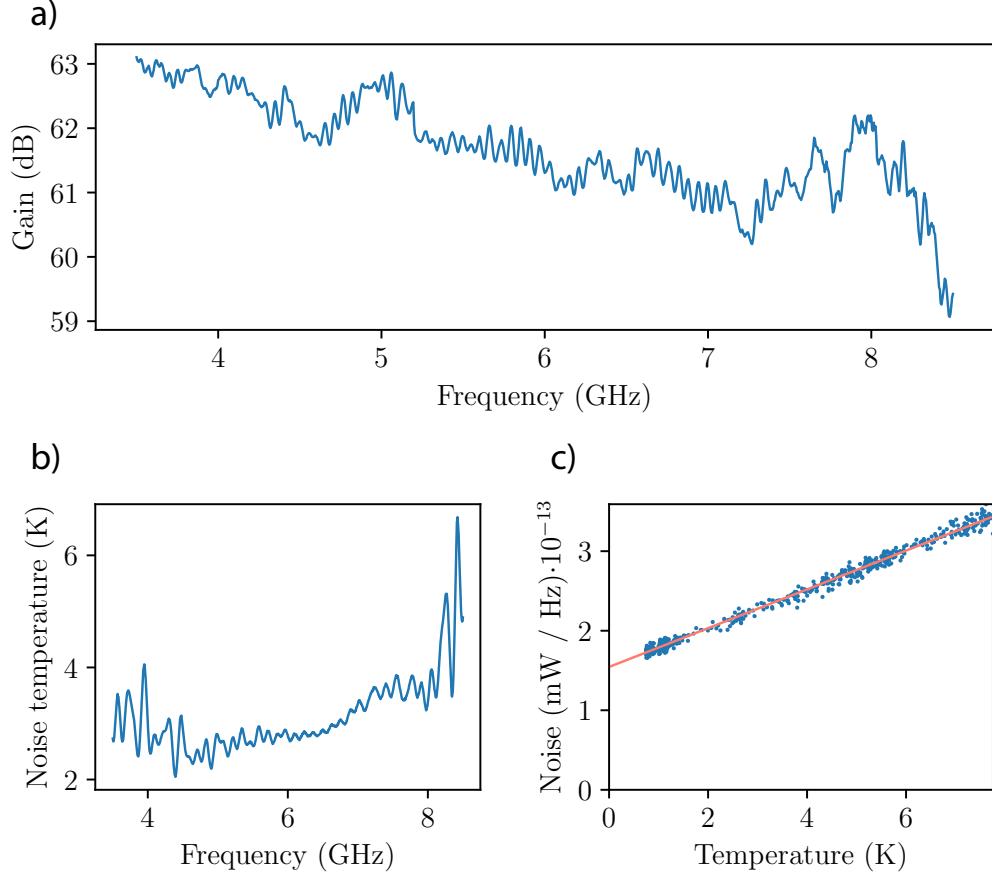


Figure 4.12 – **Example of a calibration of the HEMT amplifier in terms of gain and noise temperature.** **a)** The extracted gain curve of the amplifier in the relevant bandwidth. **b)** The measured equivalent noise temperature as a function of frequency. **c)** The output noise power for a specific frequency as a function of temperature. From this curve, the equivalent noise temperature is extracted as the y -intercept divided by the slope of a linear fit (same as the negative of the x -intercept).

we converted all noise terms into equivalent temperature. The noise temperature of the HEMT can then directly be compared to the actual temperature of the load $T^{(\text{load})}$ by fitting the curve of fig. 4.12c: it is extracted as the y -intercept divided by the slope of a linear fit (equivalent to negative of the x -intercept). The results for all measured frequencies are shown in fig. 4.12b.

As a example: the LNF-LNC1-12A 1-12 GHz HEMT amplifier (brand: Low Noise Factory) at 4.13 GHz (the relevant frequency of our noise measurement in chapter 5), the noise temperature is 3.95 ± 0.02 K, which corresponds to $n_{\text{HEMT}} = 20.0 \pm 0.1$ photons per second in a bandwidth of 1 Hz. The uncertainty on the HEMT noise is computed by combining the fitting uncertainty from statistical fluctuations and a systematic uncertainty of 16

mK from the thermometer.

4.3 Device characterization

After the sample is cooled down to the base temperature of the dilution refrigerator, the superconducting circuits are characterised in terms of their microwave and mechanical parameters. The procedure is described below and all steps are elaborated in the following sections.

1. Find the microwave resonances with the network analyser. On every chip, an LC circuit without a mechanical element inductively coupled to the feedline (simple meander inductor with an interdigitated capacitor) is fabricated to serve as a "standard candle" (to be found at $\omega_c/2\pi = (3.03 \pm 1\%)$ GHz). If this resonance cannot be observed, there is a problem with the entire measurement chain (e.g. a broken SMA connector, solder or wire bonds), which is also reflected in the overall transmission level. The rest of the resonances can be found by taking VNA measurements with a span ~ 500 MHz from 3 to 10 GHz. Although the simulation tools are powerful to calculate the expected inductance and external coupling rate, the actual resonance frequency strongly depends on the gap between the two plates of the vacuum-gap capacitor. We did not find a reliable way to accurately predict this gap - and, in turn, the resonance frequency of the electromechanical circuit - at the base temperature of the dilution refrigerator. However, for most of the working devices, a gap of ~ 40 nm was extracted. In the case when the capacitors collapse, the resonance frequencies are significantly lower than expected (~ 2 GHz, depending on the inductor design), as the collapsed top plate with the bottom plate and the aluminium oxide layer in between them form a capacitor with a large capacitance.
2. Acquire the VNA data (complex S_{21} parameter) for all resonances with a span of $\sim 10\kappa$ and extract the parameters by a fitting algorithm described below.
3. Measure the mechanical resonance frequency Ω_m . There are multiple ways to do this.
 - First, one can inject a pump tone at the microwave resonance frequency ($\omega_p = \omega_c$) and measure the sidebands generated by the thermomechanical motion at $\omega_p \pm \Omega_m$ using the electromagnetic spectrum analyser (ESA). Since Ω_m is not known a priori, a large span of ~ 5 MHz around the expected $\omega_p \pm \Omega_m$ is needed on the ESA, as well as sufficient pump power for measurable signal-to-noise ratio.

- Second, one can perform a coherent pump-probe measurement using the VNA. Specifically, one can inject a pump tone around the red motional sideband ($\omega_c - \Omega_m$) and measure the modified response of the microwave cavity due to the mechanical motion (optomechanically induced transparency). Then, the middle of the transparency window minus the pump frequency gives the mechanical resonance frequency. The advantage of this technique is that the mechanical motion is coherently probed, therefore in general the detection is easier (larger signal-to-noise ratio). The disadvantage, however, is that the transparency feature is only visible if the pump tone is within κ around the exact sideband condition. Since Ω_m is not known a priori, a frequency sweep of the pump is necessary and the cavity response needs to be recorded for each frequency, which can be time consuming.
 - Third, one can induce parametric instability by pumping at the upper (blue) motional sideband. That is, if one sweeps a pump blue detuned from the cavity resonance frequency and hits the sideband condition, the mechanical oscillator starts to self-oscillate (provided that the multiphoton cooperativity is above 1). An easily measurable consequence is that the output spectrum of the cavity will contain a forest of peaks around the pump frequency and these peaks are separated exactly by the mechanical frequency. Again, a sweep of the pump frequency is necessary to ensure that one hits the sideband condition ($\omega_p = \omega_c + \Omega_m$) but this technique is robust and $C > 1$ is typically easy to satisfy with relatively low pump power.
4. Measure the mechanical energy decay (also called dissipation) rate Γ_m . In principle, the width of the thermomechanical sideband gives the bare energy dissipation rate. However, we observed some jitter in the frequency of the thermomechanical sideband which was especially pronounced at low temperatures (at 10 mK). This jitter causes artificial broadening of the sideband (or simply a non-Lorentzian shape), which in turn gives an overestimation of Γ_m . Therefore, a more robust way is to deduce the effective dissipation rate is to measure the effective width by pumping on the red sideband and measuring the OMIT feature. This can be done for different pump powers and one can extrapolate to zero pump power to obtain Γ_m . Alternatively, ring-down measurements can also be performed as described below.
 5. Measure the optomechanical vacuum coupling strength g_0 for each microwave-mechanical mode combination. This requires elevating the temperature of the dilution refrigerator to a temperature at which we know that the mechanical oscillator is thermalized and an additional weak calibration tone.

We elaborate on all these steps in the following sections.

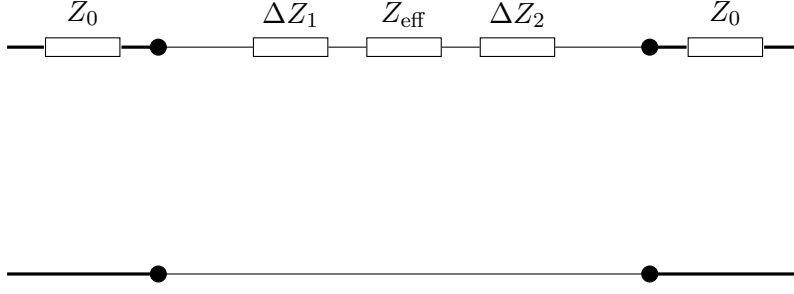


Figure 4.13 – **Equivalent circuit representation of the 2-port system with impedance mismatches.** The model used for the derivation of S_{21} in eq. (4.17) with the impedance mismatches ΔZ_1 and ΔZ_2 .

4.3.1 Extracting the parameters of the microwave resonance

The linear response measurements using the vector network analyser allow us to extract all the relevant parameters of the microwave resonances, such as their resonance frequencies, external coupling and internal loss rates.

In general, the resonances have an asymmetric Fano shape due to a potential impedance mismatch between the feedline on the chip (designed to be 50 Ohm) and the SMA pins. These impedance mismatches can cause reflections at the input and output ports and standing waves are formed on the feedline. A general circuit model takes this into account from which we can derive, based on the ABCD matrix approach, the S_{21} parameter (section 2.2.2 contains the background necessary for this derivation). Expressed in terms of the circuit impedances, as shown as an equivalent circuit diagram in fig. 4.13, the scattering matrix element is given by

$$S_{21} = \frac{2Z_0}{Z + Z_{\text{eff}}}, \quad (4.12)$$

where ΔZ_1 and ΔZ_2 are the amount of impedance mismatch at the feedline connections, $Z = 2Z_0 + \Delta Z_1 + \Delta Z_2$ and Z_{eff} is the effective impedance of the resonator as seen from the feedline, given by

$$Z_{\text{eff}} = \frac{\omega^2 M^2}{R + i\omega L - i/(\omega C)}. \quad (4.13)$$

Now, we would like to express this in terms of the internal and external quality factors (Q_{int} and Q_{ext} , respectively). Generally, the Q-factor is defined as 2π multiplied by the ratio of the energy stored in the system and the power dissipated to a specific loss channel (e.g. internal loss, external coupling) within one cycle on resonance. Therefore, in terms of the circuit parameters, the internal Q-factor is given by

$$Q_{\text{int}} = \frac{2\pi}{T} \frac{E_{\text{stored}}}{P_{\text{diss}}^{(\text{int})}} = \omega_0 \frac{L}{R}. \quad (4.14)$$

Similarly, one can express the external Q-factor as

$$Q_{\text{ext}} = \frac{2\pi}{T} \frac{E_{\text{stored}}}{P_{\text{diss}}^{(\text{ext})}} = \underbrace{\frac{ZL}{\omega_0 M^2}}_{\tilde{Q}_{\text{ext}}} \sqrt{1 + \tan^2 \Phi} e^{-i\Phi}, \quad (4.15)$$

where $\Phi = \arg[Z]$ and we use \tilde{Q}_{ext} later to simplify the expressions; note that both Q_{ext} and \tilde{Q}_{ext} are complex. Let us define $\delta x = \frac{\delta\omega}{\omega_0}$ and consider only frequencies around the resonance, i.e. $|\delta x| \ll 1$. The S_{21} parameter becomes

$$S_{21} = \frac{2Z_0}{Z} \left(1 + \frac{Q_{\text{int}}}{\tilde{Q}_{\text{ext}}(1 + 2iQ_{\text{int}}\delta x)} \right). \quad (4.16)$$

In addition to the impedance mismatch, the environment can further affect the measured S_{21} parameter, such as additional delays (τ) due to the length of the cable, additional phase (α) and amplitude factors (a), with which the full expression becomes

$$S_{21} = \underbrace{ae^{i\alpha}e^{i\omega\tau}}_{\text{environment}} \underbrace{\frac{2Z_0}{Z} \left(1 + \frac{Q_{\text{int}}}{\tilde{Q}_{\text{ext}}(1 + 2iQ_{\text{int}}\delta x)} \right)}_{\text{ideal resonator}}. \quad (4.17)$$

This expression is consistent with [89] in which the authors also describe an efficient fitting method. Here we outline the method and the results of the fitting are shown in fig. 4.14.

1. First, eliminate the cable delay τ by subtracting a linear function from the argument of S_{21} :

$$\arg[S_{21}](f) = -2\pi\tau f + g(f). \quad (4.18)$$

After this elimination, the data plotted on the complex S_{21} plane is a circle.

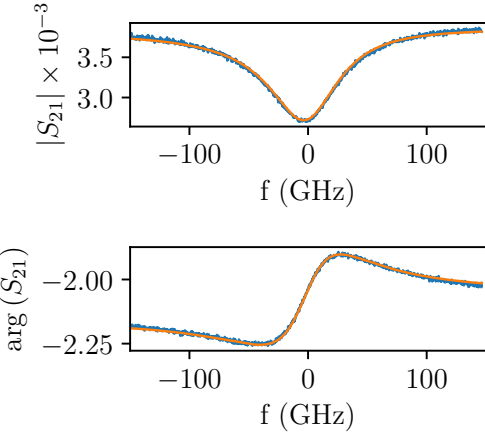
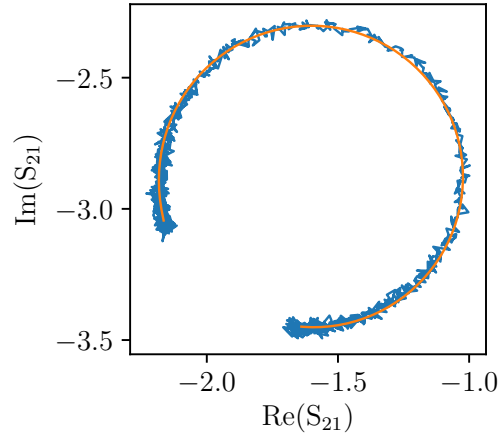
2. An algebraic fit of a circle is performed [90], giving the radius and the center point. Importantly, the radius contains information about the quality factors as it is given by $aQ_{\text{int}}/|\tilde{Q}_{\text{ext}}|$. Determining the remaining parameters of the environment is still needed, however.
3. An affin transformation is applied such that the data is centered at the origin.
4. A fit is performed for the phase-angular frequency according to

$$\theta(f) = \theta_0 + 2 \arctan \left[2Q_{\text{int}} \left(1 - \frac{\omega}{\omega_0} \right) \right]. \quad (4.19)$$

From this fit, one can readily obtain the resonance frequency ω_0 , the internal Q-factor Q_{int} and the phase offset θ_0 .

5. From θ_0 and the center position of the circle, one can obtain the off-resonant point P' , i.e. when $\delta x \gg 1$. This off-resonant point is important as $|P'|$ gives a (amplitude scaling factor) and $\arg(P')$ gives α (additional phase). Normalizing the data with these gives the canonical circle (circle for the ideal case), for which the off-resonant point lies at $(1, 0)$

(a)



(b)

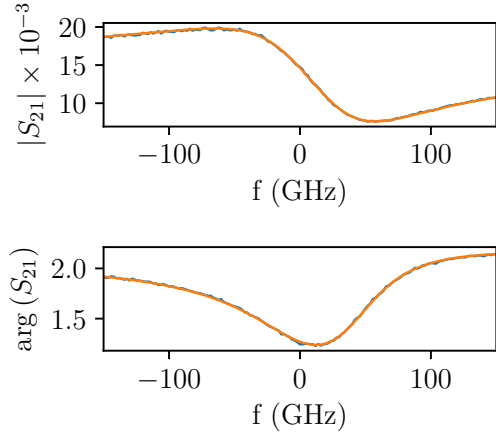
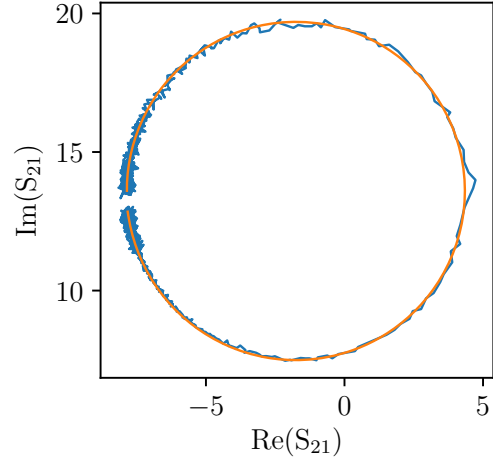


Figure 4.14 – **Fitting the vector network analyser data to extract parameters of the microwave resonances.** The complex S_{21} data of the microwave resonances from the vector network analyser is plotted on the complex plane (top panels), as well as its phase (middle panels) and amplitude (bottom panels) for a Lorentzian (**a**) and a Fano (**b**) case. The Fano shape originates from the imperfect impedance match of the feedline. The fit is performed according to the procedure outlined in section 4.3.1 to extract the resonance frequency and the internal and external coupling rates.

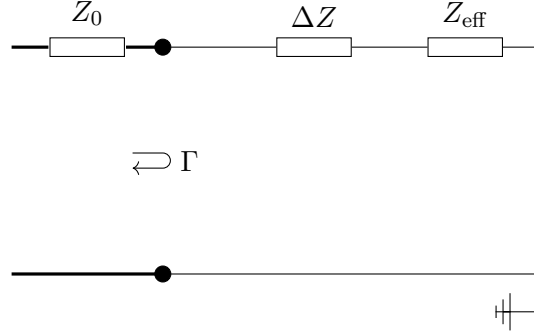


Figure 4.15 – **Equivalent circuit representation of the 1-port system with impedance mismatch.** The model used for the derivation of S_{11} in eq. (4.20) with the impedance mismatch ΔZ .

Note on extracting parameters from S_{11} in a 1-port configuration

We note that extracting the parameters in the case of a single port network, for which the diagram is shown in fig. 4.15, is more complicated. In terms of the impedances, the scattering matrix element S_{11} is given by

$$S_{11} = \frac{Z_{\text{eff}} + \Delta Z - Z_0}{Z_{\text{eff}} + \Delta Z + Z_0} = 1 - \frac{2Z_0}{Z + Z_{\text{eff}}}, \quad (4.20)$$

where $Z = Z_0 + \Delta Z$. In terms of the quality factors defined above, this can be rewritten as

$$\frac{1}{1 - S_{11}} = \frac{Z}{2Z_0} \left(1 + \frac{Q_{\text{int}} e^{-i\phi}}{\tilde{Q}_{\text{ext}}(1 + 2iQ_{\text{int}}\delta x)} \right). \quad (4.21)$$

Based on the procedure outlined above, it is possible to extract the required experimental parameters. We note that although the form at the right hand side is equivalent to the one in eq. (4.16), the value of the Q factors is different because of our redefinition of Z .

The problem appears when one takes into consideration the effect of environment, i.e. an unknown phase and amplitude factor in front of S_{11} . While in the two-port case of S_{21} these factors can be calibrated out, here they cannot be without assumptions. This problem is further elaborated in [91].

4.3.2 Optomechanically induced transparency and reaching the strong coupling regime

The optomechanical interaction gives rise to various phenomenon analogous to the ones in atomic physics. An example is optomechanically induced transparency or OMIT (an analogue of the electromagnetically induced transparency or EIT), which can be observed in a two-tone setup: a strong pump is placed on the red sideband of the

electromagnetic resonance, while a weak microwave tone (often called the probe tone) sweeps the resonance. The pump tone induces an interaction between the EM mode and the mechanical mode, while the probe tone measures the susceptibility of the EM mode. The parametric interaction changes this susceptibility and as the multiphoton coupling rate reaches $g \approx \sqrt{\Gamma_m \kappa}$, a peak - or transparency window - in the probe transmission around the resonance appears. The transmission spectrum of the superconducting resonator becomes [25, 39]

$$T_p = 1 - \frac{\kappa_{\text{ex}}(1 - i\chi)}{\kappa + 2i(\omega_{\text{probe}} - \omega_c) + 4\chi(\omega_{\text{pump}} - \omega_c)}, \quad (4.22)$$

where χ is defined as

$$\chi = \frac{4g^2\Omega_m}{(\kappa + 2i(\omega_{\text{probe}} - 2\omega_{\text{pump}} + \omega_c))(\Omega_m^2 - (\omega_{\text{probe}} - \omega_{\text{pump}})^2 + i(\omega_{\text{probe}} - \omega_{\text{pump}})\Gamma_m)}. \quad (4.23)$$

An example is shown in fig. 4.16. The peak can be fitted by a Lorentzian and its width gives the modified energy dissipation rate of the mechanical oscillator according to

$$\Gamma_{\text{eff}} = \Gamma_m(1 + \mathcal{C}), \quad (4.24)$$

where Γ_m is the bare dissipation rate and \mathcal{C} is the cooperativity. Since \mathcal{C} is proportional to g^2 , therefore the intracavity photon number, one expects a linear dependence of Γ_{eff} on the pump power. By fitting this linear function, one can extract Γ_m (y intercept) and the fit also provides a way to calibrate the intracavity photon number (if g_0 and κ are known). fig. 4.17 shows an OMIT power sweep for two different mechanical modes. The fit gives $\Gamma_m/2\pi = (100 \pm 5)$ Hz for the fundamental mode and $\Gamma_m/2\pi = (30 \pm 4)$ Hz for the second order radially symmetric mode. As one increases the power in the pump tone placed at the red sideband, Γ_{eff} increases and at high enough pumping, becomes comparable to κ . At this point, eq. (4.22) and eq. (4.24) are no longer valid and the system enters the strong coupling regime (the multiphoton coupling g exceeds the intrinsic dissipation of the original modes, i.e. $g > \kappa \gg \Gamma_m$). The new eigenmodes of the system are now hybrids of the electromagnetic and mechanical modes. The spectroscopic measurement of the electromagnetic mode reveals the well-known normal-mode splitting (level repulsion) of two strongly coupled harmonic oscillators, as shown experimentally in fig. 4.18. The frequencies of the two eigenmodes are given by

$$\tilde{\omega}_{1,2} = \frac{\omega_c + \Omega_m}{2} \pm \sqrt{\left(\frac{\omega_c - \Omega_m}{2}\right)^2 + g^2}. \quad (4.25)$$

The experimental data, obtained by sweeping the strong pump tone around the red sideband and taking the response of the microwave cavity using the vector network

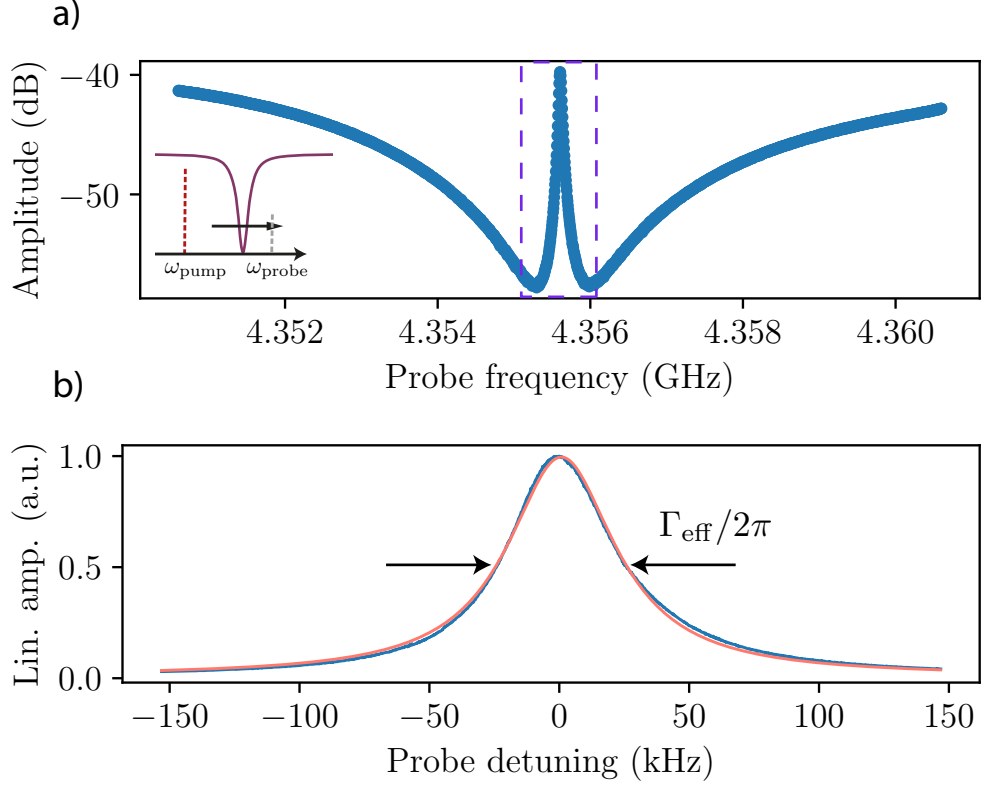


Figure 4.16 – **Experimental demonstration of optomechanically induced transparency.** **a)** Linear response measurement of the microwave cavity when a pump is placed on the red sideband. The parametric interaction changes the susceptibility of the electromagnetic mode and a transparency window opens. Inset shows the frequency scheme. **b)** Zoom-in to the OMIT region and a Lorentzian fit. The fit gives the effective energy dissipation rate of the mechanical mode.

analyser, shows excellent agreement with eq. (4.25) (red dashed line in fig. 4.18). In this particular case, the extracted $g/2\pi$ is 1.285 MHz, more than 11 times the dissipation rate of the microwave mode ($\kappa/2\pi = 0.111$ MHz).

4.3.3 Ring-down measurements

Another way measure the bare energy dissipation rate of the mechanical element is to excite the mechanical motion utilizing the optomechanical interaction and measure the time it takes for the motion to ring down (decay) as the interaction is turned off. To realize this scheme in practice (shown in fig. 4.19), we need two tones: one - the pump - placed at one of the sidebands (we choose the red sideband in order to avoid instabilities, i.e. we set the frequency of the first tone at $\omega_1 = \omega_c - \Omega_m$) and one at the resonance frequency of the microwave cavity ($\omega_2 = \omega_c$). In the presence of these two tones, there

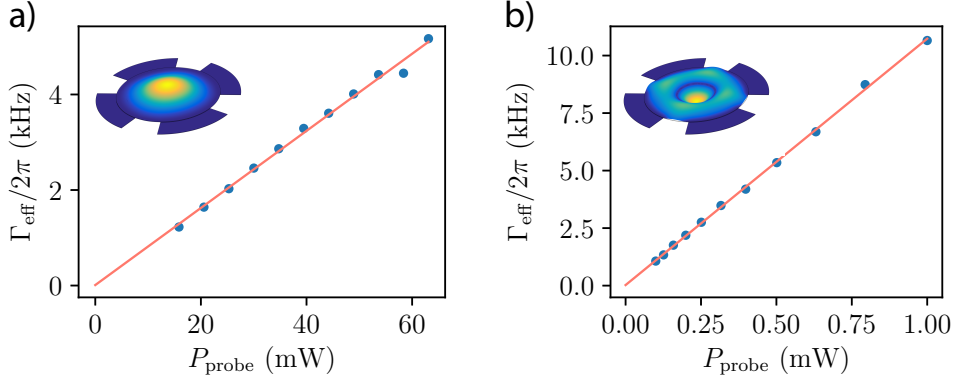


Figure 4.17 – **Power sweep of the pump placed at the red sideband versus the width of the OMIT feature for two different mechanical modes.** The y offset of the fit gives the bare dissipation rates of the mechanical modes (Γ_{eff}), according to eq. (4.24). The two modes are the fundamental mode shown in panel a) and the second order radially symmetric mode shown in panel b). The insets show the displacement profile of the two modes from COMSOL.

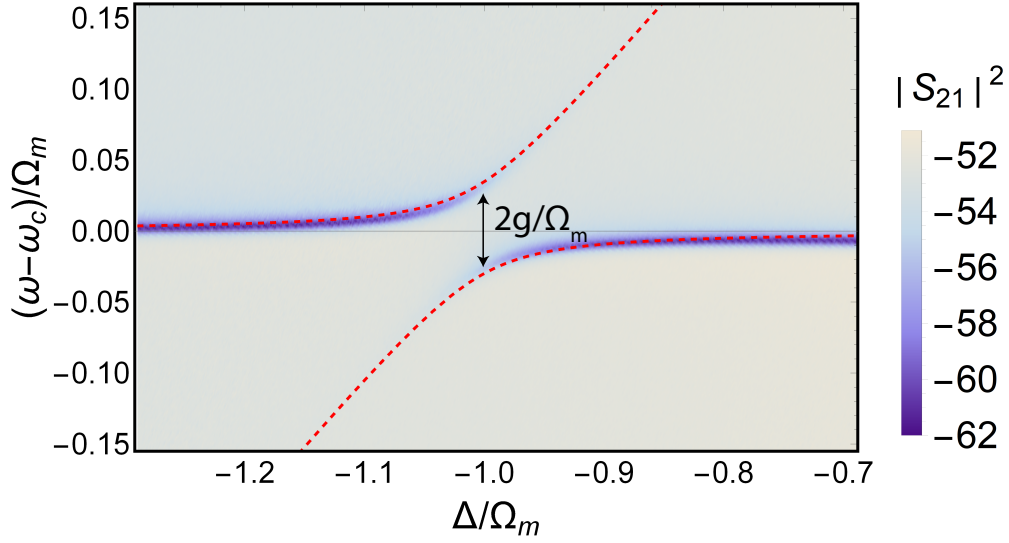


Figure 4.18 – **Experimental observation of strong coupling using two-tone spectroscopy.** The transmission of the electromagnetic resonance is measured as the pump tone around the red sideband is swept. The response exhibits the well-known level repulsion phenomenon. The frequency of the hybrid mode is well modelled by eq. (4.25) (red dashed line is a theoretical fit with no free parameters). Experimental parameters: $\omega_c/2\pi = 4.11$ GHz, $\kappa/2\pi = 0.11$ MHz, $\Omega_m/2\pi = 6.29$ MHz, $\Gamma_m/2\pi = 100$ Hz. The extracted $g/2\pi$ is 1.285 MHz, more than 11 times the dissipation rate of the microwave mode.

is a beating of the cavity field intensity at Ω_m , which creates an oscillating radiation pressure force resonantly exciting the drum. The pump tone is mixed with a square

signal coming from an arbitrary waveform generator (Tektronix AFG 3252C), creating a microwave pulse. The detection is done by the electromagnetic spectrum analyser in zero span mode. In this mode the local oscillator of the spectrum analyser is not swept but remains at a fixed frequency and the ESA becomes a fixed-tuned receiver. It allows the signal amplitude or power to be displayed as a function of time. The trailing edge of the arbitrary waveform generator is used as a trigger for the ring-down measurement. A typical ring-down signal is shown in fig. 4.20. As expected, the mechanical motion rings down as $\propto e^{-\tau\Gamma_m}$ and by fitting the exponential, one can extract Γ_m .

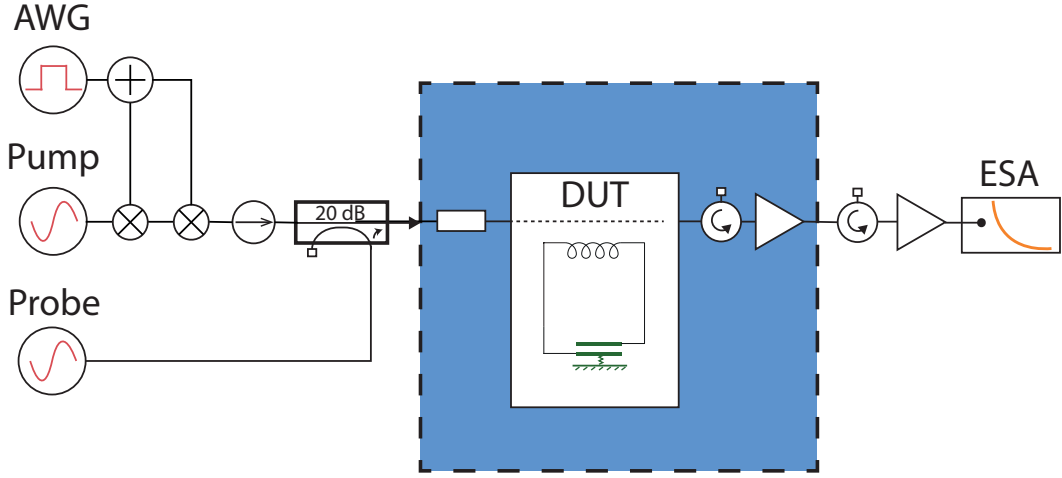


Figure 4.19 – **Experimental setup to perform ring-down measurements.** The pump tone is mixed with a square signal coming from an arbitrary waveform generator, creating a microwave pulse. The mixing is done at two stages to ensure that there is no leakage when the square signal is off. The signal is detected by the electromagnetic spectrum analyser in zero span mode.

4.3.4 Thermalization, calibration of g_0

An essential parameter to characterize an optomechanical system is the vacuum coupling strength g_0 , which corresponds to the frequency shift of the microwave (or optical) cavity induced by the zero-point displacement of the mechanical oscillator. A way to calibrate g_0 is to place a pump on resonance with the microwave cavity and measure the power in the scattered sidebands using the spectrum analyser. Provided that we have an absolute power reference (i.e. we know how much power reaches the cavity), as well as we know the temperature of the mechanical oscillator, the vacuum coupling strength can be deduced from the area under any of the motional sidebands according to

$$P_{\text{SB}} \propto n_c n_m g_0^2, \quad (4.26)$$

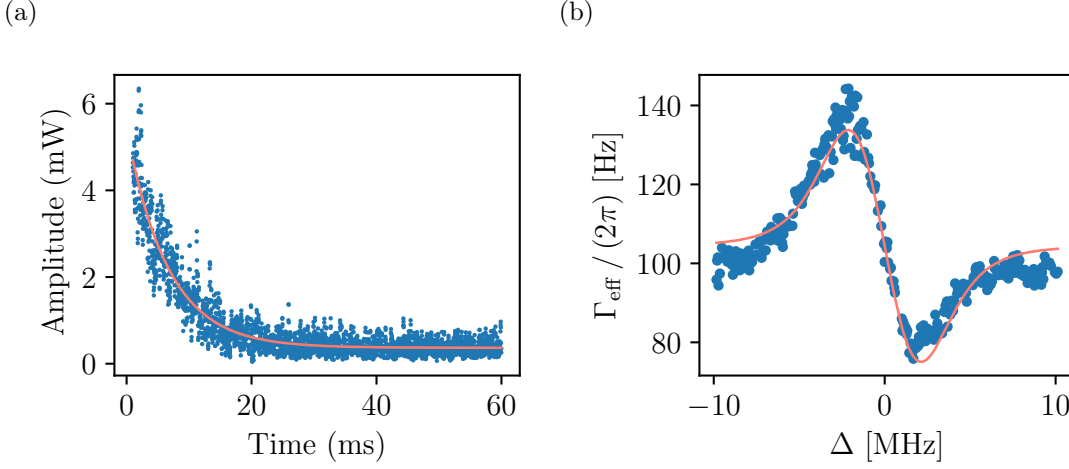


Figure 4.20 – **Example of ring-down measurements** **a)** Time series data acquired by the ring-down method. An exponential curve is fitted to obtain the energy dissipation rate Γ_m of the mechanical oscillator. **b)** The extracted energy dissipation rate versus the frequency of the probe (the frequency of the pump is adjusted such that the difference is kept at Ω_m). As the probe power is chosen to be nonnegligible, dynamical back-action damping is observed [32, 22].

where n_c is the intracavity photon number and n_m is the thermal (bosonic) occupancy of the mechanical mode.

Therefore, the first step is to show that the oscillator is in thermal equilibrium with the base plate of the refrigerator, and that the thermometer temperature can be used as an absolute measurement of the oscillator temperature. In order to confirm this, we sweep the base temperature of the DR and monitor the power in the motional sideband while pumping the microwave cavity on resonance.

We now derive the full expression for P_{SB} in terms of the cavity parameters and the state of the mechanical oscillator. In the scattering picture, the sideband is created because an intracavity photon is scattered from the mechanics, which results in a change of the photon energy by $\pm\hbar\Omega_m$ (negative for the lower, red sideband and positive for the upper, blue sideband). We denote this scattering rate by w . It can be calculated from Fermi's golden rule, which gives a formula for the transition rate from one energy state of a quantum system into another, affected by a weak interaction. Considering the initial state to be $|i\rangle$ and the final state to be $|f\rangle$ with a density of states $\rho(f)$ and an interaction

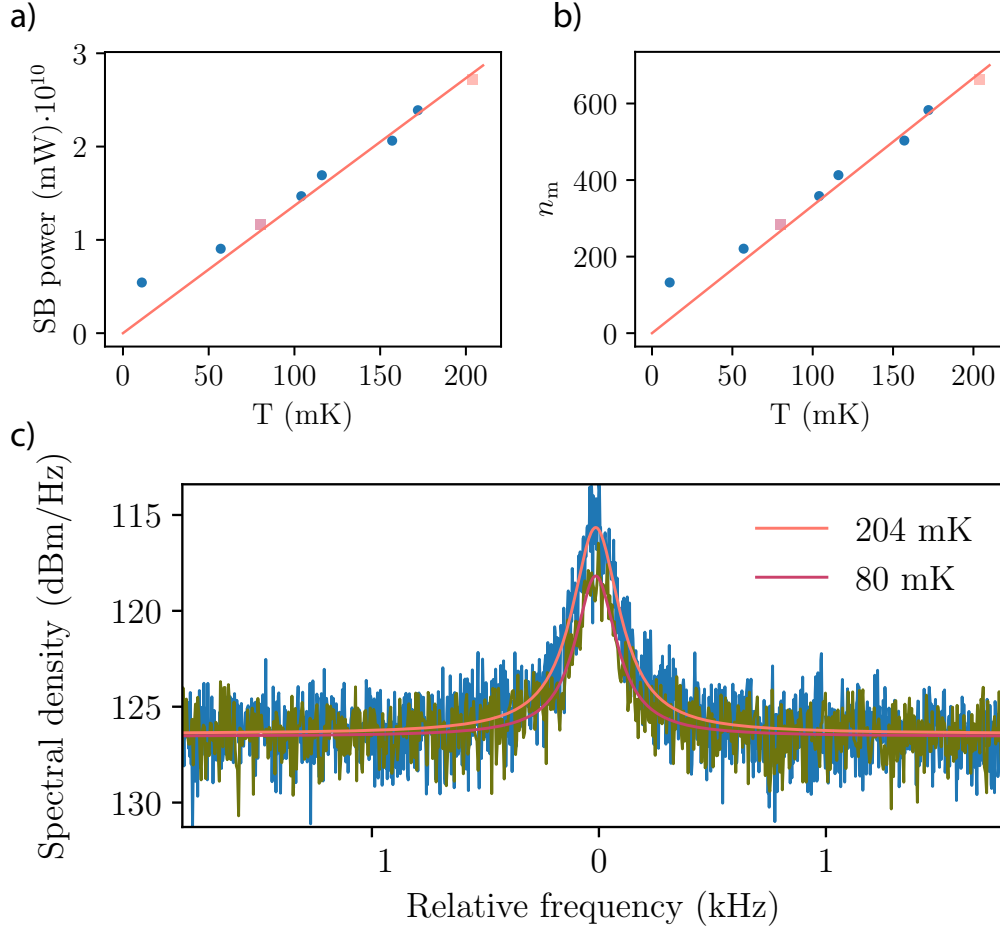


Figure 4.21 – **Thermalization of the mechanical oscillator.** Example of thermalization of the mechanical mode, showing thermal occupancy as a function of refrigerator temperature. **a)** Extracted power in one of the sidebands using a weak resonant probe. **b)** The sideband power of **a** is scaled to give thermal occupation by anchoring it to the highest temperature value, where the mechanical oscillator can be assumed to be thermalized. In both panels the data is fitted with a linear function crossing the origin (representing ideal thermalization). The mechanical mode is thermalised down to ~ 50 mK. **b)** Comparison of the sidebands at two different temperatures (204 mK and 80 mK). Panel **a-b)** - in a replotted form - also appears in the Supplementary Information of [50].

Hamiltonian \hat{H}_{int} , the scattering rate is given by

$$w_{i \rightarrow f} = \frac{2\pi}{\hbar} \left| \langle f | \hat{H}_{\text{int}} | i \rangle \right|^2 \rho(f). \quad (4.27)$$

Taking a double-sided cavity with a total external coupling rate of κ_{ex} , the power in the

Chapter 4. Measurement setup and characterization

blue sideband is given by

$$P_{\text{SB}} = \frac{\kappa_{\text{ex}}/2}{\kappa} \hbar(\omega_c + \Omega_m) w_{i \rightarrow f}. \quad (4.28)$$

Therefore, we need to evaluate $\langle f | \hat{H}_{\text{int}} | i \rangle$ and $\rho(f)$. The interaction Hamiltonian of the optomechanical system in the linearized regime (valid when $n_c \gg 1$) is given by

$$\hat{H}_{\text{int}} = -\hbar g_0 \sqrt{n_c} \left(\delta \hat{a} + \delta \hat{a}^\dagger \right) \left(\hat{b} + \hat{b}^\dagger \right). \quad (4.29)$$

Let us consider the scenario when a photon is scattered to the blue sideband by the

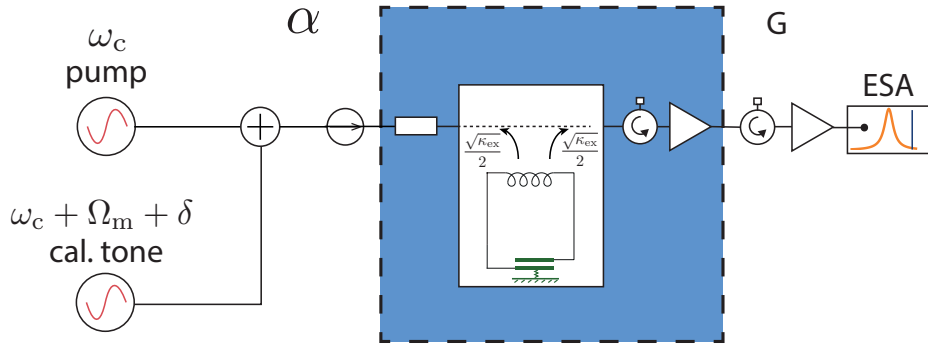


Figure 4.22 – **Schematic for calibrating the optomechanical vacuum coupling strength g_0 .** A pump is placed on resonance of the microwave cavity is combined with a calibration tone tuned slightly off the upper motional sideband. The temperature of the dilution refrigerator is elevated (> 50 mK) to ensure that the mechanical mode is thermalized.

mechanical oscillator. The initial state is the vacuum of the photon state and the thermal state of the mechanics at temperature T , with occupancy given by the Bose distribution $n_m(T) - 1)^{-1}$. In bra-ket notation, we can write $|i\rangle = |0, n_m\rangle$. In the final state, one phonon is converted to one photon: $|f\rangle = |1, n_m - 1\rangle$. This gives

$$\left| \langle f | \hat{H}_{\text{int}} | i \rangle \right|^2 = \hbar^2 g_0^2 n_c n_m. \quad (4.30)$$

The density of states evaluated at the upper sideband is given by

$$\rho(\Omega_m) = \frac{\kappa}{2\pi\hbar} \frac{1}{\Delta^2 + (\kappa/2)^2}, \quad (4.31)$$

which is normalized such that $\int \rho(\omega) d\omega = 1/\hbar$. The intracavity photon number, for a resonant drive with power P_{in} reaching the cavity, is given by

$$n_c = \frac{\kappa_{\text{ex}}}{(\kappa/2)^2} \frac{P_{\text{in}}}{\hbar n_c}. \quad (4.32)$$

Plugging eq. (4.31), eq. (4.31) and eq. (4.30) into eq. (4.28) we obtain

$$P_{\text{SB}} = 2g_0^2 n_m \left(\frac{\kappa_{\text{ex}}}{\kappa} \right)^2 \frac{1}{\Omega_m^2 + (\kappa/2)^2} P_{\text{in}}, \quad (4.33)$$

where we have used that $(\omega_c + \Omega_m)/\omega_c \approx 1$.

The next task is to determine the input pump power seen by the cavity P_{in} . The known quantity is the power at the output of the microwave source, which is attenuated at various temperature stages to reach the device, and then amplified through the output chain (see fig. 4.22). We can compensate for the overall attenuation and gain factors by sending in a reference tone close to the sideband frequency. Since the system is sideband resolved, this tone will not couple to the microwave resonance. Let us denote the ratio of the power of the pump tone and the calibration tone at the output of the sources by r . Then rearranging eq. (4.33), the optomechanical vacuum coupling strength is given by

$$g_0^2 = r \frac{P_{\text{SB}}}{P_{\text{cal}}} \frac{1}{2n_m} \left(\frac{\kappa}{\kappa_{\text{ex}}} \right)^2 (\Omega_m^2 + (\kappa/2)^2), \quad (4.34)$$

where P_{cal} is the power of the calibration tone measured at the end of the output chain with the electromagnetic spectrum analyser.

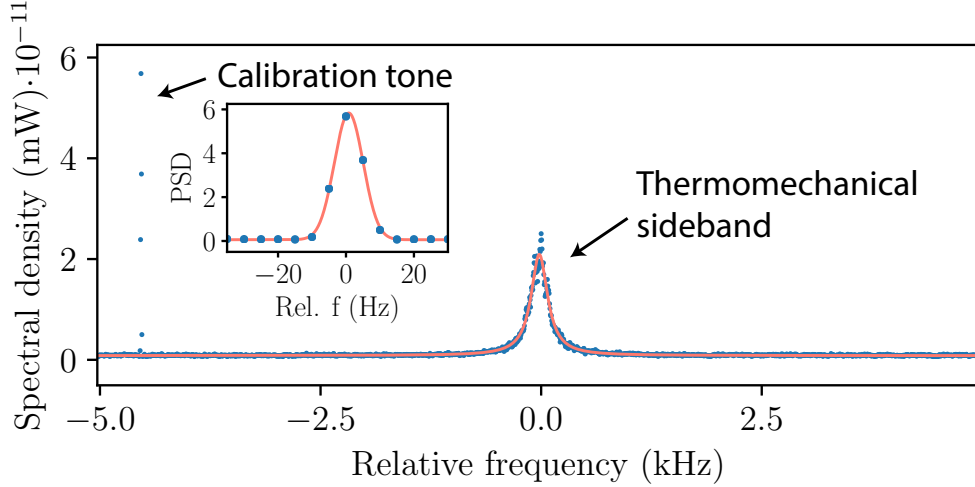


Figure 4.23 – **The thermomechanical sideband for calibrating g_0 .** Frequency spectrum of the thermomechanical sideband created by a resonant pump. The sideband is fitted with a Lorentzian. A calibration tone is placed 4.5 kHz away (and is fitted with a Gaussian function as shown in the inset). This allows to calibrate g_0 according to eq. (4.34).

5 A quantum reservoir for microwave light using a mechanical oscillator

In this chapter we demonstrate how to engineer a mechanical oscillator into a quantum reservoir for microwave light. This is achieved in a microwave optomechanical system [39] by engineering the mechanical dissipation rate to exceed that of the electromagnetic mode. This chapter is largely and explicitly based on two publications [50, 51].

We demonstrate dynamical backaction [12] on microwave light, and the control of a microwave mode by tuning its coupling to the reservoir. Backaction amplification leads to stimulated emission of microwaves and maser action using the mechanical oscillator as the gain medium. Below the masing threshold, we implement a large-gain phase-preserving amplifier that operates with added noise 0.87 quanta (or a factor 2) above the quantum limit. This work described here demonstrates that the mechanical reservoir for light can function as a useful quantum resource.

5.1 Motivation

Dissipation can significantly affect the quantum behaviour of a system and even completely suppress it [92]. However, if carefully constructed, dissipation can relax the system of interest to a desired target quantum state. This pioneering insight was originally theoretically conceived and studied in the context of trapped ions [48], experimentally first realized with trapped atomic ensembles [93] and later with trapped ions [94, 95, 96]. Moreover, reservoir engineering has recently also been realized in the context of circuit QED [97, 98, 99]. In these experiments the optical or microwave field provides a dissipative reservoir to the quantum systems. In cavity optomechanics [100], in which a mechanical oscillator and electromagnetic degree of freedom are parametrically coupled, analogous ideas have been developed and reservoir engineering for the preparation of squeezed mechanical states has been theoretically proposed [49, 101] and recently demonstrated [102, 75, 103]. As in the atomic physics case, the electromagnetic field acts as the engineered

Chapter 5. A quantum reservoir for microwave light using a mechanical oscillator

environment of the quantum system of interest.

In contrast, recent theoretical work [104, 105, 106, 107, 108] has considered the opposite scenario where the mechanical degree of freedom is employed to provide a dissipative, cold bath for light. This engineered bath can then be employed to achieve desirable quantum states of light or to modify the optical field properties. For example, such a dissipative reservoir for light can be exploited for amplification [105, 106], entanglement generation [104] or dissipative squeezing of electromagnetic modes [107]. Moreover, it provides an ingredient to realize nonreciprocal devices [108] such as isolators, circulators or directional microwave amplifiers. For a sufficiently cold dissipative mechanical reservoir, nonreciprocal devices implemented in this manner can operate in the quantum regime, with minimal added noise.

5.2 The role of dissipation in dynamical backaction

In this section we elaborate on the topic of dynamical backaction and how it relies on the dissipation hierarchy of the two coupled (electromagnetic and mechanical) modes. The aim is to put the results in the following sections in a physical, as well as a historical context.

The notion of dynamical backaction induced by radiation pressure was introduced in the late 1960s by Braginsky and coworkers [10, 11]. The context was, naturally, optomechanics (a mechanical mode coupled parametrically to an electromagnetic mode), with a motivation to understand the ultimate sensitivity of a gravitational detector based on interferometers with suspended mirrors. Braginsky showed that radiation pressure generates a force which acts on the mechanical resonator as a feedback mechanism due to the finite cavity delay. This changes the susceptibility of the mechanics and, in the case of blue-detuned light circulating in the system, poses a limitation on the power-handling capability of the interferometer due to the parametric instability (i.e. when the antidamping compensates for all the intrinsic loss in the mechanical mode). Thanks to the advent of microfabrication techniques which allowed to fabricate high-Q optical resonators to which the mechanical mode is efficiently coupled, radiation pressure parametric instability was observed in toroid micro-resonators in 2005 [24], and was shown to give rise to a rich nonlinear dynamics [109]. Soon thereafter, dynamical backaction cooling, an effect Braginsky predicted [110] to occur for red-detuned laser excitation, was demonstrated [111, 112, 22]. Although the parametric instability was first analyzed for a single electromagnetic mode coupled to a mechanical oscillator, the effect can also occur for multi-mode systems in which modes are spaced by the mechanical frequencies [113], a scenario in which the parametric oscillator stability in advanced LIGO at the Livingston observatory [15] was observed. Although undesirable in the context of LIGO, the ability to amplify and cool

5.2. The role of dissipation in dynamical backaction

mechanical motion using dynamical backaction is at the heart of the advances in cavity opto- and electromechanics over the past decade [60] that have enabled mechanical systems to be controlled at the quantum level. Dynamical backaction control over mechanical oscillators has enabled to cool micro- and nanomechanical oscillators to unprecedentedly low entropy states [27, 40, 28], and thereby opened a path to study optomechanical quantum effects ranging from optomechanical squeezing, mechanical squeezed states, sideband asymmetry, to entanglement of mechanical motion with microwaves [114, 115, 116, 117, 102, 42, 75, 103, 118].

We start by reformulating Braginsky's original derivation of dynamical backaction, in a way that showcases how the process is reversed in the case of an opposite dissipation hierarchy. Consider an electromagnetic mode with frequency ω_c and energy dissipation rate κ coupled, via the standard optomechanical coupling, to a mechanical mode with resonant frequency Ω_m and energy dissipation rate Γ_m . While Braginsky considered the limit $\Omega_m \leq \kappa$ to derive the delayed feedback force experienced by the mechanical oscillator due to the electromagnetic field, we consider here the sideband-resolved regime [119, 120, 121] $\Omega_m \gg \kappa$, relevant for our experiment. We consider the equations of motion parametrically coupling the mechanical oscillator to the electromagnetic cavity. These (for simplicity classical and linearized) equations can be written in a rotating frame for the phasors of the two modes; in the case of a pump driving the system on the upper motional sideband at a detuning $\Delta = \Omega_m$, they are given by the coupled-modes equations

$$\dot{a}^*(t) = -\frac{\kappa}{2}a^*(t) + igb(t) = -\frac{\kappa}{2}a^*(t) - iF_a(t) \quad (5.1)$$

$$\dot{b}(t) = -\frac{\Gamma_m}{2}b(t) - iga^*(t) = -\frac{\Gamma_m}{2}b(t) + iF_b(t), \quad (5.2)$$

where $b(t) = (\sqrt{m\Omega_m}x(t) + i\sqrt{1/m\Omega_m}p(t))/\sqrt{2}$ describes the state of the mechanical mode of mass m , $a(t)$ is the phasor for the electromagnetic mode and $g = g_0|\alpha_0|^2$ is the vacuum optomechanical coupling rate g_0 enhanced by the field α_0 of the blue-detuned pump. In the rotating frame, the variables describe the slowly changing amplitude and phase of the rapidly oscillating field and oscillator, at ω_c and Ω_m . Each of the two harmonic oscillators is subject to a “force” (denoted by $F_a(t)$ and $F_b(t)$) proportional to the state of the other harmonic oscillator, establishing a feedback mechanism: cavity intensity fluctuations create a radiation pressure force acting on the mechanical oscillator, while mechanical displacement modulates the cavity resonance frequency. The symmetry of the relationship is broken by the different scales of the dissipation rates.

Braginsky originally considered the case where electromagnetic dissipation dominates ($\kappa \gg \Gamma_m$). This is natural in most systems as the quality factors are comparable for the electromagnetic and mechanical modes, while there is a large (many orders of magnitude) separation of scales in their respective frequencies. In this limit, the

Chapter 5. A quantum reservoir for microwave light using a mechanical oscillator

electromagnetic field envelope almost instantly adapts to the mechanical displacement ($\dot{a}^*(t) \approx 0$) and becomes proportional to it such that $a^*(t) = i(2g/\kappa)b(t)$. The field then exerts a force on the mechanical oscillator proportional to the state of the latter, given by $F_b(t) = -i(2g^2/\kappa)b(t)$. Therefore, the interaction can be viewed as a simple feedback loop. The factor $-i$ represents a delay of a quarter period for the feedback force acting on the mechanical oscillator. This delay means that the force, acting in quadrature, increases the amplitude of the phasor, equivalent to a decrease in mechanical damping or gain. If the pump detuning Δ does not fall exactly on the sideband, the delay is not exactly i and the force has an in-phase component, modifying the frequency of the mechanical oscillator (this effective change of the mechanical spring constant is called the *optical spring* effect). The amplification process can be understood as a positive feedback that measures the state of the mechanical oscillator and returns it with a delay as a force, i.e. a dynamical backaction (see fig. 5.1a). For sufficiently high coupling strength g , this leads to a parametric oscillatory instability, that causes regenerative oscillations of the mechanical oscillator, and thus limits the maximal circulating power for a gravitational wave detector [14].

Now we describe the converse process, where the mechanical dissipation rate dominates ($\Gamma_m \gg \kappa$). In this case the envelope of mechanical oscillations nearly instantly adjusts to the state of the electromagnetic field ($\dot{b}(t) \approx 0$) and is proportional to it such that $b(t) = -i(2g/\Gamma_m)a^*(t)$. The field is then subject to an in-quadrature “force” proportional to its own state $F_a(t) = i(|\kappa_{\text{DBA}}|/2)a^*(t)$ where $\kappa_{\text{DBA}} = -4g^2/\Gamma_m = -\kappa\mathcal{C}$, introducing the multiphoton cooperativity $\mathcal{C} = 4g^2/(\kappa\Gamma_m)$. Similarly to above, the force has a delay $+i$ of a quarter period and increases the amplitude of electromagnetic oscillations, compensating for damping by an amount given by κ_{DBA} , such that the effective energy decay rate of the cavity is $\kappa + \kappa_{\text{DBA}}$. A change in detuning Δ would again slightly modify this delay and create components of the in-phase force component, changing the speed of oscillations, and displacing the resonance frequency of the cavity (thus creating a *mechanical spring* effect). This is equivalent to a feedback loop for the electromagnetic mode (see fig. 5.1b), and implies that the mechanical oscillator is responsible for *dynamical backaction on light*. As above, the positive feedback can lead to a parametric instability. For $\kappa_{\text{DBA}} = -\kappa$, the anti-damping caused by this feedback exactly compensates the losses (both intrinsic and external) of the electromagnetic mode, and the cavity develops self-sustained oscillations i.e. acts as a maser. The intrinsic optomechanical nonlinearity sets the maximum amplitudes of the oscillations [106] and the dynamics is no longer captured by the linearized eqs. (5.1) and (5.2). Experimentally, this dynamical backaction on the microwave mode can be observed by measuring the emission spectrum of the electromagnetic mode. Below the masing threshold, one expects amplified noise at the output of the device in a bandwidth which is commensurate with the effective energy decay rate $\kappa + \kappa_{\text{DBA}}$. At the threshold, this bandwidth collapses to zero and a strong,

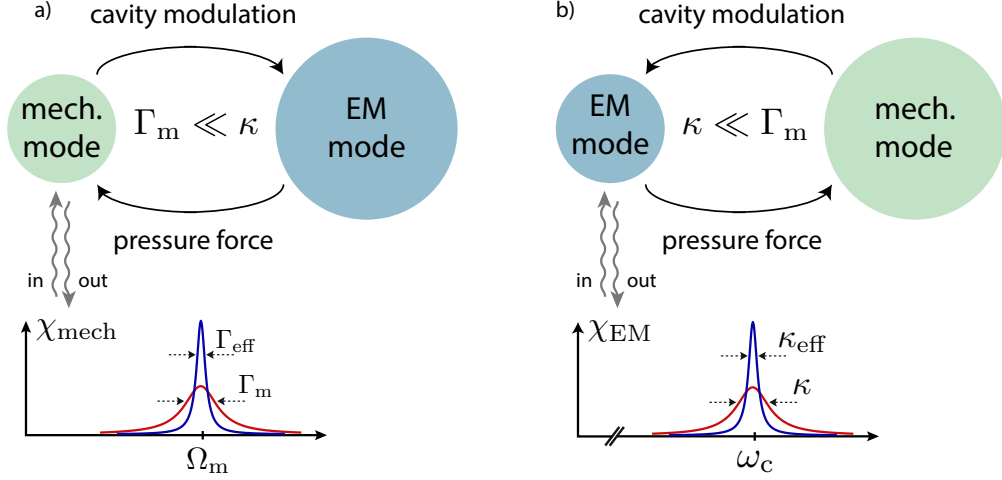


Figure 5.1 – **The role of dissipation in dynamical backaction in the feedback picture.** **a)** An electromagnetic mode (with resonant frequency ω_c and energy dissipation rate κ) is coupled to a mechanical oscillator (with resonant frequency Ω_m and energy dissipation rate Γ_m) through the optomechanical interaction, in which the former exerts radiation pressure force, while the latter modulates the resonant frequency of the cavity. In standard optomechanical systems, the dissipation rates satisfy the hierarchy $\kappa \gg \Gamma_m$ and this interaction can be viewed as a simple feedback mechanism acting on the mechanical oscillator. This modifies the oscillator’s damping rate, in a process coined as “dynamical backaction” by Braginsky. **b)** In the scenario where the optical mode is coupled to a mechanical oscillator whose dissipation rate dominates over that of the optical mode, the role of the modes is reversed. Here, the mechanical mode provides the feedback mechanism (dynamical backaction) for the optical mode, therefore modifying the light mode’s resonant frequency and damping rate.

Figure also appears in [51].

spectrally pure signal emerges from the cavity. This is described in more details in section 5.5.1.

5.3 Optomechanical circuit with dark and bright modes

We utilize a scheme in which two microwave modes are coupled to the same mechanical oscillator [106]. One (auxiliary) electromagnetic mode is used to damp the oscillator via optomechanical sideband cooling [32, 122] and engineer it into a cold bath for the other (primary) electromagnetic mode (schematic shown in fig. 5.2). A key ingredient for the scheme is an optomechanical cooling rate of the auxiliary mode which greatly exceeds the electromagnetic decay rate of the primary microwave mode, necessitating vastly different decay rates of the employed microwave cavities. This is challenging to achieve with previously realized dual-mode circuits [103], since any parasitic coupling between the two modes opens a decay channel, equilibrating their decay in energy as

Chapter 5. A quantum reservoir for microwave light using a mechanical oscillator

described in more detail in section 3.2.2. Here, we address this challenge by engineering hybridized modes with inherently dissimilar decay rates arising from interference in the output channel (cf. fig. 5.3a, b and section 5.3.1).

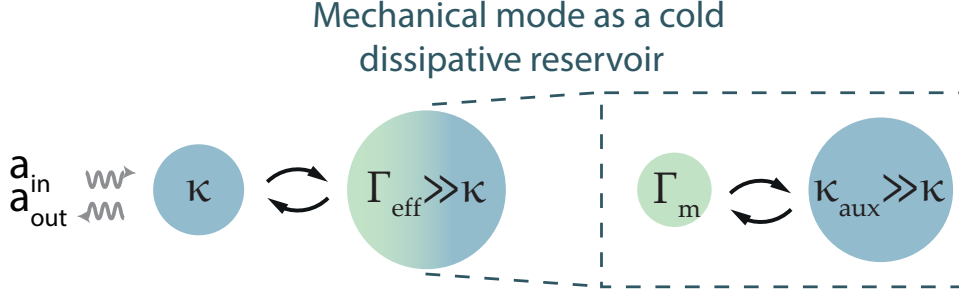


Figure 5.2 – **Schematic representation of a cold dissipative mechanical reservoir.** We utilize a multi-mode electromechanical system in which a microwave mode with energy decay rate κ is coupled to an engineered mechanical mode acting as a cold, dissipative reservoir with an effective energy decay rate Γ_{eff} much greater than κ . Figure also appears in [50].

Specifically, we design an electromechanical circuit using two LC resonators both coupled inductively to a common feedline, one of which has a mechanically compliant vacuum-gap capacitor [123] coupling mechanical vibrations to the microwave mode. The two resonators are strongly coupled through sharing a common inductor (as visualized in fig. 5.3a). In terms of the annihilation operators \hat{a}_1 and \hat{a}_2 of the bare modes, the resulting interaction Hamiltonian is given by

$$\hat{H}_{\text{int}} = \hbar J (\hat{a}_1^\dagger \hat{a}_2 + \hat{a}_2^\dagger \hat{a}_1) + \hbar \tilde{g}_0 \hat{a}_1^\dagger \hat{a}_1 (\hat{b} + \hat{b}^\dagger), \quad (5.3)$$

where \hat{b} designates the annihilation operator for the mechanical mode, J the intermode coupling strength, and \tilde{g}_0 the vacuum electromechanical coupling strength to the first mode (\hbar is the reduced Planck's constant). The symmetric and antisymmetric superpositions of the bare modes $\hat{a}_{s,a} = \frac{1}{\sqrt{2}}(\hat{a}_1 \pm \hat{a}_2)$ diagonalize the intermode coupling J . In terms of these hybridized modes the interaction Hamiltonian is given by

$$\hat{H}_{\text{int}} = \hbar J (\hat{a}_s^\dagger \hat{a}_s - \hat{a}_a^\dagger \hat{a}_a) + \hbar \frac{\tilde{g}_0}{2} (\hat{a}_s^\dagger \hat{a}_s + \hat{a}_a^\dagger \hat{a}_a) (\hat{b} + \hat{b}^\dagger). \quad (5.4)$$

If the bare modes are degenerate, the eigenmodes have an energy difference of $2\hbar J$ (fig. 5.3b) and are now, as a result of the interaction, both coupled to the micromechanical oscillator [124] with half the bare vacuum electromechanical coupling strength \tilde{g}_0 .

We consider here the limit of a coupling large compared to the mechanical resonance frequency, $J \gg \Omega_m$, implying that we can neglect the cross terms $\hat{a}_s^\dagger \hat{a}_a (\hat{b} + \hat{b}^\dagger)$ and other

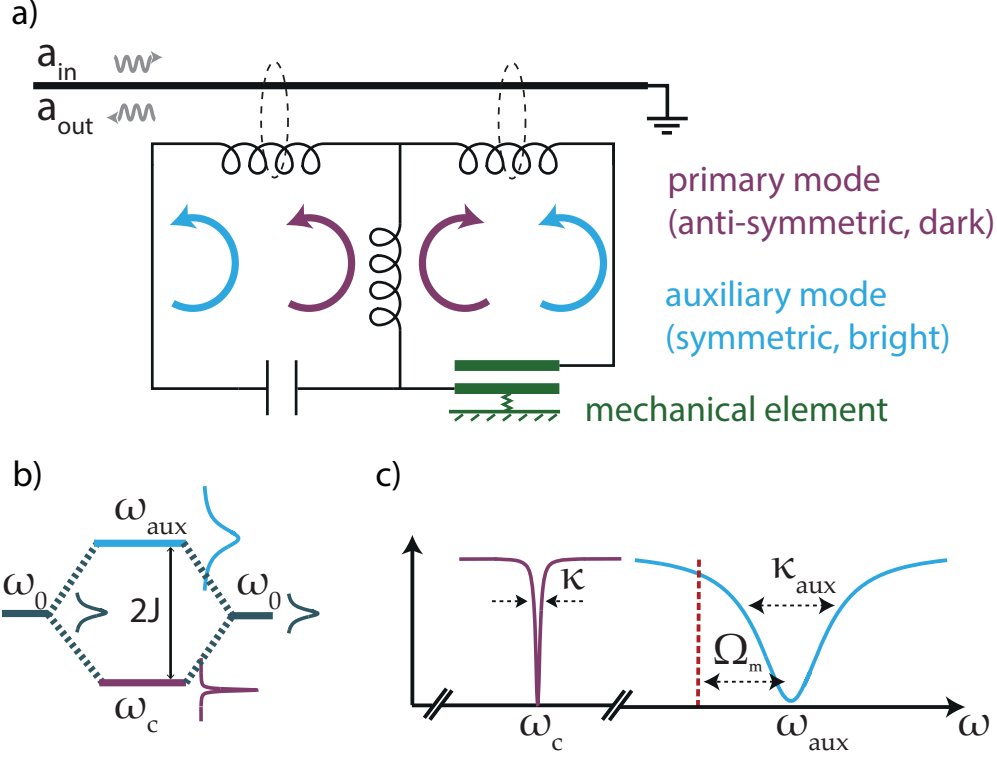


Figure 5.3 – **Circuit realization of the electromechanical system.** **a)** Two lumped-element LC circuits – one containing a mechanically compliant capacitor – with matching resonance frequencies are inductively coupled and show normal-mode splitting, forming dark and bright modes (used as the primary and auxiliary modes, respectively) to achieve $\kappa_{\text{aux}} \gg \kappa$. **b)** Visual representation of the mode structure and the resulting asymmetric dissipation rates, originating from the interference in the output coupling. **c)** Optomechanical sideband cooling the mechanical mode with the auxiliary, bright mode realizes a cold, dissipative mechanical reservoir for the primary, dark mode. Figure also appears in [50].

terms which are not resonant. Critically, the new eigenmodes will have dissimilar decay rates and form a bright (strongly coupled) and a dark (weakly coupled) mode resulting from interference of the bare-mode external coupling rates $\kappa_1^{\text{ex}}, \kappa_2^{\text{ex}}$ to the output channel. The symmetric, bright mode interferes constructively, leading to an external energy decay rate to the output feedline of $\kappa_s^{\text{ex}} = \kappa_1^{\text{ex}} + \kappa_2^{\text{ex}}$. Whereas, the antisymmetric, dark mode interferes destructively, leading to a decreased external coupling rate $\kappa_a^{\text{ex}} = |\kappa_1^{\text{ex}} - \kappa_2^{\text{ex}}|$. Physically, one can understand the difference by considering the topology of current flow in the modes, as shown in fig. 5.3a. The symmetric mode has current flowing in the same direction in both resonators, causing their external magnetic flux to create currents that add up, leading to an increased coupling rate to the feedline. The antisymmetric mode has current flowing in opposite directions in the two resonators, causing the external magnetic flux to create currents that cancel out, leading to a suppression in the external coupling

Chapter 5. A quantum reservoir for microwave light using a mechanical oscillator

to the feedline. For bare coupling rates similar in magnitude ($\kappa_1^{\text{ex}} \approx \kappa_2^{\text{ex}}$), this enforces the coupling-rate hierarchy $\kappa_a^{\text{ex}} \ll \kappa_s^{\text{ex}}$ necessary to achieve a dissipative mechanical reservoir with the present scheme [106]. In the remaining of the text, we refer to the dark mode as the primary mode and the bright mode as the auxiliary mode with resonance frequencies ω_c and ω_{aux} and energy decay rates κ and κ_{aux} , respectively.

5.3.1 System-reservoir treatment of bright and dark modes

In this section we give a theoretical description on how the dark and bright modes - used as primary and auxiliary modes - emerge from our circuit design on a more fundamental level. In particular, we present a system-reservoir treatment to describe the effect of intermode coupling on two degenerate electromagnetic modes coupled to a common bath (in our case, two electromagnetic modes inductively coupled to a common microwave feedline).

We start by considering two modes described by annihilation operators \hat{a}_1 and \hat{a}_2 that are coupled to each other with matrix element J and that can dissipate into a common bath of harmonic oscillators described by their annihilation operators \hat{b}_k . The system-bath Hamiltonian describing this problem is

$$\begin{aligned} \hat{\mathcal{H}} = & \hbar\omega_0 \left(\hat{a}_1^\dagger \hat{a}_1 + \hat{a}_2^\dagger \hat{a}_2 \right) + \sum_k \hbar\omega_k \hat{b}_k^\dagger \hat{b}_k + \hbar J \left(\hat{a}_1^\dagger \hat{a}_2 + \text{H.c.} \right) \\ & + \hbar \sum_k \left(g_k^{(1)} \hat{a}_1 \hat{b}_k^\dagger + \text{H.c.} \right) + \hbar \sum_k \left(g_k^{(2)} \hat{a}_2 \hat{b}_k^\dagger + \text{H.c.} \right). \end{aligned} \quad (5.5)$$

Note that we take the coupling amplitudes $g_k^{(1)}$ and $g_k^{(2)}$ to be non-negative real numbers. In doing so, we will neglect a relative phase factor e^{ikx} where k is the wave vector of the microwaves and x is the relative distance between the positions where the radio-frequency (RF) circuits are coupled to the common microwave feedline.

For $J \neq 0$ the degeneracy between the modes \hat{a}_1 and \hat{a}_2 is lifted and the normal modes are the symmetric and antisymmetric superpositions, $\hat{a}_{s,a} = \frac{1}{\sqrt{2}} (\hat{a}_1 \pm \hat{a}_2)$, with energies $\hbar(\omega_0 \pm J)$. In this basis, the Hamiltonian (5.5) reads

$$\begin{aligned} \hat{\mathcal{H}} = & \hbar(\omega_0 + J) \hat{a}_s^\dagger \hat{a}_s + \hbar(\omega_0 - J) \hat{a}_a^\dagger \hat{a}_a + \sum_k \hbar\omega_k \hat{b}_k^\dagger \hat{b}_k \\ & + \hbar \sum_k \left(\frac{g_k^{(1)} + g_k^{(2)}}{\sqrt{2}} \hat{a}_s \hat{b}_k^\dagger + \text{H.c.} \right) + \hbar \sum_k \left(\frac{g_k^{(1)} - g_k^{(2)}}{\sqrt{2}} \hat{a}_a \hat{b}_k^\dagger + \text{H.c.} \right). \end{aligned} \quad (5.6)$$

We see that if the coupling matrix elements are similar, i.e. $g_k^{(1)} \approx g_k^{(2)}$, the symmetric

mode \hat{a}_s features a much larger dissipation rate than that of the antisymmetric mode \hat{a}_a . Indeed, we have $g_k^{(+)} = (g_k^{(1)} + g_k^{(2)})/\sqrt{2} \approx \sqrt{2}g_k^{(1)}$ and $g_k^{(-)} = (g_k^{(1)} - g_k^{(2)})/\sqrt{2} \approx 0$ so that dissipation rate of the mode \hat{a}_s has twice the dissipation rate of that of the mode \hat{a}_1 , while the mode \hat{a}_a is approximately decoupled from the common reservoir \hat{b}_k .

The situation is closely related to the case of a three-state Λ -type system in which the two transitions are driven coherently. In that case, so-called *bright* and *dark* states are formed. The population in the dark state is trapped and cannot decay even if the upper state of the Λ -type system has a finite linewidth.

In our case, the bright state \hat{a}_s and the dark state \hat{a}_a can be addressed separately by a coherent drive as long as their frequency difference $2J$ is large compared to their decay rates. In this situation, we can take \hat{a}_s and \hat{a}_a to be the modes of our system.

5.4 Realization of a dissipative mechanical reservoir

We realize the electromechanical circuit experimentally by fabricating two lumped-element LC circuits coupled to each other via a common inductor, made from thin-film aluminium on a sapphire substrate. The primary and auxiliary modes have resonance frequencies $(\omega_c, \omega_{\text{aux}}) = 2\pi \cdot (4.26, 5.48)$ GHz with total energy decay rates $(\kappa, \kappa_{\text{aux}}) = 2\pi \cdot (118, 4478)$ kHz, respectively (thus, $\kappa_{\text{aux}}/\kappa \approx 38$). This clear hierarchy in the energy relaxation rates indeed originates from the vastly dissimilar engineered external coupling to the feedline, with $\kappa_{\text{ex}} = 2\pi \cdot 42$ kHz $\approx 1\%$ of $\kappa_{\text{aux}}^{\text{ex}}$. The linear response of the two microwave resonances are plotted in fig. 5.6, revealing the bright and dark modes. The mechanical resonator is a parallel-plate capacitor with a suspended top electrode, having a resonance frequency of the fundamental flexural mode $\Omega_m = 2\pi \cdot 5.33$ MHz and a decay rate $\Gamma_m = 2\pi \cdot 30$ Hz. This mechanical mode couples to both the primary and auxiliary modes with a vacuum electromechanical coupling strength $g_0 = \tilde{g}_0/2 = 2\pi \cdot 60$ Hz. Details of the calibration procedure are described in chapter 4 and all parameters for this device are summarized in table 5.1. Importantly, the resolved sideband regime is still attained for both microwave modes, i.e. $\Omega_m > \kappa_{\text{aux}} \gg \kappa$. fig. 5.5a, b show an optical image of the fabricated circuit and a scanning electron micrograph of the drum-type capacitor, respectively. The fabrication of the device is described in detail in chapter 3. The simplified measurement setup is shown in fig. 5.5c and explained extensively in chapter 4. In brief, the device is mounted on the base plate of a dilution refrigerator and cooled to a base temperature of ca. 10 mK. The microwave input lines are heavily attenuated to suppress residual thermal noise and, in addition, filter cavities are employed to remove unwanted frequency noise from the applied tones (cf. section 4.2.2). After amplification with a commercial high-electron-mobility transistor (HEMT) amplifier mounted on the 3 K plate, the signal is measured with a spectrum analyzer or a vector network analyzer.

Chapter 5. A quantum reservoir for microwave light using a mechanical oscillator

To prepare a cold, dissipative mechanical bath we follow the approach outlined in [106] and use optomechanical sideband cooling [32, 122] to prepare the mechanical oscillator as a strongly dissipative, cold reservoir. We proceed by pumping the auxiliary mode on the lower motional sideband (fig. 5.3c). We strongly damp the mechanical oscillator to an effective energy decay rate $\Gamma_{\text{eff}} \approx 2\pi \cdot 500$ kHz (corresponding to a mean intra-cavity photon number of $n_c^{\text{aux}} \approx 1.5 \cdot 10^8$), while still remaining in the weak-coupling regime for the auxiliary mode. This is evidenced by the optomechanically induced transparency feature shown in fig. 5.4, which is fitted with a Lorentzian to obtain Γ_{eff} (more information is in section 4.3.2).

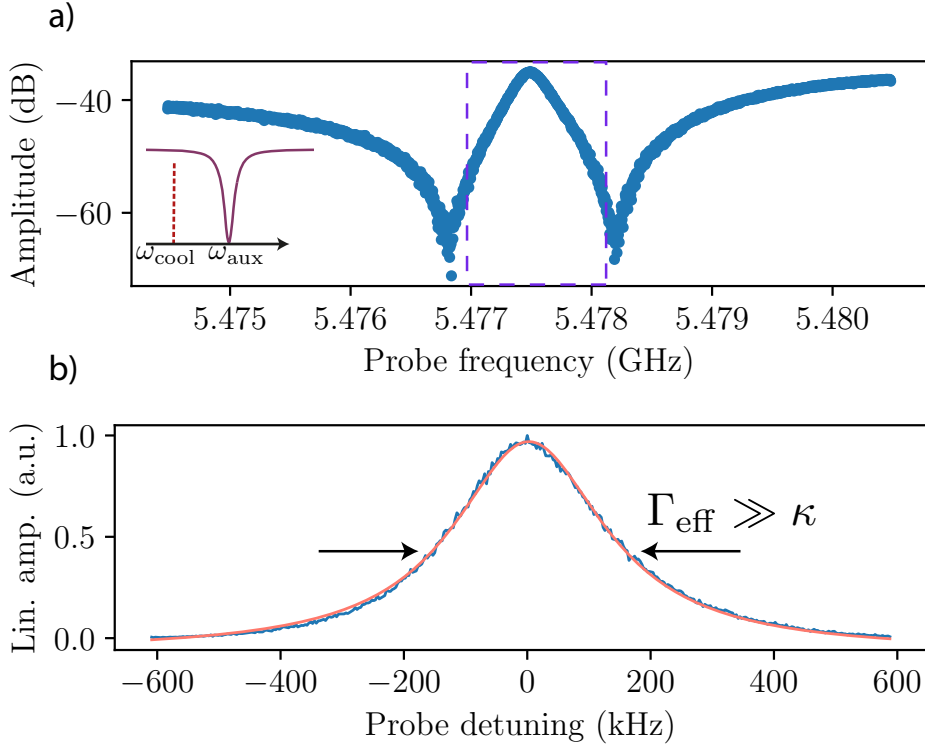


Figure 5.4 – **Optomechanically induced transparency on the bright mode demonstrating the preparation of the dissipative mechanical reservoir.** **a)** The bright, auxiliary mode is pumped on the lower motional sideband (cf. inset) with a multiphoton cooperativity of ≈ 5000 . **b)** Fitting the transparency window (corresponding to the effective energy dissipation rate according to eq. (4.24), giving $\Gamma_{\text{eff}}/2\pi = 500$ kHz.

Thereby, we realize a dissipative mechanical reservoir for the primary, high-Q mode, since $\Gamma_{\text{eff}} \gg \kappa$. The effective temperature of this reservoir and its utility as a quantum resource are studied below.

5.5. Experimental observation of dynamical backaction on microwave light

| Parameter | Symbol | Value |
|--|-----------------------------------|-----------------------|
| Resonance frequency (primary, dark mode) | ω_c | $2\pi \cdot 4.26$ GHz |
| Total decay rate (primary, dark mode) | κ | $2\pi \cdot 118$ kHz |
| Internal decay rate (primary, dark mode) | κ_0 | $2\pi \cdot 76$ kHz |
| External coupling rate (primary, dark mode) | κ_{ex} | $2\pi \cdot 42$ kHz |
| Resonance frequency (auxiliary, bright mode) | ω_{aux} | $2\pi \cdot 5.48$ GHz |
| Total decay rate (auxiliary, bright mode) | κ_{aux} | $2\pi \cdot 4478$ kHz |
| Internal decay rate (auxiliary, bright mode) | κ_{aux}^0 | $2\pi \cdot 245$ kHz |
| External coupling rate (auxiliary, bright mode) | $\kappa_{\text{aux}}^{\text{ex}}$ | $2\pi \cdot 4233$ kHz |
| Intermode coupling strength (also estimated from simulations) | J | $2\pi \cdot 0.57$ GHz |
| Resonance frequency of mechanical mode | Ω_m | $2\pi \cdot 5.33$ MHz |
| Decay rate of mechanical mode | Γ_m | $2\pi \cdot 30$ Hz |
| Effective decay rate of mechanical mode in the RDR | Γ_{eff} | $2\pi \cdot 500$ kHz |
| Vacuum electromechanical coupling strength (for the hybridized modes) | $g_0 = \tilde{g}_0/2$ | $2\pi \cdot 60$ Hz |

Table 5.1 – **Summary of the most important experimental parameters to demonstrate dynamical backaction on microwave light with a dissipative reservoir, device 1.** The device was used to obtain the results shown in section 5.4 and section 5.5.

5.5 Experimental observation of dynamical backaction on microwave light

We first study the modified microwave cavity susceptibility resulting from the dissipative cold reservoir, i.e. the dynamical backaction on the microwave light. The engineered bath provided by the mechanical resonator modifies the response of the electromagnetic mode when a microwave tone is applied [106]. With a pump detuned by Δ from the primary microwave cavity resonance, the frequency and the decay rate of the mode shift by

$$\delta\omega_{\text{om}} = \text{Re } \Sigma \quad \text{and} \quad \kappa_{\text{om}} = -2\text{Im } \Sigma, \quad (5.7)$$

called mechanical spring effect and mechanical damping, respectively. The self-energy Σ is defined as

$$\Sigma = -ig^2 \left(\frac{1}{\Gamma_{\text{eff}}/2 + i(\Delta + \Omega_m)} - \frac{1}{\Gamma_{\text{eff}}/2 + i(\Delta - \Omega_m)} \right), \quad (5.8)$$

where $g = g_0\sqrt{n_c}$ is the effective electromechanical coupling rate enhanced by the mean intracavity photon number of the primary mode n_c . This effect can be viewed as radiation pressure dynamical backaction [11, 125, 122] onto the *microwave* mode. This leads to a change in the reflection from the microwave cavity, due to a modification of its

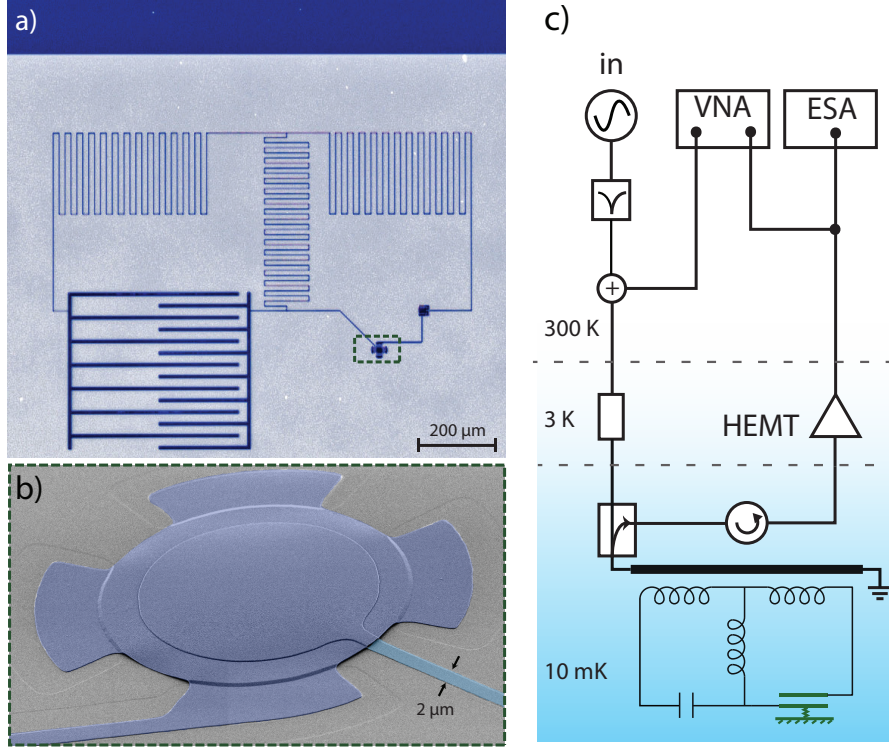


Figure 5.5 – **Device, experimental setup, and characterization of the multi-mode electromechanical circuit.** **a)** Inverted-colour optical micrograph of the circuit consisting of two coupled LC resonators, one having a mechanically compliant capacitor. Blue regions show aluminium and grey regions that are the exposed sapphire substrate. **b)** False-colour scanning electron micrograph of the mechanically compliant drum capacitor. **c)** Simplified schematics of the measurement setup with the circuit. The (multiple) input lines are filtered and attenuated at various stages before reaching the device mounted in a dilution refrigerator. Both the coherent and the spectral response can be measured. Figure also appears in [50].

susceptibility (defined as $\hat{a}_{\text{out}}(\omega) = S_{11}(\omega)\hat{a}_{\text{in}}(\omega)$, where $\hat{a}_{\text{in,out}}(\omega)$ are Fourier domain operators associated with the input and output fields. The susceptibility becomes

$$S_{11}(\omega) = \frac{\kappa_0 + \kappa_{\text{om}} - \kappa_{\text{ex}} - i2(\omega - \omega'_c)}{\kappa_0 + \kappa_{\text{om}} + \kappa_{\text{ex}} - i2(\omega - \omega'_c)}, \quad (5.9)$$

where κ_0 is the internal loss of the primary mode and $\omega'_c = \omega_c + \delta\omega_{\text{om}}$ the modified resonance frequency.

The engineered reservoir therefore supplies a way to tailor the susceptibility of the primary electromagnetic mode, which we can directly probe using a coherent response measurement. First, we fix the detuning to either motional sideband of the primary mode, and measure $S_{11}(\omega)$ while the power is varied. For this choice of detuning (i.e. $\Delta = \mp\Omega_{\text{m}}$), we have $\delta\omega_{\text{om}} = 0$ (neglecting the term $\propto \Gamma_{\text{eff}}^2/\Omega_{\text{m}}$) and the change in the

5.5. Experimental observation of dynamical backaction on microwave light

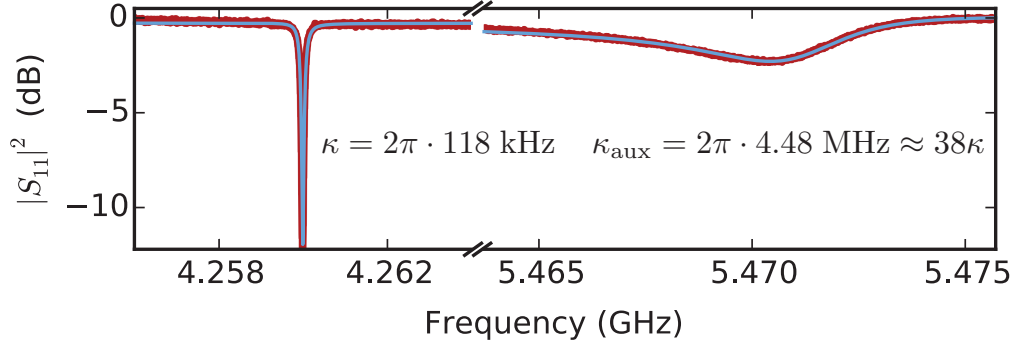


Figure 5.6 – **Linear response measurement of the hybrid-mode electromechanical device showing the bright and dark modes.** The response reveals the symmetric (bright, used as the auxiliary) and anti-symmetric (dark, used as the primary) microwave modes with Figure also appears in [50].

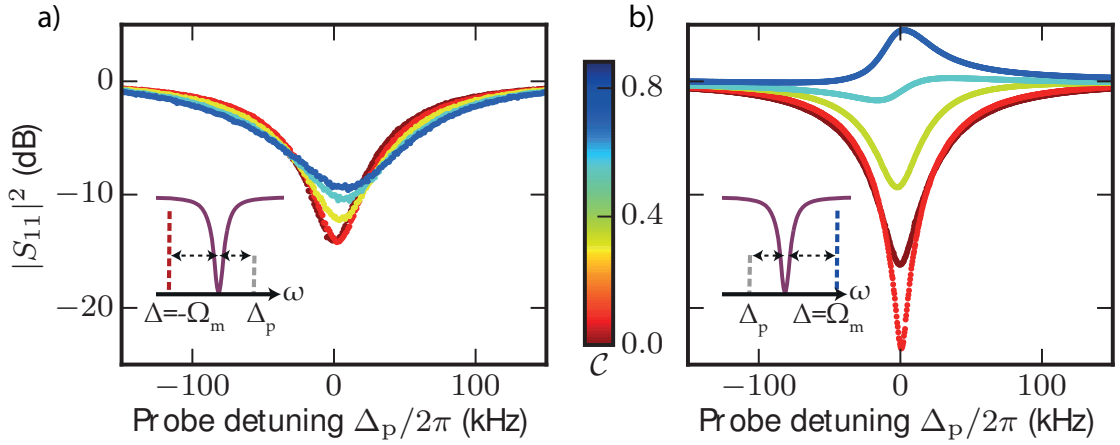


Figure 5.7 – **Coherent response of the microwave cavity coupled to the mechanical reservoir.** The modification of the susceptibility of the microwave cavity when a pump tone is placed on the lower (left panel) and upper (right panel) motional sideband of the primary mode (i.e. $\Delta = \mp\Omega_m$ cf. inset), shown for various values of the multiphoton cooperativity ($C = 1$ corresponds to a mean intracavity photon number of $n_c \approx 5 \cdot 10^6$). The slight shift of the peaks comes from the finite sideband resolution parameter of the auxiliary mode ($\Omega_m/\kappa_{\text{aux}}$). Figure also appears in [50].

microwave decay rate simplifies to

$$\kappa_{\text{om}} = \pm C\kappa, \quad (5.10)$$

directly proportional to the cooperativity $C = 4g^2/(\kappa\Gamma_{\text{eff}})$. fig. 5.7a, b show the linear response for a tone on the lower and uppersideband for various pump powers, respectively.

Chapter 5. A quantum reservoir for microwave light using a mechanical oscillator

The width of the resonance, corresponding to the cavity decay rate, increases (for $\Delta = -\Omega_m$) or decreases (for $\Delta = +\Omega_m$) linearly with \mathcal{C} , accordingly. Strikingly, the depth of reflection on resonance $|S_{11}(\omega_c)|^2$ varies significantly to reflect this change (fig. 5.8). The effective *internal* loss of the cavity $\kappa_0 + \kappa_{om}$ can be tuned on demand by changing the coupling to the dissipative reservoir via the pump tone. While the

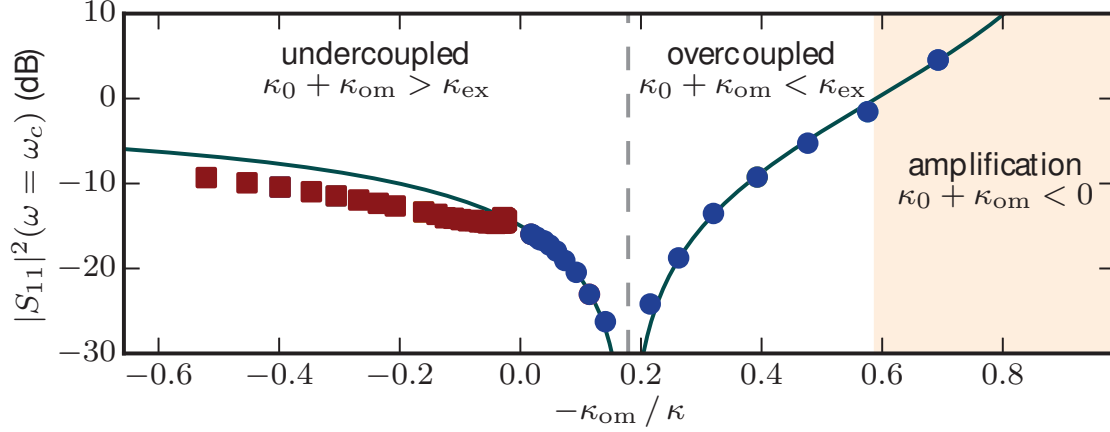


Figure 5.8 – **Modification of the microwave susceptibility on resonance.** The depth of the resonance ($|S_{11}(\omega_c)|^2$) changes depending on the effective internal losses $\kappa_0 + \kappa_{om}$. Measurements with a pump on the lower and upper sideband ($\Delta = -\Omega_m$ for the red squares and $\Delta = +\Omega_m$ for the blue circles), and a theoretical fit are shown. The cavity is originally undercoupled. When pumped on the upper motional sideband, it first becomes critically coupled, then overcoupled as the power of the pump tone is increased. For $\kappa_0 + \kappa_{om} < 0$, there is a net gain and the electromechanical system acts as a phase-preserving microwave amplifier. Figure also appears in [50].

microwave cavity is initially undercoupled ($\kappa_{ex} < \kappa_0$), pumping on the uppersideband reduces the effective internal loss and increases the depth on resonance until the cavity becomes critically coupled (the effective internal loss matches the external coupling, i.e. $\kappa_0 + \kappa_{om} = \kappa_{ex}$). Increasing the power further, the cavity becomes overcoupled ($\kappa_0 + \kappa_{om} < \kappa_{ex}$) and resonant reflection increases again. When $\kappa_0 + \kappa_{om}$ becomes negative, there is net internal gain: the absorptive feature in the cavity reflection becomes a peak, indicating amplification of the reflected microwave signal. By pumping on the lower sideband ($\Delta = -\Omega_m$), extra damping is introduced and the resonance becomes increasingly undercoupled. The mechanical mode provides a cold, dissipative bath for the microwave resonator, down-converting the cavity photons to the pump. In fig. 5.8 we plot the resonant reflection and observe good agreement with the expected dependence according to eq. (5.9). For the data corresponding to the pump tuned to the lower motional sideband ($\Delta = -\Omega_m$), the depth of the resonance is systematically lower than expected, due to a decrease in the intrinsic microwave cavity loss in the presence of a

5.5. Experimental observation of dynamical backaction on microwave light

strong pump [126]. In fig. 5.9a, b, we keep the pump power constant and sweep the detuning Δ , to measure the mechanical spring and damping effects. For the frequency

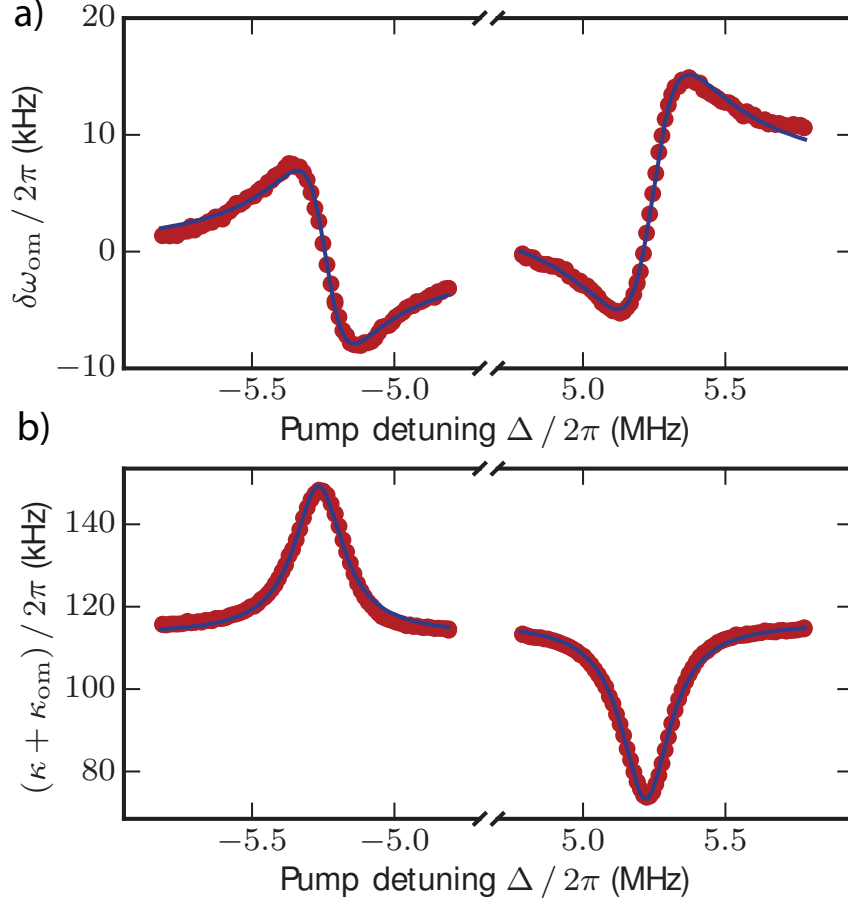


Figure 5.9 – **The mechanical spring effect.** Using a fixed pump power, the detuning Δ of the pump tone is swept and the change in the microwave resonance frequency (shown in panel **a**) and decay rate is recorded (shown in panel **b**). The theoretical fit corresponds to eq. (5.7), showing good agreement with the experimental data for both **a**) and **b**). Figure also appears in [50].

shift $\delta\omega_{\text{om}}$, intrinsic non-linearities redshift the resonance frequency in an asymmetric fashion, providing a different background for the red and blue sidebands. The spring effect agrees well with the prediction from eq. (5.7) when the two sidebands are fitted independently with different constant offsets. We note that the mechanical spring effect as a function of detuning has the opposite parity compared to the better known case of the optical spring effect [100].

Chapter 5. A quantum reservoir for microwave light using a mechanical oscillator

5.5.1 Maser action and amplification

Now we turn to the demonstration of the cold nature of the dissipative mechanical reservoir by studying the noise properties of the system. To this end, we fix the microwave drive to the uppersideband ($\Delta = +\Omega_m$) and study the regime where the pump introduces net gain in the microwave cavity ($\kappa_0 + \kappa_{om} < 0$). We use a different (second) device for this analysis, with optimized properties, due to higher coupling strength ($g_0 = 2\pi \cdot (106, 79)$ Hz for the primary and auxiliary modes, respectively) and the primary mode being overcoupled ($\kappa_{ex}/\kappa = 0.76$), with the other parameters summarized in table 5.2.

| Parameter | Symbol | Value |
|--|---------------------|---------------------------|
| Resonance frequency (primary, dark mode) | ω_c | $2\pi \cdot 4.13$ GHz |
| Total decay rate (primary, dark mode) | κ | $2\pi \cdot 197$ kHz |
| Internal decay rate (primary, dark mode) | κ_0 | $2\pi \cdot 47$ kHz |
| External coupling rate (primary, dark mode) | κ_{ex} | $2\pi \cdot 150$ kHz |
| Resonance frequency (auxiliary, bright mode) | ω_{aux} | $2\pi \cdot 5.24$ GHz |
| Total decay rate (auxiliary, bright mode) | κ_{aux} | $2\pi \cdot 3322$ kHz |
| Internal decay rate (auxiliary, bright mode) | κ_{aux}^0 | $2\pi \cdot 250$ kHz |
| External coupling rate (auxiliary, bright mode) | κ_{aux}^{ex} | $2\pi \cdot 3072$ kHz |
| Intermode coupling strength ($\approx \omega_{aux} - \omega_c /2$) | J | $2\pi \cdot 0.56$ GHz |
| Resonance frequency of mechanical mode | Ω_m | $2\pi \cdot 6.35$ MHz |
| Decay rate of the mechanical mode | Γ_m | $2\pi \cdot 100$ Hz |
| Effective decay rate of mechanical mode in the RDR | Γ_{eff} | $2\pi \cdot 400$ kHz |
| Vacuum electromechanical coupling strength (primary and auxiliary mode) | g_0, g_0^{aux} | $2\pi \cdot (106, 79)$ Hz |

Table 5.2 – **Summary of the most important experimental parameters to demonstrate masing and low-noise microwave amplification with a dissipative reservoir, device 2.** This was used to obtain the results shown in section 5.5.1, section 5.5.2 and section 5.6. The main improvement compared to device 1 is the optomechanical coupling strength, so that the mechanical reservoir can be prepared with lower pump powers.

In fig. 5.10a, the emitted noise spectra of the microwave cavity are shown for different pump powers. The measured power spectrum is rescaled to the symmetrized cavity output field spectrum [127] $\bar{S}_{aa}(\omega)$, defined as

$$\bar{S}_{aa}(\omega) = \frac{1}{2} \int_{-\infty}^{\infty} dt e^{i\omega t} \left\langle \delta \hat{a}_{out}^\dagger(t) \delta \hat{a}_{out}(0) + \delta \hat{a}_{out}(0) \delta \hat{a}_{out}^\dagger(t) \right\rangle, \quad (5.11)$$

in units of photons per second (i.e. flux) per unit bandwidth, using the noise temperature of the HEMT as an absolute noise reference (as further elaborated below in section 5.7).

5.5. Experimental observation of dynamical backaction on microwave light

As the pump compensates for the losses, the width of the emitted noise spectrum,

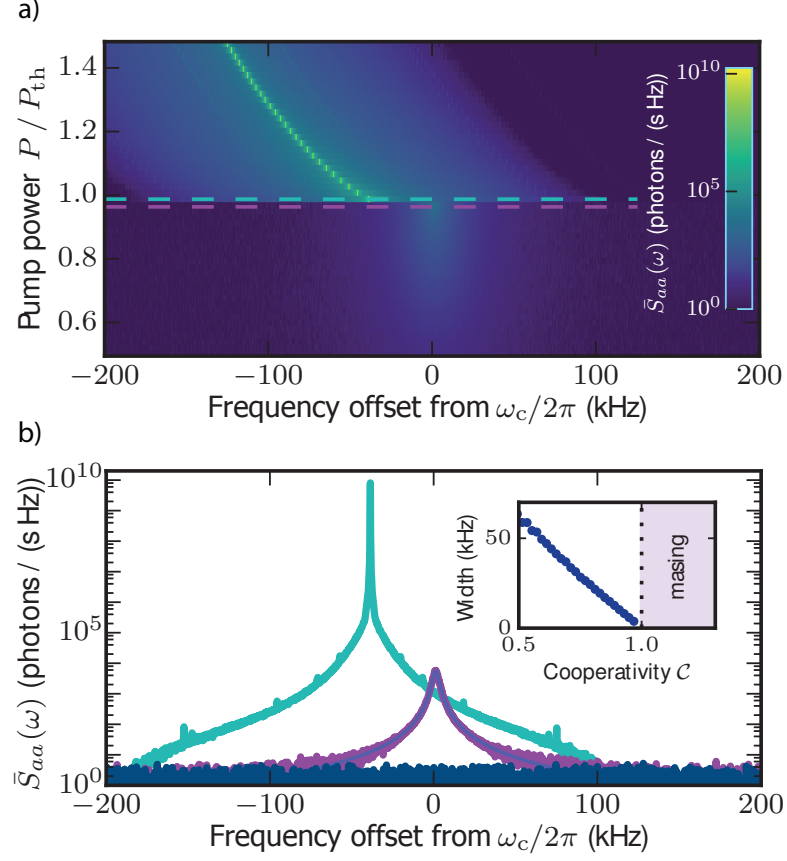


Figure 5.10 – **Amplified vacuum fluctuations and parametric instability of the microwave mode (masing).** **a).** Noise spectrum of the cavity emission as a function of the power of a pump on the upper motional sideband. The spectrum is measured in quanta using the HEMT amplifier for calibration. Above a certain threshold power P_{th} , the microwave mode undergoes self-sustained oscillations, characteristic to masing. The vertical axis is normalized by the pump power at masing threshold P_{th} , equivalent to the cooperativity $\mathcal{C} = P/P_{\text{th}}$ below threshold. **b).** Two examples of emission from the microwave mode at the input of the HEMT, below and above masing threshold (line cuts of **a**), as well as a reference measurement of the background without the pump (dark blue). The inset shows the emission linewidth narrowing below threshold. In this regime, noise emission is composed of amplified vacuum and thermal fluctuations, described by eq. (5.12). The analysis reveals that amplified vacuum noise amounts to 60% of the total, below the instability threshold.

Figure also appears in [50].

corresponding to the cavity linewidth $\kappa_{\text{eff}} = (1 - \mathcal{C})\kappa$, decreases linearly with the pump power towards zero (at unity cooperativity $\mathcal{C} = 1$), cf. inset of fig. 5.10b. In this below-threshold regime, the peak photon flux spectral density emitted from the cavity increases with power, as the vacuum noise and the residual thermal microwave noise (consisting in

Chapter 5. A quantum reservoir for microwave light using a mechanical oscillator

both a finite residual occupancy n_{eff} of the dissipative mechanical reservoir and a finite thermal microwave occupation of the cavity n_{cav}) are amplified according to

$$\bar{S}_{aa}(\omega) = \kappa_{\text{ex}} \frac{(\kappa_{\text{ex}} - \kappa_{\text{eff}})\frac{1}{2} + \mathcal{C}\kappa(n_{\text{eff}} + \frac{1}{2}) + \kappa_0(n_{\text{cav}} + \frac{1}{2})}{(\frac{\kappa_{\text{eff}}}{2})^2 + (\omega - \omega_c)^2} \quad (5.12)$$

where the thermal input noise is neglected and only the amplified noise is considered. We analyze the noise properties of the device in detail below when considering amplification and added noise. We find the residual thermal occupation of the dissipative reservoir to be $n_{\text{eff}} = 0.66$, when neglecting n_{cav} . eq. (5.12) then implies that 60% of the emitted noise from the cavity is amplified vacuum fluctuations, when $\mathcal{C} \rightarrow 1$.

For $\mathcal{C} = 1$ and greater pump powers, the microwave mode undergoes self-sustained oscillations. This regime leads to a parametric instability and electromechanical maser action of the microwave mode, via stimulated emission of microwave photons into the microwave cavity. The salient features of maser action are a transition from sub- to above-threshold masing, as well as linewidth narrowing. These observations are analogues to the radiation-pressure-induced parametric instability of a mechanical mode in the normal optomechanical regime ($\kappa \gg \Gamma_m$) [125, 128, 12, 129]. In the experiments a clear threshold behavior, characteristic of masing, is demonstrated when the emitted noise abruptly increases in strength at $\mathcal{C} = 1$ (cf. fig. 5.10b). Such microwave lasing in superconducting circuits has previously been demonstrated using a single artificial atom [130]. Due to the strong photon population generated by masing, nonlinearities of the cavities red-shift the frequency of emission. This clearly distinguishes masing from the mechanical parametric instability (i.e. phonon lasing [129]) in the normal optomechanical regime, as in the latter case the emission does not follow the cavity but has a constant detuning of $-\Omega_m$ with respect to the pump.

Below the masing threshold, the microwave mode coupled to the dissipative bath acts as a phase-insensitive parametric amplifier [131, 106] for incoming signals. For $\kappa_0 + \kappa_{\text{om}} < 0$, there is a net internal gain and the susceptibility $S_{11}(\omega)$ develops a peak, implying that reflection is larger than input for signals within the resonance bandwidth (in-band). The power gain of the amplifier is defined as the resonance peak height above the background, given by

$$\mathcal{G}(\omega_c) = |S_{11}(\omega_c)|^2 = \left| \frac{(2\frac{\kappa_{\text{ex}}}{\kappa} - 1) + \mathcal{C}}{1 - \mathcal{C}} \right|^2. \quad (5.13)$$

The bandwidth of the amplifier is the linewidth of the microwave resonance, given by $\kappa_{\text{eff}} = (1 - \mathcal{C})\kappa$. In order to measure the gain, bandwidth and noise properties of the amplifier, we inject, in addition to the pump tone on the upper sideband ($\Delta = +\Omega_m$), a weak signal tone (swept around the cavity resonance) and measure the reflected signal as a function of the pump tone power. With increasing pump power, a narrowing of

5.5. Experimental observation of dynamical backaction on microwave light

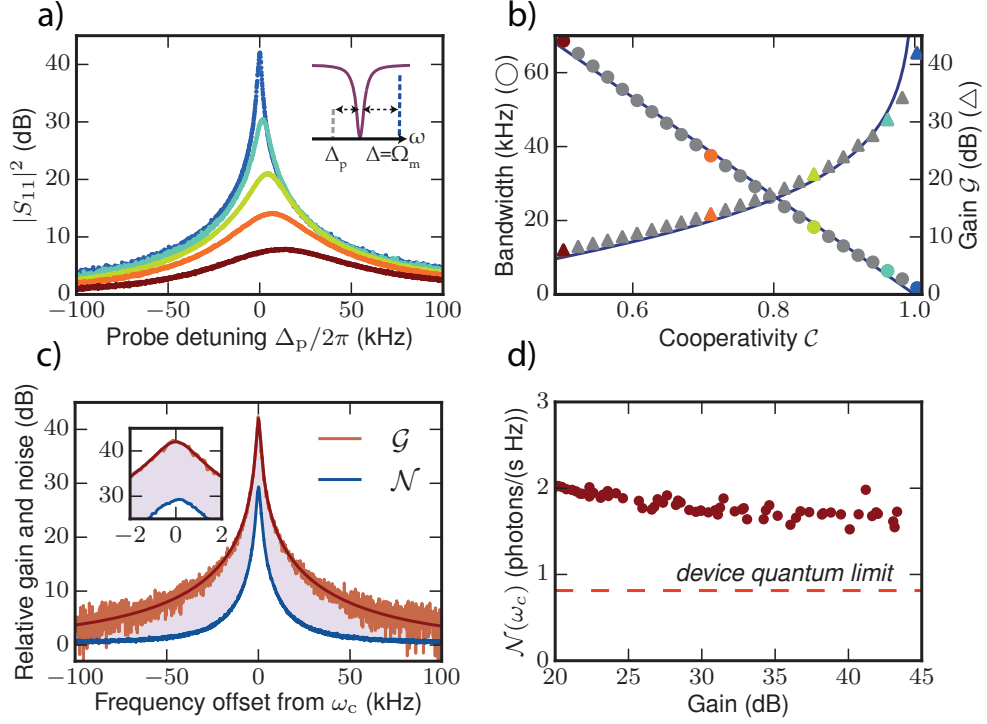


Figure 5.11 – **Near-quantum-limited phase-preserving amplification with the dissipative mechanical reservoir.** **a)** Linear response of the cavity, with increasing powers of the pump on the upper sideband from red to blue. **b).** Power gain (triangles) and bandwidth (circles) of the amplifier extracted from a fit of the linear response, as a function of the cooperativity of the pump on the upper sideband. The colored points correspond to the curves on panel **a)**. **c).** Relative gain and noise of the amplifier, sharing the same baseline. The difference from noise to gain corresponds to over 12 dB of apparent signal-to-noise ratio improvement of our device over the HEMT, from which the insertion loss between the HEMT and the device (measured separately to be 1.6 dB) must be subtracted to infer the real improvement. **d).** Added noise of the amplification referred to the input, expressed in quanta. The total added noise in the high-gain limit amounts to 1.68 ± 0.02 quanta, corroborated by an independent optomechanical calibration technique (further details in section 5.6). This is only 0.87 quanta above the device quantum limit n_{DQL} , defined in eq. (5.16).

Figure also appears in [50].

the cavity bandwidth (fig. 5.11a) is observed, as well as an increase in the power of the reflected signal (i.e. gain). By fitting the reflected power as a function of detuning, the gain and bandwidth as a function of cooperativity are extracted, and found to be in good agreement with the theoretical predictions given by eq. (5.13) (fig. 5.11b). The observed gain exceeds 42 dB.

5.5.2 Injection locking

We now demonstrate the locking of our maser with a weak injected tone. Injection locking is a synchronization phenomenon of lasers and masers [132], and has been demonstrated in many systems, including recently in a trapped-ion phonon laser [133], a quantum cascade laser [134], a quantum-dots maser [135] as well as an AC Josephson junction maser [136]. A weak tone of frequency ω_{inj} close to the maser emission frequency ω_{mas} will compete for gain with it in a way that effectively couples the two oscillations and permits synchronization. The phenomenon is generally described by the Adler equation [137]

$$\frac{d\phi}{dt} + (\omega_{\text{inj}} - \omega_{\text{mas}}) = -\frac{1}{2}\Delta\omega_{\text{inj}} \sin(\phi) \quad (5.14)$$

which models the dynamics of the relative phase ϕ of the two oscillations. If the injected tone falls within a locking range of width $\Delta\omega_{\text{inj}} = 2\kappa_{\text{ex}}\sqrt{\alpha P_{\text{inj}}/P_{\text{mas}}}$ centered around the masing frequency ω_{mas} , the two tones lock and the phase difference ϕ becomes constant. This range depends on the ratio between the injected tone power P_{inj} , attenuated by factor α at the input of the cavity, and the maser emission power P_{mas} . Outside this range, the Adler equation predicts that the maser frequency is pulled towards the injected tone and that distortion sidebands appear due to the two tones beating and the intrinsic nonlinearity [137]. We first study this phenomenon by placing the injected tone 5 kHz away from the maser and monitoring the output spectrum while the injected power P_{inj} is varied (fig. 5.12 a). The maser emission is pulled towards the injected tone and finally locks at an injected power threshold corresponding here to about -30 dBm. As the two tones become comparable in strength, distortion sidebands from the beating increase in amplitude. In the locked region, the noise surrounding the peak is considerably suppressed compared to the free-running case and the frequency jitter (originating from frequency instability of the cavity and the mechanical mode) is eliminated (fig. 5.12 b). We proceed to measure the locking range $\Delta\omega_{\text{inj}}$, by fixing the injected power P_{inj} and sweeping its frequency ω_{inj} across the maser frequency (fig. 5.12 c). When the frequency difference is below $\Delta\omega_{\text{inj}}$, the two tones lock. The noise around the peak is suppressed and the frequency jitter of the maser ceases. Repeating the measurement at different injected powers P_{inj} , the locking range is shown to obey the expected scaling law $\Delta\omega_{\text{inj}} \propto \sqrt{P_{\text{inj}}}$ (fig. 5.12d). Finally, as an inset, the limit points of locking are shown as a function of power, drawing the so-called Arnold tongue [138]. The asymmetric shape is due to drift of the masing frequency ω_{mas} during the measurement, which do not affect the locking range $\Delta\omega_{\text{inj}}$.

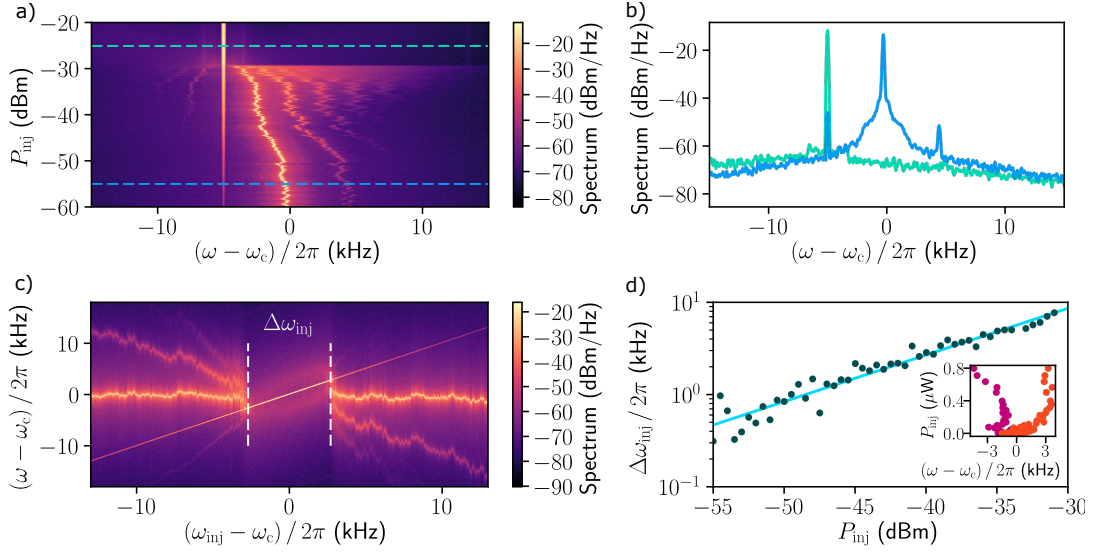


Figure 5.12 – **Injection locking of the maser based on dynamical backaction.**

a) Output spectrum of the maser, as the power P_{inj} of an injected tone detuned 5 kHz to the red is increased. The power is measured at the output of the corresponding microwave source. Above a threshold power of about -30 dBm, the maser locks to the tone, considerably suppressing the noise and eliminating the frequency jitter present in the free-running case. The intrinsic nonlinearity results in distortion sidebands from the two tones beating below threshold. **b)** Spectra corresponding to cuts of A along the dashed lines, below and above the locking threshold. **c)** Output spectrum of the maser as the frequency ω_{inj} of a weak tone of constant power $P_{\text{inj}} = -40$ dBm is swept across the free-running maser frequency ω_{mas} . The locking range $\Delta\omega_{\text{inj}}$, wherein the two oscillations are frequency locked, is highlighted. **d)** The locking range $\Delta\omega_{\text{inj}}$ as a function of the injected tone power P_{inj} . A fit on the logarithmic scale gives a slope of 0.51, confirming the expected scaling $\Delta\omega_{\text{inj}} \propto \sqrt{P_{\text{inj}}}$. The inset depicts the actual limiting points of the locking range as a function of tone power P_{inj} , illustrating the Arnold tongue of the system.

Figure also appears in [51].

5.6 Near-quantum-limited amplification

Next, we study the added noise of the dissipative amplification process. The added noise \mathcal{N} , as referred to the input of the amplifier, is given by the noise output of eq. (5.12) without the input noise and divided by the gain $\mathcal{G}(\omega_c)$. On resonance, it is found to be (cf. Appendix C)

$$\mathcal{N}(\omega_c) = \frac{4\mathcal{C} \frac{\kappa_{\text{ex}}}{\kappa} (n_{\text{eff}} + \frac{1}{2}) + 4 \frac{\kappa_{\text{ex}} \kappa_0}{\kappa^2} (n_{\text{cav}} + \frac{1}{2})}{(\mathcal{C} - 1 + \frac{2\kappa_{\text{ex}}}{\kappa})^2}, \quad (5.15)$$

Chapter 5. A quantum reservoir for microwave light using a mechanical oscillator

which, in the high gain limit ($\mathcal{C} \rightarrow 1$), simplifies to $\mathcal{N}(\omega_c) \rightarrow \frac{\kappa_0}{\kappa_{\text{ex}}}(n_{\text{cav}} + \frac{1}{2}) + \frac{\kappa}{\kappa_{\text{ex}}}(n_{\text{eff}} + \frac{1}{2})$. This quantity can be measured by recording the improvement of the signal-to-noise ratio (SNR) of amplification in and out of the bandwidth of our device. This directly compares the noise performance of our device with the commercial HEMT amplifier, which is used as a calibrated noise source (the noise temperature of the HEMT is measured separately at ω_c and found to be 3.95 ± 0.02 K, corresponding to 20.0 ± 0.1 quanta (cf. section 4.2.3). In fig. 5.11c, the gain of the device is compared to the noise output of the chain, normalized to the HEMT noise background. This calibration was corroborated by a second, *independent* calibration technique, which uses the scattered power in the motional sideband in conjunction with the knowledge of the intracavity photon number and g_0 as described in more details in section 4.3.4). The relative gain of the signal exceeds the relative noise by over 12 dB. From this apparent SNR improvement, one must subtract the insertion loss of the components between the device and the HEMT, measured independently at 77 K to be 1.6 dB. The analysis reveals therefore that the optomechanical amplifier provides more than 10 dB of improvement over the SNR of the HEMT.

To illustrate more intuitively this SNR improvement, fig. 5.13 shows the measurement of a signal in and out of band of the amplifier. This measurement was done on a previous chip and a slightly different measurement setup in terms of filtering and the SNR improvement was only 2 dB.

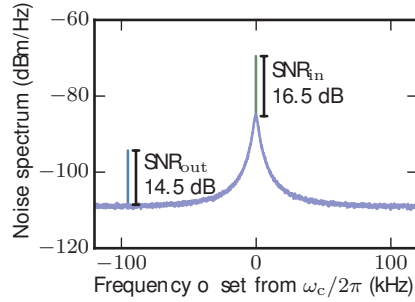


Figure 5.13 – **Improvement of the signal-to-noise ratio over the HEMT amplifier in and out of band.** Noise spectrum of the amplifier measured with a weak probe in and out of bandwidth, with the SNR highlighted for the two cases. This measurement was done using a previous sample and a slightly different setup in terms of filtering, with which the SNR improvement was measured to be about 2 dB only.

The inferred added noise on resonance is shown as a function of gain in fig. 5.11d; in the high-gain limit, it is a constant value of $\mathcal{N}(\omega_c) = 1.68 \pm 0.02$ quanta per second per unit bandwidth (with the uncertainty given by statistical fluctuations). Using eq. (5.15) and assuming $n_{\text{cav}} = 0$, the effective occupation of the dissipative reservoir is found to be $n_{\text{eff}} = 0.66$. However, the strong cooling pump increases the temperature of the cavity

thermal bath to an occupation $n_{\text{cav}} = 1.03$, obtained from measuring the emitted thermal noise of the microwave cavity. (see below in section 5.7). Taking the residual cavity thermal noise into account, the estimate for the mechanical occupation is reduced to $n_{\text{eff}} = 0.41$. This demonstrates that the dissipative mechanical reservoir constitutes a quantum resource. We note that even in the case when all the thermal noise sources are reduced to zero (i.e. $n_{\text{eff}} = n_{\text{cav}} = 0$), the added noise of the amplifier is

$$n_{\text{DQL}} = \frac{1}{2} + \frac{\kappa_0}{\kappa_{\text{ex}}}, \quad (5.16)$$

which, we call the device quantum limit and deviates from $1/2$ due to the finite internal dissipation rate κ_0 . For the present system the device quantum limit amounts to 0.81 quanta for the coupling ratio of $\kappa_{\text{ex}}/\kappa = 0.76$, which is only 0.87 quanta below the added noise we measure. Compared to other electromechanical phase-preserving amplifiers [35, 139], the preparation of an engineered cold, dissipative mechanical bath enables lower added noise. It is interesting to compare the present amplifier scheme, relying on a dissipative reservoir, to the microwave parametric amplifiers as used in circuit QED. In the latter case, typically both idler and signal are resonant with one or more microwave cavities [140, 141, 142]. As gain increases, this leads to a simultaneous increase in both the signal and idler mode population. In contrast, while the present amplifier scheme uses a parametric interaction as well, the large dissipation rate for the (mechanical) idler mode only leads to the generation of a signal photon (microwave field), suppressing the idler, a situation akin to a Raman-type interaction found in nonlinear optics [143].

5.7 Notes on noise calibrations

Output spectrum ($\bar{S}_{aa}(\omega)$)

To calibrate the output spectrum of our device $\bar{S}_{aa}(\omega)$ defined in eq. (5.11), we use the equivalent input noise of the HEMT as a calibrated reference level. The calibration of the HEMT amplifier is described in section 4.2.3. We compare the measured noise emitted by our device on resonance to the noise background, which are given by

$$N_{\text{device}} = \mathcal{G}_{\text{chain}}(\alpha \bar{S}_{aa}(\omega) + n_{\text{HEMT}}) \quad (5.17)$$

$$N_{\text{BG}} = \mathcal{G}_{\text{chain}} n_{\text{HEMT}} \quad (5.18)$$

where $\mathcal{G}_{\text{chain}}$ is the unknown total gain from the input of the HEMT to the measurement at room temperature, α is attenuation on the line between the device (DUT) and the HEMT, and n_{HEMT} the equivalent input noise of the HEMT. Since the HEMT noise dominates over other sources of noise in the chain, we can neglect them. The output

Chapter 5. A quantum reservoir for microwave light using a mechanical oscillator

spectrum can then be extracted as

$$\bar{S}_{aa}(\omega) = \frac{n_{\text{HEMT}}}{\alpha} \left(\frac{N_{\text{device}}}{N_{\text{BG}}} - 1 \right) \quad (5.19)$$

in terms of the measured noises, if n_{HEMT} and α can be calibrated.

Both α and n_{HEMT} are determined through independent measurements. As detailed above, the noise of the HEMT is calibrated with a temperature sweep. At 4.13 GHz, the frequency of our noise measurement, the HEMT noise temperature is 3.95 ± 0.02 K. This corresponds to $n_{\text{HEMT}} = 20.0 \pm 0.1$ photons per second in a bandwidth of 1 Hz. The dominant source of uncertainty comes from the attenuation α , as it is not possible to independently extract its value at base temperature. In a separate experiment, we measure at 77 K the attenuation of the components between the device (DUT) and the HEMT to be 1.6 dB. This is an upper bound of attenuation, as all passive components and cables are expected to show reduced attenuation at the lower base temperature. We therefore have an upper bound value for $\bar{S}_{aa}(\omega)$, providing a worst-case scenario value for the noise properties of the device.

Independent noise calibration of HEMT based on the mechanical sideband

In section 4.3.4 we describe the thermalization of the mechanics and the calibration procedure for g_0 in detail. The same data can be used for absolute power calibration; we use this as an *independent* way to measure the HEMT noise background, and therefore confirm the validity of the noise calibration done above. We recall that the integrated power in the (Lorentzian) mechanical sideband is

$$P_{\text{SB}} = \hbar\omega \frac{\kappa_{\text{ex}}}{\Omega_{\text{m}}^2 + (\kappa/2)^2} g_0^2 n_c n_{\text{m}}. \quad (5.20)$$

Here, provided that the intracavity photon number n_c is known, the power of the sideband at the device can be predicted and used as an absolute scale to measure the noise background. This provides an independent measure of HEMT noise divided by the attenuation $\frac{n_{\text{HEMT}}}{\alpha}$: the equivalent noise of the HEMT at the device output.

To measure the cavity occupation n_c , a secondary measurement is performed and OMIT is measured with a probe of the same power now on the red sideband of the cavity resonance. The width of the mechanics is fitted to obtain

$$\Gamma_{\text{eff}} = \Gamma_{\text{m}} + 4 \frac{g_0^2 n_{c0}}{\kappa} = \Gamma_{\text{m}} + 4 \frac{g_0^2}{\kappa} n_c \frac{(\kappa/2)^2}{\Omega_{\text{m}}^2 + (\kappa/2)^2} \quad (5.21)$$

where n_c is the intracavity photon number for the resonant probe and n_{c0} is the intracavity

photon number for the red-detuned probe used for OMIT. With this inferred intracavity photon number n_c , the absolute rate of scattered photons of the sideband can be predicted as

$$\frac{P_{\text{SB}}}{\hbar\omega} = \frac{\kappa_{\text{ex}}}{\Omega_{\text{m}}^2 + (\kappa/2)^2} g_0^2 n_c n_{\text{m}} \quad (5.22)$$

in units of photons per second. By rescaling the measured sideband to the predicted power at the device output, the background is scaled to the equivalent noise at the device input. We perform this measurement with the main mode, at temperatures above thermalization point, we obtain $\frac{n_{\text{HEMT}}}{\alpha} = 42 \pm 4$ photons / (s Hz), with the uncertainty given by the statistical fluctuations of measurements. We use a value of 31.5 ± 0.2 photons / (s Hz), obtained from the measured HEMT noise temperature of 4.27 ± 0.03 K (at 4.08 GHz frequency) and 1.6 dB of estimated attenuation. A note on the units: since the amplifier operates with traveling waves, the number of quanta in the input mode are related to the input power per bandwidth; therefore, the unit of noise is the equivalent flux of quanta per unit bandwidth, i.e. photons/(s Hz). This value is different than for the measurement presented above (3.95 K at 4.13 GHz), as the cavity resonance had drifted between the two measurements. The discrepancy of 1.4 dB between the two calibration methods is attributed to systematics for this measurement. In particular, it is assumed that the probe on resonance and on the red sideband of the resonance is attenuated the same way in order to infer n_c , which could yield a systematic error. We stress that this represents a *fully independent* check for the validity of the calibration procedure used for noise in this experiment.

Thermal occupation of the primary microwave cavity

With strong pumps near the auxiliary cavity to damp the mechanical oscillator, heating of the primary microwave mode is observed. The dual mode structure of the device enables to characterize this noise using an out-of-loop measurement. With a cooling pump at the auxiliary mode and no pump present at the primary mode, noise emission from the primary cavity is measured. Subtracting the background of HEMT noise (measured with all pumps turned off), the emission from the cavity is shown in fig. 5.14a. A Lorentzian peak of noise is emitted from the cavity, increasing in size with pump power. We interpret this as the thermal bath of the cavity mode (n_{cav}) effectively being heated by the pump. The excess total thermal noise measured corresponds to $\frac{\kappa_{\text{ex}}\kappa_0}{\kappa} n_{\text{cav}}$ in photons per second. Fitting the Lorentzian peak to extract the total emitted photon rate, we infer the cavity thermal occupation due to spurious heating. For a power corresponding to $\Gamma_{\text{eff}}/2\pi \approx 400$ kHz, as used for the measurements with device 2, the heating corresponds to $n_{\text{cav}} \approx 1$ of thermal microwave occupation, i.e. a noise temperature of 200 mK. We note that this should be considered as a lower bound on n_{cav} when the device is operated as an amplifier, as the additional tone around the primary mode can induce more heating. This implies

Chapter 5. A quantum reservoir for microwave light using a mechanical oscillator

that the number for the effective thermal occupation of the reservoir, $n_{\text{eff}} = 0.41$ (as described in section 5.6), is in fact an upper bound.

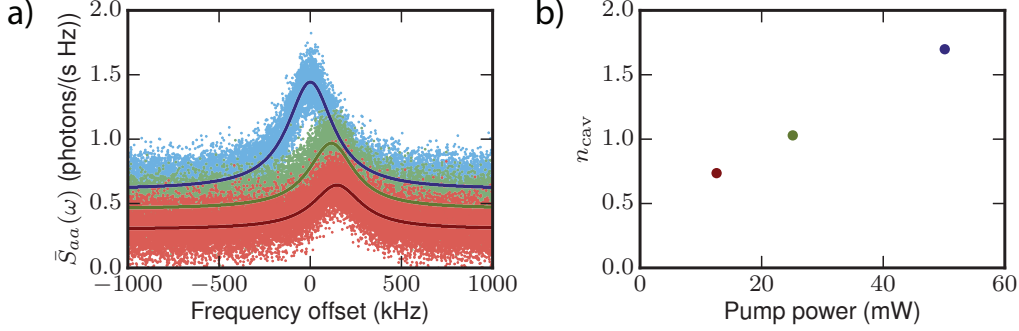


Figure 5.14 – **Thermal occupancy of the microwave cavity with respect to pump power.** **a)** Thermal noise emission from the primary cavity while a pump is applied to the red sideband of the auxiliary cavity. Increasing pump powers are shown from red to blue. The middle power (green) corresponds to $\Gamma_{\text{eff}}/2\pi \approx 400$ kHz used for the experiment in the reversed dissipation regime. **b)** Inferred cavity thermal occupation from fitting the Lorentzian peak, for the same pump powers. Figure also appears in the Supplementary Information of [50].

5.8 Conclusions

In summary, we have implemented and studied a new regime of circuit electromechanics by coupling an electromagnetic cavity mode to an engineered cold dissipative reservoir formed by a mechanical oscillator. The usual roles of the two modes are reversed, allowing for dynamical backaction on the microwave mode using the mechanical reservoir. We demonstrate the control of the internal losses of the cavity in the form of backaction-induced amplification, de-amplification, and masing of the microwave field. By performing microwave amplification close to the quantum limit, we show that the mechanical reservoir functions as a useful quantum resource.

The near-quantum-limited amplification with a mechanical reservoir extends the available quantum information manipulation toolkit, adding to the existing devices based on Josephson junctions [140, 141, 142, 144]. While the present amplifier is not frequency-tunable, recent advances in circuit electromechanics have demonstrated such functionality [145]. The observed reservoir-mediated microwave damping may allow to remove residual thermal occupancy from the microwave cavity, akin to cooling schemes developed in circuit QED [146]. Moreover, the control over internal dissipation enables all-electromechanical tuning of the coupling of the microwave resonator to the feedline, offering the potential for an electromechanical reconfigurable network [147]. While the present scheme employs

a single pump tone, dual tone pumping would lead to the preparation of squeezed states of the microwave cavity [107]. Viewed more broadly, the realization of a cold mechanical reservoir for microwave light provides a central ingredient for novel electromechanical devices. Indeed, the circuit can be extended to multiple microwave resonators coupled to a shared mechanical reservoir and implement the dissipative cavity-cavity interactions that are at the heart of recent schemes to entangle microwave photons [104] and, combined with coherent interactions, to perform nonreciprocal microwave transmission [108]. Such nonreciprocal devices can be of use for the rapidly expanding field of circuit QED [30, 148].

6 Nonreciprocal microwave conversion using a mechanical oscillator

In this chapter we present the results on the experimental implementation of a nonreciprocal isolator based on the optomechanical interaction. The text is also presented in [52]. Parts of section 6.1 and section 6.2 also appear in [149].

6.1 Introduction and motivation

Nonreciprocal devices, such as isolators, circulators, and directional amplifiers, exhibit altered transmission characteristics if the input and output channels are interchanged. They are essential to several applications in signal processing and communication, as they protect devices from interfering signals [66]. At the heart of any such device lies an element breaking Lorentz reciprocal symmetry for electromagnetic sources [150, 151]. Such elements have included ferrite materials [152, 153, 154], magneto-optical materials [155, 156, 157, 158], optical nonlinearities [159, 160, 161], temporal modulation [162, 163, 164, 165, 166, 167], chiral atomic states [168], and physical rotation [169]. Typically, a commercial nonreciprocal microwave apparatus exploits ferrite materials and magnetic fields, which leads to a propagation-direction-dependent phase shift for different field polarizations. A significant drawback of such devices is that they are ill-suited for sensitive superconducting circuits, since their strong magnetic fields are disruptive and require heavy shielding. In recent years, the major advances in quantum superconducting circuits [170], that require isolation from noise emanating from readout electronics, have led to a significant interest in nonreciprocal devices operating at the microwave frequencies that dispense with magnetic fields and can be integrated on-chip.

As an alternative to ferrite-based nonreciprocal technologies, several approaches have been pursued towards nonreciprocal microwave chip-scale devices. Firstly, the modulation in time of the parametric couplings between modes of a network can simulate rotation about an axis, creating an artificial magnetic field [162, 166, 171, 172] rendering the

Chapter 6. Nonreciprocal microwave conversion using a mechanical oscillator

system nonreciprocal with respect to the ports. Secondly, phase matching of a parametric interaction can lead to nonreciprocity, since the signal only interacts with the pump when copropagating with it and not in the opposite direction. This causes travelling-wave amplification to be directional [172, 173, 174, 175]. Phase-matching-induced nonreciprocity can also occur in optomechanical systems [60, 176], where parity considerations for the interacting spatial modes apply [177, 178, 179]. Finally, interference in parametrically coupled multi-mode systems can be used. In these systems nonreciprocity arises due to interference between multiple coupling pathways along with dissipation in ancillary modes [180]. Here, dissipation is a key resource - though not the only requirement - to break reciprocity, as it forms a flow of energy always leaving the system, even as input and output are interchanged. It has therefore been viewed as reservoir engineering [108]. Following this approach, there have been numerous demonstrations of parametric nonreciprocal devices harnessing three-wave mixing in dc-SQUIDs or Josephson parametric converters (JPCs). A three-mode nonlinear superconducting circuit built using a dc-SQUID and two linear LC-resonators was engineered to implement a reconfigurable frequency-converting three-port circulator or directional amplifier [180, 181]. Similar functionality was achieved using a single-stage JPC [144]. Meanwhile, two coupled JPCs enabled implementation of frequency-preserving Josephson directional amplifiers [182, 183, 184] and a gyrator [185], which can easily be converted into a four-port circulator. A four-port on-chip superconducting circulator was also demonstrated using a combination of frequency conversion and delay [186], which can be viewed as a “synthetic rotation” [171].

Another class of superconducting devices that exhibit directionality is travelling-wave parametric amplifiers (TWPA) [172]. Near-quantum-limited TWPAs were realized employing nonlinearity of Josephson junctions [173, 174] and kinetic inductance [187, 188]. The TWPA gain directionality arises from phase matching of parametric interaction, since amplification occurs only when the signal is copropagating with the pump and the signal travelling in the reverse direction stays unmodified. Hence, the reverse gain of an ideal TWPA is 0 dB. Another intrinsically directional amplifier utilizes a superconducting low-inductance undulatory galvanometer (SLUG, a version of a dc-SQUID) [189] in a finite voltage state. In contrast to TWPAs, SLUG microwave amplifiers feature reverse isolation comparable to commercial isolators [190].

6.2 A canonical nonreciprocal device: the gyrator

We start by defining the scattering matrix S for a two-port device which links the incoming modes $\hat{a}_{i,\text{in}}$ to the outgoing modes $\hat{a}_{i,\text{out}}$ by

$$\begin{pmatrix} \hat{a}_{1,\text{out}} \\ \hat{a}_{2,\text{out}} \end{pmatrix} = \begin{pmatrix} S_{11} & S_{12} \\ S_{21} & S_{22} \end{pmatrix} \begin{pmatrix} \hat{a}_{1,\text{in}} \\ \hat{a}_{2,\text{in}} \end{pmatrix}. \quad (6.1)$$

A starting definition for nonreciprocity is that a device is nonreciprocal when $S_{21} \neq S_{12}$ at some Fourier frequency ω . Physically, this corresponds to a modification of the scattering process when input and output modes are interchanged.

The gyrator is a 2-port device which provides a nonreciprocal phase shift [66], as illustrated in fig. 6.1a. In one direction, it imparts a phase shift of π , while in the other direction it leaves the signal unchanged. The scattering matrix of a lossless, matched gyrator is given by

$$S_{\text{gyr}} = \begin{pmatrix} 0 & 1 \\ -1 & 0 \end{pmatrix}. \quad (6.2)$$

While the gyrator is only nonreciprocal in the phase, it can be a useful building block to construct nonreciprocal devices in amplitude. For example, an isolator can be assembled from a gyrator and additional reciprocal elements [66]. Consider a beam splitter which divides a signal in two; one part goes through a gyrator while the other propagates without any phase shift. Recombining the signals with a second beam splitter results in a 4-port device that interferes the signal nonreciprocally, as illustrated in fig. 6.2a. For a signal injected in port 1, the recombined signal after the second beam splitter interferes destructively in port 4, but constructively in port 2. In contrast, a signal injected from port 2, reaches port 3 instead of port 1, since one arm of the signal is in this case subjected to a π phase shift. To obtain a two-port isolator, two of the four ports are terminated by matched loads to absorb the unwanted signal. The scattering matrix for the remaining two ports is that of an ideal isolator,

$$S_{\text{is}} = \begin{pmatrix} 0 & 0 \\ 1 & 0 \end{pmatrix}. \quad (6.3)$$

Now we turn to the simplest optomechanical scheme which couples two electromagnetic modes, in which \hat{a}_1 and \hat{a}_2 both interact through a mechanical oscillator \hat{b} as shown in fig. 6.1b. The optomechanical coupling terms $\hbar g_{0,i} \hat{a}_i^\dagger \hat{a}_i (\hat{b} + \hat{b}^\dagger)$ ($i = 1, 2$), where $g_{0,i}$ is the vacuum coupling rate of \hat{a}_i and \hat{b} , can be linearized by two applied tones, detuned by Δ_i with respect to each cavity resonance. Focusing on the resonant case $\Delta_1 = \Delta_2 = -\Omega_m$, the frequency conversion between the two modes through mechanical

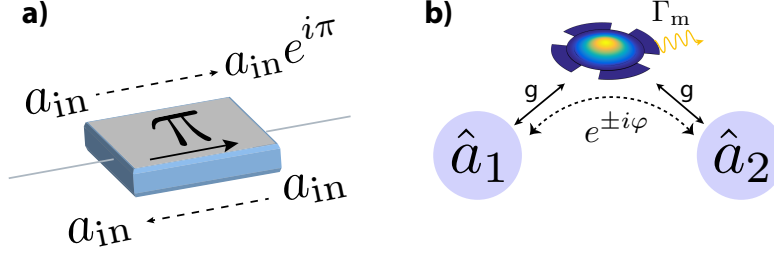


Figure 6.1 – **The gyrator and optomechanical frequency conversion.** **a)** The gyrator is a canonical nonreciprocal component. It is a two-port device, which adds a π phase shift when a wave is traveling one way but no phase shift in the reverse direction. **b)** A simple multimode optomechanical system consists of two electromagnetic modes coupled to the same mechanical oscillator. Due to the two microwave drive tones which linearize the optomechanical coupling, the conversion from \hat{a}_1 to \hat{a}_2 formally imparts a nonreciprocal phase shift, similarly to the gyrator. In the case of frequency conversion, this phase shift between tones at different frequencies is not measureable, as it depends on the reference frame.

Figure also appears, with a different color scheme, in [149].

motion is characterized by the scattering matrix elements (in the middle of the conversion frequency window) [191]

$$S_{21} = \frac{2\sqrt{\mathcal{C}_1\mathcal{C}_2}}{1 + \mathcal{C}_1 + \mathcal{C}_2} e^{i(\phi_1 - \phi_2)} \text{ and } S_{12} = S_{21}^*, \quad (6.4)$$

where κ_i is the energy decay rate of mode \hat{a}_i , and $\mathcal{C}_i = 4g_i^2/(\kappa_i\Gamma_m)$ the cooperativity with Γ_m the energy decay rate of the mechanical oscillator (for simplicity, the cavities are assumed to be overcoupled). It is interesting to see that eq. (6.4) apparently fulfills the condition $S_{21} \neq S_{12}$ for nonreciprocity, i.e. it effectively implements a gyrator. However, we note that this is only true if the two modes are at the same frequency; otherwise, a new reference frame can always be chosen such that the system is phase-reciprocal [149] (in this sense, a nonreciprocal phase shift is unphysical for frequency conversion, for which reason Ranzani and Aumentado [180] pose the stricter requirement $|S_{12}| \neq |S_{21}|$ for nonreciprocity in coupled-modes systems). Crucially, however, a change of the origin of time turns reciprocal systems phase-nonreciprocal. For example, choosing a new origin of time $(\omega_2 - \omega_1)t_0 = \pi/2$ (which turns the gyrator reciprocal) transforms the scattering matrix of a simple transmission line according to

$$S_{\text{tl}} = \begin{pmatrix} 0 & 1 \\ 1 & 0 \end{pmatrix} \longrightarrow S'_{\text{tl}} = e^{i\pi/2} \begin{pmatrix} 0 & 1 \\ -1 & 0 \end{pmatrix}, \quad (6.5)$$

which is the scattering matrix of a lossless gyrator. Gyrators and transmission lines are mapped to each other using this transformation; importantly, the combination of a gyrator

6.3. Theoretical model of nonreciprocity in the 4-mode plaquette

and a transmission line is preserved. One interpretation is that the frame-dependent nonreciprocal phase acts as a gauge symmetry, that can realize the Aharonov-Bohm effect when a loop is created [192, 193, 194]. To build an optomechanical isolator, one method is to realize two paths between \hat{a}_1 and \hat{a}_2 , one similar to a gyrator and the other to a transmission line.

Summarising the ingredients of nonreciprocity and optomechanical implementations

The gyrator-based scheme helps to summarize three sufficient ingredients to realize an isolator. Firstly, an element *breaks reciprocity* by inducing a nonreciprocal phase shift. Secondly, an additional path is introduced for signals to *interfere* such that the scattering matrix becomes asymmetric in the amplitude with $|S_{21}| \neq |S_{12}|$. Finally, *dissipation* is required for an isolator, since its scattering matrix between the two ports is non-unitary and some signals must necessarily be redirected to an external degree of freedom. The gyrator-based isolator provides a framework to understand how nonreciprocity arises in microwave optomechanical implementations.

In the optomechanical domain, there are multiple strategies to fulfill the criteria above. The first scheme, shown in fig. 6.2b, combines an optomechanical link between two electromagnetic modes \hat{a}_1 and \hat{a}_2 and a direct coherent coupling of strength J . The second scheme to realize isolation, shown in fig. 6.2c and a possible experimental implementation in the circuit domain in fig. 6.2d, uses two optomechanical conversion links with two different mechanical modes. This scheme, which we experimentally investigate, is described in detail below.

6.3 Theoretical model of nonreciprocity in the 4-mode plaquette

In contrast to previous implementation of nonreciprocal devices mentioned in the introduction, we describe a scheme to attain reconfigurable nonreciprocal transmission without a need for any direct coherent coupling between input and output modes, using purely optomechanical interactions [60, 176]. This scheme neither requires cavity-cavity interactions nor phonon-phonon coupling, which are necessary for the recently demonstrated optomechanical nonreciprocity in the optical domain [195]. Two paths of transmission between the microwave modes are established, through two distinct mechanical modes. Interference between those paths with differing phases forms the basis of the nonreciprocal process [196, 197]. In fact, due to the finite quality factor of the intermediary mechanical modes, both conversion paths between the electromagnetic modes are partly dissipative

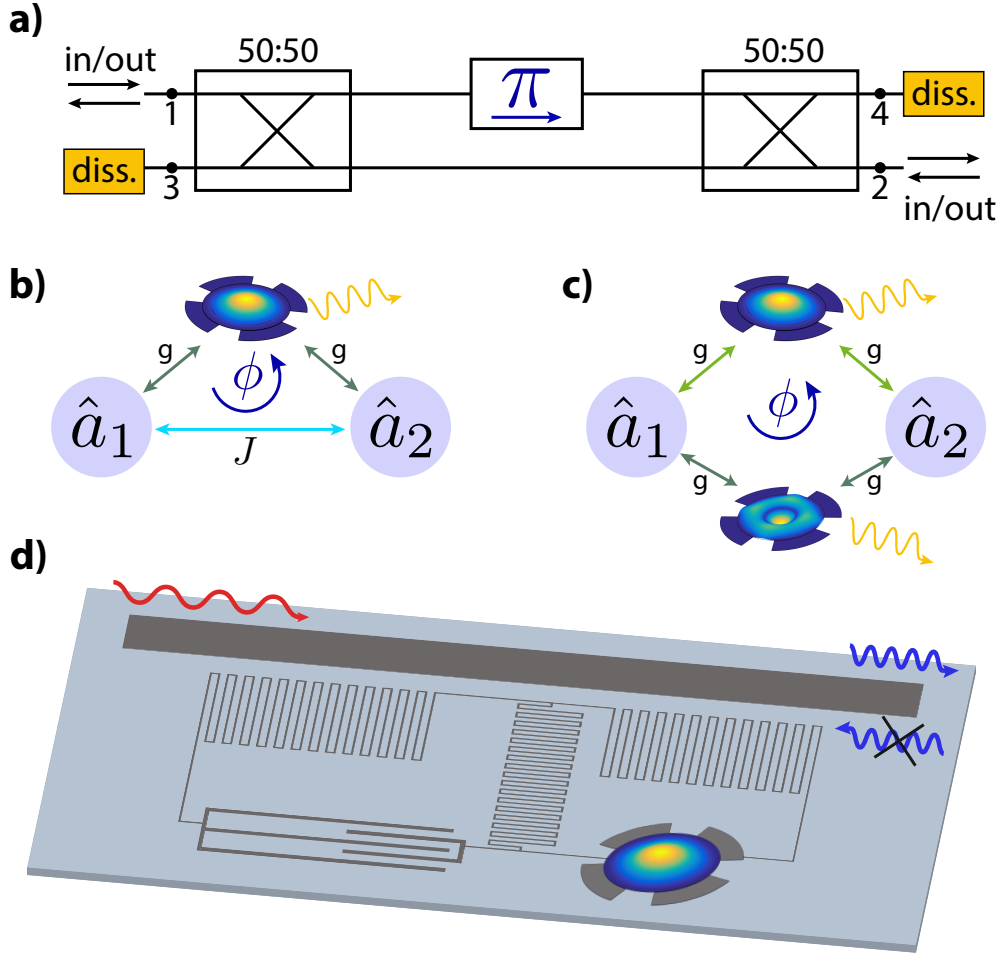


Figure 6.2 – **Gyration-based isolator and its implementation in a multimode optomechanical scheme.** **a)** An isolator can be built by combining the gyrator with other reciprocal elements. By combining the gyrator with two beam splitters and a transmission line, a four-port circulator is realized. Dissipation (provided by line terminations) eliminates the unwanted ports. **b)** The three-mode optomechanical isolator in which two electromagnetic modes have a direct coherent J -coupling, and interact through a shared mechanical mode. **c)** The four-mode optomechanical isolator, in which two electromagnetic modes interact through to different mechanical modes. **d)** In order to realize the mode structure of **c)**, a multimode electromechanical circuit can be constructed. In the example shown, the circuit supports two modes, each coupled to the motion of the top plate of a vacuum-gap capacitor that supports two vibrational modes. Figure adapted from [149].

in nature. Nonreciprocity is in this case only possible by breaking the symmetry between the two dissipative coupling pathways. We describe this framework for understanding how nonreciprocity arises in this system in detail below.

6.3. Theoretical model of nonreciprocity in the 4-mode plaquette

We first theoretically model our system to reveal how nonreciprocity arises in this picture. We consider two microwave modes (described by their annihilation operators \hat{a}_1, \hat{a}_2) having resonance frequencies $\omega_{c,1}, \omega_{c,2}$ and dissipation rates κ_1, κ_2 , which are coupled to two mechanical modes (described by the annihilation operators \hat{b}_1, \hat{b}_2) having resonance frequencies Ω_1, Ω_2 and dissipation rates $\Gamma_{m,1}, \Gamma_{m,2}$ (fig. 6.3a). The radiation-pressure-type optomechanical interaction has the form [60, 176] $g_{0,ij}\hat{a}_i^\dagger\hat{a}_i(\hat{b}_j + \hat{b}_j^\dagger)$ (in units where $\hbar = 1$), where $g_{0,ij}$ designates the vacuum optomechanical coupling strength of the i^{th} microwave mode to the j^{th} mechanical mode. Here we have assumed that the frequency separation between the two microwave modes is not resonant with any of the mechanical frequencies, suppressing cross coupling terms of the type $Ga_i^\dagger a_k b_j$. Four microwave tones are applied, close to each of the two lower sidebands of the two microwave modes, with detunings of $\Delta_{11} = \Delta_{21} = -\Omega_1 - \delta$ and $\Delta_{12} = \Delta_{22} = -\Omega_2 + \delta$ (fig. 6.4c). We linearise the Hamiltonian, neglect counter-rotating terms, and write it in a rotating frame with respect to the mode frequencies

$$H = -\delta \hat{b}_1^\dagger \hat{b}_1 + \delta \hat{b}_2^\dagger \hat{b}_2 + g_{11}(\hat{a}_1 \hat{b}_1^\dagger + \hat{a}_1^\dagger \hat{b}_1) + g_{21}(\hat{a}_2 \hat{b}_1^\dagger + \hat{a}_2^\dagger \hat{b}_1) \\ + g_{12}(\hat{a}_1 \hat{b}_2^\dagger + \hat{a}_1^\dagger \hat{b}_2) + g_{22}(e^{i\phi} \hat{a}_2 \hat{b}_2^\dagger + e^{-i\phi} \hat{a}_2^\dagger \hat{b}_2) \quad (6.6)$$

where \hat{a}_i and \hat{b}_j are redefined to be the quantum fluctuations around the linearised mean fields. Here $g_{ij} = g_{0,ij}\sqrt{n_{ij}}$ are the field-enhanced optomechanical coupling strengths, where n_{ij} is the contribution to the mean intracavity photon number due to the drive with detuning Δ_{ij} . Although in principle each coupling is complex, without loss of generality we can take all to be real except the one between \hat{a}_2 and \hat{b}_2 with a complex phase ϕ .

We start by considering frequency conversion through a single mechanical mode. Neglecting the noise terms, the field exiting the cavity \hat{a}_2 is given by $\hat{a}_{2,\text{out}} = S_{21}\hat{a}_{1,\text{in}} + S_{22}\hat{a}_{2,\text{in}}$, which defines the scattering matrix S_{ij} . For a single mechanical pathway, setting $g_{12} = g_{22} = 0$ and $\delta = 0$, the scattering matrix between input and output mode becomes

$$S_{21}(\omega) = \sqrt{\frac{\kappa_{\text{ex},1}\kappa_{\text{ex},2}}{\kappa_1\kappa_2}} \frac{\sqrt{\mathcal{C}_{11}\mathcal{C}_{21}}\Gamma_{m,1}}{\frac{\Gamma_{\text{eff},1}}{2} - i\omega}, \quad (6.7)$$

where $\kappa_{\text{ex},1}, \kappa_{\text{ex},2}$ denote the external coupling rates of the microwave modes to the feedline, and the (multiphoton) cooperativity for each mode pair is defined as $\mathcal{C}_{ij} = 4g_{ij}^2/(\kappa_i\Gamma_{m,j})$. Conversion occurs within the modified mechanical response over an increased bandwidth $\Gamma_{\text{eff},1} = \Gamma_{m,1}(1 + \mathcal{C}_{11} + \mathcal{C}_{21})$. This scenario, where a mechanical oscillator mediates frequency conversion between electromagnetic modes, has recently been demonstrated [198] with a microwave optomechanical circuit [39], and moreover used to create a bidirectional link between a microwave and an optical mode [199]. Optimal conversion, limited by

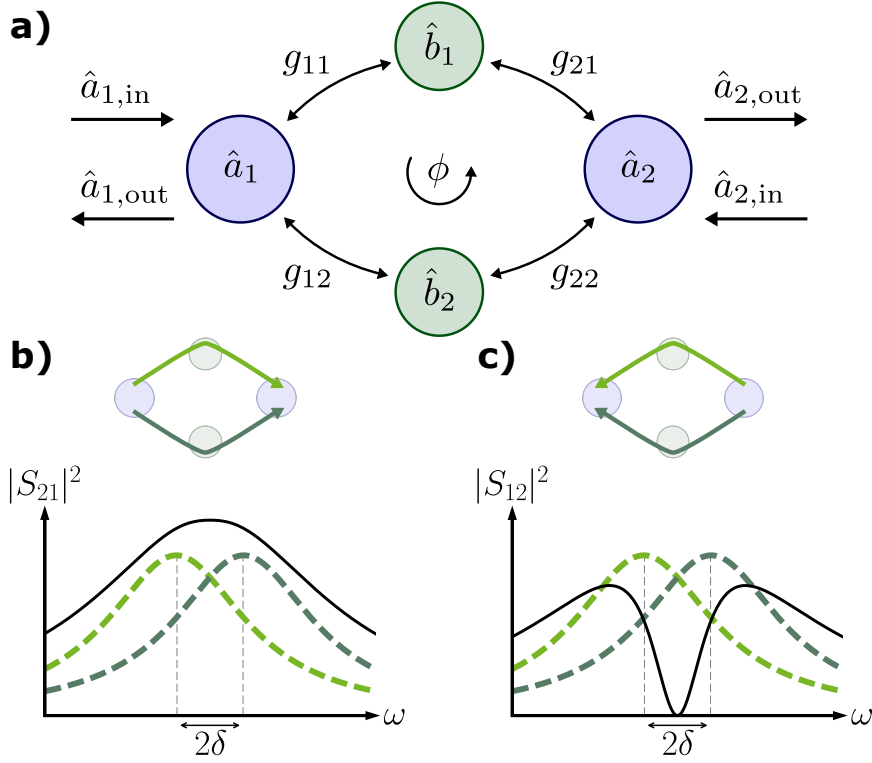


Figure 6.3 – **Optomechanical nonreciprocal transmission via interference of two asymmetric dissipative coupling pathways.** **a.** Two microwave modes \hat{a}_1 and \hat{a}_2 are coupled via two mechanical modes \hat{b}_1 and \hat{b}_2 through optomechanical frequency conversion (as given by the coupling constants $g_{11}, g_{21}, g_{12}, g_{22}$). Nonreciprocity is based on the interference between the two optomechanical (conversion) pathways g_{11}, g_{21} and g_{12}, g_{22} , in the presence of a suitably chosen phase difference ϕ between the coupling constants as well as the deliberate introduction of an asymmetry in the pathways. **b-c.** The symmetry between the pathways can be broken by off-setting the optomechanical transmission windows through each mechanical mode (dashed lines in dark and light green) by a frequency difference 2δ , resulting in different $|S_{21}|$ and $|S_{12}|$ (solid lines; we note here that the indices of the scattering matrix refer to the modes, not physical ports). Each single pathway, in the absence of the other mode, is described by eq. (6.7). In the forward direction (**b**), the two paths interfere constructively, allowing transmission and a finite scattering matrix element S_{21} on resonance with the first microwave cavity. In contrast, in the backward direction (**c**), the paths interfere destructively, such that $S_{12} \approx 0$, thereby isolating mode 1 from mode 2 on resonance with the second microwave cavity. The isolation bandwidth is determined by the intrinsic dissipation rate of the mechanical modes.

Figure also appears in [52].

internal losses in the microwave cavities, reaches at resonance $|S_{21}|_{\text{max}}^2 = \frac{\kappa_{\text{ex},1}\kappa_{\text{ex},2}}{\kappa_1\kappa_2}$ in the limit of large cooperativities $\mathcal{C}_{11} = \mathcal{C}_{21} \gg 1$.

We next describe nonreciprocal transmission of the full system with both mechanical

6.3. Theoretical model of nonreciprocity in the 4-mode plaquette

modes. We consider the ratio of transmission amplitudes given by

$$\frac{S_{12}(\omega)}{S_{21}(\omega)} = \frac{g_{11}\chi_1(\omega)g_{21} + g_{12}\chi_2(\omega)g_{22}e^{+i\phi}}{g_{11}\chi_1(\omega)g_{21} + g_{12}\chi_2(\omega)g_{22}e^{-i\phi}} \quad (6.8)$$

with the mechanical susceptibilities defined as $\chi_1^{-1}(\omega) = \Gamma_{m,1}/2 - i(\delta + \omega)$ and $\chi_2^{-1}(\omega) = \Gamma_{m,2}/2 + i(\delta - \omega)$. Conversion is nonreciprocal if the above expression has a magnitude that differs from 1. If S_{21} and S_{12} differ only by a phase, it can be eliminated by a redefinition of either \hat{a}_1 or \hat{a}_2 [172, 180]. Upon a change in conversion direction, the phase ϕ of the coherent coupling (between the microwave and mechanical mode) is conjugated, while the complex phase associated with the response of the dissipative mechanical modes remains unchanged. Physically, scattering from $1 \rightarrow 2$ is related to scattering from $2 \rightarrow 1$ via time-reversal, which conjugates phases due to coherent evolution of the system. Dissipation is untouched by such an operation and thus remains invariant. Indeed, the mechanical dissipation is an essential ingredient for the nonreciprocity to arise in this system, but not sufficient on its own. In fact, if we align the frequency conversion windows corresponding to the two mechanical modes by setting $\delta = 0$, the system becomes reciprocal on resonance ($\omega = 0$), since there is no longer any phase difference between numerator and denominator. This situation corresponds to two symmetric pathways resulting from purely dissipative couplings; they can interfere only in a reciprocal way.

6.3.1 Conditions for isolation

We study the conditions for isolation, when backward transmission S_{12} vanishes while forward transmission S_{21} is non-zero. A finite offset 2δ between the mechanical conversion windows causes an intrinsic phase shift for a signal on resonance ($\omega = 0$) travelling one path compared to the other, as it falls either on the red or the blue side of each mechanical resonance. The coupling phase ϕ is then adjusted to cancel propagation in the backward direction S_{12} (fig. 6.3c), by cancelling the two terms in the numerator of eq. (6.8). While we consider for simplicity the symmetric case, nonreciprocal isolation is robust under changes of the system parameters. In general, there is always a frequency ω for which $|g_{11}\chi_1(\omega)g_{21}| = |g_{12}\chi_2(\omega)g_{22}|$, such that the phase ϕ can be tuned to cancel transmission in one direction. Specifically, for two mechanical modes with identical decay rates ($\Gamma_{m,1} = \Gamma_{m,2} = \Gamma_m$) and symmetric couplings ($g_{11}g_{21} = g_{12}g_{22}$), we find that transmission from ports 2 to 1 vanishes on resonance if

$$\frac{\Gamma_m}{2\delta} = \tan \frac{\phi}{2}. \quad (6.9)$$

The corresponding terms of the denominator will have a different relative phase, and the signal will add constructively instead, in the forward direction (fig. 6.3b). The

Chapter 6. Nonreciprocal microwave conversion using a mechanical oscillator

device thus acts as an isolator from \hat{a}_1 to \hat{a}_2 , realised without relying on the Josephson nonlinearity [144, 181]. We now describe the conditions to minimise insertion loss of the isolator in the forward direction. Still considering the symmetric case, the cooperativity is set to be the same for all modes ($\mathcal{C}_{ij} = \mathcal{C}$). For a given separation δ , transmission on resonance ($\omega = 0$) in the isolating direction has the maximum

$$|S_{21}|_{\max}^2 = \frac{\kappa_{\text{ex},1}\kappa_{\text{ex},2}}{\kappa_1\kappa_2} \left(1 - \frac{1}{2\mathcal{C}}\right) \quad (6.10)$$

for a cooperativity $\mathcal{C} = 1/2 + 2\delta^2/\Gamma_{\text{m}}^2$. As in the case for a single mechanical pathway in eq. (6.7), for large cooperativity the isolator can reach an insertion loss only limited by the internal losses of the microwave cavities.

The unusual and essential role of dissipation in this nonreciprocal scheme is also apparent in the analysis of the bandwidth of the isolation. Although the frequency conversion through a single mechanical mode has a bandwidth $\Gamma_{\text{eff},j}$ (see eq. (6.7)), caused by the optomechanical damping of the pumps on the lower sidebands, the nonreciprocal bandwidth is set by the intrinsic mechanical damping rates. Examination of eq. (6.8) reveals that nonreciprocity originates from the interference of two mechanical susceptibilities of widths $\Gamma_{\text{m},j}$. One can conclude that the intrinsic mechanical dissipation, which takes energy out of the system regardless of the transmission direction, is an essential ingredient for the nonreciprocal behaviour reported here, as discussed previously [180, 108]. In contrast, optomechanical damping works symmetrically between input and output modes. By increasing the coupling rates, using higher pump powers, the overall conversion bandwidth increases, while the nonreciprocal bandwidth stays unchanged.

6.4 Experimental results

We experimentally realise this nonreciprocal scheme using a superconducting circuit optomechanical system in which mechanical motion is capacitively coupled to a multi-mode microwave circuit [39]. The circuit, schematically shown in fig. 6.4a, supports two electromagnetic modes with resonance frequencies $(\omega_{\text{c},1}, \omega_{\text{c},2}) = 2\pi \cdot (4.1, 5.2)$ GHz and energy decay rates $(\kappa_1, \kappa_2) = 2\pi \cdot (0.2, 3.4)$ MHz, both of them coupled to the same vacuum-gap capacitor. We utilise the fundamental and second order radially symmetric $(0, 2)$ modes of the capacitor's mechanically compliant top plate [37] (see fig. 6.4b and d) with resonance frequencies $(\Omega_1, \Omega_2) = 2\pi \cdot (6.5, 10.9)$ MHz, intrinsic energy decay rates $(\Gamma_{\text{m},1}, \Gamma_{\text{m},2}) = 2\pi \cdot (30, 10)$ Hz and optomechanical vacuum coupling strengths $(g_{0,11}, g_{0,12}) = 2\pi \cdot (91, 12)$ Hz, respectively (with $g_{0,11} \approx g_{0,21}$ and $g_{0,12} \approx g_{0,22}$, i.e. the two microwave cavities are symmetrically coupled to the mechanical modes). The device is placed at the mixing chamber of a dilution refrigerator at 200 mK and all four incoming

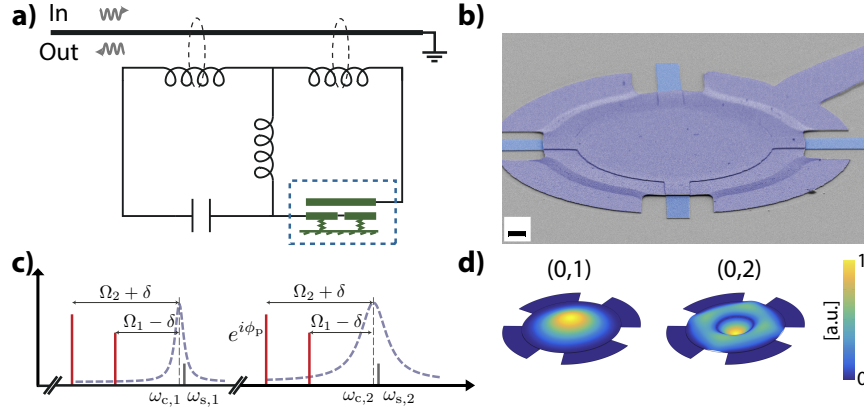


Figure 6.4 – **Implementation of a superconducting microwave circuit optomechanical device for nonreciprocity.** (a) A superconducting circuit featuring two electromagnetic modes in the microwave domain is capacitively coupled to a mechanical element (a vacuum-gap capacitor, dashed rectangle) and inductively coupled to a microstrip feedline. The end of the feedline is grounded and the circuit is measured in reflection. (b) Scanning electron micrograph of the drum-head-type vacuum gap capacitor (dashed rectangle in a) with a gap distance below 50 nm, made from aluminium on a sapphire substrate. The scale bar indicates 2 μm . (c) Frequency domain schematic of the microwave pump setup to achieve nonreciprocal mode conversion. Microwave pumps (red bars) are placed at the lower motional sidebands - corresponding to the two mechanical modes - of both microwave resonances (dashed purple lines). The pumps are detuned from the exact sideband condition by $\pm\delta = 2\pi \cdot 18$ kHz, creating two optomechanically induced transparency windows detuned by 2δ from the microwave resonance frequencies (denoted by $\omega_{c,1}$ and $\omega_{c,1}$, vertical dashed line). All pumps are phase-locked using a common clock distributor. The phase ϕ_p of one of the pumps is tuned, which corresponds to tuning the overall plaquette phase defined in fig. 6.3. The propagation of an incoming signal (with frequency $\omega_{s,1}$ or $\omega_{s,2}$, solid grey bar) in the forward and backward direction depends on this phase and nonreciprocal microwave transmission can be achieved. (d) Finite-element simulation of the displacement of the fundamental (0,1) and second order radially symmetric (0,2) mechanical modes (with measured resonant frequencies $\Omega_1/2\pi = 6.5$ MHz and $\Omega_2/2\pi = 10.9$ MHz, respectively) which are exploited as intermediary dissipative modes to achieve nonreciprocal microwave conversion.

Figure also appears in [52].

pump tones are heavily filtered and attenuated to eliminate Johnson and phase noise (details are published elsewhere [50]). We establish a parametric coupling between the two electromagnetic and the two mechanical modes by introducing four microwave pumps with frequencies slightly detuned from the lower motional sidebands of the resonances, as shown in fig. 6.4c and as discussed above. An injected probe signal $\omega_{s1(s2)}$ around the lower (higher) frequency microwave mode is then measured in reflection using a vector network analyser.

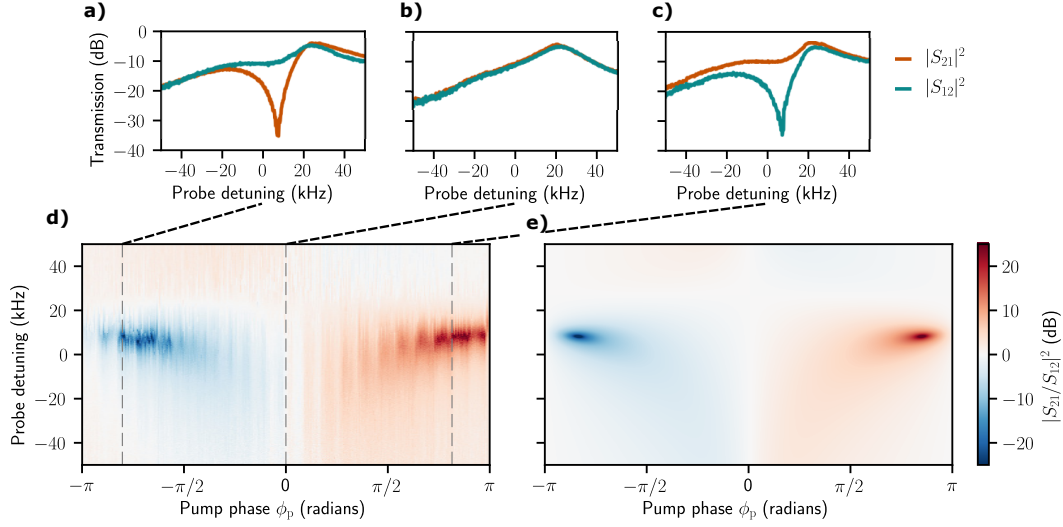


Figure 6.5 – **Experimental demonstration of nonreciprocity.** **a-c.** Power transmission between modes 1 and 2 as a function of probe detuning, shown in both directions for pump phases $\phi_p = -0.8\pi, 0, 0.8\pi$ radians (respectively **a**, **b** and **c**). Isolation of more than 20 dB in the forward (**c**) and backward (**a**) directions is demonstrated, as well as reciprocal behaviour (**b**). **d.** The ratio of transmission $|S_{21}/S_{12}|^2$, representing a measure of nonreciprocity, is shown as a function of pump phase ϕ_p and probe detuning. Two regions of nonreciprocity develop, with isolation in each direction. The system is reconfigurable as the direction of isolation can be swapped by taking $\phi_p \rightarrow -\phi_p$. **e.** Theoretical ratio of transmission from eq. (6.8), calculated with independently estimated experimental parameters. The theoretical model includes effectively lowered cooperativities for the mechanical mode \hat{b}_1 due to cross-damping (optomechanical damping of the lower frequency mechanical mode by the pump on the sideband of the higher frequency mechanical mode) acting as an extra loss channel.

Figure also appears in [52].

6.4.1 Isolation

Frequency conversion in both directions, $|S_{21}(\omega)|^2$ and $|S_{12}(\omega)|^2$, are measured and compared in fig. 6.5a-c. The powers of the four pumps are chosen such that the associated individual cooperativities are given by $\mathcal{C}_{11} = 520$, $\mathcal{C}_{21} = 450$, $\mathcal{C}_{12} = 1350$ and $\mathcal{C}_{22} = 1280$. The detuning from the lower motional sidebands is set to $\delta = 2\pi \cdot 18$ kHz. By pumping both cavities on the lower sideband associated with the same mechanical mode, a signal injected on resonance with one of the modes will be frequency converted to the other mode. This process can add negligible noise, when operating with sufficiently high cooperativity, as demonstrated recently [198]. In the experiment, the four drive tones are all phase-locked using a central clock distributor and the phase of one tone ϕ_p is varied continuously from $-\pi$ to π . The pump phase is linked to the coupling phase ϕ by a constant offset, in our case $\phi_p \approx \phi + \pi$. Between the two transmission peaks corresponding to each mechanical

mode, a region of nonreciprocity develops, depending on the relative phase ϕ_p .

The amount of reciprocity that occurs in this process is quantified and measured by the ratio of forward to backward conversion $|S_{21}/S_{12}|^2$. Figure 6.5d shows this quantity as a function of probe detuning and the relative pump phase. Isolation of more than 20 dB is demonstrated in each direction in a reconfigurable manner, i.e. the direction of isolation can be switched by taking $\phi_p \rightarrow -\phi_p$, as expected from eq. (6.9). The ideal theoretical model, which takes into account $\Gamma_{m,1} \neq \Gamma_{m,2}$, predicts that the bandwidth of the region of nonreciprocity is commensurate with the arithmetic average of the bare mechanical dissipation rates, $\sim 2\pi \cdot 20$ Hz. However, given the significantly larger coupling strength of the fundamental mechanical mode compared to the second order mode, and that $\kappa_2/\Omega_{1,2}$ is not negligible, the pump detuned by $\Omega_2 - \delta$ from the microwave mode \hat{a}_2 introduces considerable cross-damping (i.e. resolved sideband cooling) for the fundamental mode. This cross-damping, measured separately to be $\Gamma_{m,1}^{(\text{cross})} \approx 2\pi \cdot 20$ kHz at the relevant pump powers, widens the bandwidth of nonreciprocal behaviour by over two orders of magnitude and effectively cools the mechanical oscillator. It also acts as loss in the frequency conversion process and therefore effectively lowers the cooperativities to $(\mathcal{C}_{11}, \mathcal{C}_{21}) \approx (0.78, 0.68)$. This lowered cooperativity accounts for the overall ~ 10 dB loss in the forward direction. This limitation can be overcome in a future design by increasing the sideband resolution with decreased κ_i or utilising the fundamental modes of two distinct mechanical elements with similar coupling strengths. To compare the experiment to theory we use a model that takes into account the cross-damping and an increased effective mechanical dissipation of the fundamental mode. The model is compared to the experimental data in fig. 6.5e, showing good qualitative agreement.

6.4.2 Noise properties

From a technological standpoint, it does not suffice for an isolator to have the required transmission properties; since its purpose is to protect the input from any noise propagating in the backward direction, the isolator's own noise emission is relevant. We therefore return to the theoretical description of the ideal symmetric case and derive the noise properties expected from the device, in the limit of overcoupled cavities ($\kappa_{\text{ex},i} \approx \kappa_i$). In the forward direction and on resonance, the emitted noise amounts to $N_{\text{fw}}(0) = 1/2 + (\bar{n}_{m,1} + \bar{n}_{m,2})/(4\mathcal{C})$, where $\bar{n}_{m,j}$ is the thermal occupation of each mechanical mode. In the limit of low insertion loss and large cooperativity, the added noise becomes negligible in the forward direction. More relevant for the purpose of using an isolator to protect sensitive quantum apparatus is the noise emitted in the backward direction, given by $N_{\text{bw}}(0) = 1/2 + (\bar{n}_{m,1} + \bar{n}_{m,2})/2$. Here the noise is directly commensurate with the occupation of the mechanics which can be of hundreds of quanta even at cryogenic millikelvin temperatures, due to the low mechanical frequencies. This is a

Chapter 6. Nonreciprocal microwave conversion using a mechanical oscillator

direct consequence of isolation without reflection, since it prevents fluctuations from either cavity to emerge in the backward direction. In order to preserve the commutation relations of the bosonic output modes, the fluctuations consequently have to originate from the mechanical modes. A practical low-noise design therefore requires a scheme to externally cool the mechanical modes, e.g. via sideband cooling using an additional auxiliary microwave mode.

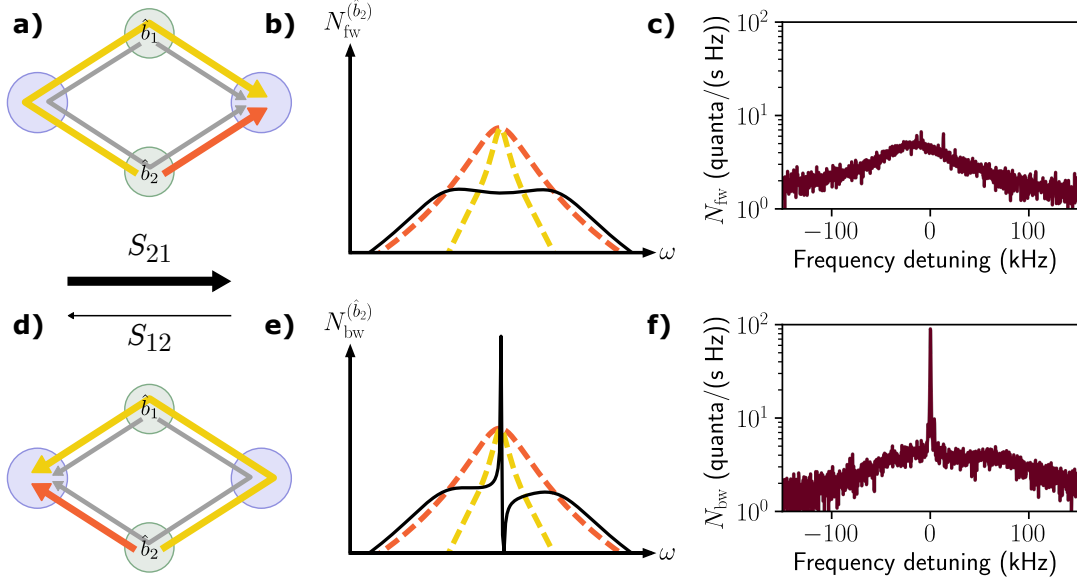


Figure 6.6 – **Asymmetric noise emission of the nonreciprocal circuit.** The noise emission is mainly due to mechanical thermal noise, that is converted through two paths to the microwave modes. The resulting interference creates a different noise pattern in the forward (**a-c**) and the backward (**d-f**) directions when the circuit is tuned as an isolator from mode \hat{a}_1 to \hat{a}_2 . **a, d.** The two possible paths for the noise are shown for each mechanical mode. For \hat{b}_2 , the direct path (orange) and the indirect path going through mode \hat{b}_1 (yellow) are highlighted (the corresponding paths for \hat{b}_1 are shown in grey). **b, e.** Each path on its own would result in a wide noise spectrum that is equally divided between the two microwave cavities (dashed yellow and orange lines). When both paths are available, however, the noise interferes differently in each direction (solid lines). In the backward direction (**e**), a sharp interference peak appears, of much larger amplitude than the broad base. The theoretical curves (on an arbitrary logarithmic scale) are shown for the symmetric case ($\Gamma_{m,1} = \Gamma_{m,2}$) and for the single mode \hat{b}_2 . Note that for the mode \hat{b}_1 , the shape of the asymmetric peak in the backward noise would be the mirror image. **c, f.** Measured output spectra of modes \hat{a}_2 (**c**) and \hat{a}_1 (**f**), calibrated to show the photon flux leaving the circuit. Because cross-damping provides extra cooling for the mode \hat{b}_1 , the thermal noise of \hat{b}_2 is expected to dominate. Figure also appears in [52].

The origin of this noise asymmetry can be understood as noise interference. The thermal

fluctuations of one mechanical oscillator are converted to microwave noise in each cavity through two paths, illustrated in fig. 6.6a, d): a direct (orange) and an indirect (yellow) link. Each pathway, on its own and with the same coupling strength, would result in symmetric noise that decreases in magnitude with increasing cooperativity. When both are present, however, the noise interferes with itself differently in each direction. In the forward direction, the noise interferes destructively (fig. 6.6b) leading to low added noise, but in the backward direction a sharp interference peak arises (fig. 6.6e) with finite noise in the nonreciprocal bandwidth even in the high-cooperativity limit. In an intuitive picture, the circuit acts as a circulator that routes noise from the output port to the mechanical thermal bath and in turn the mechanical noise to the input port. We demonstrate experimentally the noise asymmetry by detecting the output spectra at each microwave mode while the device isolates the mode \hat{a}_1 from \hat{a}_2 by more than 25 dB (fig. 6.6c, f). The cooperativities are here set to $(\mathcal{C}_{11}, \mathcal{C}_{21}, \mathcal{C}_{12}, \mathcal{C}_{22}) = (20.0, 14.2, 106, 89)$ with a cross-damping $\Gamma_{m,1}^{(\text{cross})} \approx 2\pi \cdot 2.6$ kHz, in order to optimise the circuit for a lower insertion loss and increase the noise visibility. As there is additional cooling from the off-resonant pump on mode \hat{b}_1 , we expect noise from \hat{b}_2 to dominate.

7 Summary and outlook

In summary, during this thesis work we have built up the fabrication and laboratory capabilities to perform measurements with multimode superconducting electromechanical circuits. In one experiment, the circuit is used to engineer the mechanical mode into a cold, dissipative reservoir for microwave light. The mechanical reservoir is then utilized to tailor the susceptibility of the microwave mode - dynamical back-action on light caused by the mechanical motion - and to implement a low-noise amplifier close to the quantum limit. The system can be driven to the parametric instability threshold, above which self-sustained oscillations of the microwave field (masing) is observed. Injection-locking of the maser is demonstrated. Below the masing threshold, the added noise property of this amplifier reveals that the reservoir is close to its quantum ground state with a mean thermal occupation number well below 1. This experiment is the first one achieving the reversed dissipation regime in optomechanics and one of the first demonstrating that a ground-state cooled mechanical element can be useful.

In a second experiment, we demonstrate nonreciprocity using purely optomechanical interactions. As in the previous experiment, dissipation of the mechanical mode is one of the key ingredients to attain the the results: nonreciprocal frequency conversion and isolation. The device does not require static magnetic fields, on-chip integrable and compatible with superconducting circuit fabrication techniques. Over 20 dB of isolation is demonstrated and its direction can be easily reconfigured by tuning the phase of the control pumps. We analyse the noise properties, which reveals that while the forward noise is inversely proportional to the cooperativity (and therefore can be straightforwardly reduced), the backward noise is directly proportional to the mechanical fluctuations.

The development of this work opens various research directions; we briefly outline three of them below.

Increasing measurement efficiency with a travelling wave parametric amplifier

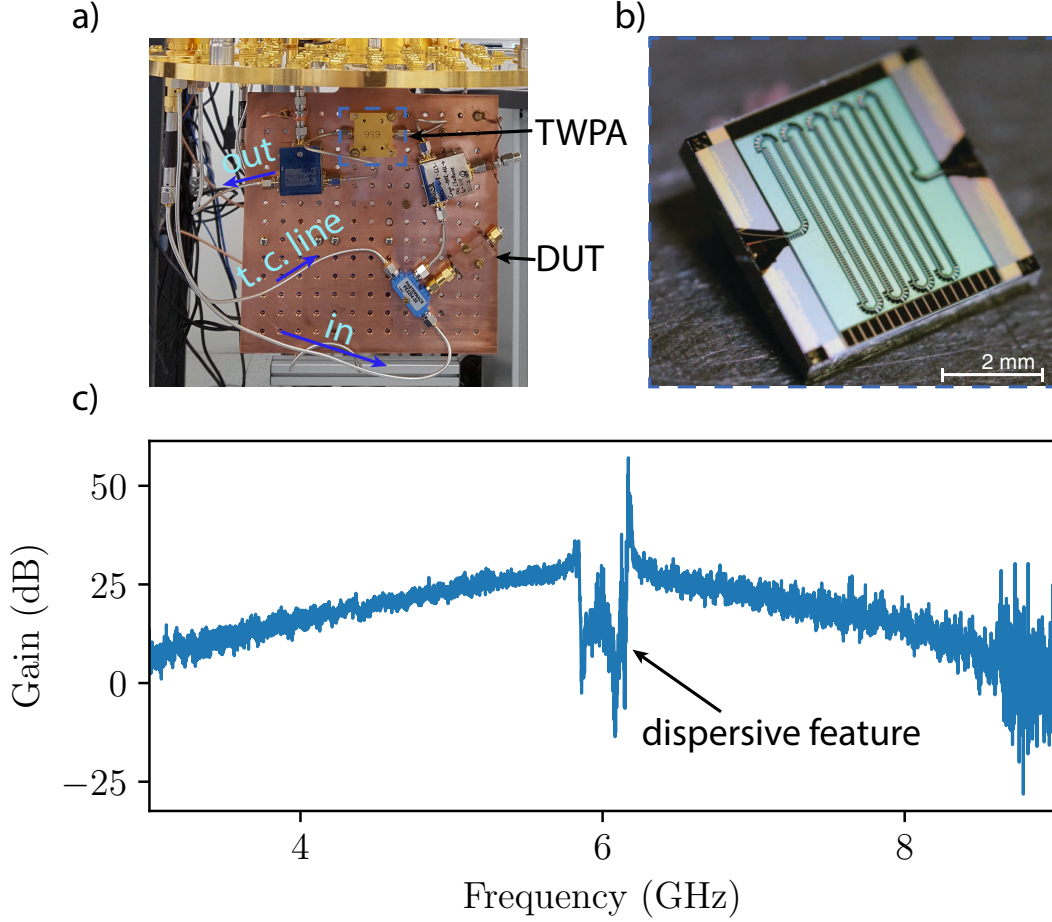


Figure 7.1 – **Integrating a Josephson travelling wave parametric amplifier (TWPA) into the setup.** **a)** Microwave circuit at the mixing chamber, featuring the TWPA in a reflection setup. The TWPA is pumped through the tone cancellation line (denoted as t.c. line). **b)** Photograph of a TWPA. The line is meandered several times on the 5 mm by 5 mm chip to achieve the desired amplifier gain. Figure taken from [174]. **c)** Gain of a TWPA measured in the lab. The device features more than 20 dB gain in a large bandwidth sufficient to overwhelm a cryogenic HEMT amplifier noise.

The readout sensitivity of measurement chains in the microwave domain is limited by the added noise of the HEMT amplifiers. For example, in the case of a HEMT which adds 20 noise quanta per second per unit bandwidth as described in chapter 4, the readout efficiency is limited to a few percent. In order to robustly observe microwave squeezing or entanglement of mechanical motion down to the quantum level, wideband parametric amplifiers which add $\mathcal{O}(1)$ photon of noise per second per Hz are a necessity;

still, to date, almost all circuit optomechanical experiments were performed with readout efficiencies far from the quantum limit. The bandwidth should be sufficient to read out both sidebands simultaneously and, in the case of multimode electromechanical circuits, on both microwave modes (which are typically separated by at least $\mathcal{O}(100 \text{ MHz})$).

Generation of squeezed microwave light

The dissipative reservoir demonstrated in chapter 5 can be used to generate one of the simplest, still intriguing non-classical states of the electromagnetic mode: a squeezed state. In a quantum squeezed state, the uncertainty in one quadrature is below the level of the zero-point vacuum fluctuation. Squeezed states can be used to increase measurement sensitivity (as was already demonstrated in advanced LIGO) or to reach even lower levels of thermal occupancy in sideband cooling [200].

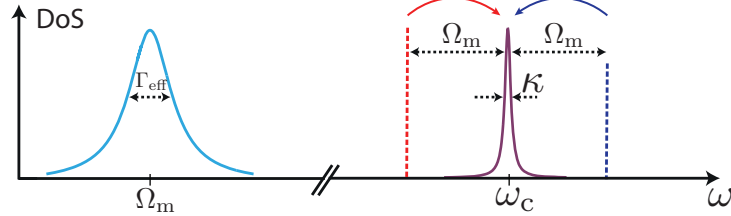


Figure 7.2 – **Frequency scheme for generating squeezed light with a dissipative mechanical reservoir.** After the dissipative reservoir is prepared using an auxiliary mode (not shown), the scheme requires two pumps placed at the lower and upper motional sidebands. Strong squeezing can be achieved by carefully tuning the amplitudes of the pumps.

To generate squeezed vacuum fluctuations in an optical or microwave cavity using reservoir engineering, one can implement the scheme proposed by Kronwald *et al.* [49, 107], in which the a squeezed mechanical bath is prepared using a bichromatic drive and then coupled to an optical mode. This proposal has been implemented already to squeeze the mechanical motion below the vacuum level in the normal dissipation regime [102]. The bright squeezed light can then be generated by reflecting a resonant tone from the optical cavity. When an impedance matching condition is satisfied, the vacuum fluctuations of the incident light are replaced by the squeezed vacuum fluctuations of the squeezed mechanical bath. The proposed frequency landscape to implement this scheme is shown in fig. 7.2.

Optomechanics with superconducting 2D materials

One interesting approach is to functionalize the vacuum gap capacitors with 2D superconducting materials [201]. One example is monolayer of NbSe₂ which is indeed

superconducting [202]. The approach may have unique properties, since the mass of the 2D material is significantly reduced due to the atomically thin layer even when encapsulated within boron nitride (by a factor of around 30). Moreover, 2D materials have

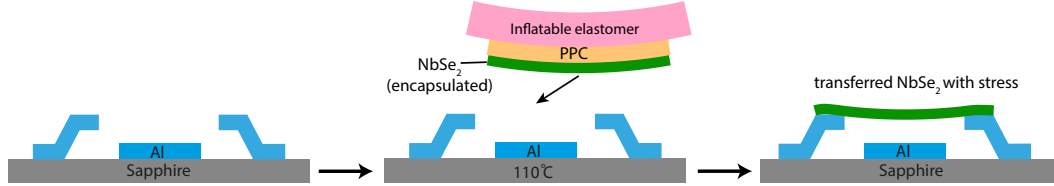


Figure 7.3 – **Envisioned process flow to fabricated stressed NbSe₂ vacuum gap capacitors.** Transfer using the elastomer ensures that the transferred material is stressed, enhancing its mechanical quality factor.

significantly higher yield strengths. For example, 2D transition metal di-chalcogenides support up to 10% strain, which enables much larger stress compared to Si₃N₄ which has a yield strength of ≈ 6 GPa that corresponds to about 3% strain. Therefore, provided that the material can be transferred to the membrane with stress (an envision process flow using an elastomer is shown in fig. 7.3) the mechanical quality factor should be exceptional, with the promise of significantly increasing the single photon cooperativity (as the membrane is superconducting, no significant decrease in the microwave quality factor is expected). Alternatively, this direction allows one to probe the mechanical properties of superconducting 2D materials.

A Fabrication process runcards

The final process runcards are presented here which were developed and used to fabricate the devices presented in Chapter 3. table A.1 details the process for the fabrication utilizing the direct laser aligner (Heidelberg MLA150), a tool which was beta-tested during (and with) the development of the process. Some standard steps are described in table A.1 and in table A.3.

Appendix A. Fabrication process runcards

| Nr. | Step name | Machine | Process params | Notes |
|-----|--------------------------------------|----------------------|---|--|
| 1 | Initial cleaning | Piranha bath (Z2) | 10 mins at 100 C | |
| 2 | Initial cleaning | Tepla O2 plasma (Z2) | 5 mins at 700 W (high) | |
| 3 | 1st metal layer deposition | LAB600 (Z4) | 100nm of Al 4A/s | Load right after step 2 so wafer is clean and dry |
| 4 | Direct laser lithography (table A.2) | | Dose: 55, defocus: -4 | Mask should be inverted |
| 5 | Etch 1st metal layer | STS (Z2) | Recipe: Al_etch, 30 s | Next cleaning step should be performed immediately after etch |
| 6 | Standard cleaning (table A.3) | | | |
| 7 | Sacrificial layer deposition | SPIDER600 (Z4) | 200nm of Si | |
| 8 | Direct laser lithography (table A.2) | | Dose: 57, defocus: -4 | No inversion |
| 9 | Reflow | Hotplate (Z7) | Setpoint 180 C (corresponds to 160 C); 1:45 | |
| 10 | Etch sacrificial layer I. | STS (Z2) | Recipe: Sub_Si, 45 s | Next cleaning step should be performed immediately after etch. |
| 11 | Standard cleaning (table A.3) | | | |
| 12 | Direct laser lithography (table A.2) | | Dose: 57, defocus: -4 | No inversion |
| 13 | Etch sacrificial layer II. | AMS (Z2) | Recipe: Si_opto, 15 s | |
| 14 | Standard cleaning (table A.3) | | | |
| 15 | 2nd metal layer deposition | LAB600 (Z4) | 100nm of Al 4A/s | Deposition technique can vary (see main section) |

| Nr. | Step name | Machine | Process params | Notes |
|-----|--------------------------------------|-------------|---|---|
| 16 | Direct laser lithography (table A.2) | | Dose: 55, defocus: -4 | Mask should be inverted and exposure area extended to the outer boundaries of the bottom layer. |
| 17 | Etch 2nd metal layer | STS (Z2) | Recipe: Al_etch, 30 s | Next cleaning step should be performed immediately after etch |
| 18 | Standard cleaning (table A.3) | | | |
| 19 | Resist for dicing | EVG150 (Z6) | Any resist with $> 8\mu\text{m}$ thickness, e.g. AZ9260 | Any other coater machine works. Careful with adhesion. |

Table A.1 – Runcard for the standard direct laser lithography.

| Nr. | Step name | Machine | Process params | Notes |
|-----|--------------------------|----------------------|---|-----------------------------------|
| 1 | Resist coating | EVG150 (Z6) | AZ15120 1.1um Quartz No EBR | Recipe has bake at 121 C for 210s |
| 2 | Direct laser lithography | Heidelberg DLA | laser: 405 nm, dose: ≈ 55 , \approx defocus: -4 | Mask should be inverted |
| 3 | Development | EVG150 (Z6) | DEV AZ15120 1.1um Quartz No EBR | Recipe has bake at 121 C for 210s |
| 4 | Rinse and dry | R&D tool (Z2) | Recipe 1 (full R&D) | |
| 5 | Descum | Tepla O2 plasma (Z2) | 20 s at 400 W (low) | |

Table A.2 – Runcard for the standard direct laser lithography.

Appendix A. Fabrication process runcards

| Nr. | Step name | Machine | Process params | Notes |
|-----|-----------|----------------------------|--|-------|
| 1 | Cleaning | Tepla O2 plasma (Z2) | 1 min at 700 W (high) | |
| 2 | Cleaning | 1165 wet re- moval (Z2) | \approx 5 mins in 1st bath, 20 mins in clean | |
| 3 | Cleaning | Tepla O2 plasma (Z2) | 3 mins at 700 W (high) | |

Table A.3 – Runcard for the standard cleaning (performed after each lithography step and at the very end before release).

B Wafer and chip layout

Here we present the layout of an example wafer. With the current generation of our sample holder (fig. 4.2), the chip size is $9.6 \text{ mm} \times 6.5 \text{ mm}$. Thus, up to ≈ 64 chips can be fabricated on a single wafer. Typically, we fabricate $6 \times 8 = 48$ chips, featuring different designs.

fig. B.2 shows the layout of a single chip.

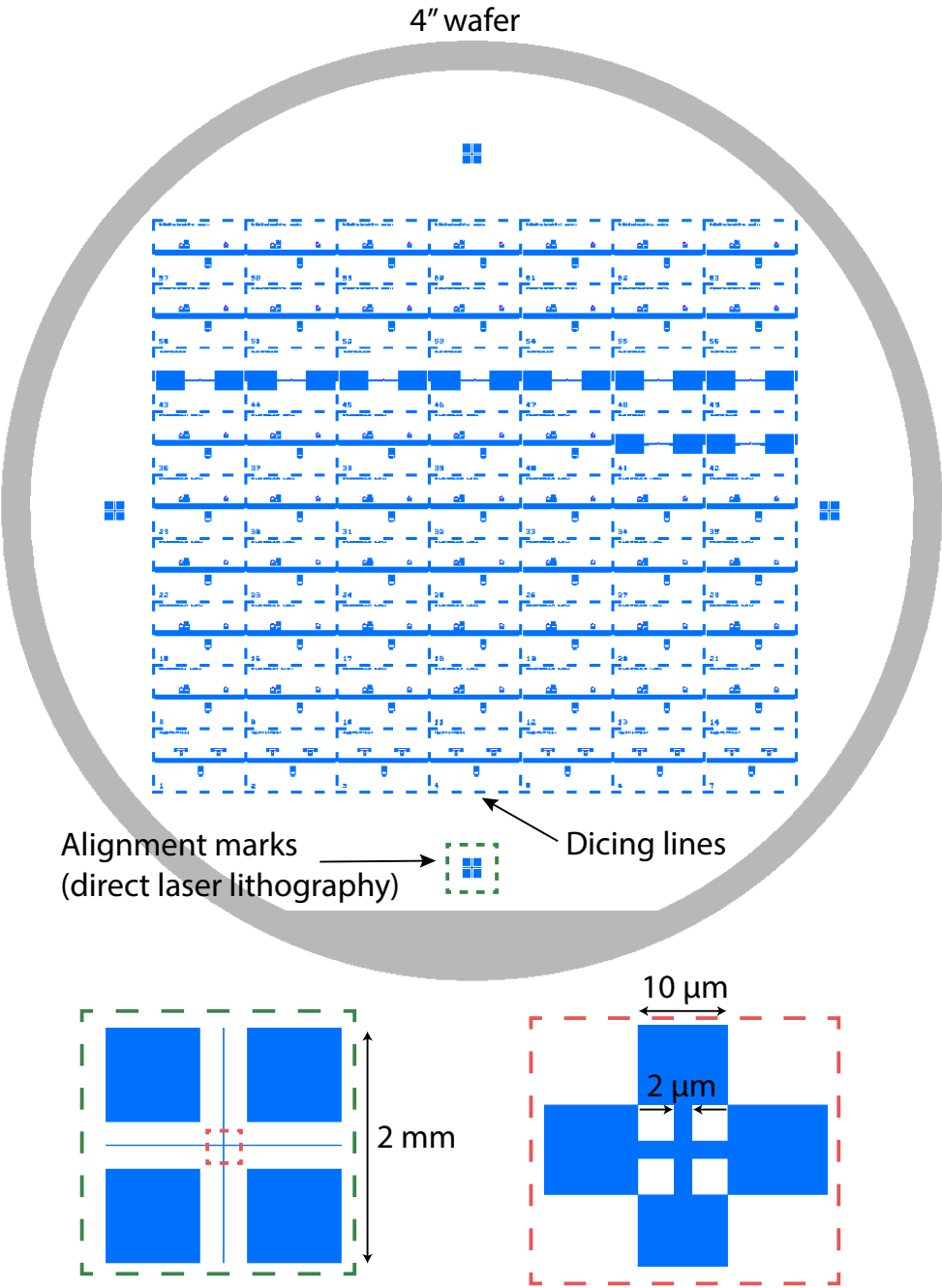


Figure B.1 – Layout of the wafer.

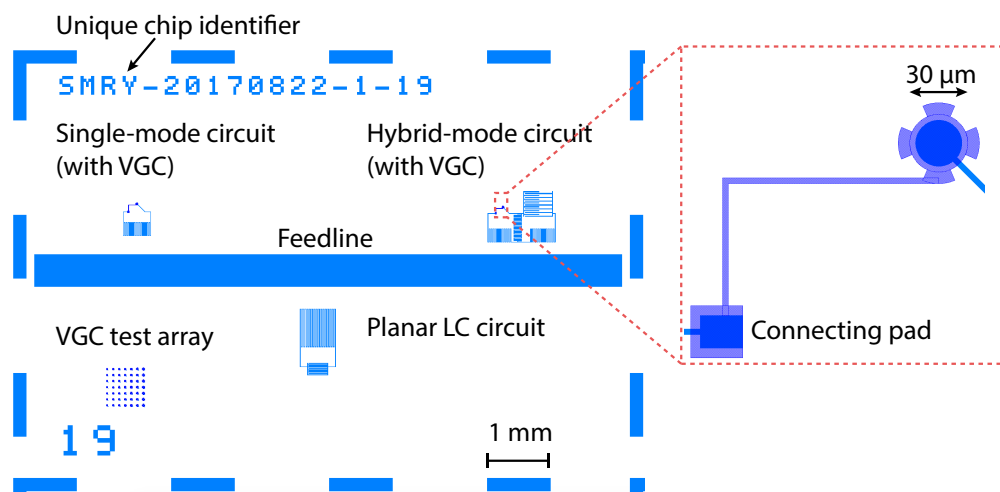


Figure B.2 – Layout of a typical chip.

C Derivation of the gain, added noise and output spectrum

In this Appendix we give details about the model used to derive the expressions presented in chapter 5 for amplifier gain, added noise, and device quantum limit as well as the output spectrum of our device. This also appears in the Supplementary Information of [50].

Let us start by writing down the linearized equations of motion for our device consisting of one mechanical \hat{b} and two optical modes, primary (anti-symmetric, dark) mode $\hat{a} = \hat{a}_a$ and auxiliary (symmetric, bright) mode $\hat{a}_{\text{aux}} = \hat{a}_s$

$$\dot{\delta\hat{a}} = +i\Delta\delta\hat{a} - \frac{\kappa}{2}\delta\hat{a} + ig(\delta\hat{b} + \delta\hat{b}^\dagger) + \sqrt{\kappa_{\text{ex}}}\delta\hat{a}_{\text{in,ex}} + \sqrt{\kappa_0}\delta\hat{a}_{\text{in},0} \quad (\text{C.1})$$

$$\dot{\delta\hat{b}} = -i\Omega_{\text{m}}\delta\hat{b} - \frac{\Gamma_{\text{m}}}{2}\delta\hat{b} + ig(\delta\hat{a} + \delta\hat{a}^\dagger) + ig_{\text{aux}}(\delta\hat{a}_{\text{aux}} + \delta\hat{a}_{\text{aux}}^\dagger) + \sqrt{\Gamma_{\text{m}}}\delta\hat{b}_{\text{in}} \quad (\text{C.2})$$

$$\dot{\delta\hat{a}_{\text{aux}}} = +i\Delta_{\text{aux}}\delta\hat{a}_{\text{aux}} - \frac{\kappa_{\text{aux}}}{2}\delta\hat{a}_{\text{aux}} + ig_{\text{aux}}(\delta\hat{b} + \delta\hat{b}^\dagger) + \sqrt{\kappa_{\text{aux}}^{\text{ex}}}\delta\hat{a}_{\text{in,ex}}^{(\text{aux})} + \sqrt{\kappa_{\text{aux}}^{(0)}}\delta\hat{a}_{\text{in},0}^{(\text{aux})}, \quad (\text{C.3})$$

where $\dot{\delta\hat{a}}$ is the time derivative of $\delta\hat{a}$ (similarly for $\delta\hat{b}$), the detunings are defined as $\Delta = \omega_L - \omega_c$ and $\Delta_{\text{aux}} = \omega_L^{\text{aux}} - \omega_{\text{aux}}$, the drive frequencies ω_L and ω_L^{aux} , the electromechanical coupling strengths $g = g_0|\bar{a}|$ and $g_{\text{aux}} = g_0^{\text{aux}}|\bar{a}_{\text{aux}}|$ enhanced by the mean number of photons $|\bar{a}|^2$ and $|\bar{a}_{\text{aux}}|^2$, and the input noise operators which satisfy bosonic commutation relations as well as

$$\langle \delta\hat{a}_{\text{in,ex}}(t)\delta\hat{a}_{\text{in,ex}}^\dagger(t') \rangle = (n_{\text{in}} + 1)\delta(t - t') \quad (\text{C.4})$$

$$\langle \delta\hat{a}_{\text{in},0}(t)\delta\hat{a}_{\text{in},0}^\dagger(t') \rangle = (n_{\text{cav}} + 1)\delta(t - t') \quad (\text{C.5})$$

$$\langle \delta\hat{b}_{\text{in}}(t)\delta\hat{b}_{\text{in}}^\dagger(t') \rangle = (n_{\text{th}} + 1)\delta(t - t') \quad (\text{C.6})$$

$$\langle \delta\hat{a}_{\text{in,ex}}^{(\text{aux})}(t)\delta\hat{a}_{\text{in,ex}}^{(\text{aux})\dagger}(t') \rangle = (n_{\text{in}}^{(\text{aux})} + 1)\delta(t - t') \quad (\text{C.7})$$

$$\langle \delta\hat{a}_{\text{in},0}^{(\text{aux})}(t)\delta\hat{a}_{\text{in},0}^{(\text{aux})\dagger}(t') \rangle = (n_{\text{cav}}^{(\text{aux})} + 1)\delta(t - t') \quad (\text{C.8})$$

Appendix C. Derivation of the gain, added noise and output spectrum

which describe thermal fluctuations of the external feedlines and cavity modes as well as the mechanical oscillator.

In the rotating-wave approximation $\kappa, \kappa_{\text{aux}} \ll \Omega_{\text{m}}$ this set of equations simplifies considerably. Pumping the primary mode close to the blue sideband $\Delta \approx \Omega_{\text{m}}$ and the auxiliary mode close to the red sideband $\Delta_{\text{aux}} \approx -\Omega_{\text{m}}$, we obtain

$$\dot{\delta\hat{a}} = +i\Delta\delta\hat{a} - \frac{\kappa}{2}\delta\hat{a} + ig\delta\hat{b}^\dagger + \sqrt{\kappa_{\text{ex}}}\delta\hat{a}_{\text{in,ex}} + \sqrt{\kappa_0}\delta\hat{a}_{\text{in},0} \quad (\text{C.9})$$

$$\dot{\delta\hat{b}^\dagger} = +i\Omega_{\text{m}}\delta\hat{b}^\dagger - \frac{\Gamma_{\text{m}}}{2}\delta\hat{b}^\dagger - ig\delta\hat{a} - ig_{\text{aux}}\delta\hat{a}_{\text{aux}}^\dagger + \sqrt{\Gamma_{\text{m}}}\delta\hat{b}_{\text{in}}^\dagger \quad (\text{C.10})$$

$$\dot{\delta\hat{a}_{\text{aux}}^\dagger} = -i\Delta_{\text{aux}}\delta\hat{a}_{\text{aux}}^\dagger - \frac{\kappa_{\text{aux}}}{2}\delta\hat{a}_{\text{aux}}^\dagger - ig_{\text{aux}}\delta\hat{b}^\dagger + \sqrt{\kappa_{\text{aux}}^{\text{ex}}}\delta\hat{a}_{\text{in,ex}}^{(\text{aux})\dagger} + \sqrt{\kappa_{\text{aux}}^{(0)}}\delta\hat{a}_{\text{in},0}^{(\text{aux})\dagger}. \quad (\text{C.11})$$

The auxiliary mode can be eliminated from this set of equations

$$\dot{\delta\hat{a}} = +i\Delta\delta\hat{a} - \frac{\kappa}{2}\delta\hat{a} + ig\delta\hat{b}^\dagger + \sqrt{\kappa_{\text{ex}}}\delta\hat{a}_{\text{in,ex}} + \sqrt{\kappa_0}\delta\hat{a}_{\text{in},0} \quad (\text{C.12})$$

$$\dot{\delta\hat{b}^\dagger} = +i\Omega_{\text{m}}\delta\hat{b}^\dagger - \frac{\Gamma_{\text{eff}}}{2}\delta\hat{b}^\dagger - ig\delta\hat{a} + \sqrt{\Gamma_{\text{eff}}}\delta\hat{b}_{\text{in}}^\dagger. \quad (\text{C.13})$$

where for $\Delta_{\text{aux}} = -\Omega_{\text{m}}$ we introduced an effective mechanical linewidth $\Gamma_{\text{eff}} = \Gamma_{\text{m}} + \frac{4g_{\text{aux}}^2}{\kappa_{\text{aux}}}$ and input noise correlators

$$\langle \delta\hat{b}_{\text{in}}(t)\delta\hat{b}_{\text{in}}^\dagger(t') \rangle = (n_{\text{eff}} + 1)\delta(t - t') \quad (\text{C.14})$$

with an effective mechanical occupation

$$n_{\text{eff}} = \frac{1}{\Gamma_{\text{eff}}} \left[\Gamma_{\text{m}} n_{\text{th}} + \frac{4g_{\text{aux}}^2}{\kappa_{\text{aux}}^2} \left(\kappa_{\text{aux}}^{\text{ex}} n_{\text{in}}^{(\text{aux})} + \kappa_{\text{aux}}^{(0)} n_{\text{cav}}^{(\text{aux})} \right) \right]. \quad (\text{C.15})$$

In this approximation equations (C.12) and (C.13) are those of a non-degenerate parametric amplifier which can be solved in terms of the mechanical response function $\chi_{\text{eff}}[\omega] = [\Gamma_{\text{eff}}/2 - i(\omega - \Omega_{\text{m}})]^{-1}$

$$\delta\hat{b}^\dagger[\omega] = \chi_{\text{eff}}^*[-\omega] \left[\sqrt{\Gamma_{\text{eff}}}\delta\hat{b}_{\text{in}}^\dagger[\omega] - ig\delta\hat{a}[\omega] \right] \quad (\text{C.16})$$

and

$$\left[\frac{\kappa}{2} - i(\omega + \Delta) - g^2\chi_{\text{eff}}^*[-\omega] \right] \delta\hat{a}[\omega] = \sqrt{\kappa_{\text{ex}}}\delta\hat{a}_{\text{in,ex}}[\omega] + \sqrt{\kappa_0}\delta\hat{a}_{\text{in},0}[\omega] + ig\chi_{\text{eff}}^*[-\omega]\sqrt{\Gamma_{\text{eff}}}\delta\hat{b}_{\text{in}}^\dagger[\omega]. \quad (\text{C.17})$$

For $\Delta = \Omega_{\text{m}}$, we have $\delta\omega_{\text{om}} = 0$ and $\kappa_{\text{om}} = -\frac{4g^2}{\Gamma_{\text{eff}}}$. For $\kappa \ll \Gamma_{\text{eff}}$ we can neglect the

frequency dependence of $\chi_{\text{eff}}[\omega]$

$$\left[\frac{\kappa_{\text{ex}} + \kappa_0 + \kappa_{\text{om}}}{2} - i(\omega + \Delta) \right] \delta \hat{a}[\omega] = \sqrt{\kappa_{\text{ex}}} \delta \hat{a}_{\text{in,ex}}[\omega] + \sqrt{\kappa_0} \delta \hat{a}_{\text{in},0}[\omega] + i\sqrt{\mathcal{C}\kappa} \delta \hat{b}_{\text{in}}^\dagger[\omega] \quad (\text{C.18})$$

making explicit that the cavity mode \hat{a} is coupled to three different reservoirs: to the external feedline at rate κ_{ex} , to internal dissipation at rate κ_0 , and to the mechanical oscillator at rate $\mathcal{C}\kappa$.

Using the input-output relation $\delta \hat{a}_{\text{out}} = \delta \hat{a}_{\text{in,ex}} - \sqrt{\kappa_{\text{ex}}} \delta \hat{a}$ and defining a modified cavity response function as

$$\tilde{\chi}_R[\omega] = \left[\frac{\kappa}{2} - i(\omega + \Delta) - g^2 \chi_{\text{eff}}^*[-\omega] \right]^{-1}, \quad (\text{C.19})$$

we express the fluctuations at the output in terms of the fluctuations at the input

$$\delta \hat{a}_{\text{out}}[\omega] = A(\omega) \delta \hat{a}_{\text{in,ex}}[\omega] + B(\omega) \delta \hat{a}_{\text{in},0}[\omega] + C(\omega) \delta \hat{b}_{\text{in}}^\dagger[\omega] \quad (\text{C.20})$$

with

$$A(\omega) = 1 - \kappa_{\text{ex}} \tilde{\chi}_R[+\omega] \quad (\text{C.21})$$

$$B(\omega) = -\sqrt{\kappa_{\text{ex}} \kappa_0} \tilde{\chi}_R[+\omega] \quad (\text{C.22})$$

$$C(\omega) = -ig\sqrt{\kappa_{\text{ex}} \Gamma_{\text{eff}}} \tilde{\chi}_R[+\omega] \chi_{\text{eff}}^*[-\omega] \quad (\text{C.23})$$

satisfying $|A(\omega)|^2 + |B(\omega)|^2 - |C(\omega)|^2 = 1$. For consistency, we note that our notation of $S_{11}(\omega)$ in the main text corresponds to $A(\omega)$ in this derivation.

The symmetrized cavity output field spectrum is given by

$$\begin{aligned} \bar{S}_{aa}(\omega) &= \frac{1}{2} \int_{-\infty}^{\infty} dt e^{i\omega t} \langle \delta \hat{a}_{\text{out}}^\dagger(t) \delta \hat{a}_{\text{out}}(0) + \delta \hat{a}_{\text{out}}(0) \delta \hat{a}_{\text{out}}^\dagger(t) \rangle \\ &= |A(-\omega)|^2 (n_{\text{in}} + \tfrac{1}{2}) + |B(-\omega)|^2 (n_{\text{cav}} + \tfrac{1}{2}) + |C(-\omega)|^2 (n_{\text{eff}} + \tfrac{1}{2}) \\ &= |1 - \kappa_{\text{ex}} \tilde{\chi}_R[-\omega]|^2 (n_{\text{in}} + \tfrac{1}{2}) + \kappa_{\text{ex}} \kappa_0 |\tilde{\chi}_R[-\omega]|^2 (n_{\text{cav}} + \tfrac{1}{2}) + \\ &\quad + |g|^2 \kappa_{\text{ex}} \Gamma_{\text{eff}} |\tilde{\chi}_R[-\omega]|^2 |\chi_{\text{eff}}[+\omega]|^2 (n_{\text{eff}} + \tfrac{1}{2}). \end{aligned} \quad (\text{C.24})$$

For $\Gamma_{\text{eff}} \gg \kappa_{\text{eff}} = \kappa_{\text{ex}} + \kappa_0 + \kappa_{\text{om}}$ and $\Delta = \Omega_{\text{m}}$ we obtain in the lab frame

$$\begin{aligned} \bar{S}_{aa}(\omega) &= \left[1 + \frac{\kappa_{\text{ex}}(\kappa_{\text{ex}} - \kappa_{\text{eff}})}{(\frac{\kappa_{\text{eff}}}{2})^2 + (\omega - \omega_c)^2} \right] (n_{\text{in}} + \tfrac{1}{2}) + \frac{\kappa_{\text{ex}} \kappa_0}{(\frac{\kappa_{\text{eff}}}{2})^2 + (\omega - \omega_c)^2} (n_{\text{cav}} + \tfrac{1}{2}) \\ &\quad + \frac{\mathcal{C} \kappa_{\text{ex}} \kappa}{(\frac{\kappa_{\text{eff}}}{2})^2 + (\omega - \omega_c)^2} (n_{\text{eff}} + \tfrac{1}{2}). \end{aligned} \quad (\text{C.25})$$

Appendix C. Derivation of the gain, added noise and output spectrum

We see that the output spectrum $\bar{S}_{aa}(\omega)$ can be understood as amplified noise (thermal and zero-point fluctuations) from the three reservoirs. Indeed, with the expressions for gain and added noise below we obtain in the rotating frame

$$\bar{S}_{aa}(\omega) = \mathcal{G}(-\omega) \left[n_{\text{in}} + \frac{1}{2} + \mathcal{N}(-\omega) \right]. \quad (\text{C.26})$$

The power gain of the amplifier is $\mathcal{G}(\omega) = |A(\omega)|^2$ and for pump on sideband $\Delta = \Omega_m$ signal on resonance $\omega = -\Delta_{\text{eff}}$

$$\mathcal{G}(\omega_c) = \left(1 - \frac{2\kappa_{\text{ex}}}{\kappa_{\text{eff}}} \right)^2 = \left(\frac{1 - \mathcal{C} - 2\frac{\kappa_{\text{ex}}}{\kappa}}{1 - \mathcal{C}} \right)^2. \quad (\text{C.27})$$

and the added noise of the amplifier is

$$\mathcal{N}(\omega) = (n_{\text{cav}} + \frac{1}{2}) \left| \frac{B(\omega)}{A(\omega)} \right|^2 + (n_{\text{eff}} + \frac{1}{2}) \left| \frac{C(\omega)}{A(\omega)} \right|^2 \quad (\text{C.28})$$

and for pump on sideband $\Delta = \Omega_m$ and signal on resonance $\omega = -\Delta_{\text{eff}}$ we obtain

$$\mathcal{N}(\omega_c) = \frac{\kappa_{\text{ex}}\kappa_0(n_{\text{cav}} + \frac{1}{2})}{(\frac{\kappa_{\text{eff}}}{2} - \kappa_{\text{ex}})^2} + \frac{\mathcal{C}\kappa_{\text{ex}}\kappa(n_{\text{eff}} + \frac{1}{2})}{(\frac{\kappa_{\text{eff}}}{2} - \kappa_{\text{ex}})^2} = \frac{4\frac{\kappa_{\text{ex}}\kappa_0}{\kappa^2}(n_{\text{cav}} + \frac{1}{2})}{(1 - \mathcal{C} - 2\frac{\kappa_{\text{ex}}}{\kappa})^2} + \frac{4\mathcal{C}\frac{\kappa_{\text{ex}}}{\kappa}(n_{\text{eff}} + \frac{1}{2})}{(1 - \mathcal{C} - 2\frac{\kappa_{\text{ex}}}{\kappa})^2}. \quad (\text{C.29})$$

At small gain $\mathcal{C} \rightarrow 0$ the added noise is mostly intracavity noise, in particular close to critical coupling, i.e. $\kappa_{\text{ex}} \approx \kappa_0$, where the gain goes to zero, $\mathcal{G}(\omega_c) \rightarrow 0$, since the signal is perfectly absorbed by the internal dissipation of the cavity,

$$\mathcal{N}(\omega_c) \rightarrow \frac{4\kappa_{\text{ex}}\kappa_0(n_{\text{cav}} + \frac{1}{2})}{(\kappa_{\text{ex}} - \kappa_0)^2} = \frac{4\frac{\kappa_0}{\kappa_{\text{ex}}}(n_{\text{cav}} + \frac{1}{2})}{(1 - \frac{\kappa_0}{\kappa_{\text{ex}}})^2}. \quad (\text{C.30})$$

Due to finite internal dissipation the added noise of the amplifier for large gain $\mathcal{C} \rightarrow 1$ becomes

$$\mathcal{N}(\omega_c) \rightarrow \frac{\kappa_0}{\kappa_{\text{ex}}}(n_{\text{cav}} + \frac{1}{2}) + \frac{\kappa}{\kappa_{\text{ex}}}(n_{\text{eff}} + \frac{1}{2}) = \frac{1}{2} + n_{\text{eff}} + \frac{\kappa_0}{\kappa_{\text{ex}}}(n_{\text{eff}} + n_{\text{cav}} + 1) > \frac{1}{2}. \quad (\text{C.31})$$

In the main manuscript we refer to $n_{\text{DQL}} = \frac{1}{2} + \frac{\kappa_0}{\kappa_{\text{ex}}}$ as the *device quantum limit* for the added noise of our amplifier due to the presence of a finite coupling to the output feedline with rate κ_{ex} compared to an intrinsic damping rate κ_0 .

D Impact of noise on the microwave source

In this section the limits of cooling for the final phonon occupancy due to the phase noise of the microwave sources reaching the auxiliary, cooling mode is presented. This also appears in the Supplementary Information of [50]. We note that the noise reaching the primary mode is already taken into account in our analysis through n_{in} in chapter 5, and does not constitute added noise in the amplification process.

We start from the Langevin equations describing the interaction between the auxiliary mode and the mechanical oscillator

$$\dot{\delta\hat{a}} = +i\Delta\delta\hat{a} - \frac{\kappa}{2}\delta\hat{a} + ig\delta\hat{b} + \sqrt{\kappa_0}\hat{a}_{\text{in,ex}} + \sqrt{\kappa_{\text{ex}}}\hat{a}_{\text{in},0} \quad (\text{D.1})$$

$$\dot{\delta\hat{b}} = -i\Omega_{\text{m}}\delta\hat{b} - \frac{\Gamma_{\text{m}}}{2}\delta\hat{b} + ig\delta\hat{a} + \sqrt{\Gamma_{\text{m}}}\hat{b}_{\text{in}} \quad (\text{D.2})$$

where $\Delta = -\Omega_{\text{m}}$, $g = g_0\sqrt{n_{\text{c}}}$, and $\delta\hat{a}$ is now the annihilation operator for the auxiliary mode. For simplicity of notation, we write in this section κ , κ_0 and κ_{ex} to refer to the auxiliary mode. Taking the Fourier transform and solving for $\delta\hat{b}$, one obtains

$$\delta\hat{b}(\omega) = \frac{1}{i(\Omega_{\text{m}} - \omega) + (\Gamma_{\text{m}} + \Gamma_{\text{om}})/2} \cdot \left(\sqrt{\Gamma_{\text{m}}}\hat{b}_{\text{in}}(\omega) + i\sqrt{\Gamma_{\text{om}}}\sqrt{\frac{\kappa_0}{\kappa}}\hat{a}_{\text{in,ex}}(\omega) + i\sqrt{\Gamma_{\text{om}}}\sqrt{\frac{\kappa_{\text{ex}}}{\kappa}}\hat{a}_{\text{in},0}(\omega) \right) \quad (\text{D.3})$$

where the optomechanical coupling rate of the mechanics is given by $\Gamma_{\text{om}} = 4g^2/\kappa$. The noise input of the auxiliary mode is transduced to the mechanics and should be taken into account as an effective mechanical noise, when considering the interaction of the mechanical oscillator with the primary mode in eq. (C.13). In terms of equivalent noise,

Appendix D. Impact of noise on the microwave source

this translates to

$$n_{\text{eq}} = \frac{\Gamma_m n_m + \Gamma_{\text{om}} \frac{\kappa_0}{\kappa} n_{\text{in}} + \Gamma_{\text{om}} \frac{\kappa_{\text{ex}}}{\kappa} n_{\text{cav}}}{\Gamma_m + \Gamma_{\text{om}}} \quad (\text{D.4})$$

where n_{in} and n_{cav} refer to the auxiliary mode. The microwave noise is part of the effective bath that the mechanical oscillator equilibrates to, at the same time as the cavity damps the intrinsic mechanical noise. The added noise due to microwave noise reaching the auxiliary cavity amounts to

$$n_{\text{added}} = 4 \frac{\kappa_0}{\kappa} \frac{g_0^2 n_c}{\kappa \Gamma_{\text{eff}}} n_{\text{in}} \quad (\text{D.5})$$

with $\Gamma_{\text{eff}} = \Gamma_m + \Gamma_{\text{om}}$. The cavity occupation due to the red-detuned pump n_c and the microwave noise n_{in} can both be expressed in terms of the pump flux of photons $P/\hbar\omega$ as

$$n_c = \frac{\kappa_{\text{ex}}}{(\kappa/2)^2 + \Omega_m^2} \frac{P}{\hbar\omega} \quad \text{and} \quad n_{\text{in}} = \frac{P}{\hbar\omega} \mathcal{S}_{\varphi\varphi} \quad (\text{D.6})$$

where $\mathcal{S}_{\varphi\varphi}$ the phase noise of the source expressed in power below the carrier in a unit bandwidth (dBc/Hz). The added phonons from phase fluctuations after cooling amount therefore to

$$n_{\text{added}} = 4 \left(\frac{\kappa_{\text{ex}}}{\kappa} \right)^2 \frac{g_0^2}{\Omega_m^2 + (\kappa/2)^2} \left(\frac{P}{\hbar\omega} \right)^2 \frac{1}{\Gamma_{\text{eff}}} \mathcal{S}_{\varphi\varphi}. \quad (\text{D.7})$$

The power of the pump reaching each resonator P is not an independent variable, but constrained in our experiment. For the cooling pump at the auxiliary mode, the pump damps mechanical mode at a rate $\Gamma_{\text{eff}} \approx \Gamma_{\text{om}}$ of $2\pi \times 400$ kHz in the experiment. The required power for this cooling rate is then given by

$$\frac{P}{\hbar\omega} = \frac{1}{4} \frac{(\kappa/2)^2 + \Omega_m^2}{g_0^2} \frac{\kappa}{\kappa_{\text{ex}}} \Gamma_{\text{eff}}. \quad (\text{D.8})$$

Inserting the expression in eq. (D.7), we obtain ¹

$$n_{\text{added}} = \frac{1}{4} \frac{(\kappa/2)^2 + \Omega_m^2}{g_0^2} \Gamma_{\text{eff}} \mathcal{S}_{\varphi\varphi}. \quad (\text{D.9})$$

The maximum allowed phase noise to increase the occupation by less than 1 is

$$\mathcal{S}_{\varphi\varphi}^{\text{max}} = 4 \frac{1}{(\kappa/2)^2 + \Omega_m^2} \frac{g_0^2}{\Gamma_{\text{eff}}}. \quad (\text{D.10})$$

For the microwave source used, the phase noise was measured to be -147 dBc/Hz at a

¹ Note that the apparent scaling of the added noise with $\Gamma_{\text{eff}}/g_0^2$ is inverted between eq. (D.7) and eq. (D.9), when adding the constraint on power.

detuning of 6 MHz. With the parameters of our system, this amounts to added noise of $n_{\text{added}} \approx 9$. This justifies the necessity of filter cavities to reduce the noise within the bandwidth of the cavity by more than 10 dB in order to reach occupations below 1.

Bibliography

- [1] Hosten, O., Engelsen, N. J., Krishnakumar, R. & Kasevich, M. A. Measurement noise 100 times lower than the quantum-projection limit using entangled atoms. *Nature* **529**, 505–508 (2016).
- [2] Boto, A. N. *et al.* Quantum Interferometric Optical Lithography: Exploiting Entanglement to Beat the Diffraction Limit. *Physical Review Letters* **85**, 2733–2736 (2000).
- [3] Walther, P. *et al.* De Broglie wavelength of a non-local four-photon state. *Nature* **429**, 158–161 (2004).
- [4] Maxwell, J. C. A dynamical theory of the electromagnetic field. *Phil. Trans. R. Soc. Lond.* **155**, 459–512 (1865).
- [5] Kepler, J. *De cometis libelli tres* (Typis Andreae Apergeri, sumptibus Sebastiani Mylii bibliopolæ Augustani, 1619).
- [6] Lebedew, P. Untersuchen uber die druckkrafte des lichtes. *Ann. Phys.* **6** (1901).
- [7] Nichols, E. F. & Hull, G. F. A preliminary communication on the pressure of heat and light radiation. *Phys. Rev.* **13** (1901).
- [8] Nichols, E. F. & Hull, G. F. The pressure due to radiation. (second paper.). *Phys. Rev.* **17** (1901).
- [9] LIGO Scientific Collaboration and Virgo Collaboration *et al.* Observation of Gravitational Waves from a Binary Black Hole Merger. *Physical Review Letters* **116**, 061102 (2016).
- [10] Braginski, V. B. & Manukin, A. B. Ponderomotive effects of electromagnetic radiation. *Sov. Phys. JETP* **25**, 653–655 (1967).
- [11] Braginsky, V. B., Manukin, A. B. & Tikhonov, M. Y. Investigation of Dissipative Ponderomotive Effects of Electromagnetic Radiation. *Soviet Journal of Experimental and Theoretical Physics* **31**, 829 (1970).

Bibliography

- [12] Braginsky, V. & Manukin, A. *Measurement of weak forces in Physics experiments* (Univ. of Chicago Press, 1977).
- [13] Dykman, M. Heating and cooling of local and quasilocal vibration by a nonresonance field. *Sov. Phys. Solid State* **20**, 1306–1311 (1978).
- [14] Braginsky, V. B., Strigin, S. E. & Vyatchanin, S. P. Parametric oscillatory instability in Fabry–Perot interferometer. *Physics Letters A* **287**, 331–338 (2001).
- [15] Evans, M. *et al.* Observation of Parametric Instability in Advanced LIGO. *Physical Review Letters* **114**, 161102 (2015).
- [16] Hänsch, T. W. & Schawlow, A. L. Cooling of gases by laser radiation. *Optics Communications* **13**, 68–69 (1975).
- [17] Ashkin, A. Trapping of Atoms by Resonance Radiation Pressure. *Physical Review Letters* **40**, 729–732 (1978).
- [18] Wineland, D. J. & Itano, W. M. Laser cooling of atoms. *Physical Review A* **20**, 1521–1540 (1979).
- [19] Chu, S., Hollberg, L., Bjorkholm, J. E., Cable, A. & Ashkin, A. Three-dimensional viscous confinement and cooling of atoms by resonance radiation pressure. *Physical Review Letters* **55**, 48–51 (1985).
- [20] Aspelmeyer, M., Kippenberg, T. J. & Marquardt, F. Cavity optomechanics. *Reviews of Modern Physics* **86**, 1391–1452 (2014).
- [21] Poot, M. & van der Zant, H. S. J. Mechanical systems in the quantum regime. *Physics Reports* **511**, 273–335 (2012).
- [22] Schliesser, A., Del’Haye, P., Nooshi, N., Vahala, K. J. & Kippenberg, T. J. Radiation Pressure Cooling of a Micromechanical Oscillator Using Dynamical Backaction. *Physical Review Letters* **97**, 243905 (2006).
- [23] Cohadon, P. F., Heidmann, A. & Pinard, M. Cooling of a Mirror by Radiation Pressure. *Physical Review Letters* **83**, 3174–3177 (1999).
- [24] Kippenberg, T. J., Rokhsari, H., Carmon, T., Scherer, A. & Vahala, K. J. Analysis of Radiation-Pressure Induced Mechanical Oscillation of an Optical Microcavity. *Physical Review Letters* **95**, 033901 (2005).
- [25] Weis, S. *et al.* Optomechanically induced transparency. *Science* **330**, 1520–1523 (2010).

-
- [26] Safavi-Naeini, A. H. *et al.* Electromagnetically induced transparency and slow light with optomechanics. *Nature* **472**, 69–73 (2011).
- [27] Verhagen, E., Deléglise, S., Weis, S., Schliesser, A. & Kippenberg, T. J. Quantum-coherent coupling of a mechanical oscillator to an optical cavity mode. *Nature* **482**, 63–67 (2012).
- [28] Chan, J. *et al.* Laser cooling of a nanomechanical oscillator into its quantum ground state. *Nature* **478**, 89–92 (2011).
- [29] Nakamura, Y., Pashkin, Y. A. & Tsai, J. S. Coherent control of macroscopic quantum states in a single-cooper-pair box. *Nature* **398**, 786–788 (1999).
- [30] Wallraff, A. *et al.* Strong coupling of a single photon to a superconducting qubit using circuit quantum electrodynamics. *Nature* **431**, 162–167 (2004).
- [31] Regal, C. A., Teufel, J. D. & Lehnert, K. W. Measuring nanomechanical motion with a microwave cavity interferometer. *Nature Physics* **4**, 555–560 (2008).
- [32] Teufel, J. D., Harlow, J. W., Regal, C. A. & Lehnert, K. W. Dynamical backaction of microwave fields on a nanomechanical oscillator. *Phys. Rev. Lett.* **101**, 197203 (2008).
- [33] Teufel, J. D., Donner, T., Castellanos-Beltran, M. A., Harlow, J. W. & Lehnert, K. W. Nanomechanical motion measured with an imprecision below that at the standard quantum limit. *Nature Nanotechnology* **4**, 820–823 (2009).
- [34] Hertzberg, J. B. *et al.* Back-action-evading measurements of nanomechanical motion. *Nature Physics* **6**, 213–217 (2010).
- [35] Massel, F. *et al.* Microwave amplification with nanomechanical resonators. *Nature* **480**, 351–354 (2011).
- [36] Zhou, X. *et al.* Slowing, advancing and switching of microwave signals using circuit nanoelectromechanics. *Nature Physics* **9**, 179–184 (2013).
- [37] Cicak, K. *et al.* Low-loss superconducting resonant circuits using vacuum-gap-based microwave components. *Applied Physics Letters* **96**, 093502 (2010).
- [38] Cicak, K., Allman, M. S., Strong, J. A., Osborn, K. & Simmonds, R. W. Vacuum-Gap Capacitors for Low-Loss Superconducting Resonant Circuits. *IEEE Transactions on Applied Superconductivity* **19**, 948–952 (2009).
- [39] Teufel, J. D. *et al.* Circuit cavity electromechanics in the strong-coupling regime. *Nature* **471**, 204–208 (2011).

Bibliography

- [40] Teufel, J. D. *et al.* Sideband cooling of micromechanical motion to the quantum ground state. *Nature* **475**, 359–363 (2011).
- [41] Palomaki, T. A., Harlow, J. W., Teufel, J. D., Simmonds, R. W. & Lehnert, K. W. Coherent state transfer between itinerant microwave fields and a mechanical oscillator. *Nature* **495**, 210–214 (2013).
- [42] Palomaki, T. A., Teufel, J. D., Simmonds, R. W. & Lehnert, K. W. Entangling Mechanical Motion with Microwave Fields. *Science* **342**, 710–713 (2013).
- [43] O’Connell, A. D. *et al.* Quantum ground state and single-phonon control of a mechanical resonator. *Nature* **464**, 697–703 (2010).
- [44] Pirkkalainen, J.-M. *et al.* Hybrid circuit cavity quantum electrodynamics with a micromechanical resonator. *Nature* **494**, 211 (2013).
- [45] Lecocq, F., Teufel, J. D., Aumentado, J. & Simmonds, R. W. Resolving the vacuum fluctuations of an optomechanical system using an artificial atom. *Nat Phys* **11**, 635–639 (2015).
- [46] Milburn, G. & Woolley, M. An Introduction to Quantum Optomechanics. *Acta Physica Slovaca. Reviews and Tutorials* **61** (2011).
- [47] Chen, Y. Macroscopic quantum mechanics: theory and experimental concepts of optomechanics. *Journal of Physics B: Atomic, Molecular and Optical Physics* **46**, 104001 (2013).
- [48] Poyatos, J. F., Cirac, J. I. & Zoller, P. Quantum Reservoir Engineering with Laser Cooled Trapped Ions. *Physical Review Letters* **77**, 4728–4731 (1996).
- [49] Kronwald, A., Marquardt, F. & Clerk, A. A. Arbitrarily large steady-state bosonic squeezing via dissipation. *Physical Review A* **88**, 063833 (2013).
- [50] Tóth, L. D., Bernier, N. R., Nunnenkamp, A., Feofanov, A. K. & Kippenberg, T. J. A dissipative quantum reservoir for microwave light using a mechanical oscillator. *Nature Physics* **13**, 787–793 (2017).
- [51] Tóth, L. D., Bernier, N. R., Feofanov, A. K. & Kippenberg, T. J. A maser based on dynamical backaction on microwave light. *Physics Letters A* (2017).
- [52] Bernier, N. R. *et al.* Nonreciprocal reconfigurable microwave optomechanical circuit. *Nature Communications* **8**, 604 (2017).
- [53] Malz, D. *et al.* Quantum-limited directional amplifiers with optomechanics. *Phys. Rev. Lett.* **120**, 023601 (2018).

-
- [54] Marquardt, F. & Girvin, S. M. Optomechanics. *Physics* **2**, 40 (2009).
- [55] Rodgers, P. Nanomechanics: Welcome to the quantum ground state. *Nature Nanotechnology* **5**, 245–245 (2010).
- [56] Marquardt, F. Quantum mechanics: The gentle cooling touch of light. *Nature* **478**, 47–48 (2011).
- [57] Aspelmeyer, M., Meystre, P. & Schwab, K. Quantum optomechanics. *Physics Today* **65**, 29–35 (2012).
- [58] Meystre, P. A short walk through quantum optomechanics. *Annalen der Physik* **525**, 215–233 (2013).
- [59] Aspelmeyer, M., Kippenberg, T. J. & Marquardt, F. (eds.) *Cavity Optomechanics: Nano- and Micromechanical Resonators Interacting with Light*. Quantum Science and Technology (Springer-Verlag, Berlin Heidelberg, 2014). URL [//www.springer.com/de/book/9783642553110](http://www.springer.com/de/book/9783642553110).
- [60] Aspelmeyer, M., Kippenberg, T. J. & Marquardt, F. Cavity optomechanics. *Rev. Mod. Phys.* **86**, 1391–1452 (2014).
- [61] Gardiner, C. W. & Collett, M. J. Input and output in damped quantum systems: Quantum stochastic differential equations and the master equation. *Physical Review A* **31**, 3761–3774 (1985).
- [62] Gardiner, C. & Zoller, P. *Quantum Noise: A Handbook of Markovian and Non-Markovian Quantum Stochastic Methods with Applications to Quantum Optics*. Springer Series in Synergetics (Springer-Verlag, Berlin Heidelberg, 2004), 3 edn. URL [//www.springer.com/us/book/9783540223016](http://www.springer.com/us/book/9783540223016).
- [63] Haken, H. *Light and Matter Ic / Licht und Materie Ic*. Optik / Optics (Springer-Verlag, Berlin Heidelberg, 1970). URL [//www.springer.com/us/book/9783662220917](http://www.springer.com/us/book/9783662220917).
- [64] Scully, M. O. & Zubairy, M. S. *Quantum Optics* (Cambridge University Press, 1997).
- [65] Barchielli, A. & Vacchini, B. Quantum Langevin equations for optomechanical systems. *New Journal of Physics* **17**, 083004 (2015).
- [66] Pozar, D. M. *Microwave Engineering* (Wiley, 2011), 4th edn.
- [67] Suh, J. *et al.* Mechanically detecting and avoiding the quantum fluctuations of a microwave field. *Science* **344**, 1262–1265 (2014).

Bibliography

- [68] Clerk, A. A., Marquardt, F. & Jacobs, K. Back-action evasion and squeezing of a mechanical resonator using a cavity detector. *New Journal of Physics* **10**, 095010 (2008).
- [69] Rocheleau, T. *et al.* Preparation and detection of a mechanical resonator near the ground state of motion. *Nature* **463**, 72 (2010).
- [70] Barzanjeh, S. *et al.* Mechanical on-chip microwave circulator. *Nature Communications* **8**, 953 (2017).
- [71] Martinis, J. M. & Megrant, A. UCSB final report for the CSQ program: Review of decoherence and materials physics for superconducting qubits. *arXiv:1410.5793 [cond-mat, physics:quant-ph]* (2014). ArXiv: 1410.5793.
- [72] Paik, H. & Osborn, K. D. Reducing quantum-regime dielectric loss of silicon nitride for superconducting quantum circuits. *Applied Physics Letters* **96**, 072505 (2010).
- [73] Suh, J., Shaw, M. D., LeDuc, H. G., Weinstein, A. J. & Schwab, K. C. Thermally Induced Parametric Instability in a Back-Action Evading Measurement of a Micromechanical Quadrature near the Zero-Point Level. *Nano Letters* **12**, 6260–6265 (2012).
- [74] Suh, J., Weinstein, A. J. & Schwab, K. C. Optomechanical effects of two-level systems in a back-action evading measurement of micro-mechanical motion. *Applied Physics Letters* **103**, 052604 (2013).
- [75] Pirkkalainen, J.-M., Damskäg, E., Brandt, M., Massel, F. & Sillanpää, M. Squeezing of Quantum Noise of Motion in a Micromechanical Resonator. *Physical Review Letters* **115**, 243601 (2015).
- [76] Kusaka, K., Hanabusa, T., Nishida, M. & Inoko, F. Residual stress and in-situ thermal stress measurement of aluminum film deposited on silicon wafer. *Thin Solid Films* **290–291**, 248–253 (1996).
- [77] Thornton, J. A. & Hoffman, D. W. Stress-related effects in thin films. *Thin Solid Films* **171**, 5–31 (1989).
- [78] Pletea, M., Koch, R., Wendrock, H., Kaltoven, R. & Schmidt, O. G. In situ stress evolution during and after sputter deposition of Al thin films. *Journal of Physics: Condensed Matter* **21**, 225008 (2009).
- [79] Chinmulgund, M., Inturi, R. B. & Barnard, J. A. Effect of Ar gas pressure on growth, structure, and mechanical properties of sputtered Ti, Al, TiAl, and Ti3Al films. *Thin Solid Films* **270**, 260–263 (1995).

-
- [80] Abermann, R. Internal stress of vapour-deposited aluminium films: Effect of O₂ and water vapour present during film deposition. *Thin Solid Films* **186**, 233–240 (1990).
- [81] Sage, J. M., Bolkhovsky, V., Oliver, W. D., Turek, B. & Welander, P. B. Study of loss in superconducting coplanar waveguide resonators. *Journal of Applied Physics* **109**, 063915 (2011).
- [82] Ohya, S. *et al.* Room temperature deposition of sputtered TiN films for superconducting coplanar waveguide resonators. *Superconductor Science and Technology* **27**, 015009 (2014).
- [83] Megrant, A. *et al.* Planar superconducting resonators with internal quality factors above one million. *Applied Physics Letters* **100**, 113510 (2012).
- [84] Vissers, M. R. *et al.* Low loss superconducting titanium nitride coplanar waveguide resonators. *Applied Physics Letters* **97**, 232509 (2010).
- [85] Sandberg, M. *et al.* Etch induced microwave losses in titanium nitride superconducting resonators. *Applied Physics Letters* **100**, 262605 (2012).
- [86] Ghadimi, A. H. *et al.* Strain engineering for ultra-coherent nanomechanical oscillators. *arXiv:1711.06247 [cond-mat, physics:physics, physics:quant-ph]* (2017). ArXiv: 1711.06247.
- [87] Mets501. URL <https://commons.wikimedia.org/>.
- [88] Pavese, F. & Molinar, G. *Modern Gas-Based Temperature and Pressure Measurements* (Springer Science+Business Media LLC, 1992).
- [89] Probst, S., Song, F. B., Bushev, P. A., Ustinov, A. V. & Weides, M. Efficient and robust analysis of complex scattering data under noise in microwave resonators. *Review of Scientific Instruments* **86**, 024706 (2015).
- [90] Chernov, N. & Lesort, C. Least Squares Fitting of Circles. *Journal of Mathematical Imaging and Vision* **23**, 239–252 (2005).
- [91] Stevens, J. *Theory and Design of Multimode Electromechanical Circuits*. Master’s thesis, EPFL (2017).
- [92] Caldeira, A. O. & Leggett, A. J. Influence of dissipation on quantum tunneling in macroscopic systems. *Phys. Rev. Lett.* **46**, 211–214 (1981).
- [93] Krauter, H. *et al.* Entanglement generated by dissipation and steady state entanglement of two macroscopic objects. *Phys. Rev. Lett.* **107**, 080503 (2011).

Bibliography

- [94] Barreiro, J. T. *et al.* An open-system quantum simulator with trapped ions. *Nature* **470**, 486–491 (2011).
- [95] Lin, Y. *et al.* Dissipative production of a maximally entangled steady state of two quantum bits. *Nature* **504**, 415–418 (2013).
- [96] Kienzler, D. *et al.* Quantum harmonic oscillator state synthesis by reservoir engineering. *Science* **347**, 53–56 (2015).
- [97] Murch, K. W. *et al.* Cavity-Assisted Quantum Bath Engineering. *Physical Review Letters* **109**, 183602 (2012).
- [98] Shankar, S. *et al.* Autonomously stabilized entanglement between two superconducting quantum bits. *Nature* **504**, 419–422 (2013).
- [99] Leghtas, Z. *et al.* Confining the state of light to a quantum manifold by engineered two-photon loss. *Science* **347**, 853–857 (2015).
- [100] Aspelmeyer, M., Kippenberg, T. J. & Marquardt, F. Cavity optomechanics. *Reviews of Modern Physics* **86**, 1391–1452 (2014).
- [101] Woolley, M. J. & Clerk, A. A. Two-mode squeezed states in cavity optomechanics via engineering of a single reservoir. *Physical Review A* **89**, 063805 (2014).
- [102] Wollman, E. E. *et al.* Quantum squeezing of motion in a mechanical resonator. *Science* **349**, 952–955 (2015).
- [103] Lecocq, F., Clark, J., Simmonds, R., Aumentado, J. & Teufel, J. Quantum Nondemolition Measurement of a Nonclassical State of a Massive Object. *Physical Review X* **5**, 041037 (2015).
- [104] Wang, Y.-D. & Clerk, A. A. Reservoir-Engineered Entanglement in Optomechanical Systems. *Physical Review Letters* **110**, 253601 (2013).
- [105] Metelmann, A. & Clerk, A. Quantum-Limited Amplification via Reservoir Engineering. *Physical Review Letters* **112**, 133904 (2014).
- [106] Nunnenkamp, A., Sudhir, V., Feofanov, A. K., Roulet, A. & Kippenberg, T. J. Quantum-Limited Amplification and Parametric Instability in the Reversed Dissipation Regime of Cavity Optomechanics. *Physical Review Letters* **113**, 023604 (2014).
- [107] Kronwald, A., Marquardt, F. & Clerk, A. A. Dissipative optomechanical squeezing of light. *New Journal of Physics* **16**, 063058 (2014).

-
- [108] Metelmann, A. & Clerk, A. Nonreciprocal Photon Transmission and Amplification via Reservoir Engineering. *Physical Review X* **5**, 021025 (2015).
- [109] Marquardt, F., Harris, J. & Girvin, S. Dynamical Multistability Induced by Radiation Pressure in High-Finesse Micromechanical Optical Cavities. *Physical Review Letters* **96**, 103901 (2006).
- [110] Braginsky, V. B. & Vyatchanin, S. P. Low quantum noise tranquilizer for Fabry–Perot interferometer. *Physics Letters A* **293**, 228–234 (2002).
- [111] Gigan, S. *et al.* Self-cooling of a micromirror by radiation pressure. *Nature* **444**, 67–70 (2006).
- [112] Arcizet, O., Cohadon, P.-F., Briant, T., Pinard, M. & Heidmann, A. Radiation-pressure cooling and optomechanical instability of a micromirror. *Nature* **444**, 71–74 (2006).
- [113] Kells, W. & D’Ambrosio, E. Considerations on parametric instability in Fabry–Perot interferometer. *Physics Letters A* **299**, 326–330 (2002).
- [114] Safavi-Naeini, A. H. *et al.* Squeezed light from a silicon micromechanical resonator. *Nature* **500**, 185–189 (2013).
- [115] Purdy, T. P., Yu, P.-L., Peterson, R. W., Kampel, N. S. & Regal, C. A. Strong Optomechanical Squeezing of Light. *Physical Review X* **3**, 031012 (2013).
- [116] Sudhir, V. *et al.* Appearance and Disappearance of Quantum Correlations in Measurement-Based Feedback Control of a Mechanical Oscillator. *Physical Review X* **7**, 011001 (2017).
- [117] Nielsen, W. H. P., Tsaturyan, Y., Møller, C. B., Polzik, E. S. & Schliesser, A. Multimode optomechanical system in the quantum regime. *Proceedings of the National Academy of Sciences* **114**, 62–66 (2017).
- [118] Riedinger, R. *et al.* Non-classical correlations between single photons and phonons from a mechanical oscillator. *Nature* **530**, 313–316 (2016).
- [119] Marquardt, F., Chen, J. P., Clerk, A. A. & Girvin, S. M. Quantum Theory of Cavity-Assisted Sideband Cooling of Mechanical Motion. *Physical Review Letters* **99** (2007).
- [120] Wilson-Rae, I., Nooshi, N., Zwerger, W. & Kippenberg, T. J. Theory of Ground State Cooling of a Mechanical Oscillator Using Dynamical Backaction. *Physical Review Letters* **99** (2007).

Bibliography

- [121] Schliesser, A., Rivière, R., Anetsberger, G., Arcizet, O. & Kippenberg, T. J. Resolved-sideband cooling of a micromechanical oscillator. *Nature Physics* **4**, 415–419 (2008).
- [122] Schliesser, A., Rivière, R., Anetsberger, G., Arcizet, O. & Kippenberg, T. J. Resolved-sideband cooling of a micromechanical oscillator. *Nat Phys* **4**, 415–419 (2008).
- [123] Cicak, K. *et al.* Low-loss superconducting resonant circuits using vacuum-gap-based microwave components. *Applied Physics Letters* **96** (2010).
- [124] Dobrindt, J. M., Wilson-Rae, I. & Kippenberg, T. J. Parametric normal-mode splitting in cavity optomechanics. *Phys. Rev. Lett.* **101**, 263602 (2008).
- [125] Kippenberg, T. J., Rokhsari, H., Carmon, T., Scherer, A. & Vahala, K. J. Analysis of radiation-pressure induced mechanical oscillation of an optical microcavity. *Phys. Rev. Lett.* **95**, 033901 (2005).
- [126] Megrant, A. *et al.* Planar superconducting resonators with internal quality factors above one million. *Applied Physics Letters* **100**, 113510 (2012).
- [127] Clerk, A. A., M. H. Devoret, Girvin, S. M., Marquardt, F. & Schoelkopf, R. J. Introduction to quantum noise, measurement, and amplification. *Reviews of Modern Physics* **82**, 1155–1208 (2010).
- [128] Marquardt, F., Harris, J. G. E. & Girvin, S. M. Dynamical multistability induced by radiation pressure in high-finesse micromechanical optical cavities. *Phys. Rev. Lett.* **96**, 103901 (2006).
- [129] Grudinin, I. S., Lee, H., Painter, O. & Vahala, K. J. Phonon laser action in a tunable two-level system. *Phys. Rev. Lett.* **104**, 083901 (2010).
- [130] Astafiev, O. *et al.* Single artificial-atom lasing. *Nature* **449**, 588–590 (2007).
- [131] Caves, C. M. Quantum limits on noise in linear amplifiers. *Physical Review D* **26**, 1817–1839 (1982).
- [132] Siegman, A. E. *Lasers* (Univ. Science Books, Mill Valley, Calif, 1986).
- [133] Knünz, S. *et al.* Injection Locking of a Trapped-Ion Phonon Laser. *Physical Review Letters* **105**, 013004 (2010).
- [134] St-Jean, M. R. *et al.* Injection locking of mid-infrared quantum cascade laser at 14 GHz, by direct microwave modulation. *Laser & Photonics Reviews* **8**, 443–449 (2014).

-
- [135] Liu, Y.-Y., Stehlik, J., Gullans, M. J., Taylor, J. M. & Petta, J. R. Injection locking of a semiconductor double-quantum-dot micromaser. *Physical Review A* **92**, 053802 (2015).
- [136] Cassidy, M. C. *et al.* Demonstration of an ac Josephson junction laser. *Science* **355**, 939–942 (2017).
- [137] Adler, R. A Study of Locking Phenomena in Oscillators. *Proceedings of the IRE* **34**, 351–357 (1946).
- [138] Pikovsky, A., Rosenblum, M. & Kurths, J. *Synchronization: A Universal Concept in Nonlinear Sciences* (Cambridge University Press, 2003).
- [139] Ockeloen-Korppi, C. F. *et al.* Low-Noise Amplification and Frequency Conversion with a Multiport Microwave Optomechanical Device. *Physical Review X* **6**, 041024 (2016).
- [140] Bergeal, N. *et al.* Phase-preserving amplification near the quantum limit with a josephson ring modulator. *Nature* **465**, 64–68 (2010).
- [141] Eichler, C., Salathe, Y., Mlynek, J., Schmidt, S. & Wallraff, A. Quantum-limited amplification and entanglement in coupled nonlinear resonators. *Phys. Rev. Lett.* **113**, 110502 (2014).
- [142] Castellanos-Beltran, M. A., Irwin, K. D., Hilton, G. C., Vale, L. R. & Lehnert, K. W. Amplification and squeezing of quantum noise with a tunable josephson metamaterial. *Nat Phys* **4**, 929–931 (2008).
- [143] Bloembergen, N. *Nonlinear Optics* (World Scientific Pub Co Inc, 1996), 4th edn.
- [144] Sliwa, K. *et al.* Reconfigurable josephson circulator / directional amplifier. *Physical Review X* **5**, 041020 (2015).
- [145] Andrews, R. W., Reed, A. P., Cicak, K., Teufel, J. D. & Lehnert, K. W. Quantum-enabled temporal and spectral mode conversion of microwave signals. *Nature Communications* **6**, 10021 (2015).
- [146] Grajcar, M. *et al.* Sisyphus cooling and amplification by a superconducting qubit. *Nat Phys* **4**, 612–616 (2008).
- [147] Kerckhoff, J. *et al.* Tunable coupling to a mechanical oscillator circuit using a coherent feedback network. *Phys. Rev. X* **3**, 021013 (2013).
- [148] Devoret, M. H. & Schoelkopf, R. J. Superconducting circuits for quantum information: An outlook. *Science* **339**, 1169–1174 (2013).

Bibliography

- [149] Bernier, N. R., Tóth, L. D., Feofanov, A. K. & Kippenberg, T. Nonreciprocity in microwave optomechanical circuits. *To appear in IEEE Antennas and Wireless Propagation Letters* (2018).
- [150] Feynman, R. P. *QED: The Strange Theory of Light and Matter* (Princeton University Press, 1988), New Ed edn.
- [151] Jalas, D. *et al.* What is — and what is not — an optical isolator. *Nature Photonics* **7**, 579–582 (2013).
- [152] Auld, B. A. The Synthesis of Symmetrical Waveguide Circulators. *IRE Transactions on Microwave Theory and Techniques* **7**, 238–246 (1959).
- [153] Milano, U., Saunders, J. H. & Davis, L. A Y-Junction Strip-Line Circulator. *IRE Transactions on Microwave Theory and Techniques* **8**, 346–351 (1960).
- [154] Fay, C. E. & Comstock, R. L. Operation of the Ferrite Junction Circulator. *IEEE Transactions on Microwave Theory and Techniques* **13**, 15–27 (1965).
- [155] Aplet, L. J. & Carson, J. W. A Faraday Effect Optical Isolator. *Applied Optics* **3**, 544–545 (1964).
- [156] Shirasaki, M. & Asama, K. Compact optical isolator for fibers using birefringent wedges. *Applied Optics* **21**, 4296–4299 (1982).
- [157] Sato, T., Sun, J., Kasahara, R. & Kawakami, S. Lens-free in-line optical isolators. *Optics Letters* **24**, 1337–1339 (1999).
- [158] Bi, L. *et al.* On-chip optical isolation in monolithically integrated non-reciprocal optical resonators. *Nature Photonics* **5**, 758–762 (2011).
- [159] Manipatruni, S., Robinson, J. T. & Lipson, M. Optical Nonreciprocity in Optomechanical Structures. *Physical Review Letters* **102**, 213903 (2009).
- [160] Fan, L. *et al.* An All-Silicon Passive Optical Diode. *Science* **335**, 447–450 (2012).
- [161] Guo, X., Zou, C.-L., Jung, H. & Tang, H. X. On-Chip Strong Coupling and Efficient Frequency Conversion between Telecom and Visible Optical Modes. *Physical Review Letters* **117**, 123902 (2016).
- [162] Anderson, B. D. O. & Newcomb, R. W. On reciprocity and time-variable networks. *Proceedings of the IEEE* **53**, 1674–1674 (1965).
- [163] Yu, Z. & Fan, S. Complete optical isolation created by indirect interband photonic transitions. *Nature Photonics* **3**, 91–94 (2009).

-
- [164] Lira, H., Yu, Z., Fan, S. & Lipson, M. Electrically Driven Nonreciprocity Induced by Interband Photonic Transition on a Silicon Chip. *Physical Review Letters* **109**, 033901 (2012).
- [165] Kang, M. S., Butsch, A. & Russell, P. S. J. Reconfigurable light-driven opto-acoustic isolators in photonic crystal fibre. *Nature Photonics* **5**, 549–553 (2011).
- [166] Estep, N. A., Sounas, D. L., Soric, J. & Alù, A. Magnetic-free non-reciprocity and isolation based on parametrically modulated coupled-resonator loops. *Nature Physics* **10**, 923–927 (2014).
- [167] Peng, B. *et al.* Parity-time-symmetric whispering-gallery microcavities. *Nature Physics* **10**, 394–398 (2014).
- [168] Scheucher, M., Hilico, A., Will, E., Volz, J. & Rauschenbeutel, A. Quantum optical circulator controlled by a single chirally coupled atom. *Science* **354**, 1577–1580 (2016).
- [169] Fleury, R., Sounas, D. L., Sieck, C. F., Haberman, M. R. & Alù, A. Sound Isolation and Giant Linear Nonreciprocity in a Compact Acoustic Circulator. *Science* **343**, 516–519 (2014).
- [170] Devoret, M. H. & Schoelkopf, R. J. Superconducting circuits for quantum information: An outlook. *Science* **339**, 1169 (2013).
- [171] Kerckhoff, J., Lalumière, K., Chapman, B. J., Blais, A. & Lehnert, K. W. On-Chip Superconducting Microwave Circulator from Synthetic Rotation. *Physical Review Applied* **4**, 034002 (2015).
- [172] Ranzani, L. & Aumentado, J. A geometric description of nonreciprocity in coupled two-mode systems. *New Journal of Physics* **16**, 103027 (2014).
- [173] White, T. C. *et al.* Traveling wave parametric amplifier with Josephson junctions using minimal resonator phase matching. *Applied Physics Letters* **106**, 242601 (2015).
- [174] Macklin, C. *et al.* A near-quantum-limited Josephson traveling-wave parametric amplifier. *Science* **350**, 307–310 (2015).
- [175] Hua, S. *et al.* Demonstration of a chip-based optical isolator with parametric amplification. *Nature Communications* **7**, 13657 (2016).
- [176] Bowen, W. P. & Milburn, G. J. *Quantum Optomechanics* (CRC Press, 2015).
- [177] Hafezi, M. & Rabl, P. Optomechanically induced non-reciprocity in microring resonators. *Optics Express* **20**, 7672–7684 (2012).

Bibliography

- [178] Shen, Z. *et al.* Experimental realization of optomechanically induced non-reciprocity. *Nature Photonics* **10**, 657–661 (2016).
- [179] Ruesink, F., Miri, M.-A., Alù, A. & Verhagen, E. Nonreciprocity and magnetic-free isolation based on optomechanical interactions. *Nature Communications* **7**, 13662 (2016).
- [180] Ranzani, L. & Aumentado, J. Graph-based analysis of nonreciprocity in coupled-mode systems. *New Journal of Physics* **17**, 023024 (2015).
- [181] Lecocq, F. *et al.* Nonreciprocal microwave signal processing with a field-programmable josephson amplifier. *Phys. Rev. Applied* **7**, 024028 (2017).
- [182] Abdo, B., Sliwa, K., Frunzio, L. & Devoret, M. Directional Amplification with a Josephson Circuit. *Physical Review X* **3**, 031001 (2013).
- [183] Abdo, B. *et al.* Josephson Directional Amplifier for Quantum Measurement of Superconducting Circuits. *Physical Review Letters* **112**, 167701 (2014).
- [184] Abdo, B. *et al.* Multi-path interferometric josephson directional amplifier for qubit readout. *Quantum Science and Technology* **3**, 024003 (2018).
- [185] Abdo, B., Brink, M. & Chow, J. M. Gyrator Operation Using Josephson Mixers. *Physical Review Applied* **8**, 034009 (2017).
- [186] Chapman, B. J. *et al.* Widely Tunable On-Chip Microwave Circulator for Superconducting Quantum Circuits. *Physical Review X* **7**, 041043 (2017).
- [187] Ho Eom, B., Day, P. K., LeDuc, H. G. & Zmuidzinas, J. A wideband, low-noise superconducting amplifier with high dynamic range. *Nature Physics* **8**, 623–627 (2012).
- [188] Vissers, M. R. *et al.* Low-noise kinetic inductance traveling-wave amplifier using three-wave mixing. *Applied Physics Letters* **108**, 012601 (2016). <https://doi.org/10.1063/1.4937922>.
- [189] Hover, D. *et al.* Superconducting low-inductance undulatory galvanometer microwave amplifier. *Applied Physics Letters* **100**, 063503 (2012). <https://doi.org/10.1063/1.3682309>.
- [190] Thorbeck, T. *et al.* Reverse isolation and backaction of the slug microwave amplifier. *Phys. Rev. Applied* **8**, 054007 (2017).
- [191] Safavi-Naeini, A. H. & Painter, O. Proposal for an optomechanical traveling wave phonon–photon translator. *New Journal of Physics* **13**, 013017 (2011).

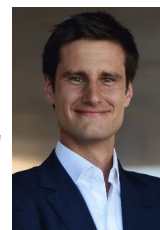
-
- [192] Fang, K., Yu, Z. & Fan, S. Photonic Aharonov-Bohm Effect Based on Dynamic Modulation. *Physical Review Letters* **108**, 153901 (2012).
- [193] Fang, K., Yu, Z. & Fan, S. Experimental demonstration of a photonic Aharonov-Bohm effect at radio frequencies. *Physical Review B* **87**, 060301 (2013).
- [194] Tzuang, L. D., Fang, K., Nussenzeig, P., Fan, S. & Lipson, M. Non-reciprocal phase shift induced by an effective magnetic flux for light. *Nature Photonics* **8**, 701–705 (2014).
- [195] Fang, K. *et al.* Generalized non-reciprocity in an optomechanical circuit via synthetic magnetism and reservoir engineering. *Nat Phys* **13**, 465–471 (2017).
- [196] Xu, X.-W., Li, Y., Chen, A.-X. & Liu, Y.-x. Nonreciprocal conversion between microwave and optical photons in electro-optomechanical systems. *Physical Review A* **93**, 023827 (2016).
- [197] Tian, L. & Li, Z. Nonreciprocal State Conversion between Microwave and Optical Photons. *arXiv:1610.09556 [cond-mat, physics:quant-ph]* (2016). ArXiv: 1610.09556.
- [198] Lecocq, F., Clark, J., Simmonds, R., Aumentado, J. & Teufel, J. Mechanically Mediated Microwave Frequency Conversion in the Quantum Regime. *Physical Review Letters* **116**, 043601 (2016).
- [199] Andrews, R. W. *et al.* Bidirectional and efficient conversion between microwave and optical light. *Nature Physics* **10**, 321–326 (2014).
- [200] Clark, J. B., Lecocq, F., Simmonds, R. W., Aumentado, J. & Teufel, J. D. Sideband cooling beyond the quantum backaction limit with squeezed light. *Nature* **541**, 191–195 (2017).
- [201] Manzeli, S., Ovchinnikov, D., Pasquier, D., V. Yazyev, O. & Kis, A. 2d transition metal dichalcogenides. *Nature Reviews Materials* **2** (2017).
- [202] Staley, N. E. *et al.* Electric field effect on superconductivity in atomically thin flakes of nbse2. *Physical Review B* **80**, 184505 (2009).

László Dániel Tóth

GRADUATING PHD CANDIDATE IN PHYSICS · KEEN INTEREST IN TECHNOLOGY AND BUSINESS

Date of birth: 10 July 1988 Nationality: Hungarian Address: Avenue du Chablais 30, 1007 Lausanne, CH

☎ (+41) 787581250 | ✉ laszlo.daniel.toth.88@gmail.com | 📱 laszlo-daniel-toth-2ab99499



Education

Swiss Federal Institute of Technology in Lausanne (EPFL)

Lausanne, Switzerland

PHD IN PHYSICS, MARIE CURIE FELLOW

Sept. 2013 - Exp. Spring 2018

- started a new direction in the research group, including setting up a laboratory and a fabrication process
- 1st author publication in Nature Physics and co-author on 6 other peer-reviewed scientific publications
- given 8 talks on international conferences (Europe, US, Asia)
- 4 successful master theses were carried out in this new scientific direction

King Abdullah University of Science and Technology (KAUST)

Thuwal, Saudi Arabia

MSC. IN ELECTRICAL ENGINEERING (PHOTONICS), WITH DISTINCTION (GPA: 3.91/4)

2011 - 2013

University of Cambridge

Cambridge, United Kingdom

MS IN APPLIED MATHEMATICS AND THEORETICAL PHYSICS, WITH MERIT

2010 - 2011

- graduated with merit with a highlighted thesis on quantum feedback control

Eötvös Loránd University

Budapest, Hungary

BSC. IN PHYSICS, WITH DISTINCTION (CUM. GPA: 4.8/5, TOP 5%)

2007 - 2010

- work derived from the BSc thesis was later published in *Physical Review Letters*

Experience

ShARE, global student consultancy and think tank

EPFL, Switzerland

GLOBAL PRESIDENT (EUROPE REGION) AND LOCAL PRESIDENT (EPFL)

2014 - present

A global, nonprofit association for students who wish to acquire a consulting toolkit through trainings and projects with companies.

- **Negotiation and project management:** managed and/or negotiated multiple **consulting-like projects** - market research and entry strategy, governance and compliance, interviewing experts etc. - with **2 multinational companies, an NGO, 3 startups and the university**; derived local revenue of over **12k CHF in a year**
- **Teamwork:** worked in a team of 3-5 on 2 different projects which were presented by the team to senior managers (finance department of a multinational company; co-founder of Tech. Transfer Office at EPFL); engaged in the management team of ShARE Global
- **Leadership:** as president, overseeing a team of 15-20 students, maintaining the quality of projects and establishing new partnerships (new long-term partners: Tech. Transfer Office at EPFL, Sustainable Campus at EPFL, startup with > \$50M in investment)

The Consulting Society

EPFL, Switzerland

VICE-PRESIDENT

Jan. 2016 - present

TCS organizes networking and informational events, workshops and discussion forums related to consultancy and business at EPFL.

- **Responsible:** established and maintained the relationship with external partners (main contacts: BCG, PwC, Open Web Technology)
- **Proactive:** organizer of the 1st and 2nd Business Case Competition at EPFL (negotiating corporate partnerships [over 6k CHF raised], reviewing case study material etc.) and lead organizer of a consulting round table with 4 consulting companies and over 100 students
- **Strategic:** defining the strategy and the structure of the society; oversaw **growth of over 70%** (membership and student engagement)

Institute of Materials Research and Engineering, A*STAR's R&D center

Singapore

R&D INTERN UNDER THE SINGAPOREAN PRE-GRADUATE AWARD

2012 Summer

- Exposition to industrial R&D management and processes, labs and clean rooms

University of California, Berkeley

Berkeley, USA

SUMMER RESEARCH STUDENT

2009 Summer

Scientific output

Publications

- N. R. Bernier, **L. D. Tóth**, A. K. Feofanov and T. J. Kippenberg: Nonreciprocity in microwave optomechanical circuits. To appear in a special issue “Magnet-less Nonreciprocity in Electromagnetics” in IEEE Antennas and Wireless Propagation Letters.
- N. R. Bernier, **L. D. Tóth**, A. K. Feofanov and T. J. Kippenberg: Observation of level attraction in a circuit optomechanical system. Submitted.
- D. Malz, **L. D. Tóth**, N. R. Bernier, A. K. Feofanov, T. J. Kippenberg and A. Nunnenkamp: Quantum-limited directional amplifiers with optomechanics. *Physical Review Letters* **120**, 023601 (2018)
- **L. D. Tóth**, N. R. Bernier, A. Nunnenkamp, A. K. Feofanov and T. J. Kippenberg: A dissipative quantum reservoir for microwave light using a mechanical oscillator. *Nature Physics* **13**, 787-793 (2017)
- **L. D. Tóth**, N. R. Bernier, A. K. Feofanov and T. J. Kippenberg: A maser based on dynamical backaction on microwave light. *Physics Letters A*, In press, available online: <https://doi.org/10.1016/j.physleta.2017.05.045> (2017)
- N. R. Bernier, **L. D. Tóth**, A. Koottandavida, M. A. Ioannou, D. Malz, A. Nunnenkamp, A. K. Feofanov and T. J. Kippenberg: Nonreciprocal reconfigurable microwave optomechanical circuit. *Nature Communications* **8**, 604 (2017)
- C. Javerzac-Galy, K. Plekhanov, N. R. Bernier, **L. D. Tóth**, A. K. Feofanov and T. J. Kippenberg: On-chip microwave-to-optical quantum coherent converter based on a superconducting resonator coupled to an electro-optic microresonator. *Physical Review A* **94**, 053815 (2016)
- T. Kiss, S. Vymětal, **L. D. Tóth**, A. Gábris, I. Jex, G. Alber: Measurement-Induced Chaos with Entangled States, *Physical Review Letters* **107**, 100501 (2011)

Talks at international conferences

PRESENTER

- *A nonreciprocal reconfigurable optomechanical circuit*. APS March meeting, Los Angeles, CA, USA (March 2018).
- *Dissipation as a resource in circuit optomechanics*. Marie Skłodowska Curie OMT-HOT annual meeting, Saanen, Switzerland (Feb 2018).
- *Dissipation as a resource for quantum-limited amplification and nonreciprocal devices in circuit optomechanics*. ISNTT Symposium on Nanoscale Transport and Technology, Atsugi, Japan (November 2017).
- *A dissipative quantum reservoir for microwave light using a mechanical oscillator*. APS March meeting, New Orleans, LA, USA (March 2017).
- *A dissipative quantum reservoir for microwave light using a mechanical oscillator*. Frontiers in Nanomechanical Systems, La Thuile, Italy (Feb 2017).
- *The reversed dissipation regime of cavity optomechanics*. Marie Curie ITN cQOM annual meeting, Diavolezza, Switzerland (Feb 2016).
- *Fabrication of superconducting microwave circuits for applications in quantum electromechanics*. Harvard Center for Nanoscale Systems, Boston, MA, USA (June 2015).
- *Implementing a quantum-limited amplifier in microwave optomechanics*. Marie Curie ITN cQOM annual meeting, Diavolezza, Switzerland (Feb 2015).

Business certificates, workshops

Competitions and courses at EPFL

EPFL, Switzerland

- Participant of a business case competition organized by Deloitte for student associations (2nd place)
- Organizer of the 1st and 2nd university-wide business case competition
- Management of Innovation and Technology Transfer: a 3-day course and a group project given by the Tech Transfer Office

Cornell Entrepreneurship Certificate Program by the Johnson Business School

KAUST, Saudi Arabia

PARTICIPANT

2012 January

- A two weeks long course on a wide range of entrepreneurship- and business-related topics
- Our startup idea on a heavy metal detector based on microfluidics received a **\$200k seed fund** and is still an active company

Honors & Awards

| | | |
|------|--|---------------------|
| 2013 | Marie Curie Fellowship (early-stage researcher, network: cQOM), | European Union |
| 2012 | Singapore International Pre-Graduate Award (SIGPA), | A*STAR, Singapore |
| 2012 | Provost Award and KAUST Fellowship, | KAUST, Saudi Arabia |
| 2011 | Highlighted project essay, | Cambridge, UK |
| 2009 | Excellent Student of the Faculty, | Hungary |
| 2009 | Honourable mention, Ortvy Rudolf Problem Solving Contest in Physics, | Hungary |
| 2007 | 1st place, National Competition for High School Students (philosophy), | Hungary |

Languages and technical skills

| | |
|---------------------|---|
| Languages | Hungarian (native), English (full working proficiency), French (B1, active), German (B1, passive) |
| Programming | Python, JavaScript, Matlab, Mathematica, C/C++, LaTeX |
| Presentation | Advanced Microsoft PowerPoint, Keynote and Beamer |
| Office | Advanced MS Excel and Word. Familiarity with MySQL |
| Simulations | Various software packages (COMSOL, Sonnet) for finite element modelling and time-domain simulations |
| Industry | Micro- and nanofabrication techniques across various fields (semiconductor and superconductor technology etc.), ultra-low temperature measurements, microwave electronics, optics |

Interests and hobbies

| | |
|-------------------|--|
| Education | Passionate about teaching, private tutoring and contributor to online education platforms (e.g. Khan Academy) |
| Sports | Paragliding (working hard on my first 100 km flight), downhill mountain biking, snowboarding, diving |
| Music | Enjoy playing the piano and the guitar, as well as reading (and teaching) about music theory |
| Philosophy | Current interests: analytical philosophy; ethics of eating and animal rights; Alan Watts and the Eastern tradition |